# ABSTRACT

Title of Document: Guided Lamb Wave Based 2-D Spiral Phased Array for Structural Health Monitoring of Thin Panel Structures

Byungseok Yoo, Doctor of Philosophy, 2011

Directed By: Professor Darryll J. Pines
Department of Aerospace Engineering

In almost all industries of mechanical, aerospace, and civil engineering fields, structural health monitoring (SHM) technology is essentially required for providing the reliable information of structural integrity of safety-critical structures, which can help reduce the risk of unexpected and sometimes catastrophic failures, and also offer cost-effective inspection and maintenance of the structures. State of the art SHM research on structural damage diagnosis is focused on developing global and real-time technologies to identify the existence, location, extent, and type of damage.

In order to detect and monitor the structural damage in plate-like structures, SHM technology based on guided Lamb wave (GLW) interrogation is becoming more attractive due to its potential benefits such as large inspection area coverage in short time, simple inspection mechanism, and sensitivity to small damage. However, the GLW method has a few critical issues such as dispersion nature, mode conversion and separation, and multiple-mode existence.

Phased array technique widely used in all aspects of civil, military, science, and medical industry fields may be employed to resolve the drawbacks of the GLW method. The GLW-based phased array approach is able to effectively examine and analyze complicated structural vibration responses in thin plate structures. Because the phased sensor array operates as a spatial filter for the GLW signals, the array signal processing method can enhance a desired signal component at a specific direction while eliminating other signal components from other directions.

This dissertation presents the development, the experimental validation, and the damage detection applications of an innovative signal processing algorithm based on two-dimensional (2-D) spiral phased array in conjunction with the GLW interrogation technique. It starts with general backgrounds of SHM and the associated technology including the GLW interrogation method. Then, it is focused on the fundamentals of the GLW-based phased array approach and the development of an innovative signal processing algorithm associated with the 2-D spiral phased sensor array. The SHM approach based on array responses determined by the proposed phased array algorithm implementation is addressed. The experimental validation of the GLW-based 2-D spiral phased array technology and the associated damage detection applications to thin isotropic plate and anisotropic composite plate structures are presented.

# GUIDED LAMB WAVE BASED 2-D SPIRAL PHASED ARRAY FOR STRUCTURAL HEALTH MONITORING OF THIN PANEL STRUCTURES

By

Byungseok Yoo

Dissertation submitted to the Faculty of the Graduate School of the
University of Maryland, College Park, in partial fulfillment
of the requirements for the degree of
Doctor of Philosophy
2011

Advisory Committee:
Professor Darryll J. Pines, Chair/Advisor
Professor Norman M. Wereley
Professor Sung W. Lee
Professor James E. Hubbard Jr.
Associate Professor Yunfeng Zhang

# Dedications

*To my wife, Soo Ja*

*And to my wonderful daughters, Somyoung* (*Connie*) *and Sohyang* (*Anna*)

*And to my parents*

# Acknowledgements

First of all, I want to acknowledge my Lord and my God, Jesus Christ, who gives me a new life and provides strength and support to continuously pursue a hope and dream in my journey of life. Without him, I could not have accomplished this study.

I would like to express my sincere gratitude to my advisor, Prof. Darryll Pines, who gave me great opportunity to pursue my Ph.D degree in this field of engineering. I really appreciate his consistent support, instruction, valuable opinions and insights, encouragement and patience. With his special trust in me, I could take control of my own learning and discover ideas as making progress on research projects, so that I could develop how to learn and solve problems on my own. I have no doubt that these skills will be the most important assets for my lifetime as a professional engineer.

I am deeply indebted to Dr. Ashish Purekar (at Techno-Sciences Inc.) for his invaluable help in understanding the fundamentals of phased array signal processing, and for his advice and technical support for experimental studies. I have learned a lot from his experience in research and technical writing skills. I also appreciate that he shared his time to review and provide many valuable comments for my academic outputs.

I would like to thank my committee members, Dr. Norman Wereley, Dr. Sung W. Lee, Dr. James Hubbard Jr., and Dr. Yunfeng Zhang for reading this dissertation and for serving on my dissertation committee. Especially, my appreciation goes to Dr. Norman Wereley who helped me start my Ph.D study in Aerospace Engineering at University of Maryland, College Park (UMCP).

I am grateful to Dr. Jin-Hyeong Yoo (now at US Army Research Laboratory), Dr. Suok-Min Na, and Dr. Young-Tai Choi for their valuable discussions and suggestions not only for my research, but also for life as an engineer and a Christian. I would like to thank the graduate students and colleagues of the Composites Research (CORE) laboratory for their understanding, help and support. I also thank my fellow graduate student, Sachit Butail, for his help with technical writing and for his sincere friendship. We have shared exciting and difficult moments together since we entered the Ph.D program in 2007. I am thankful to all my friends and collogues for their support and help during my graduate study.

I appreciate the financial support provided by the NASA Constellation University Institutes Project (CUIP) program, Contract NCC3989, Claudia Meyer, Project Manager. This work was co-supported by the US Air Force Office of Scientific Research under a Phase I STTR Project, Contract FA9550-09-C-0045, with Dr. Victor Giurgiutiu and Dr. David Stargel serving as technical monitors. The support of these agencies is gratefully acknowledged.

I would like to thank my parents for their unconditional love and support. Without their support, I could not have finished my graduate study here at UMCP. Lastly but not least, I am deeply thankful to my devoted wife, Soo Ja for her endless love, understanding, patience and encouragement.

# Table of Contents

**Dedications** ii

**Acknowledgements** iii

**Table of Contents** v

**List of Tables** viii

**List of Figures** ix

**List of Publications Related to This Dissertation** xv

**1. Introduction** 1
- 1.1 Motivation 1
- 1.2 Overview of Structural Health Monitoring 3
- 1.3 Methods of Structural Health Monitoring 6
- 1.4 Research Objectives 10
- 1.5 Dissertation Organization 10

**2. Fundamental Backgrounds** 12
- 2.1 Overview of Guided Lamb Wave Method 12
  - 2.1.1 Guided Lamb Wave for Isotropic Panel 13
  - 2.1.2 Guided Lamb Wave for Anisotropic Panel 18
  - 2.1.3 Excitation and Sensing of Guided Lamb Wave 25
  - 2.1.4 Tuning of Guided Lamb Wave 28
  - 2.1.5 Dispersion Compensation and Removal 30
  - 2.1.6 Guided Lamb Wave Based Structural Health Monitoring 33
  - 2.1.7 Mode Conversion and Separation of Guided Lamb Wave 39
- 2.2 Spectral Analysis for Structural Health Monitoring 40
  - 2.2.1 Time-domain Analysis 40
  - 2.2.2 Frequency-domain Analysis 40
  - 2.2.3 Time-frequency Analysis 42
- 2.3 Guided Lamb Wave Imaging for Damage Detection 49
  - 2.3.1 Tomography 49
  - 2.3.2 Time-Reversal Imaging 51
  - 2.3.3 Sparse Array Imaging 52
  - 2.3.4 Phased Array Technique 53
- 2.4 Chapter Summary 59

**3. Phased Sensor Array Signal Processing** 61
- 3.1 Fundamentals of Phased Sensor Array Analysis 63
- 3.2 Beam Pattern of Phased Array 68
- 3.3 Wavenumber Selectivity for Phased Array Steering 70

3.4 Overview of 1-D Phased Sensor Array and Phased Array Analysis .......... 71
3.5 2-D Phased Sensor Array .......... 75
  3.5.1 Cruciform Array .......... 77
  3.5.2 Circular Array .......... 79
  3.5.3 Spiral Array .......... 80
3.6 Evaluation of 2-D Phased Sensor Arrays and Phased Array Analysis .......... 82
  3.6.1 Analytical Evaluation of 2-D Phased Sensor Arrays .......... 82
  3.6.2 Array Steering of 2-D Phased Sensor Arrays .......... 86
  3.6.3 Evaluation of 2-D Spiral Phased Array .......... 89
3.7 Structural Health Monitoring with Array Response .......... 92
3.8 MVDR-based Phased Array Technique .......... 95
3.9 Chapter Summary .......... 96

**4. Damage Detection in Thin Isotropic Panels** .......... 98
4.1 Single-Actuator-based 2-D Phased Sensor Array System .......... 98
  4.1.1 Introduction .......... 98
  4.1.2 Evaluation of Piezopaint Sensor Elements .......... 99
  4.1.3 Fabrication of Piezopaint Based 2-D Phased Sensor Arrays .......... 109
  4.1.4 Experimental Setup .......... 113
  4.1.5 Validation of algorithm of 2-D phased array .......... 115
  4.1.6 Experimental Damage Detection Results .......... 120
  4.1.7 Hole Damage .......... 123
  4.1.8 Damage Detections Using Cruciform and Circular Phased Arrays .......... 127
  4.1.9 Crack Damage .......... 130
  4.1.10 Damage Sizing .......... 131
  4.1.11 Compensation Techniques for Piezopaint Spiral Array .......... 141
4.2 Multi-Location-Actuator-based 2-D Phased Sensor Array System .......... 145
  4.2.1 Introduction .......... 145
  4.2.2 Estimation of Baseline Response Using Virtual Source Image .......... 147
  4.2.3 Experimental Setup .......... 151
  4.2.4 Damage Detection with Differential Array Response .......... 157
  4.2.5 Damage Location Evaluation .......... 163
  4.2.6 Summary and Discussions .......... 169
4.3 Chapter Summary .......... 170

**5. Damage Detection in Composite Panels** .......... 174
5.1 Motivation and Introduction .......... 174
5.2 2-D Phased Sensor Array System for Orthotropic Composite Panels .......... 175
  5.2.1 Introduction .......... 175
  5.2.2 Experimental Setup with Unidirectional Composite Panel .......... 176
  5.2.3 Wave Propagation Characteristics in Unidirectional Composite Panel 179
  5.2.4 Damage Detection Test of Unidirectional Composite Panel .......... 188
  5.2.5 Damage Detection Results .......... 191
  5.2.6 Experimental Setup with Cross-ply Composite Panel .......... 195
  5.2.7 Wave Propagation Characteristics in Cross-ply Composite Panel .......... 197
  5.2.8 Damage Detection Test of Cross-ply Composite Panel .......... 199

5.2.9 Vector-Based Damage Localization in Cross-ply Composite Panels ... 207
5.3 Chapter Summary ... 212

**6. Concluding Remarks** ... 214
6.1 Conclusions and Contributions ... 214
6.2 Limitation of Current Method ... 221
6.3 Recommendations of Future Research ... 223

**Appendices** ... 226

**A. Fundamentals of Hilbert-Huang Transform (HHT)** ... 227
A.1 Hilbert Transform (HT) ... 227
A.2 Instantaneous Mode Function (IMF) ... 233
A.3 Empirical Mode Decomposition (EMD) ... 234

**Bibliography** ... 241

# List of Tables

Table 1: Damage identification levels ........................................................................ 5
Table 2: Material properties of 2024-T3 aluminum panel......................................... 16
Table 3: Typical material properties of IM7/8552 Prepreg [28]................................ 24
Table 4: Properties of elements used for evaluations .............................................. 101
Table 5: Material properties of PZT-5A and Piezopaint ......................................... 101
Table 6: Damage locations........................................................................................ 123
Table 7: Capacitance measurement examples for the spiral array............................ 142
Table 8: Vp-p measurement examples of incident A0 modes for the spiral array ... 142
Table 9: Experimentally determined wavenumber................................................... 155
Table 10: Material properties of IM7/8552 composite............................................. 176
Table 11: Damage type and location according to actuator (for unidirectional laminate) ...................................................................................................................... 190
Table 12: Damage type and location according to actuator (for cross-ply laminate)202

# List of Figures

Figure 1.1: Damage of aerospace structural components (photo credit: Google Image) ........ 3
Figure 1.2: Structural health monitoring (SHM) process [1]........ 4
Figure 1.3: Classification of SHM methods and the associated inspection approaches 6
Figure 2.1: Plate geometry of guided Lamb wave modeling........ 14
Figure 2.2: Dispersion curves for aluminum plate........ 17
Figure 2.3: Fundamental modes of GLWs in a plate........ 18
Figure 2.4: GLW model geometry for composite laminate........ 19
Figure 2.5: Dispersion curves for $[0/90]_4$ cross-ply composite laminate........ 24
Figure 2.6: Conventional ultrasonic transducers (photo credit: www.olympus-ims.com)........ 25
Figure 2.7: Diagrams of piezoelectric element operation........ 26
Figure 2.8: Strain response of fundamental GLW modes [41]........ 30
Figure 2.9: Comparison of dispersive and non-dispersive modes........ 31
Figure 2.10: Schematic diagrams of GLW methods (in the thickness view)........ 34
Figure 2.11: Schematic diagrams of GLW methods (in the plate view)........ 34
Figure 2.12: Sample sensor signals using the GLW methods........ 36
Figure 2.13: Damage location estimation using the GLW methods with three transducers........ 36
Figure 2.14: Ellipse construction in Cartesian coordinate........ 37
Figure 2.15: Schematic diagram of GLW mode conversion due to a notch........ 39
Figure 2.16: Examples of Hilbert-Huang Transform........ 48
Figure 2.17: Circular array for GLW-based computed tomography (CT)........ 49
Figure 2.18: Schematic of time-reversal imaging method........ 51
Figure 2.19: Examples of the phased array technique applications (photo credit: Google Image)........ 54
Figure 2.20: Phased array transducers for NDE/SHM applications (photo credit: www.olympus-ims.com)........ 55
Figure 2.21: Inspection area comparison between two array imaging methods........ 56
Figure 3.1: Schematic of phased sensor array signal processing........ 61
Figure 3.2: Fundamental concepts of the phased array signal processing........ 62
Figure 3.3: Plane wave approaching to an array with cruciform layout........ 65
Figure 3.4: Comparison of $\pi/2$ phase shift method........ 67
Figure 3.5: Flow diagram of phased array signal processing........ 68
Figure 3.6: Directivity function for an 1-D linear array........ 72
Figure 3.7: Beamwidth for the 1-D linear array with 13 sensor elements........ 73
Figure 3.8: Steering of 1-D linear array with 13 sensor elements........ 74
Figure 3.9: Candidate configurations for the 2-D phased sensor array........ 75
Figure 3.10: Beam pattern comparison of 1-D linear array and 2-D cruciform array 76
Figure 3.11: Cruciform array........ 78
Figure 3.12: Circular array........ 80
Figure 3.13: Spiral array........ 81
Figure 3.14: Beamwidth of candidate 2-D arrays........ 83

Figure 3.15: Peak and average side lobe heights of candidate 2-D arrays ................ 84
Figure 3.16: Beamwidth averaged across steering angle for candidate 2-D arrays.... 85
Figure 3.17: Side lobe properties averaged across steering angle for candidate 2-D arrays.......................................................................................................... 86
Figure 3.18: Directional array steering with 2-D spiral array.................................... 87
Figure 3.19: Comparison of directional array steering with candidate 2-D arrays..... 88
Figure 3.20: Spiral array characteristics variation due to the increase of total number of sensor elements.............................................................................................. 90
Figure 3.21: Variation of the steered directivity functions of the 2-D spiral phased arrays as increasing the total number of sensor elements.......................................... 92
Figure 3.22: Flow chart of proposed damage detection algorithm ............................ 94
Figure 4.1: Piezoelectric elements used for sensitivity evaluations ......................... 100
Figure 4.2: M-bond 200 adhesive kit....................................................................... 102
Figure 4.3: Experimental setup for evaluation of piezopaint elements ................... 102
Figure 4.4: Data acquisition systems for laboratory evaluations............................. 103
Figure 4.5: Pictures of amplifiers............................................................................ 103
Figure 4.6: Schematic diagram of experimental test set-up..................................... 104
Figure 4.7: GLW signals obtained sensing elements (40 kHz) ............................... 105
Figure 4.8: GLW signals obtained sensing elements (100 kHz) ............................. 106
Figure 4.9: GLW signals obtained sensing elements (160 kHz) ............................. 106
Figure 4.10: Average Vp-p of A0 mode as a function of excitation frequency........ 107
Figure 4.11: Comparison of piezopaint sensor response to piezoceramic............... 108
Figure 4.12: Comparison of different size piezopaint elements (normalized to 1/4 in. diameter element)..................................................................................................... 109
Figure 4.13: Piezopaint patches for 2-D phased sensor array................................. 110
Figure 4.14: Electroding of piezopaint patches ...................................................... 111
Figure 4.15: Equipment used to polarize piezopaint material ................................. 111
Figure 4.16: Construction of discrete 2-D phased sensor array (cruciform array)... 112
Figure 4.17: Piezopaint based 2-D spiral sensor array ............................................ 112
Figure 4.18: Silver conductive epoxy...................................................................... 113
Figure 4.19: Instrumented aluminum panel and 2-D spiral sensor array................. 115
Figure 4.20: Off-centered piezoceramic element used as excitation source............ 116
Figure 4.21: Excitation signal and sample GLW signals obtained from spiral array 117
Figure 4.22: Wavenumber filtering array response for the off-centered excitation source case (60 kHz)................................................................................................ 119
Figure 4.23: Comparison of wavenumber-frequency relationship .......................... 119
Figure 4.24: Directional filtering array response for the off-centered excitation source case (60 kHz) ...................................................................................................... 120
Figure 4.25: Testing set-up for mass mounted on panel.......................................... 121
Figure 4.26: Comparison of array responses for mass damage case (60 kHz)......... 121
Figure 4.27: Instrumented aluminum panel and 2-D spiral sensor array (for damage detection).................................................................................................................. 122
Figure 4.28: Comparison of array responses for hole damage case (60 kHz).......... 124
Figure 4.29: Differential array responses for three hole damage cases (60 kHz)..... 125
Figure 4.30: Consecutive differential array responses for three hole damage cases (60 kHz)......................................................................................................................... 126

Figure 4.31: EMD enhanced array responses for three hole damage cases (60 kHz) ........ 126
Figure 4.32: Experimental test set-up for hole damage detection tests using cruciform and circular arrays ........ 127
Figure 4.33: EMD enhanced array responses for three hole damage cases when using cruciform array (60 kHz) ........ 129
Figure 4.34: EMD enhanced array responses for three hole damage cases when using circular array (60 kHz) ........ 129
Figure 4.35: Comparison of array response for simulated crack damage case (60 kHz) ........ 130
Figure 4.36: Consecutive differential array responses as D2 hole damage increases (60 kHz) ........ 132
Figure 4.37: Final array responses after setting a threshold for D3 hole damage (60 kHz) ........ 132
Figure 4.38: Normalized parameters of Damage Index computation for D2 hole damage case ........ 134
Figure 4.39: Damage Index variation as D2 hole damage increases (60 kHz) ........ 134
Figure 4.40: HHT amplitude at 280 deg. direction for D2 hole damage case (60 kHz) ........ 134
Figure 4.41: Final array responses after a threshold setting for D3 hole damage (60 kHz) ........ 135
Figure 4.42: Damage Index variation as D3 hole damage increases (60 kHz) ........ 136
Figure 4.43: HHT amplitude at 60 deg. direction for D3 hole damage case (60 kHz) ........ 136
Figure 4.44: Final array responses after a threshold setting, 0.8*max($|\psi_d(t,\theta)|$), for D1 hole damage (60 kHz) ........ 137
Figure 4.45: Final array responses after a threshold setting, 0.6*max($|\psi_d(t,\theta)|$), for D1 hole damage (60 kHz) ........ 138
Figure 4.46: Damage Index variation as simulated D1 hole damage increases (60 kHz) ........ 138
Figure 4.47: Consecutive differential array responses as D1 hole damage increases (60 kHz) ........ 139
Figure 4.48: HHT amplitude of 225 deg. direction for D1 hole damage (60 kHz) .. 139
Figure 4.49: Final array responses after a threshold setting for crack damage (60 kHz) ........ 140
Figure 4.50: Damage Index variation as crack damage increases (60 kHz) ........ 141
Figure 4.51: HHT amplitude at 60 deg. direction (60 kHz) ........ 141
Figure 4.52: Compensation factor maps ........ 143
Figure 4.53: Comparison of differential array responses with compensation factors ........ 144
Figure 4.54: Diagram of wave reflection and transmission with respect to type of damage; (a) for circular damage and (b) linear crack damage ........ 146
Figure 4.55: Diagram of modeling for virtual source image evaluation ........ 148
Figure 4.56: Virtual source images for an excitation source and the associated wave paths ........ 148

Figure 4.57: Configuration for virtual image source modeling with a rectangular panel with multi-location actuators and a sensor at the center of a panel .......................... 149
Figure 4.58: Virtual source image evaluation according to four excitation sources (Circles in blue)........................................................................................ 150
Figure 4.59: Picture of piezoceramic based 2-D spiral phased array ....................... 152
Figure 4.60: Testing panel with multi-location actuators and 2-D spiral array ........ 153
Figure 4.61: Sample sensor signals when exciting EO1 actuator at 60 kHz; (a) excitation signal and (b) three sensor signals obtained from the spiral array........... 153
Figure 4.62: Baseline array responses for four actuator cases (60 kHz) ................. 155
Figure 4.63: Wave propagation path based on actuator (red circles) and sensor (blue circles) locations .................................................................................... 156
Figure 4.64: Two different damages (green circles) in the testing panel.................. 156
Figure 4.65: Differential array responses for rubber patch case with EO1 actuator case at various excitation frequencies............................................................... 159
Figure 4.66: Frequency averaged differential array responses of four different actuator cases (for rubber patch case)...................................................... 160
Figure 4.67: Frequency averaged differential array responses of different actuator cases (for linear crack case) .......................................................................... 161
Figure 4.68: Frequency averaged differential array responses of EO2 actuator case for various crack length ................................................................................ 162
Figure 4.69: Frequency averaged differential array responses of different actuator cases and damage location estimation for rubber patch case................................... 165
Figure 4.70: Damage location estimation for linear crack case using frequency averaged differential array responses for EO1, EO2, and EO3 actuators................ 166
Figure 4.71: Damage location estimation based on frequency averaged differential array response of EO2 actuator case for 2 in. linear crack case .............................. 167
Figure 4.72: Detailed diagram of damage location estimation for 2 in. linear crack case................................................................................................................ 167
Figure 4.73: Comparison of frequency averaged array responses when using EO2 actuator.......................................................................................................... 168
Figure 5.1: Plane GLW propagation in two different types of panels...................... 175
Figure 5.2: Picture of unidirectional composite panel............................................. 176
Figure 5.3: Schematic diagram of the unidirectional composite panel for the experimental testing to evaluate wave propagation characteristics .......................... 177
Figure 5.4: Piezoceramic based 2-D spiral phased array for unidirectional laminate ........................................................................................................................ 178
Figure 5.5: Sample sensor signals obtained from ‘S25’ sensor element as exciting EO1 ~ EO7 actuators in the unidirectional laminate (60 kHz)................................ 178
Figure 5.6: Directional wavenumber curve for A0 mode of guided Lamb wave for unidirectional composite laminate ........................................................... 180
Figure 5.7: Array responses using conventional wavenumber filtering approach for various off-centered excitation sources located at different directions .................... 182
Figure 5.8: Array response results and the associated information .......................... 183
Figure 5.9: Parametric ellipse construction with group velocity information (60 kHz) ........................................................................................................................ 184

Figure 5.10: Wavefront curves with ellipse construction determined by experimental group velocity information ........................................................................... 185
Figure 5.11: Comparisons of wavefront curves constructed by parametric ellipse (solid line in red) estimation and cubic spline curve fitting (dashed line in blue) with the group velocity information (60 kHz) ............................................................... 185
Figure 5.12: Group velocity direction estimation with two different wavefront curves (60 kHz) ............................................................................................................ 186
Figure 5.13: Comparison of maximum array response locations using two different methods of 2-D phased array signal processing (for unidirectional composite panel) ........................................................................................................................ 188
Figure 5.14: Schematic diagram of the unidirectional laminate for the experimental testing of damage detection ......................................................................... 189
Figure 5.15: Pictures of simulated damages ............................................................ 190
Figure 5.16: Differential array response for EO8 actuator case (60 kHz) ................ 191
Figure 5.17: Differential array response for EO9 actuator case (60 kHz) ................ 192
Figure 5.18: Differential array response for EO10 actuator case (60 kHz) .............. 192
Figure 5.19: Shadowed area due to rubber patch as using EO10 actuator ............... 193
Figure 5.20: Differential array response result (with EO10 actuator) for rubber patches on various positions at 0 deg. direction ...................................................... 194
Figure 5.21: Normalized magnitude comparison between shadowed areas and maximum values of array responses for rubber patch cases .................................... 195
Figure 5.22: Instrumented cross-ply composite panel ............................................. 196
Figure 5.23: Schematic diagram of the cross-ply composite panel for the experimental testing to evaluate wave propagation characteristics ............................................... 197
Figure 5.24: Modification features for new 2-D phased array algorithm for a cross-ply composite panel .......................................................................................... 198
Figure 5.25: Comparison of maximum array response locations using two different methods of 2-D phased array signal processing (for cross-ply composite panel) .... 199
Figure 5.26: Schematic diagram of the cross-ply composite panel for the experimental testing for damage detection ........................................................................ 201
Figure 5.27: Sample sensor signals obtained from ‘S25’ sensor element as exciting EO1 ~ EO7 actuators in the cross-ply laminate (60 kHz) ....................................... 201
Figure 5.28: Estimation of damage detection coverage for proposed sensor system using ‘Spiral array I’ with EC1 actuator and Spiral array II’ with EC2 actuator ..... 203
Figure 5.29: Threshold-filtered differential array response results, using EC1 actuator and Spiral array I.......................................................................................... 205
Figure 5.30: Threshold-filtered differential array response results, using EC2 actuator and Spiral array II ......................................................................................... 206
Figure 5.31: Illustration to explain the array response results for CL_EC2_SA2_D4 ........................................................................................................................ 207
Figure 5.32: Concept of vector-based damage localization method......................... 208
Figure 5.33: Comparison of damage direction evaluation for CL_EC2_SA2_D2 damage case ............................................................................................................ 209
Figure 5.34: Damage direction evaluation based on the threshold-filtered differential array response results for D1, D2, and D4 damage cases ........................................ 210

Figure 5.35: Damage location estimation based on intersection of two vectors obtained from threshold filtered differential array response results ......................... 211
Figure A.1: Hilbert transform of sine wave ............................................................ 227
Figure A.2: Properties of Hilbert transform of the sine wave.................................. 229
Figure A.3: Analysis of linear chirp signal .............................................................. 230
Figure A.4: Analysis of various sine wave signals .................................................. 231
Figure A.5: Analysis of amplitude and frequency modulated signals ...................... 232
Figure A.6: Example of an Intrinsic Mode Function ............................................... 233
Figure A.7: Steps in Empirical Mode Decomposition ............................................. 238
Figure A.8: Intrinsic Mode Functions and the corresponding Fourier spectra ......... 239
Figure A.9: EMD process results of a sample sensor signal.................................... 240

# List of Publications Related to This Dissertation

JOURNALS

1. **B. Yoo**, A. S. Purekar, Y. -T. Choi, D. J. Pines, 2010, "Damage Detection on a Curved Composite Panel Using Guided Lamb Wave and Hilbert-Huang Transform," *Smart Materials and Structures*. (**In Preparation**)
2. **B. Yoo**, D. J. Pines, "Piezoelectric 2-D Spiral Phased Array for Structural Health Monitoring of Composite Panels," *Smart Materials and Structures*. (**In Preparation**)
3. **B. Yoo**, A. Purekar, and D. J. Pines, 2011, "Piezoceramic-based 2D Spiral Array and Multiple Actuators for Structural Health Monitoring: Thin Isotropic Panel with Straight Boundaries," *Journal of Intelligent Material Systems and Structures*, vol. 22 no. 12 1327-1343
4. **B. Yoo**, A. S. Purekar, Y. Zhang, D. J. Pines, 2010, "Piezoelectric-Paint-Based Two-dimensional Phased Sensor Arrays for Structural Health Monitoring of Thin Panels," *Smart Materials and Structures*, 19 (2010) 075017

CONFERENCE PROCEEDINGS

1. **B. Yoo**, D. J. Pines, "Piezoceramic-Based 2-D Spiral Phased Array for Damage Detection of Thin Orthotropic Composite Laminates," *Proceedings of the 8th International Workshop on Structural Health Monitoring*, September 2011, Stanford, CA

2. **B. Yoo**, D. J. Pines, "Piezoelectric 2-D Spiral Phased Array for Structural Health Monitoring of Thin Unidirectional Composite Panel," *Proceedings of the AHS International 67th Annual Forum & Technology Display*, May 2011, Virginia Beach, VA
3. **B. Yoo**, A. S. Purekar, D. J. Pines, "Multi-location Transducers and Piezoceramic Based 2-D Spiral Array for Structural Health Monitoring: Thin Isotropic Panels," *Proceedings of the ASME Conference on Smart Materials, Adaptive Structures and Intelligent Systems*, September 2010, Philadelphia, PA. (**Best Student Paper Award**)
4. **B. Yoo**, A. S. Purekar, Y. Zhang, D. J. Pines, "Piezoelectric Paint Based 2-D Sensor Array for Detecting Damage in Aluminum Plate," *AIAA Structures, Structural Dynamics, and Materials Conference*, Apr 2010, Orlando, FL.
5. **B. Yoo**, A. S. Purekar, D. J. Pines, "2-D Directional Phased Array Using Piezoelectric Paint To Detect Damages In Isotropic Plates," *Proceedings of the ASME Conference on Smart Materials, Adaptive Structures and Intelligent Systems*, September 2009, Oxnard, CA.
6. **B. Yoo**, D. J. Pines, A. S. Purekar, "Guided Lamb Wave Interrogation of a Curved Composite Plate [0/90] Using the Hilbert-Huang Transform Approach," *Proceedings of the ASME Conference on Smart Materials, Adaptive Structures and Intelligent Systems*, October 2008, Ellicott City, MD.

# 1. Introduction

## 1.1 *Motivation*

Structural health monitoring (SHM) is widely required in almost all of private and government engineering fields that want to secure structural integrity of their products in the earliest possible stage. Such SHM system should provide reliable information not only for damage detection, but also for remaining useful life of the structures used in mechanical, aerospace, and civil engineering applications. Ideally, the SHM system is designed to provide the capability of rapid, global, and real-time inspection during the operation of the structures.

Aerospace industries have great interests in implementing the SHM technology to reduce the maintenance and life cycles costs of their products, as well as to protect life safety, because their aerospace structures are aging and approaching the initial design life. Currently, time-based maintenance is performed for the health monitoring of the aerospace structures. The maintenance approach is labor intensive and not cost-effective, which is also ineffective in identifying potential damage that might develop between scheduled inspections. In addition, the time-based maintenance method is unable to provide early/real-time warning to aircraft operation and maintenance personals. The failure of proper maintenance and maintenance planning would result in risking aircraft safety and operational performance, and often lead to catastrophic consequences. Fatigue crack and corrosion damage are critical damages of metallic components of the aerospace structures. For composite structures, delamination and impact damage might decrease the operational performance and result in critical failure of the aerospace systems. Figure 1.1 shows several examples of the serious aerospace structural damage due to the lack of the in-situ SHM system. The severe fuselage detachment of the Aloha Airlines Flight 243 incident on April 1988 is shown in Figure 1.1(a). The aircraft experienced an explosive decompression and structural failure in flight. The National Transportation Safety Board (NTSB) concluded the presence of significant disbanding and fatigue damage of the fuselage area had caused the failure of the aircraft. Most recently, Southwest Airlines Flight 2294 made an emergency landing on July 2009 because the aircraft experienced a rapid decompression due to the damaged section (a size of football) of its fuselage skin. The investigation of the accident was conducted by the Federal Aviation Administration (FAA) and the NTSB and concluded that fatigue damage was the cause of the crack, which made a hole. The damaged section of fuselage skin of the aircraft is shown in Figure 1.1(b). On November 2007, US Air Force F-15 broke apart and crashed due to fatigue cracks developed by manufacturing defects in a fuselage longeron. The crack damage location is shown in Figure 1.1(c). In the spacecraft field, the Space Shuttle Columbia disaster on February 2003 can be an example for the need of the reliable and real-time SHM system. Due to the thermal protection system damaged by foam impact on the leading edge of the wing, the spacecraft suffered a catastrophic failure upon reentry into the Earth's atmosphere. Figure 1.1(d) shows a mock-up of the leading edge of a space shuttle wing after a foam impact condition was simulated. The SHM technology combined with an advanced sensor system would enable to move from the time-based to condition-based maintenance, which is conducted when need arises even if in service. The condition-based maintenance system would monitor the status of the aerospace structure; enable to maintain the efficiency of the operational performance of the structure; save monetary loss from the unnecessary replacement of structural components.

(a) Aloha Airlines Flight 243

(b) Southwest Airlines Flight 2294

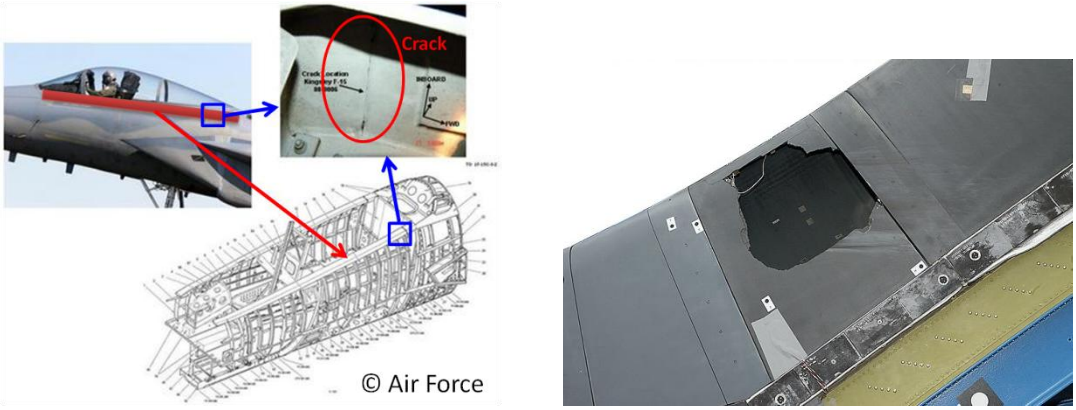

(c) Upper longeron location in F-15 forward fuselage

(d) Foam impact test on mock-up of a space shuttle leading edge

Figure 1.1: Damage of aerospace structural components (photo credit: Google Image)

## 1.2 *Overview of Structural Health Monitoring*

SHM is analogous to non-destructive testing (NDT), and both technologies are derived from non-destructive evaluation (NDE). The NDT is implemented locally with off-line execution of NDE. On the other hand, SHM is on-line damage identification technology in a global manner. It is noted that not all NDT methods are off-line and not all SHM techniques are on-line. For damage detection in rotating machinery, SHM may be replaced by condition-based monitoring (CBM).

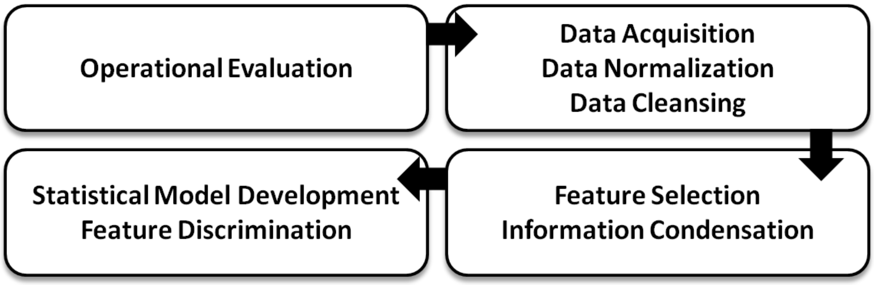

Figure 1.2: Structural health monitoring (SHM) process [1]

The process of SHM is organized by the four steps as shown in Figure 1.2 [1]. All of the researches in the field of SHM address some parts of the process. Operational Evaluation addresses life-safety and/or economic issues, definition of possible damage, environmental and/or operational conditions, and data management constraints. The step of Data Acquisition, Fusion, and Cleansing discusses how to select excitation and sensing methods, and to configure data collection parameters such as strain, displacement, and acceleration. Also, for a better feature extraction performance, the data cleansing process is performed for noise removal, spike removal, and outlier removal. The step of Feature Extraction and Information Condensation addresses data analysis parameters and signal processing methods like time and/or frequency analysis. The last step, Statistical Model Development for Feature Discrimination, discusses how to determine changes between undamaged and damaged structures, and how to develop a model based on only undamaged structures. This process is generally classified into two types; Supervised Learning and Unsupervised Learning mode. The supervised learning mode provides the information about damage presence and its possible location. The unsupervised learning mode is used for damage type discrimination, the extent of damage, and the remaining lifetime of structures. For damage identification, SHM technology requires including all the damage information obtained from both supervised and unsupervised learning modes.

Damage identification level for SHM technology was first proposed by Rytter [2], separated into four steps. Farrar and Worden [1] divided the damage identification steps into five levels as shown in Table 1. Due to the importance of the damage classification when multiple damage mechanisms are active, the type and the extent of the damage were organized into the separate steps for damage identification.

Table 1: Damage identification levels

| Damage Level | Damage State | Description |
|---|---|---|
| Level 1 | Detection | Qualitative indication of the presence of damage |
| Level 2 | Location | Possible position of damage |
| Level 3 | Classification | Estimate of the type of damage |
| Level 4 | Assessment | Quantification of the extent of damage |
| Level 5 | Prognosis | Estimate of the remaining useful life of structure |

Each damage level requires all of the lower-level information. Levels 1 through 4 are associated with damage diagnostic process. On the other hand, Level 5 is distinguished from others because this step is to develop validated simulation models to expect structural failure based on the understanding of the physics of failure. Hence, the remaining lifetime of structures/components can be predicted by the model development. For this study, the damage diagnostic process (Level 1 ~ Level 4) is focused on experimental investigation for the SHM technology.

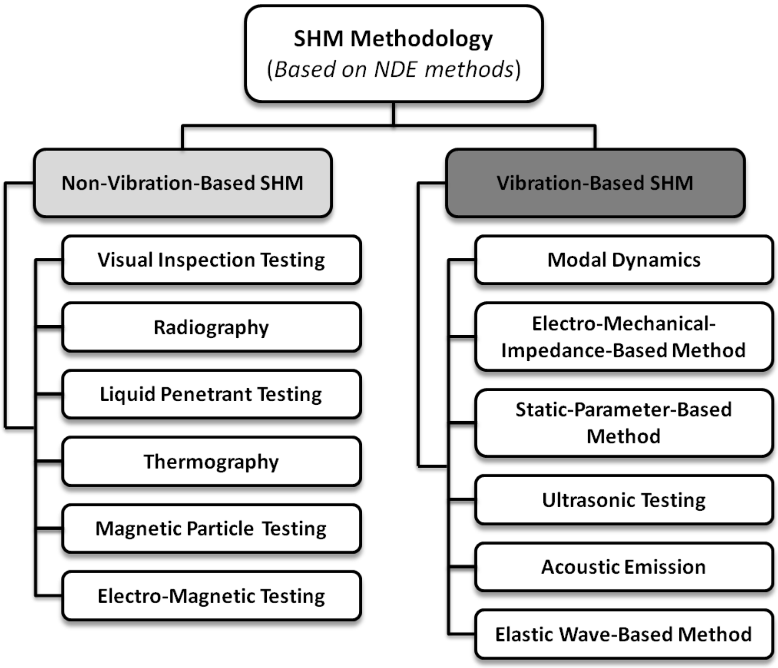

Figure 1.3: Classification of SHM methods and the associated inspection approaches

### *1.3 <u>Methods of Structural Health Monitoring</u>*

The methods of SHM technology are derived from modern NDE methods, shown in Figure 1.3 [3, 4]. The SHM methodology is categorized into two groups: non-vibration-based and vibration-based inspection methods. Both damage identification methods are interested in monitoring the variation of material properties such as mechanical properties, thermal properties, and electro-magnetic properties of structures or components.

The non-vibration-based SHM methods include: the most basic visual/optical inspection; liquid penetrant testing with a visible or fluorescent dye solution; magnetic particle testing accomplished by inducing a magnetic field in a ferromagnetic material; radiography testing using gamma-rays or X-rays for structural illumination; infrared thermography using a camera containing large numbers of sensors sensitive to infrared radiation, which can detect and measure small temperature differences of a structure; eddy current testing using electro-magnetic induction to detect flaws in conductive materials. There are a few drawbacks associated with the non-vibration based methods: (1) application limitation for on-board SHM systems; (2) labor intensiveness; (3) inspection efficiency dependence on operator's skills; (4) inspection equipment accessibility limitations; (5) constraints for inspection materials, e.g. for the eddy current testing, only conductive materials can be inspected.

The vibration-based methods are focused on investigating the variation of the dynamic mechanical properties of structures to identify the presence of damage. Modal dynamics method is based on the variations of natural frequencies and mode shapes of a structure due to damage, which can reduce structural stiffness. This method is useful to identify large damage in a structure. However, small/local damage would not significantly change the modal quantities. Also, the method is ineffective to monitor the extent of damage. Electro-mechanical impedance-based method utilizes electrical signals at high frequency bands to excite a host structure, and monitor any variations in the electro-mechanical impedance or admittance signatures. This simple and low cost method is effective for large damage of a structure. In addition, the location of a sensor is important to accurately identify the presence of damage, i.e. the method is unable to detect damage distant from sensors. Static-parameter-based method uses distributed sensors to monitor the changes in displacement and strain parameters, as compared to baseline/benchmark information. The method is simple and cost-effective, but sensitive to local changes due to damage. Ultrasonic testing (UT) method is the most popular method in the NDE field. The method requires specialized ultrasonic transducers made of piezoelectric materials, to insert acoustic waves into a host structure and to capture wave reflections. The excited waves pass though the structure and reflect from discontinuities such as damage and boundaries. The transducers should scan the entire structure to provide an ultrasonic image for damage detection. The ultrasonic method is useful to detect even small amounts of damage, but a transducer must be local to the location of damage. The limitation of transducer accessibility and the use of coupling material (e.g. ultrasonic couplant) may be disadvantages of the ultrasonic method. Acoustic emission (AE) method is based on rapid release of strain energy due to sudden change in the stress field around defect. The strain energy generates transient acoustic waves into a host structure. By capturing the damage-emitted acoustic waves, the presence or extent of damage can be evaluated. The location of the acoustic emission source may be estimated by using the arrival time information of the acoustic waves obtained from a set of sensors positioned over the structure. The AE method using a limited number of sensors has relatively good coverage for damage detection and monitoring. However, the passive AE method is unable to detect damage until it grows and generates non-repeatable acoustic waves. In addition, environmental noise and complex signal discrimination are key issues that need to be resolved.

Among the various vibration-based SHM methods, elastic-wave-based method, referred as guided Lamb wave (GLW) method in this study, is employed as the fundamental tool for damage identification. The GLW method is an active SHM technology, which is a combination of UT and AE approaches. The technique is a global SHM method, which also has capability to detect local damages of a structure. A ultrasonic transducer, mounted at a given locations, generates acoustic waves propagating in a structure. The acoustic waves interact with anything in the propagation path, and then the waves are scattered from discontinuities due to structural impedance change. The ultrasonic transducer used as an actuator or another transducer can capture the scattered waves which can provide structural information of the host structure. Structural damage causes unique wave scattering and mode conversion phenomena. The damage can be evaluated by analyzing the scattered acoustic wave signals associated with the damage. There are a number of advantages of the GLW method [5]: (1) simple inspection methodology; (2) time- and cost-effectiveness; (3) ability of wide area inspection with a limited number of transducers; (4) fast and repeatable inspection capability; (5) sensitivity to small damages; (6) mode and frequency tuning capability. However, there are a few important issues of the GLW technique: (1) sophisticated signal processing; (2) multiple wave mode propagation; (3) mode conversion and separation; (4) the GLW dispersion feature.

## 1.4 *Research Objectives*

The goal of this research is to develop a robust and reliable SHM technology with the GLW-based phased sensor array system. By using the phased sensor array for the damage detection approach, the critical issues of the GLW technique may be resolved. The SHM method will be employed for damage detection of thin metallic plates and composite laminates. This research will be focused on developing (1) an innovative signal processing algorithm associated with two-dimensional (2-D) phased sensor array system; and (2) structural damage diagnostic methods to detect the presence, the location, the growth and the type of damage simulated in plate-like structure; and (3) a general SHM technology based on the proposed phased array method not only for isotropic panels, but also anisotropic panels.

## 1.5 *Dissertation Organization*

This dissertation is organized as follows:

- In Chapter 2, an overview of the GLW technique and the associated SHM applications are introduced. This chapter provides signal processing techniques to analyze the GLW signal data.
- In Chapter 3, fundamentals of phased array signal processing and the proposed directional wavenumber filtering method with phased sensor array

are described. The SHM methods based on the array signal processing technique are provided.

- In Chapter 4, experimental studies for damage detection of thin aluminum plates are examined. Single-actuator-based senor array system and multi-location-actuator-based sensor array system are introduced.
- In Chapter 5, additional experimental studies are introduced to apply the phased array technique for thin anisotropic plates. This chapter explores damage detection tests of thin orthotropic composite laminates by using new phased array signal processing algorithm.
- In Chapter 6, this paper summaries conclusions with expected contributions and limitations. In addition, recommendations for future research are presented.

# 2. Fundamental Backgrounds

## 2.1 *Overview of Guided Lamb Wave Method*

After Lord Rayleigh [6] had investigated two-dimensional waves, known as Rayleigh (surface) waves, on the plane free surface of an infinite homogeneous isotropic elastic solid, Horace Lamb [7] discovered Lamb waves and presented the associated mathematical descriptions. Lamb waves are elastic waves propagating in a solid plate with free boundaries, whose particle motions occur both in the wave propagation direction and the normal direction to the plate plane [8]. However, Lamb waves were not attractive due to the complicated equations. In 1950s, Mindlin unraveled a comprehensive solution for Lamb waves, and developed frequency equations for such waves. Based on the insight, Mindlin also developed simple plate theories, known as Mindlin plate theory, which account for the lowest modes. Firestone and Ling have conducted researches to clarify the theoretical Lamb waves from an ultrasonic testing standpoint. Especially, Firestone theoretically demonstrated the wave motion of Lamb waves [9]. Viktorov [8] demonstrated ultrasonic Lamb waves and evaluated the dispersion features of the waves. The displacement potential method was applied by Achenbach [10] and Graff [11] to solve the propagation characteristics of Lamb waves in an isotropic plate. The method of partial waves for Lamb wave solutions were used by Auld [12]. In order to support theoretical studies on Lamb waves, Worlton [9] conducted experimental investigation. It was observed that the experimental results were correlated with the theory. The capability of the use of specific modes for the NDE/NDT applications was demonstrated.

Lamb waves usually occur on waveguides such as bars, plates and shells, so denoted by guided Lamb waves (GLWs) in this dissertation. The propagation of the GLWs is complicated due to two unique features such as dispersion relations and an infinite number of wave modes. In general, the GLWs include symmetric and anti-symmetric modes according to their displacement pattern. Those modes may be determined by satisfying Rayleigh-Lamb frequency equations and free plate boundary conditions. Phase velocities of the GLW modes are dependent on a plate thickness ($2h$) and frequency $f$. The relationships between the phase velocity and frequency are known as dispersion curves, which is key information to analyze the GLW propagation.

In recent years, the GLW-based damage detection techniques have been popular for the NDE and SHM applications for isotropic and anisotropic structures such as plates, beams, and pipes [13-23]

### 2.1.1 Guided Lamb Wave for Isotropic Panel

The geometric model of a thin isotropic panel structure to evaluate the GLW characteristics is illustrated in Figure 2.1. Substituting strain-displacement relations into Hooke's law, equations of motion in terms of displacement can be obtained as

$$\mu u_{i,jj} + (\lambda + \mu) u_{j,ji} + \rho f_i = \rho \ddot{u}_i \text{ for } i,j = 1,2,3 \tag{2.1}$$

where $u_i$ are the displacements; $f_i$ are body forces; $\lambda$ and $\mu$ are Lame constants and $\rho$ is the material density of medium [10]. The absence of the body forces is assumed for the above equations.

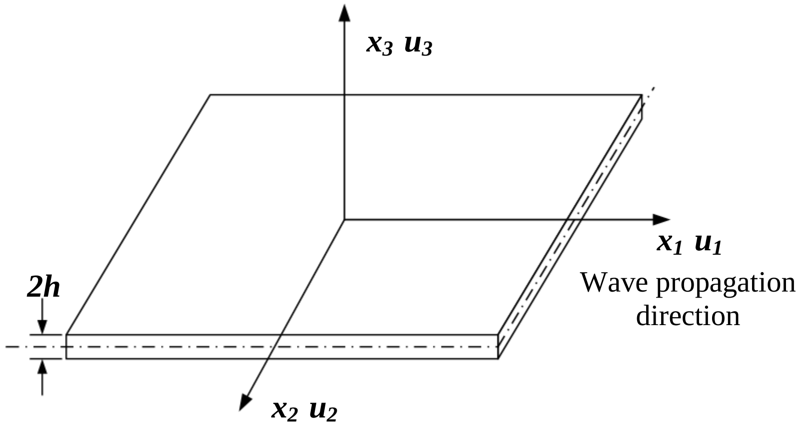

Figure 2.1: Plate geometry of guided Lamb wave modeling

For motion in plane strain in ($x_1$ $x_3$)-plane, Equation (2.2) should be satisfied.

$$u_2 \equiv 0 \text{ and } \frac{\partial}{\partial x_2}(\,) \equiv 0 \tag{2.2}$$

Hence, the displacement components are defined in the reduced form of

$$u_1 = \frac{\partial \phi}{\partial x_1} + \frac{\partial \psi}{\partial x_3} \tag{2.3}$$

$$u_3 = \frac{\partial \phi}{\partial x_3} - \frac{\partial \psi}{\partial x_1} \tag{2.4}$$

where $\phi$ and $\psi$ represent the decomposed displacement variables such as scalar and vector potentials, respectively. Using the Helmholtz decomposition, the wave equations for the plane strain can be written as

$$\frac{\partial^2 \phi}{\partial x_1^2} + \frac{\partial^2 \phi}{\partial x_3^2} = \frac{1}{C_L}\frac{\partial^2 \phi}{\partial t^2} \text{ for longitudinal waves} \tag{2.5}$$

$$\frac{\partial^2 \psi}{\partial x_1^2} + \frac{\partial^2 \psi}{\partial x_3^2} = \frac{1}{C_T}\frac{\partial^2 \psi}{\partial t^2} \text{ for transverse (shear) waves} \tag{2.6}$$

where $C_L$ indicates the velocity of longitudinal waves whereas $C_T$ is the velocity of shear/transverse waves. The acoustic properties ($C_L$ and $C_T$) depend on the material properties, defined by

$$C_L = \sqrt{\frac{E(1-\nu)}{\rho(1+\nu)(1-2\nu)}} \text{ and } C_T = \sqrt{\frac{E}{2\rho(1+\nu)}} \tag{2.7}$$

where $E$ is Young's modulus and $\nu$ is Poisson's ratio of a given material.

For the solutions of the decomposed governing wave equations (Equations (2.5) and (2.6)), time harmonic waves, i.e. traveling waves in the $x_1$ direction and standing waves in the $x_3$ direction, are assumed by

$$\phi = \Phi(\mathrm{x}_3)e^{i(kx_1-\omega t)} \tag{2.8}$$

$$\psi = \Psi(x_3)e^{i(kx_1-\omega t)} \tag{2.9}$$

where $k$ is a wavenumber and $\omega$ is an angular frequency. The wavenumber is defined as $k = \frac{2\pi}{\lambda}$ where $\lambda$ is a wavelength, and the angular frequency is defined as $\omega = 2\pi f$ where $f = \frac{1}{T}$ and $T$ is a period.

Substituting Equations (2.8) and (2.9) into the Equations (2.5) and (2.6), respectively, the solutions of the wave equations can be obtained by

$$\Phi(x_3) = A_1\sin(px_3) + A_2\cos(px_3) \tag{2.10}$$

$$\Psi(x_3) = B_1\sin(qx_3) + B_2\cos(qx_3) \tag{2.11}$$

where $p$ and $q$ are defined by

$$\begin{gathered} p^2 = \left({}^{\omega}/_{C_L}\right)^2 - k^2 \\ q^2 = \left({}^{\omega}/_{C_T}\right)^2 - k^2 \end{gathered} \tag{2.12}$$

and $A_1$, $A_2$, $B_1$, and $B_2$ are arbitrary constants. Since both displacement field variables involve sine and cosine functions, which are odd and even respectively, the solutions are often split into symmetric and anti-symmetric modes. The displacements for the symmetric modes are

$$\begin{gathered} u_1 = ikA_2 \cos(px_3) + qB_1 \cos(qx_3) \\ u_3 = -pA_2 \sin(px_3) - ikB_1 \sin(qx_3) \end{gathered} \tag{2.13}$$

whereas the solutions for the anti-symmetric modes can be given as

$$\begin{gathered} u_1 = ikA_1 \sin(px_3) - qB_2 \sin(qx_3) \\ u_3 = pA_1 \cos(px_3) - ikB_2 \cos(qx_3) \end{gathered} \tag{2.14}$$

Applying the traction-free boundary conditions on the top and bottom surfaces of the panel structure (Equation (2.15)), the arbitrary constants, $A_1$, $A_2$, $B_1$, and $B_2$, can be determined. The $h$ is the half thickness of the panel.

$$\sigma_{31} = \sigma_{33} \equiv 0 \text{ at } x_3 = \pm h \tag{2.15}$$

This leads to Rayleigh-Lamb frequency relations known as dispersion equations, defined by

$$\frac{\tan(qh)}{\tan(ph)} = -\frac{4k^2pq}{(q^2 - k^2)^2} \text{ for symmetric modes} \tag{2.16}$$

$$\frac{\tan(qh)}{\tan(ph)} = -\frac{(q^2 - k^2)^2}{4k^2pq} \text{ for antisymmetric modes.} \tag{2.17}$$

Table 2: Material properties of 2024-T3 aluminum panel

| **Material** | ***t*, inch** | ***E*, MPa** | ***G*, MPa** | ***ν*** | ***ρ*, g/cc** |
|---|---|---|---|---|---|
| Al 2024-T3 | 0.04 | 73.1 | 28 | 0.33 | 2.78 |

The typical material properties of 2024-T3 aluminum plate are shown in Table 2. For the aluminum plate, the longitudinal wave speed ($C_L$) and the transverse wave speed ($C_T$) are determined by using the Equation (2.7).

Phase velocity of the GLW modes, denoted by $C_p$, is defined by a simple relation, $C_p = \omega/k$. The group velocity, denoted by $C_g$, can be found from the phase velocity by using the formula defined by $C_g = d\omega/dk$. Substituting $k = \omega/C_p$ into the group velocity formula, we obtain the relations between the phase velocity and the group velocity of the GLW modes, given as [24]

$$C_g = d\omega\left[d\left(\frac{\omega}{C_p}\right)\right]^{-1} = d\omega\left[\frac{d\omega}{C_p} - \omega\left(\frac{dC_p}{C_p^2}\right)\right]^{-1} = C_p^2\left[C_p - \omega\frac{dC_p}{d\omega}\right]^{-1} \qquad (2.18)$$

Dispersion curves (i.e. frequency-wavenumber relations) of the GLW modes for the 2024-T3 aluminum plate are determined as shown in Figure 2.2.

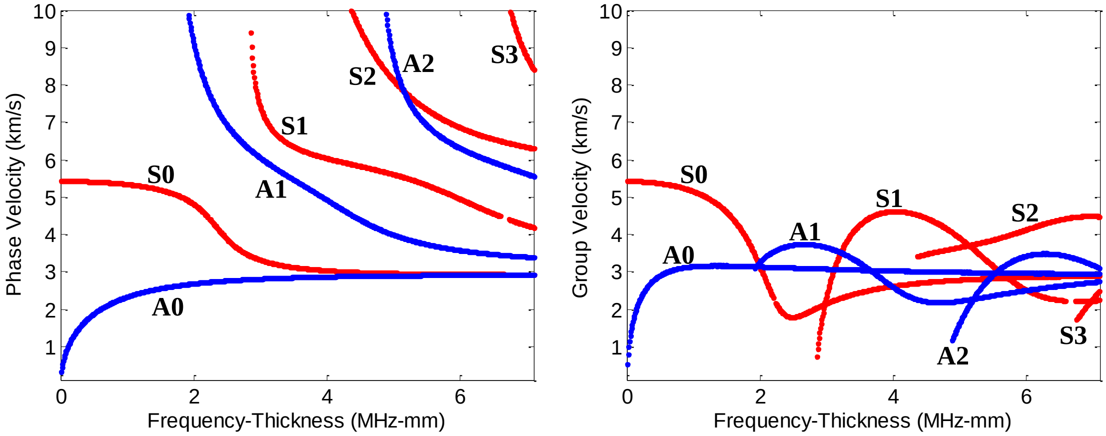

(a) Phase velocity (b) Group velocity

Figure 2.2: Dispersion curves for aluminum plate

Each curve represents a specific mode, which is conventionally called A0, S0, A1, S1, A2, S2, etc. where ‘An’ and ‘Sn’ denote anti-symmetric modes and symmetric modes, respectively. The wavenumber and frequency information obtained from the dispersion curves can be used to evaluate the displacement fields of the GLW modes. From the results of the displacement fields, the mode shape of the GLW can be determined. The mode shapes of the fundamental GLWs such as S0 and A0 modes are shown in Figure 2.3.

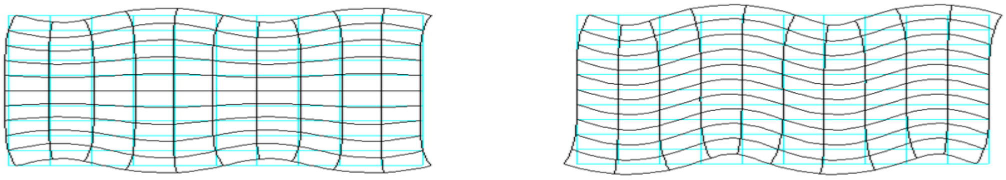

(a) Symmetric mode (S0 mode)

(b) Anti-symmetric mode (A0 mode)

Figure 2.3: Fundamental modes of GLWs in a plate

### 2.1.2 Guided Lamb Wave for Anisotropic Panel

Wave propagation in composite laminates is studied on the analytical method. Rose and Nayfeh discussed the details of harmonic wave propagation in anisotropic media [24, 25]. For the laminated composites, the equation of motion is obtained from the governing equation of wave propagation in an arbitrary medium and given as

$$\frac{\partial \sigma_{ij}}{\partial x_j} = \rho \frac{\partial^2 u_i}{\partial t^2} \tag{2.19}$$

and the general stress-strain relations

$$\sigma_{ij} = c_{ijkl}\varepsilon_{kl} \tag{2.20}$$

with stress-displacement relations

$$\varepsilon_{kl} = \frac{1}{2}\left(\frac{\partial u_l}{\partial x_k} + \frac{\partial u_k}{\partial x_l}\right) \text{ for } i, j, k, l = 1,2,3. \tag{2.21}$$

where $\sigma_{ij}$ and $\varepsilon_{kl}$ are the stress and strain tensor, respectively. $u_i$ is displacement vector and $\rho$ is the material density. $c_{ijkl}$ is the stiffness tensor. In the matrix form of the stress-strain relations with contracted index notation [26],

$$c_{ijkl} = [\boldsymbol{C}] = \begin{bmatrix} C_{11} & C_{12} & C_{13} & C_{14} & C_{15} & C_{16} \\ C_{12} & C_{22} & C_{23} & C_{24} & C_{25} & C_{26} \\ C_{13} & C_{23} & C_{33} & C_{34} & C_{35} & C_{36} \\ C_{14} & C_{24} & C_{34} & C_{44} & C_{45} & C_{46} \\ C_{15} & C_{25} & C_{35} & C_{45} & C_{55} & C_{56} \\ C_{16} & C_{26} & C_{36} & C_{46} & C_{56} & C_{66} \end{bmatrix} \tag{2.22}$$

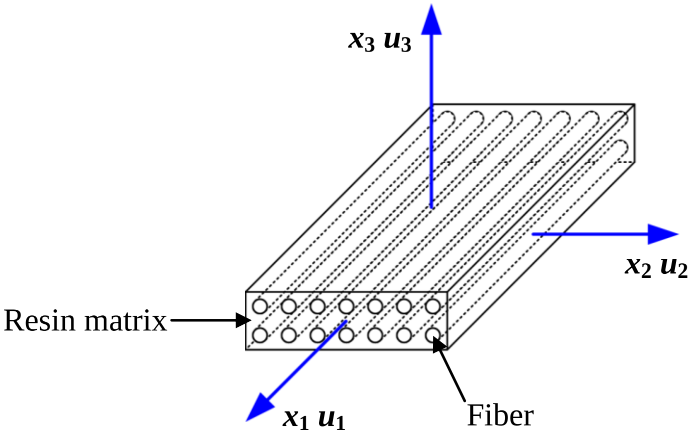

Figure 2.4: GLW model geometry for composite laminate

Figure 2.4 shows the geometry of the GLW modeling. Assuming a harmonic wave for the solution of the governing wave equations, the displacement vector can be expressed as

$$u_j = U_j e^{ik(x_1+\alpha x_3 - C_p t)} \text{ for } j = 1,2,3 \tag{2.23}$$

Where $U_j$ is the displacement amplitude; $k$ is the wavenumber in $x_1$ direction; $\alpha$ is the unknown ratio of the wavenumber components along the $x_3$ and $x_1$ directions; $C_p$ is the phase velocity.

Substituting the displacement equations into the governing wave equations, we can obtain

$$\begin{aligned} K_{11}(\alpha)U_1 + K_{12}(\alpha)U_2 + K_{13}(\alpha)U_3 &= 0 \\ K_{12}(\alpha)U_1 + K_{22}(\alpha)U_2 + K_{23}(\alpha)U_3 &= 0 \\ K_{13}(\alpha)U_1 + K_{23}(\alpha)U_2 + K_{33}(\alpha)U_3 &= 0 \end{aligned} \tag{2.24}$$

$$\begin{aligned} K_{11}(\alpha) &= C_{11} - \rho C_p^2 + 2C_{15}\alpha + C_{55}\alpha^2 \\ K_{12}(\alpha) &= C_{16} + (C_{14} + C_{56})\alpha + C_{45}\alpha^2 \\ K_{13}(\alpha) &= C_{15} + (C_{13} + C_{55})\alpha + C_{35}\alpha^2 \\ K_{22}(\alpha) &= C_{66} - \rho C_p^2 + 2C_{46}\alpha + C_{44}\alpha^2 \\ K_{23}(\alpha) &= C_{56} + (C_{36} + C_{45})\alpha + C_{34}\alpha^2 \\ K_{33}(\alpha) &= C_{55} - \rho C_p^2 + 2C_{35}\alpha + C_{33}\alpha^2 \end{aligned} \tag{2.25}$$

Since $U_1$, $U_2$, and $U_3$ cannot be zero, the coefficient $\boldsymbol{K}$ matrix should be singular. Setting the determinant of the $\boldsymbol{K}$ matrix equal to zero, we obtain a sixth-degree polynomial equation in $\alpha$.

$$\alpha^6 + A_1\alpha^5 + A_2\alpha^4 + A_3\alpha^3 + A_4\alpha^2 + A_5\alpha + A_6 = 0 \tag{2.26}$$

where the various coefficients are dependent on $\boldsymbol{C}$ (the stiffness matrix), $C_p$ and $\rho$. Six distinct solutions for $\alpha$ can be obtained from the above equation, and the six solutions are denoted as $\alpha_q$ for $q = 1,2,\dots,6$. For each $\alpha_q$, we can have the displacement component ratios as

$$V_q = \frac{U_{2q}}{U_{1q}} = \frac{K_{11}(\alpha_q)K_{23}(\alpha_q) - K_{13}(\alpha_q)K_{12}(\alpha_q)}{K_{13}(\alpha_q)K_{22}(\alpha_q) - K_{12}(\alpha_q)K_{23}(\alpha_q)} \tag{2.27}$$

$$W_q = \frac{U_{3q}}{U_{1q}} = \frac{K_{11}(\alpha_q)K_{23}(\alpha_q) - K_{13}(\alpha_q)K_{12}(\alpha_q)}{K_{12}(\alpha_q)K_{33}(\alpha_q) - K_{23}(\alpha_q)K_{13}(\alpha_q)} \tag{2.28}$$

By using the Equations (2.27) and (2.28), the formal solutions for the displacement and stresses can be determined as

$$[u_1, u_2, u_3] = \sum_{q=1}^{6} [1, V_q, W_q]\, U_{1q} e^{ik(x_1 + \alpha_q x_3 - C_p t)} \tag{2.29}$$

$$[\sigma_{33}, \sigma_{13}, \sigma_{23}] = \sum_{q=1}^{6} ik[D_{1q}, D_{2q}, D_{3q}]\, U_{1q} e^{ik(x_1 + \alpha_q x_3 - C_p t)} \tag{2.30}$$

where

$$\begin{aligned} D_{1q} &= C_{13} + \alpha_q C_{35} + (C_{36} + \alpha_q C_{34})V_q + (C_{35} + \alpha_q C_{33})W_q \\ D_{2q} &= C_{15} + \alpha_q C_{55} + (C_{56} + \alpha_q C_{45})V_q + (C_{55} + \alpha_q C_{35})W_q \\ D_{3q} &= C_{14} + \alpha_q C_{45} + (C_{46} + \alpha_q C_{44})V_q + (C_{45} + \alpha_q C_{34})W_q \end{aligned} \tag{2.31}$$

The six displacement amplitudes $U_{1q}$ are the unknowns.

For the orthotropic material case, the stiffness matrix (tabled in the Equation (2.22)) is reduced by setting as

$$\begin{gathered} C_{14} = C_{15} = C_{16} = 0 \\ C_{24} = C_{25} = C_{26} = 0 \\ C_{34} = C_{35} = C_{36} = 0 \\ C_{45} = C_{46} = 0 \\ C_{56} = 0 \end{gathered} \tag{2.32}$$

Hence, the coefficient $\boldsymbol{K}$ matrix is simplified as

$$\begin{gathered} K_{11}(\alpha) = C_{11} - \rho C_p^2 + C_{55}\alpha^2 \\ K_{12}(\alpha) = 0 \\ K_{13}(\alpha) = (C_{13} + C_{55})\alpha \\ K_{22}(\alpha) = C_{66} - \rho C_p^2 + C_{44}\alpha^2 \\ K_{23}(\alpha) = 0 \\ K_{33}(\alpha) = C_{55} - \rho C_p^2 + C_{33}\alpha^2 \end{gathered} \tag{2.33}$$

Setting the determinant of the $\boldsymbol{K}$ matrix equal to zero, we obtain a sixth-degree polynomial equation in $\alpha$.

$$\left(C_{66}-\rho C_p^2+C_{44}\alpha^2\right)\begin{pmatrix}\left(C_{55}-\rho C_p^2+C_{33}\alpha^2\right)\left(C_{11}-\rho C_p^2+C_{55}\alpha^2\right)\\ -(C_{13}+C_{55})^2\alpha^2\end{pmatrix}=0 \tag{2.34}$$

The resultant polynomial equation can be divided into two parts such as the shear horizontal (SH) wave and the plane wave types. The first term in the above equation is for the SH wave type, and the latter term is for the plane wave type. For the plane wave type, we obtain fourth-degree polynomial equation, defined by

$$A\alpha^4+B\alpha^2+C=0 \tag{2.35}$$

where the coefficients of the equation are given by

$$\begin{gathered}A=C_{33}C_{55}\\ B=\left(C_{11}-\rho C_p^2\right)C_{33}-\left(C_{55}-\rho C_p^2\right)C_{55}-(C_{13}+C_{55})^2\\ C=\left(C_{11}-\rho C_p^2\right)\left(C_{55}-\rho C_p^2\right)\end{gathered} \tag{2.36}$$

By solving the Equation (2.35), there are four solutions for $\alpha$ having $\alpha_2=-\alpha_1$ and $\alpha_4=-\alpha_3$. The formal solutions for the displacement and stresses can be determined as

$$[u_1,u_3]=\sum_{q=1}^{4}\left[1,W_q\right]U_{1q}e^{ik(x_1+\alpha_q x_3-C_p t)} \tag{2.37}$$

$$[\sigma_{33},\sigma_{13}]=\sum_{q=1}^{6}ik\left[D_{1q},D_{2q}\right]U_{1q}e^{ik(x_1+\alpha_q x_3-C_p t)} \tag{2.38}$$

where

$$\begin{gathered}W_q=\frac{\rho C_p^2-C_{11}-C_{55}\alpha_q^2}{(C_{13}+C_{55})\alpha}\\ D_{1q}=C_{13}+\alpha_q C_{33}W_q\\ D_{2q}=C_{55}\left(\alpha_q+W_q\right)\end{gathered} \tag{2.39}$$

The displacement and the stress components can be combined in the matrix form, given by

$$\begin{Bmatrix} \tilde{u}_1 \\ \tilde{u}_3 \\ \tilde{\sigma}_{33} \\ \tilde{\sigma}_{13} \end{Bmatrix} = \begin{bmatrix} 1 & 1 & 1 & 1 \\ W_1 & W_2 & W_3 & W_4 \\ ikD_{11} & ikD_{12} & ikD_{13} & ikD_{14} \\ ikD_{21} & ikD_{22} & ikD_{23} & ikD_{24} \end{bmatrix} \begin{Bmatrix} U_{11}e^{ik\alpha_1 x_3} \\ U_{12}e^{ik\alpha_2 x_3} \\ U_{13}e^{ik\alpha_3 x_3} \\ U_{14}e^{ik\alpha_4 x_3} \end{Bmatrix} \tag{2.40}$$

Traction-free boundary conditions on the top surface of the laminate are given by

$$\{\tilde{\sigma}_{33}, \tilde{\sigma}_{13}\}|_{x_3=\pm h} = 0 \tag{2.41}$$

where $h$ is the half thickness of the composite laminate. In this case, the symmetric and anti-symmetric modes cannot be decoupled. However, the two modes can be decoupled by using a robust method. The method uses modified boundary conditions at both top and mid-plane surface [27]. For symmetric mode, the new boundary conditions are given by

$$\begin{gathered} \{\tilde{\sigma}_{33}, \tilde{\sigma}_{13}\}|_{x_3=h} = 0 \\ \{\tilde{u}_3, \tilde{\sigma}_{13}\}|_{x_3=0} = 0 \end{gathered} \tag{2.42}$$

and the new boundary conditions for the anti-symmetric mode are given by

$$\begin{gathered} \{\tilde{\sigma}_{33}, \tilde{\sigma}_{13}\}|_{x_3=h} = 0 \\ \{\tilde{u}_1, \tilde{\sigma}_{33}\}|_{x_3=0} = 0 \end{gathered} \tag{2.43}$$

Typical material properties of IM7/8552 unidirectional composite prepreg are shown in Table 3. A cross-ply composite laminate with $[0/90]_4$ lay-up sequences is evaluated to determine dispersion curves (i.e. wave propagation characteristics). The stiffness matrix can be determined by using the given material properties and the Classical Laminated Plate Theory (CLPT) [26]. The CLPT code was written in MATLAB to calculate the composite elastic matrices for the cross-ply composite laminate (orthotropic material).

Table 3: Typical material properties of IM7/8552 Prepreg [28]

| $E_{11}$, GPa | $E_{22}$, GPa | $E_{33}$, GPa | $\nu_{12}$ | $\nu_{13}$ | $\nu_{23}$ |
|---|---|---|---|---|---|
| 161 | 11.38 | 11.38 | 0.32 | 0.32 | 0.45 |
| **$G_{12}$, GPa** | **$G_{13}$, GPa** | **$G_{23}$, GPa** | **$\rho$, g/cc** | **$t_{ply}$, mm** | |
| 5.17 | 5.17 | 3.92 | 1.58 | 0.142 | |

The dispersion curves for the cross-ply composite laminate are plotted in Figure 2.5. The blue dots are for the symmetric modes, and the red dots are for the anti-symmetric modes. Figure 2.5(a) shows the dispersion curves when the wave is incident at $x_1$ direction. On the other hand, Figure 2.5(b) shows the dispersion curves when the wave is incident at 45° from the $x_1$ direction. It is observed that the phase velocity of the modes at $x_1$ direction is faster than the modes at 45° direction due to the stiffness difference dependent on the lay-up sequence.

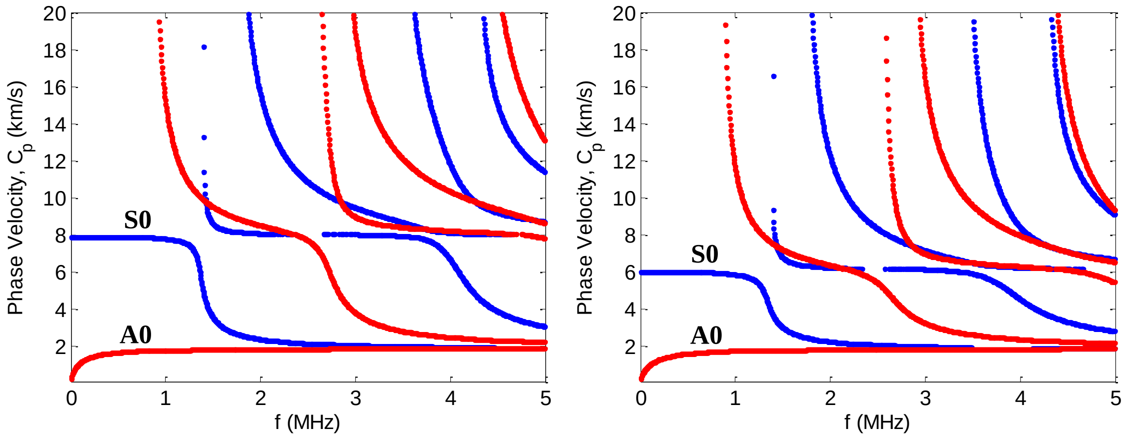

(a) Phase velocity at 0 deg. direction (b) Phase velocity at 45 deg. direction

Figure 2.5: Dispersion curves for $[0/90]_4$ cross-ply composite laminate

### 2.1.3 Excitation and Sensing of Guided Lamb Wave

In the ultrasonic or acousto-ultrasonic tests of the conventional non-destructive evaluation (NDE), ultrasonic transducers, shown in Figure 2.6, have been used to transmit and receive the GLW propagating within various structures such as pipes, plates, beams, rods, and layered structures. Wedge-coupled ultrasonic transducers shown in Figure 2.6(b) are the most common probes to transmit and receive the GLW [29]. Comb-type ultrasonic transducers [30] are another alternatives for the GLW-based NDE/SHM. Both transducers are capable of selecting a specific mode of the GLW. The mode can be tuned by changing the angle of the wedge coupled transducers, and for the comb type transducers, a mode can be tuned by changing the spacing between the ultrasonic elements. However, the ultrasonic transducers are bulky and expensive. In addition, ultrasonic couplants should be used in all contact testing applications between the transducers and the test articles.

(a) Ultrasonic transducers (b) Ultrasonic transducer with wedges

Figure 2.6: Conventional ultrasonic transducers (photo credit: www.olympus-ims.com)

In this study, the guided Lamb waves are excited and captured by using piezoelectric material-based elements due to their size, weight, and inexpensive price. The piezoelectric elements can be permanently attached onto the test structures in order for the SHM applications. The piezoelectric materials are governed by the piezoelectric constitutive equations,

$$\begin{aligned} \boldsymbol{S} &= \boldsymbol{s}^{\mathrm{E}}\boldsymbol{T} + \boldsymbol{dE} \ \text{ for actuation} \\ \boldsymbol{D} &= \boldsymbol{dT} + \boldsymbol{\varepsilon}^{\boldsymbol{T}}\boldsymbol{E} \ \text{ for sensing.} \end{aligned} \tag{2.44}$$

In these equations, mechanical, electrical and piezoelectric variables are coupled in the material. For the actuation, $\boldsymbol{S}$ is the mechanical strain, $\boldsymbol{s}^{\mathrm{E}}$ is the mechanical compliance of the material measured at zero electric field, $\boldsymbol{T}$ is the mechanical stress, $\boldsymbol{d}$ is the piezoelectric coefficient that represents the electro-mechanical coupling in the material, and $\boldsymbol{E}$ is the electric field. For the sensing, $\boldsymbol{D}$ is the electric displacement, $\boldsymbol{\varepsilon}^{\boldsymbol{T}}$ is the dielectric permittivity measured at zero mechanical stress.

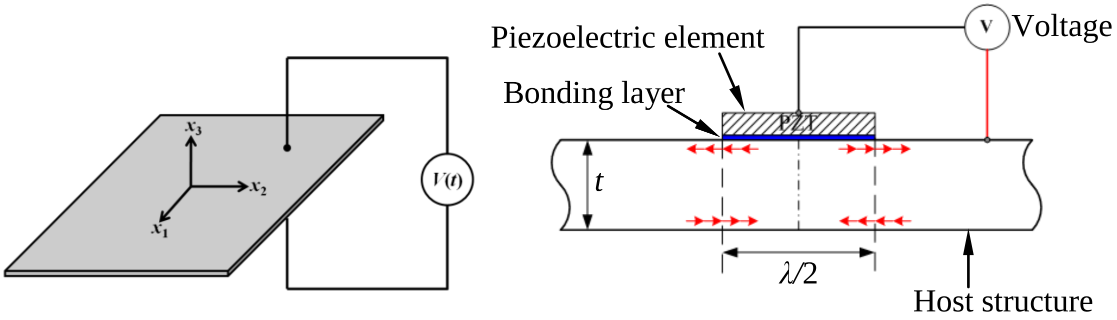

(a) Electric field applied (b) GLW excitation in the panel structure

Figure 2.7: Diagrams of piezoelectric element operation

The piezoelectric based-material element was coated by conductive electrode layers on both top and bottom surfaces. The surface-electroded piezoelectric element was bonded onto a structure and instrumented to be operated as an actuator and a sensor, shown in Figure 2.7. As the actuator, an applied voltage inserted into the piezoelectric material and the associated mechanical deformation is produced. On the other hand, as the sensor, a deformation of the piezoelectric material induced by a mechanical deformation of the host structure produces a charge in the piezoelectric material.

Various transducers based on the piezoelectric effects were developed to embed onto plate-like structures, and to monitor structural health and to detect damages in the structures. The PZT (zirconium titanate ceramics) is the most commonly used piezoelectric materials in the NDE/SHM fields [23]. However, the PZT ceramics is brittle so that it is necessary to be handled with care. To overcome the limitation of the PZT ceramics, Bent and Hagood [31] developed the Active Fiber Composite (AFC) transducer to the piezoelectric fiber composite performance through an interdigitated electroding scheme. In the similar way, Wilkie and High [32] developed Macro-Fiber Composite (MFC) transducers. The MFC was constructed by unidirectional piezoceramic fibers embedded in a polymer matrix. Polyimide films with an interdigitated electrode patterns were boned on the top and bottom surfaces. In the recent years, Salas and Cesnik [33] developed a Composite Long-range Variable-length Emitting Radar (CLoVER) transducer composed of independent piezocomposite sectors. The CLoVER transducer is capable of exciting directional GLWs into the structures and inspecting the structural integrity. In addition, polymer-based piezoelectric paint (piezopaint) sensors were developed by a few researchers [34-36]. The piezopaint was fabricated by mixing piezoelectric ceramic powder (filler) with epoxy resin (binder). Zhang [37] used the piezopaint material as acoustic emission sensors for the fatigue crack detection.

The PVDF (polyvinylidene fluoride) film is an alternative piezoelectric material. Monkhouse et al. [38] developed the PVDF transducers for the generation and detection of GLWs in plates. The PVDF transducers included interdigitated electrode patterns with a straight-finger shape in order to select a GLW mode for damage detection. Wilcox et al. [39] developed the PVDF transducer including interdigitated electrode patterns with a curved-finger shape. Gao et al. [40] developed a PVDF annular sensor and used for corrosion damage detection in aluminum plates. The PVDF material, however, have a drawback as using a transducer because the piezoelectric effect of the PVDF is weak for the SHM applications.

For the experimental tests based on the GLW-based SHM technique, the PZT ceramics were used for actuators as well as sensors due to its powerful GLW generation capability and the high sensitivity. Also, piezopaint materials were used for sensing devices. Especially, the piezopaint patches were used to construct phased sensor arrays. The manufacturing process of the piezopaint-based phased sensor arrays will be discussed in the later experimental testing sections.

### 2.1.4 Tuning of Guided Lamb Wave

The technique of mode tuning of the GLW by using piezocermic elements was well discussed by Giurgiutiu [41] and Santoni et al. [42]. Theoretical and experimental studies of the GLW mode tuning with piezoelectric wafer active sensors (PWASs) were presented. The classical integral transform was used for the evaluation of the GLW transduction. The PWAS transducer was bonded on the upper surface of an isotropic plate. Closed-form solution for ideal bonding of the PWAS transducer onto the isotropic plate is defined by

$$\varepsilon_{11}(x_1,t)|_{x_3=+h} = -i\frac{a\tau_0}{\mu}\left[\begin{array}{l}\displaystyle\sum_{k^S}\sin(k^S a)\frac{N_S(k^S)}{D_S'(k^S)}e^{-i(k^S x_1-\omega t)} \\ \displaystyle+\sum_{k^A}\sin(k^A a)\frac{N_A(k^A)}{D_A'(k^A)}e^{-i(k^A x_1-\omega t)}\end{array}\right] \tag{2.45}$$

where

$$\begin{aligned} N_S(k) &= kq(k^2+q^2)\cos(ph)\cos(qh) \\ N_A(k) &= kq(k^2+q^2)\sin(ph)\sin(qh) \end{aligned} \tag{2.46}$$

$$\begin{aligned} D_S(k) &= (k^2-q^2)^2\cos(ph)\sin(qh) + 4pqk^2\sin(ph)\cos(qh) \\ D_A(k) &= (k^2-q^2)^2\sin(ph)\cos(qh) + 4pqk^2\cos(ph)\sin(qh) \end{aligned} \tag{2.47}$$

where $h$ is the half thickness of the panel structure and $+$ indicates the top surface of the panel; $a$ is the half width of a piezoceramic boned onto the panel structure; $a\tau_0$ is the pin force applied at the both ends of the piezoceramic; $\mu$ is the Lame constant; $k^S$ and $k^A$ are the wavenumbers for the symmetric and anti-symmetric modes obtained from the Rayleigh-Lamb frequency equations (see Equations (2.16) and (2.17)); $p$ and $q$ are found by the Equation (2.12).

The strain response of two fundamental GLW modes was evaluated by using the Equation (2.45) for a 1.6 mm thick aluminum plate under the 7 mm PZT excitation, shown in Figure 2.8.

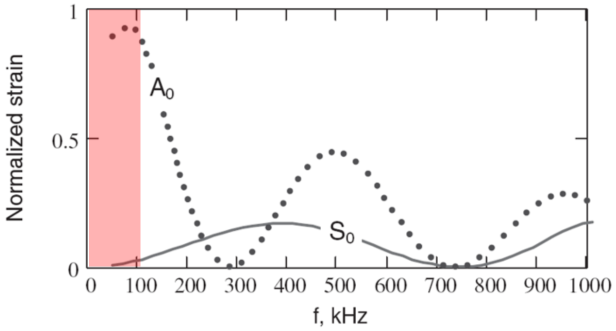

Figure 2.8: Strain response of fundamental GLW modes [41]

Raghavan and Cesnik [43, 44] discussed the GLW mode tuning with circular piezoceramics (i.e. PWASs) in isotropic plates and 3D elasticity modeling of the GLW fields excited by piezoelectric actuators in various configurations.

In the experimental study (see chapter 4 and 5), the GLW would be excited by using piezoceramics (e.g. PZT element). The range of input excitation frequency for the experiments is highlighted in Figure 2.8, and the A0 mode of the GLW is dominant. Therefore, the A0 mode would be monitored and filtered by using directional wavenumber filtering algorithm in order to detect various structural damages. The directional filtering algorithm is related to the phased array virtual steering for the phased array signal processing.

### 2.1.5 Dispersion Compensation and Removal

The GLWs have a number of wave modes and most of them are highly dispersive wave modes. Due to wave propagation characteristics depending on the frequency, the GLWs have dispersion features as they propagate through structures. A waveform of a dispersive mode will spread out in space and time. Figure 2.9 shows the characteristics of non-dispersive and dispersive modes of the GLWs.

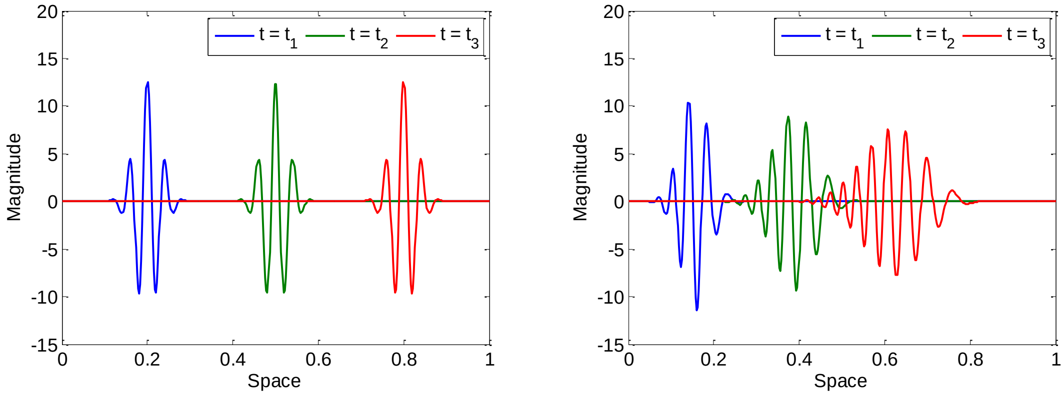

(a) for non-dispersive mode ($C_p = C_g$)

(b) for dispersive mode ($C_p > C_g$)

Figure 2.9: Comparison of dispersive and non-dispersive modes

Wilcox [45] proposed a dispersion compensation technique that makes use of *a priori* knowledge of the dispersion characteristics of a GLW mode to map signals from the time domain to the spatial domain. Xu et al. [46] discussed the GLW dispersion compensation and the dispersion removal algorithms used for both theoretical and experimental investigation. The dispersion removal technique was based on the Taylor expansion study conducted by Liu and Yuan [47]. The dispersion compensation and removal approach was applied to embedded ultrasonic structural radar (EUSR) methodology to improve the array signal processing image. Like the research conducted by Xu et al. [46], these techniques are expected to be used for detecting multiple damages, located at close locations, after a phased array signal processing rooted in wavenumber filtering approach.

Dispersion Compensation

Dispersion compensated waveform can be determined by letting a dispersed reflection waveform (denoted by $g(t)$) propagate backward to its source position, i.e. setting $(x, t) = (-x, 0)$, defined by [46, 48]

$$h(x) = u(x,t)|_{\substack{x=-x \\ t=0}} = \int_{-\infty}^{\infty} G(\omega) e^{ikx} d\omega \tag{2.48}$$

where $h(x)$ is dispersion-compensated waveform; $G(\omega)$is the Fourier transform of the $g(t)$ that is the dispersed GLW reflected from an artificial damage.

$$g(t) = A_R u(x,t)|_{x=x_0} \tag{2.49}$$

$$u(x,t) = \int_{-\infty}^{\infty} F(\omega) e^{-i(kx-\omega t)} d\omega \tag{2.50}$$

where $A_R$ is reflection coefficient constant; $u(x,t)$ is the propagated $f(t)$ that is input signal waveform; $F(\omega)$is the Fourier transform of $f(t)$.

The Equation (2.48) is the fundamental dispersion compensation equation. This equation leads the time series signal to convert into special domain signal and reverse the dispersion process.  By recalling the definitions of phase and group velocities, the dispersion equation is redefined by

$$h(x) = \int_{-\infty}^{\infty} H(k) e^{ikx} dk \tag{2.51}$$

where the $H(\omega)$ is defined by $H(k) = G(\omega) C_g(\omega)$; the group velocity is given by $C_g(\omega) = d\omega/dk$; the frequency is a function of wavenumber, defined by $\omega = \omega(k)$. The inverse Fourier transform (IFFT) can be used to obtain the dispersion compensated waveform, $h(x)$.

Dispersion Removal

Since $k(\omega)$is a nonlinear function, the resultant GLW waveform has the dispersion feature. The nonlinear $k(\omega)$can be changed to the linear form by using the Taylor expansion, defined by [46]

$$k(\omega) \approx k_{linear}(\omega) = k(\omega_0) + k'(\omega_0)(\omega - \omega_0) \tag{2.52}$$

where $\omega_0$ is the center frequency of the excitation signal for the Taylor expansion.

Xu et al. [46] described the procedure to remove the dispersion features in a dispersed wave and observed that the dispersion removal algorithm does better than the dispersion compensation algorithm and takes less computation time. Liu and Yuan [47] developed a linear mapping technique to remove dispersion of the GLW mode in isotropic plates. The technique assumed that nonlinear dispersion curve can be approximated by using a finite polynomial (e.g. the second order term of polynomial).

### 2.1.6 Guided Lamb Wave Based Structural Health Monitoring

In the conventional ultrasonic testing of the Non-Destructive Evaluation (NDE), there are two GLW methods to evaluate plate-like structures. The pulse-echo method and the pitch-catch method based on the GLWs are illustrated in the thickness view, shown in Figure 2.10. The upper half thickness region of the panel structure is for the pulse-echo method. One piezoelectric transducer is bonded on the panel, or both an actuator and a sensor are collocated at the same location of the panel. On the other hand, the lower half thickness region of the panel structure is for the pitch-catch method. For the method, the actuator and the sensor are boned at different location within the panel. The both GLW methods are illustrated in the plate view, shown in Figure 2.11.

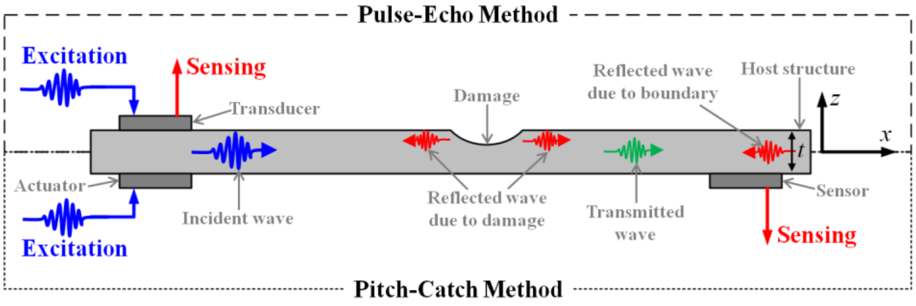

Figure 2.10: Schematic diagrams of GLW methods (in the thickness view)

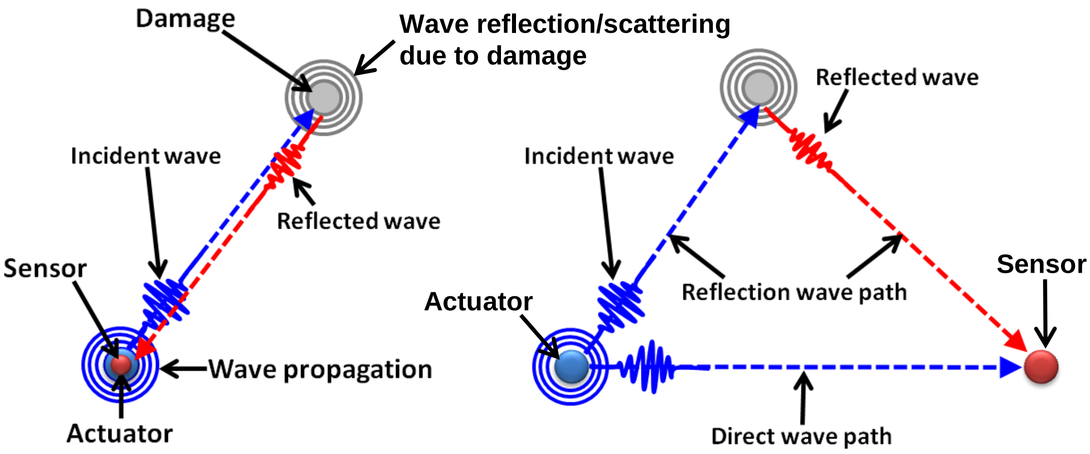

(a) Pulse-echo method

(b) Pitch-catch method

Figure 2.11: Schematic diagrams of GLW methods (in the plate view)

GLWs are generated from the actuator and the incident waves omni-directionally propagate in the panel. If a structural damage is present in the panel, the traveling GLWs bounce from the damage, and travel and arrive at the sensor. For a semi-infinite boundary condition, i.e. there is no edge boundary, sensor signals may be obtained as shown in Figure 2.12. In the figure, signals in blue are the normalized excitation signals, and signals in red are the sensor signals. For the pulse-echo method, the sensor signal included only the reflected waveform due to damage, shown in Figure 2.12(a). On the other hand, for the pitch-catch method, the direct waveform/transmitted waveform and damage reflection waveform appear in the sensor signal, shown in Figure 2.12(b). Due to the semi-infinite boundary condition, there are no boundary reflection waveforms in the sensor signals. The Time-of-Flight (ToF) information of the target GLW mode can be estimated from the sensor signals, and it can be used to detect damage location in the panel structure. Using three transducers, it is sufficient to identify the damage location in the panel structure with semi-infinite boundaries. The damage detection approaches for the GLW methods, using three transducers denoted by S1, S2, and S3, are shown in Figure 2.13. From the pulse-echo method shown in Figure 2.12(a), the ToF information of the reflected waveform due to the damage represents the double traveling distance of the incident GLW wave. Evaluating damage location based on the ToF information from the pulse-echo method, a circle with radius can be constructed for each transducer as shown in Figure 2.13(a). A simple computation, $\mathrm{r}_1 = \left(\frac{\mathrm{ToF}_1}{2}\right) * C_g$ , should be performed for the radius of the circle construction. In the computation, the $C_g$ is the group velocity of the incident GLW mode. The group velocity can be determined by experiment or theoretical modeling (e.g. dispersion curves). In contrast, with ToF information from the pitch-catch method, an ellipse can be constructed by using the actuator and sensor locations and the corresponding ToF information. The governing equations for the ellipse construction are given by Equations (2.53) and (2.54), and the associated illustration can be found in Figure 2.14.

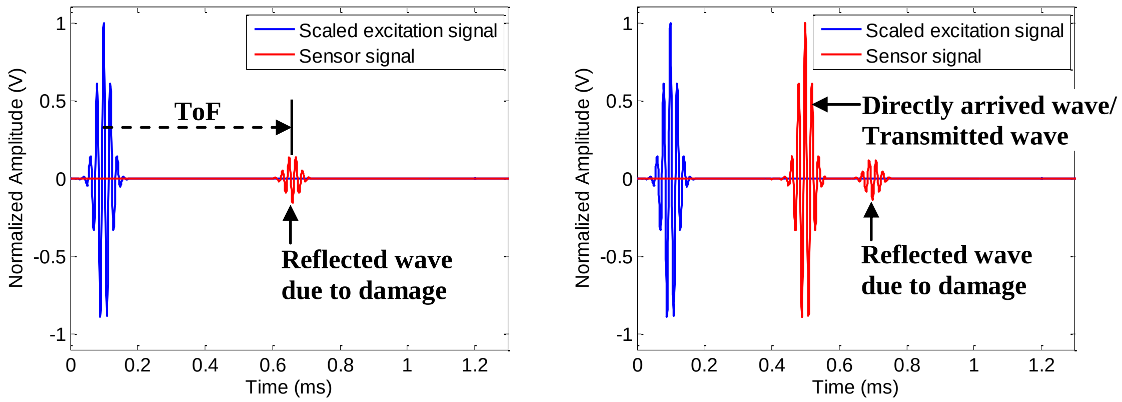

(a) Pulse-echo method (b) Pitch-catch method

Figure 2.12: Sample sensor signals using the GLW methods

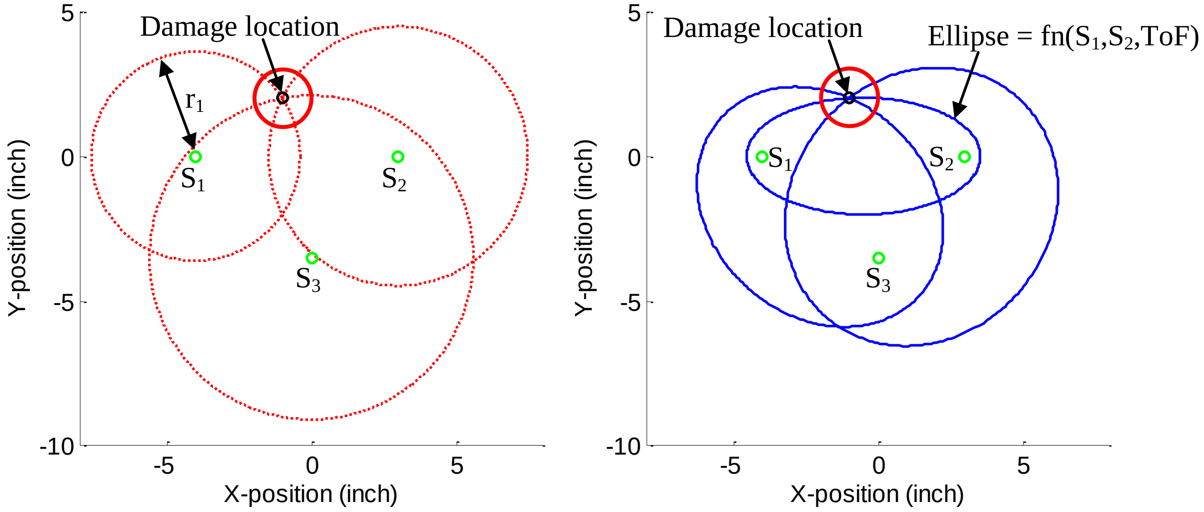

(a) with pulse-echo method (b) with pitch-catch method

Figure 2.13: Damage location estimation using the GLW methods with three transducers

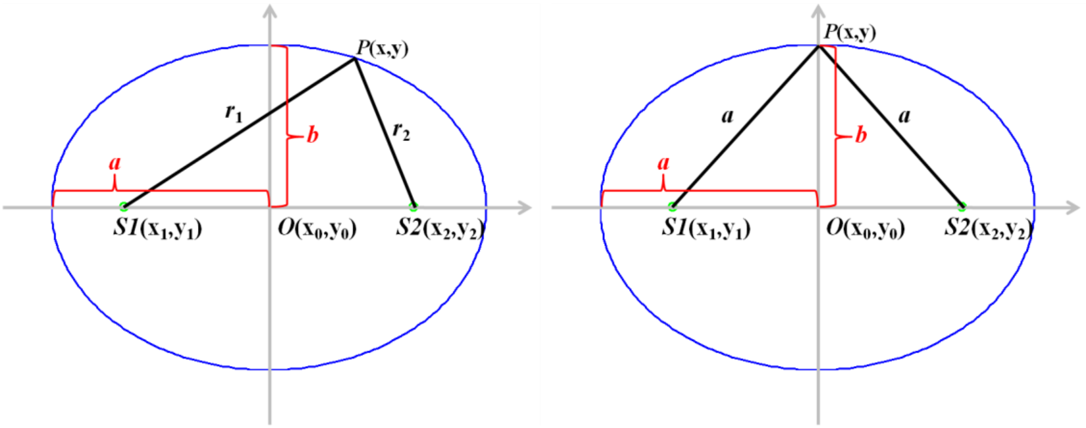

Figure 2.14: Ellipse construction in Cartesian coordinate

$$\frac{(x-x_0)^2}{a^2}+\frac{(y-y_0)^2}{b^2}=1 \tag{2.53}$$

$$a=\frac{r_1+r_2}{2}$$
$$b=\sqrt{a^2+\sqrt{(x_1-x_2)^2+(y_1-y_2)^2}} \tag{2.54}$$

In the above ellipse construction equations, the $a$ can be determined by using the equation, $a_{ij}=\frac{\mathrm{ToF}_{ij}*C_g}{2}$. The ToF information for the pitch-catch method is depending on the actuator-sensor combination with the relation, $\mathrm{ToF}_{ij}=\mathrm{ToF}_{ji}$. The $C_g$ is the group velocity of the GLW propagating the panel structure.

Alleyne and Cawley [49, 50] discussed the GLW interaction with defects (notches) in the theoretical modeling (finite element analysis (FEA)) and experimental investigations. Giurgiutiu et al. [51] conducted theoretical and experimental studies of GLW reflections from crack damages in an aluminum plate. The GLWs were excited by using piezoelectric wafer active sensors (PWASs) bonded on the plate. Using built-in piezoelectric sensor/actuators, Ihn and Chang [52, 53] investigated and developed damage detection/monitoring techniques for cracks in metallic structures. In the study, a damage index (DI) based on the GLW scattering information due to its interactions with a crack damage was proposed and evaluated as a SHM indicator.

For SHM of composite laminates, Chimenti and Nayfeh [54] performed to understand leaky Lamb waves (LLW) propagating in unidirectional composite laminates. The LLW approach was employed for damage detection applications for composite laminates [55]. Guo and Cawley [56] performed numerical and experimental GLW study to detect delaminations in composite laminates. The S0 mode of the GLW was inserted into the composite panels and measured the wave interaction with the simulated delaminations. Keilers and Chang [57] researched on damage detection of composite plates using built-in piezoelectrics. The size and location of the delamination damage were estimated. Su et al. [58] developed a damage identification approach for delamination detection in quasi-isotropic composite laminates. Transducer network approach combined with the symmetric S0 mode propagation and wavelet transform analysis was used to identify the delamination location within the panel. Ng and Veidt [59] presented the GLW technique to inspect damage in composite laminates. Transducer network (transmitter-receiver pair) method with the cross-correlation signal analysis technique was employed for damage detection applications. Kessler et al. [60] explored the optimization and application of the GLW methods to damage detection in composite structures.

The GLW-based damage detection, however, is very complicated because several important features such as multiple-mode excitation, boundary reflections, and mode conversion/separation due to damage should be consider for the actual experimental testing. In this study, to solve the critical issues, the phased sensor array technique with GLW approach is applied for damage detection.

### 2.1.7 Mode Conversion and Separation of Guided Lamb Wave

In order to understanding the GLW propagation, additional important feature, which is mode conversion/separation, should be addressed. If the GLWs propagating in a thin plate encounter a discontinuity, the GLWs experience three physical phenomena such as reflection, transmission, and mode conversion/separation. When a incident mode of the GLW (e.g. S0 mode) arrives at a notch in a plate as shown in Figure 2.15, the S0 mode is separated into S0 and A0 modes, some portion of the modes transmitted and others are reflected. In similar manner, an A0 mode is also divided into S0 and A0 modes due to a notch [61].

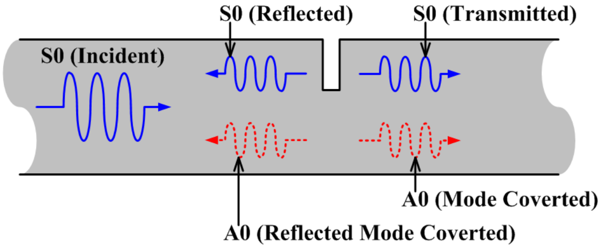

Figure 2.15: Schematic diagram of GLW mode conversion due to a notch

Cho and Rose [62, 63] well discussed boundary element method (BEM) application to investigate mode conversion on the edge reflection of the GLW and on thickness variation of a plate. Alleyne and Cawley [50] conducted experimental study to measure the amplitude of A0 and S0 modes caused by mode conversion at a notch in a thin plate. Kim and Sohn [61] developed a new NDT technique to detect a crack by extracting mode conversion features from the experimental GLW signals. Using time-dependant finite element method (FEM), Oppenheim et al. [64, 65] simulated how incident S0 and A0 modes experience mode conversion, reflection, and transmission features.

## 2.2 *Spectral Analysis for Structural Health Monitoring*

### 2.2.1 Time-domain Analysis

Various spectral analysis methods have been used to analyze vibration signals for structural health monitoring. The fundamental method to evaluate the vibration signals is time-domain analysis method. The method is based on the observation of waveforms in the time-domain signals. Intimately examining the healthy and damaged signals, researchers may find the amplitude variation and phase shift of the target waveforms. Based on these findings, the structural integrity can be evaluated for the testing article. However, this method provides a limited amount of information such as damage presence/extent in the structure.

### 2.2.2 Frequency-domain Analysis

The fast Fourier transform (FFT) analysis, which is the most commonly used spectral analysis in addition to the time-domain analysis, was developed after the discovery of

Fourier transform by Joseph Fourier [66]. The continuous Fourier transform for the time-series signal, $x(t)$, is defined by

$$\begin{aligned} X(f) &= \int_{-\infty}^{\infty} x(t)e^{-i2\pi ft}dt \\ x(t) &= \int_{-\infty}^{\infty} X(f)e^{i2\pi ft}df \end{aligned} \tag{2.55}$$

where $f$ is the frequency and $i$ is unit complex. $X(f)$ is the Fourier counterpart of $x(t)$ in the frequency domain. The Fourier transform provides a spectral density distribution (i.e. power spectrum) which identifies the amplitudes and phases at the various frequencies that contribute to time series.

Alleyne and Cawley [67] presented a two-dimensional Fourier transform (2-D FT/ 2-D FFT) technique including the spatial and time transformations to separate different wave components of the GLW signals. The technique is defined by

$$H(k,f) = \iint u(x,t)\, e^{-i(kx-\omega t)}dxdt \tag{2.56}$$

$$u(x,t) = A(\omega)e^{i(kx-\omega t-\varphi)} \tag{2.57}$$

where $A(\omega)$ is the frequency-dependent amplitude of the wave; $k$ and $\omega$ are wavenumber and angular frequency, respectively; $\varphi$ is the initial phase. This method allows plotting a GLW signal in a three-dimensional plot of magnitude versus wavenumber and frequency.

Alleyne and Cawley [49] demonstrated that the 2-D FFT method may be used to theoretically and experimentally evaluate the GLW interactions with defects in steel plates. Gao et al. [68] presented a laser ultrasonic technique and 2-D FFT method to analyze the GLW modes in a thin plate. Loewke, et. al. [69] demonstrated that the 2-

D FFT is a useful method because of its capability to determine the relative magnitudes of different spatial wavelengths in a material.

The FFT-based techniques are very useful in many applications, but there is a major problem in using the FFT for non-stationary signals (e.g. GLW signals). The FFT results provide the integration information of the time domain signals over the entire signal length. It means the FFT provides no information on their temporal/spatial localization within the time series.

### 2.2.3 Time-frequency Analysis

The frequency domain analysis in conjunction with the time domain analysis leads to the time-frequency analysis which is the most commonly used spectral analysis method to evaluate the GLW signals. The time-frequency analysis method provides the frequency component variation of the GLW signals as a function of time.

#### Short-Time Fourier Transform (STFT)

The short-time Fourier transform (STFT) applies the Fourier transform to a small signal segment of time moment by multiplying a time window function and neglecting the rest of the signal. The signal is assumed to be stationary within each segment. This process is repeated as moving the time window function over the full period of the signal. The STFT for a transient signal, $x(t)$, is defined by

$$X_{STFT}(t,f) = \int_{-\infty}^{\infty} x(\tau) h(\tau - t) e^{-i2\pi f\tau} d\tau \tag{2.58}$$

where $h(t)$ is a window function and has a short time duration. In general, the squared magnitude of the STFT of a signal is spectrogram, defined by $|X_{STFT}(t,f)|^2$.

Ihn and Chang [52] applied the STFT to the GLW signals in order to show the amplitude distribution of the sensor signals over a wide range of frequencies and the time domain. Sung et al. [70] presented the implementation of the STFT for the acoustic emission (AE) signals due to low-speed impact damage on composite laminates. Niethammer et al. [71] developed the reassigned spectrogram (the reassigned energy density spectrum of the STFT) to evaluate the dispersion curves for the GLWs in an aluminum plate. The reassigned spectrogram improves the time-frequency resolution of the dispersion curves.

Due to the fixed window size, however, there is trade-off between time and frequency resolution. In addition, since the STFT is based on the Fourier transform, the signal segment data should be stationary, which is not be always true for non-stationary signals [72]. Therefore, the STFT may not be the best signal processing tool for the GLW signal analysis.

<u>Wigner-Ville Distribution Transform</u>

The Wigner-Ville distribution (WVD) provides an increased resolution relative to the spectrogram. The WVD transform uses a flexible choice of window size [4] . The Wigner-Ville distribution is defined by

$$X_{WVD}(t,f) = \int_{-\infty}^{\infty} x\left(t+\frac{\tau}{2}\right) x^*\left(t-\frac{\tau}{2}\right) e^{-i2\pi f\tau} d\tau \qquad (2.59)$$

where * denotes the complex conjugate. The Wigner-Ville distribution is a measure of the local time-frequency energy of the signal.

Prosser et al. [73] demonstrated the pseudo WVD method to characterize GLW mode dispersion in an aluminum plate. Niethammer et al. [71] discussed the smoothed WVD method (with the Gaussian filter) for the mode localization of the GLW signals. However, the basic nature of the WVD causes significant interference cross-terms, which do not permit a straightforward interpretation of the energy distribution [74].

Wavelet Transform (WT)

The wavelet transform (WT) was applied for the analysis of vibration signals by Daubechies [75] and Newland [76, 77]. The WT method was widely used as an efficient means of signal processing to analyze the GLW-based damage detection technique of the NDE/SHM field. The continuous wavelet transform (CWT) of a transient signal, $x(t)$, is defined by

$$\begin{gathered} CWT_{x(t)}(a,b) = \frac{1}{\sqrt{a}} \int_{-\infty}^{\infty} x(t) \psi^{*}\left(\frac{t-b}{a}\right) dt \\ \psi_{a,b}(t) = \frac{1}{\sqrt{a}} \psi\left(\frac{t-b}{a}\right) \end{gathered} \tag{2.60}$$

where $a$ is a scaling parameter and $b$ is a time shift parameter; * denotes the complex conjugate; The function $\psi(t)$ is a mother wavelet and $\psi_{a,b}(t)$ is a daughter wavelet. The accuracy and efficiency of the transform are depending on the mother wavelet selection. Gabor, Gaussian, Haar, Daubechies, bi-orthogonal, Coiflets, Symlets, Morlet, Mexican Hat and Meyer are some popular wavelet functions in practice. The squared magnitude of the CWT of a signal is the energy density spectrum (i.e. wavelet scalogram), defined by $\left|CWT_{x(t)}(a,b)\right|^{2}$.

Ip et al. [78] applied CWT employing the Gabor wavelet to extract the dominant GLW modes from the measured acceleration signals obtained from beam structures. Li et al. [79] presented criteria of optimal mother wavelet selection in the GLW analysis for the delamination damage detection of composite laminates. Jeong and Jang [80] discussed the wavelet transform using the Gabor wavelet to analyze the GLW propagating in composite laminates. Legendre [81] et al. used the wavelet transform algorithm to extract the required time information from the received signals with noisy nature. Paget et al. [82] demonstrated the wavelet transform for the GLW damage detection application to composite laminates. The GLW responses were decomposed into wavelet coefficients by the wavelet transform, and the variation of the wavelet coefficient amplitude was referred as damage indicator.

### Hilbert-Huang Transform (HHT)

A new time-frequency domain analysis, Hilbert-Huang transform (HHT), which is based on a combination of the Hilbert transform with the Empirical Mode Decomposition (EMD) method, has been developed by Huang [83]. The HHT analysis is the generalized Fourier transform analysis using instantaneous amplitudes and frequencies as variables.

The process of EMD provides a set of well-defined Intrinsic Mode Functions (IMFs). The original signal, $X(t)$, can be decomposed into several IMFs as given by

$$X(t) = \sum_{j=1}^{n} C_j(t) + r_N \tag{2.61}$$

where $C_j(t)$ is $j$-th IMF and $r_N$ is a residue that is a monotonic function or constant. The original signal divided into the $n$ empirical modes, $C_j(t)$, and the residue. The procedure to determine the IMFs, $C_j(t)$, from an original time-series data, $X(t)$ is described in Appendix A.

Applying the Hilbert transform to the each IMF, the analytical signal is given by

$$Z_j(t) = C_j(t) + iD_j(t) \tag{2.62}$$

$$D_j(t) = \mathrm{HT}\big[C_j(t)\big] = \frac{1}{\pi} P \int_{-\infty}^{\infty} \frac{C_j(\tau)}{t-\tau}\, d\tau \tag{2.63}$$

where $\mathrm{HT}\big[C_j(t)\big]$ is the Hilbert transformed form of the $C_j(t)$; $P$ denotes the Cauchy principle value of the integral. The analytical signal can be rewritten in the polar coordinate system,

$$Z_j(t) = a_j(t) e^{i\theta_j(t)} \tag{2.64}$$

$$a_j(t) = \sqrt{C_j(t)^2 + D_j(t)^2} \text{ and } \theta_j(t) = \arctan\left(\frac{D_j(t)}{C_j(t)}\right) \tag{2.65}$$

where $a_j(t)$ is the $j$-th instantaneous amplitude; $\theta_j(t)$ is the $j$-th instantaneous phase. If the IMFs can be considered to be strictly local, instantaneous angular velocity is defined by

$$\omega_j(t) = \frac{d\theta_j(t)}{dt} = 2\pi f_j(t) \tag{2.66}$$

where $f_j(t)$ is the $j$-th instantaneous frequency. Then the real part of the analytical signal is the IMFs, as given by

$$C_j(t) = \mathrm{Re}\left(Z_j(t)\right) = \mathrm{Re}\left(a_j(t) e^{i2\pi \int f_j(\tau) d\tau}\right) \tag{2.67}$$

The original time-series data, $X(t)$, is reconstructed by

$$X(t) = \mathrm{Re}\left(\sum_{j=1}^{n} a_j(t) e^{i2\pi \int f_j(\tau) d\tau}\right) + r_N \tag{2.68}$$

Using $a_j(t)$ and $f_j(t)$ for $j = 1,2,3, \dots, n$, a two-dimensional image, $A_j(t, f_j)$, can be estimated for the IMFs. The Hilbert-Huang spectrum (HHS) can be defined by

$$HHS_{X(t)}(t, f) = \sum_{j=1}^{n} A_j(t, f_j) \tag{2.69}$$

To show the efficiency of the Hilbert-Huang spectrum with the EMD process, several simple signals were examined through the procedure, shown in Figure 2.16.

Quek et al. [84] and Zemmour [72] demonstrated the feasibility of the HHT technique to detect various damage such as a crack, delamination, and stiffness loss in the GLW signals obtained from beams and plates. Yoo et al. [85] applied the HHT for the GLW signals obtained form a curved composite panel, and successfully monitored the torque loss on joint bolts. Pines and Salvino [86] discussed a novel signal processing tool using EMD, HHT, and the Hilbert phase and applied to track unique features in the vibratory response of civil structures.

In this study, the powerful HHT analysis technique would be used to provide additional information for damage detection based on the phased array signal processing results.

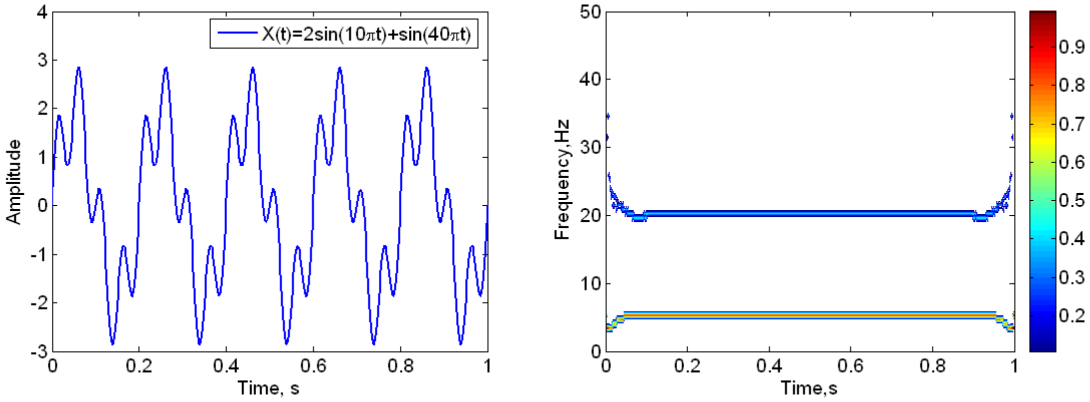

(a) Simple harmonic signal (b) HHT spectrum for signal on left

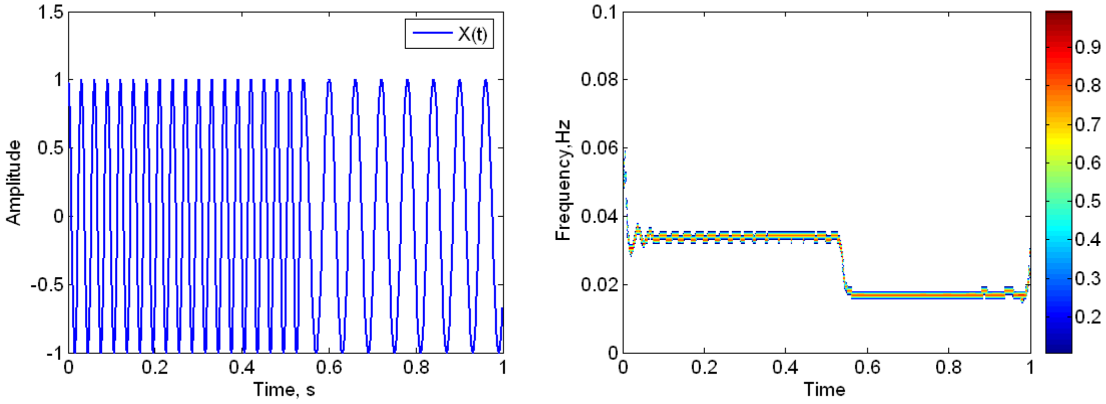

(c) Cosine wave with frequency switch (d) HHT spectrum for signal on left

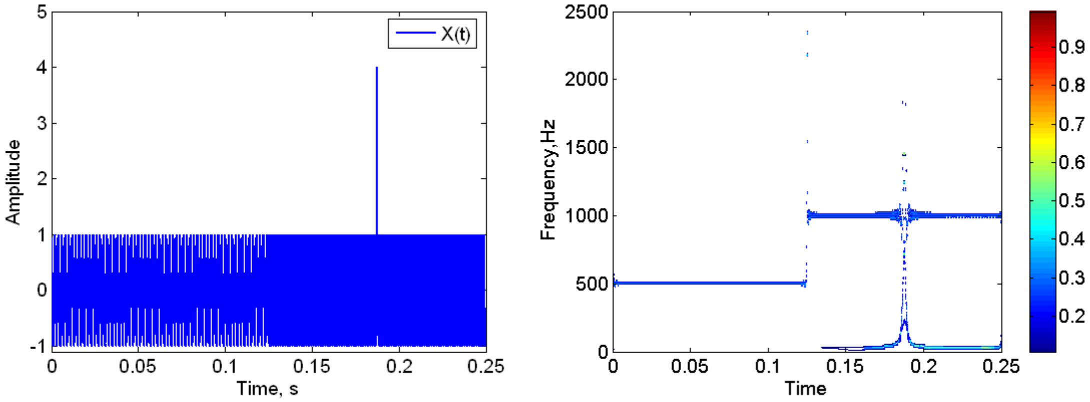

(e) Cosine wave with frequency switch and impulse (f) HHT spectrum for signal on left

Figure 2.16: Examples of Hilbert-Huang Transform

## *2.3 Guided Lamb Wave Imaging for Damage Detection*

A number of researches have been conducted to create damage map of a testing structure by using the GLW technique. Lamb wave tomography, time-reversal imaging, probability-based array imaging, and phased array techniques are widely used in the NDE/SHM field. In this study, the phased array technique in conjunction with the GLW interrogation approach would be used for experimental damage detection of thin metallic plates and composite laminates.

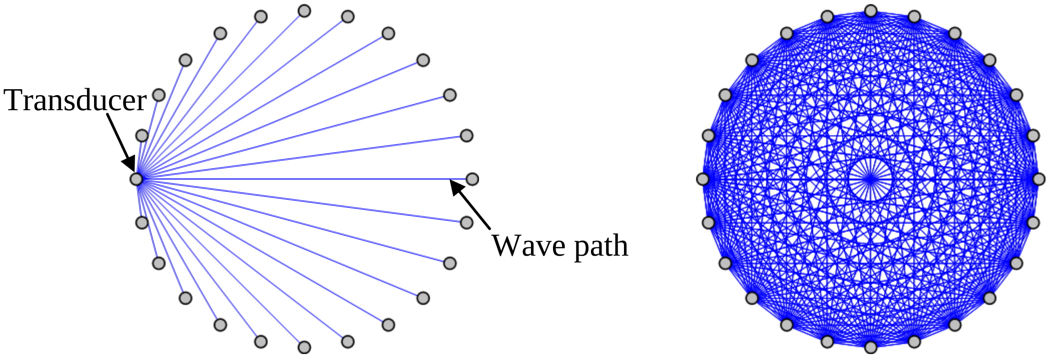

(a) Single transducer actuation (b) Multiple transducer actuation

Figure 2.17: Circular array for GLW-based computed tomography (CT)

### 2.3.1 Tomography

Distributed transducers surrounded the area of interest are used for GLW based tomography. The GLW propagates through the investigation area between a set of transducers on a testing structure. As shown in Figure 2.17, a transducer acts as a transmitter that generates the GLW, which propagates to other transducers operate as receivers. By repeating this process, wave propagation paths for all of the distributed transducers can be constructed to create an image of the interested region of the structure.

If there is any damage within the testing region, the GLWs propagating the wave paths through the damaged area may be attenuated due to the damage. Any abnormality in the testing region is highlighted in the reconstructed tomography image. The location, size, and the shape of the damage can be visualized with this technique.

Jansen and Hutchins [87] conducted Lamb wave based tomography to detect a damage in a thin aluminum plate submerged in water using immersion transducers. Wright et al. [88] used air-coupled transducers for the Lamb wave tomography of thin plates. Leonard et al. [89] developed double-crosshole scheme for the Lamb wave tomography and compared to parallel-projection tomography scheme. The parallel-projection tomography scheme uses a transmitter-receiver pair of transducers mechanically moved in parallel over the investigation area. The double-crosshole scheme is a fast and practical alternative to the parallel-projection scheme, which borrows the concepts from seismology.

However, there are a few critical issues of this technique because the velocity of GLW mode depends on the excitation frequency and the thickness of a structure. In addition, it is complicated to analyze the GLW signals obtained from a receiver due to the GLW characteristics such as mode conversion/separation, wave reflection, and the dispersion feature.

### 2.3.2 Time-Reversal Imaging

The concept of ultrasonic time-reversal was first extensively studied by Fink [90], Wu et al. [91], and Cassereau and Fink [92]. Time-reversal is an acoustic wave focusing technique. As shown in Figure 2.18, the acoustic waves generated from the excitation source are sampled by receiver transducers. The acoustic waves are then time-reversed and transmitted from the transducers obtained the waves. The time-reversed acoustic waves can propagate and arrive at the acoustic source location. This process allows the time-reversed acoustic waves to re-focus on its original source location.

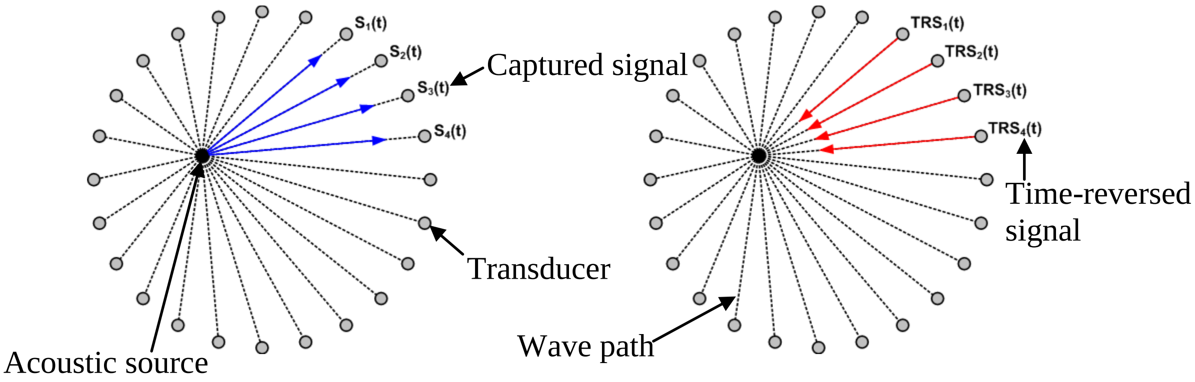

(a) Acoustic source wave recording step (b) Time-reversal step

Figure 2.18: Schematic of time-reversal imaging method

Ing and Fink [93] demonstrated that the time-reversal process allows to compensate the fundamental GLW problems such as dispersion and multiple modes generation. In the experiments, a laser impact to generate the GLWs was identified by using the wave refocusing method based on the time-reversal technique. Kim et al. [94] adopted the time reversal technique to focus the ultrasonic GLWs generated by array transducers on defects. Park et al. [95] introduced the time-reversal method as a baseline-free SHM technique with the GLW propagation. Wang et al. [96] developed a digital imaging method based on the time-reversal of the GLWs. Xu and Giurgiutiu [97] theoretically and experimentally demonstrated the single mode tuning effects on the GLW based time-reversal technique.

### 2.3.3 Sparse Array Imaging

For the damage detection of a complicated structure, which is more realistic and not a simple plate, a few researchers developed the sparse array imaging technique that is a probability-based diagnostic imaging method. The GLW signal parameters such as time-of-flight (ToF), magnitude (i.e. amplitude), signal energy, and correlation coefficients are used to develop the algorithm for the array imaging technique [4]. The sparse array imaging technique was applied for damage detection of metallic structures and composite structures [98-101]. Reconstruction algorithm for probabilistic inspection of defects (RAPID) was introduced by Gao et al. [102] and widely used for the sparse array imaging of the damaged structures [103-106]. The governing equation for signal different coefficients (SDC) based RAPID technique is defined by

$$SDC_{ij} = 1 - \left| \frac{\int (S_i(t) - \bar{S}_i)(S_j(t) - \bar{S}_j)dt}{\sqrt{\int (S_i(t) - \bar{S}_i)^2 dt \int (S_j(t) - \bar{S}_j)^2 dt}} \right| \tag{2.70}$$

where $S_i$ is the beseline signal; $S_j$ is sensor signal data; $\bar{S}_i$ and $\bar{S}_j$ are the mean value of the corresponding signals. The estimation of the defect probability at (x,y) location may be given by

$$P(x,y) = \sum_{i=1}^{N-1} \sum_{j=i+1}^{N} SDC_{ij}\, s_{ij} \tag{2.71}$$

$$\begin{aligned} s_{ij} &= \frac{\beta - R_{ij}(x,y)}{\beta - 1} \ \text{ for } \beta > R_{ij}(x,y) \\ s_{ij} &= 0 \ \text{ otherwise,} \end{aligned} \tag{2.72}$$

$$R_{ij}(x,y) = \frac{\sqrt{(x-x_i)^2+(y-y_i)^2} + \sqrt{\left(x-x_j\right)^2+\left(y-y_j\right)^2}}{\sqrt{\left(x_j-x_i\right)^2+\left(y_j-y_i\right)^2}} \tag{2.73}$$

where $s_{ij}$ is the transmitter *i* and receiver *j* pair; $R_{ij}$ is the ratio of the sum of distance of the point (x,y) to the transmitter *i* and receiver *j* to the distance between the transmitter and receiver; $\beta$ is a scaling parameter and is selected to be around 1.05.

Recently, minimum variance distortionless response (MVDR) method was applied for the GLW-based sparse array imaging (especially delay-and-sum imaging) to improve image quality for localization of damage over a large area [107-109].

### 2.3.4 Phased Array Technique

Phased array is a device consisting of a group of transducers located at distinct spatial locations. Due to the spatial location variation of transducer, there are time delays of the respective signals of the transducers and the associated phase shift relative to the time delays. Appropriately adjusting individual time delays for the transducers, the phase differences may be compensated so that the effective wave propagation pattern of the phased array is reinforced in a desired direction and suppressed in other (undesired) directions. In addition, a phased array may be used to focus the wave radiation to a specific point, and to scan rapidly in azimuth and elevation. Because of its robustness as a spatial signal processing tool, the phased array technique has been widely used in all aspects of civil, military, science, and medical industry fields. The application examples of the phased array technique are shown in Figure 2.19.

(a) The Very Large Array (VLA)

(b) Phased array radar for a warship (c) Ultrasound phased array

Figure 2.19: Examples of the phased array technique applications (photo credit: Google Image)

After the phased array technique had developed for radar positioning and tracking, phased array transducers (Figure 2.20) and the associated signal processing technique were widely applied for ultrasonic-based NDE applications to detect various damages such as hole, crack, corrosion, and welding flaw in structural components. In general, the phased array transducer can scan the thickness direction and then move to another location to scan another thickness direction. By repeating this process, the whole structure can be three-dimensionally scanned.

(a) Phased array transducer samples

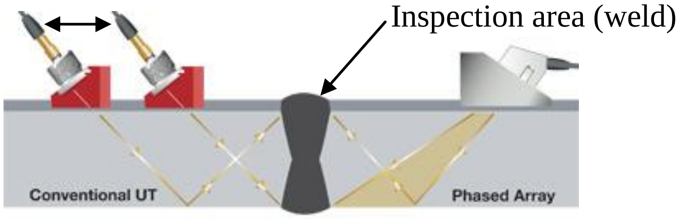

(b) Comparison between conventional ultrasonic testing and phased array methods

Figure 2.20: Phased array transducers for NDE/SHM applications (photo credit: www.olympus-ims.com)

A signal processing method with the phased array refers to beamforming for directional signal transmission or reception. The beamforming is characterized by directivity pattern of the phased array, which includes a main lobe, side lobes, and grating lobes. The phased array signal processing (i.e. the beamforming technique) is divided into four different methods such as directional transmission, directional reception, target focusing, and beam steering. All of the approaches are purposed on target detection and monitoring.

Phased array technique in conjunction with the GLW approach has recently been applied for damage identification of plate-like structures. The GLW-based phased array system is capable of scanning a large area of the hosting structure from a relatively small test area. The comparison of the GLW inspection area for the two different methods can be found in Figure 2.21. The main advantage of the phased array technique is cost- and time-effectiveness due to the inspection duration and accessibility of the transducers to the structure under inspection.

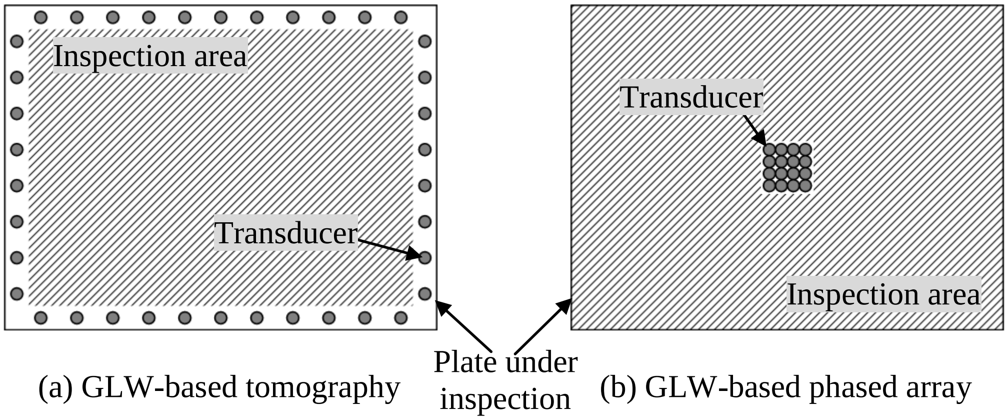

(a) GLW-based tomography (b) GLW-based phased array

Figure 2.21: Inspection area comparison between two array imaging methods

Deutsch et al. [110] performed experimental GLW study by using a linear array. The time reversal method was used to focus the GLWs, which are transmitted from the linear array, on a single defect. Wilcox et al. [111, 112] intensively examined the GLW-based phase array technique to identify defects in plate-like structures. PZT ceramics and electromagnetic acoustic transducers (EMAT) elements were used to construct circular arrays and linear array. S0, A0, and SH0 modes of the GLWs were excited and captured by the arrays. A phased-addition algorithm was developed for virtual steering of the array fixed at a specific position. The phased addition algorithm with deconvolution was presented to suppress side lobes due to the circular array configuration. Fromme et al. [113] developed a GLW-based circular array for the structural integrity monitoring of large plate-like structures. The circular array with a ring shape was constructed by a number of PZT elements. Dispersive A0 mode was excited and measure by the array, and the group of the GLW signals were processed by using the phased-addition algorithm with dispersion compensation and deconvolution. Purekar et al. used GLW-based phased sensor arrays as directional spatial filters and presented the associated damage detection approach in thin isotropic plates [114] and composite laminates [115]. The phased sensor array was virtually swept over the plates and the reflected GLWs from discontinuities (e.g. damage and edge boundary) were captured. The algorithm for the directional filtering approach allowed the phased sensor array to track a selective GLW mode from a damage of the plate. Rajagopalan et al. [116] introduced a single transmitter multi-receiver (STMR) PZT array for the GLW-based damage detection of isotropic plates, orthotropic [117], and anisotropic composite plates [118]. A ring type PZT array was used as receiver while a single PZT located at the center of the array was used as a single transmitter for the GLW excitation. A phase addition reconstruction algorithm was used to detect wave reflections from damage and boundaries.

Embedded-ultrasonic structural radar (EUSR) using piezoelectric wafer active sensors (PWASs) was introduced for damage detection application of thin plates, by Giurgiutiu and Bao [119]. The EUSR algorithm based on a standard beamforming technique (delay-and-sum method) was formulated for transmission and reception beamforming. A linear phased array consisted of PWASs was instrumented and used as a structural radar to detect crack damages [119] and the growth of a crack [120] in a thin metallic plate. By Yu and Giurgiutiu [121, 122], the EUSR methodology using the linear array was advanced to a study with optimized linear array and two-dimensional (2-D) phased array with cross-shape, rectangular grid, rectangular ring, circular ring, and concentric circular shape. A generic beamforming formula (triangular algorithm), commonly used in antenna theory [123], was developed for the GLW-based EUSR system. To improve the EUSR image quality, various signal processing techniques such as Hilbert transform and wavelet transform were applied. Phantom image due to the back lobe of the beamforming characteristics was also discussed. Yan et al. [104] demonstrated GLW-based phased array application with beamforming technique and back-propagation signal synthesis for damage detection in a thin metallic plate. A circular array with PZT transducers was attached at the center of the plate. The beamforming technique with the GLW-based phased array was applied for unidirectional, cross-ply, and quasi-isotropic composite plates [124]. Kim and Philen [125] examined the beamsteering with a linear phased array consisted of macro-fiber composites (MFC) transducers. The MFC beamforming characteristics were compared with the PZT phased array. Olson et al. [126] demonstrated experimental study for the beamforming technique (transmission and reception) using GLW based linear phased arrays in an aluminum plate.

For high resolution inspection, Velichko and Wilcox [127, 128] optimized the phased-addition algorithm for GLW-based phased arrays with linear and circular layouts. Maximization of contrast method was introduced to reduce the possible side lobes of a given array configurations. An extension of the approach for multiple modes was also presented. Recently, Engholm and Stepinski presented an adaptive beamforming technique with a GLW-based uniform circular array [129] and a rectangular array [130] for damage detection of thin isotropic panels. The adaptive beamforming was based on the standard delay-and-sum beamfoming in conjunction with minimum variance distortionless response (MVDR) method. Both cases used single-transmitter-multiple-receiver (STMR) approach and the adaptive beamforming technique study was extended to multiple-transmitter-multiple-receiver (MTMR) approach in the recent work [131]. The GLW dispersion was compensated for the signal processing by using theoretically calculated dispersion curves.

## 2.4 *Chapter Summary*

This chapter discussed general backgrounds of the guided Lamb wave (GLW) and the associated non-destructive evaluation (NDE) and structural health monitoring (SHM) applications. The dispersion curves, i.e. frequency-wavenumber relations, were investigated to understand the GLW propagation in metallic and composite plates. The GLW excitation and sensing were described based on the piezoelectric-ceramic elements (e.g. PZT ceramics). The GLW mode tuning method with the peizoceramic element was discussed. The GLWs contain a number of wave modes and most of them are high dispersive. The dispersion compensation and removal techniques were explained to help analyze the GLW propagation and the associated damage detection applications. The mode conversion and separation of the GLWs interaction with discontinuities were discussed. A review of spectral analysis methods for the GLW signal processing was described. Fundamental time and frequency analysis methods and the combined time-frequency analysis method and its application to the GLW interrogation were reviewed. The state-of-art of the advanced GLW signal processing methods to visualize structural defects was reviewed. The GLW-based array imaging techniques including the phased array technique were intensively discussed.

# 3. Phased Sensor Array Signal Processing

In this study, the phased array acts only as a receiver consisting of multiple sensor elements. Sensors, in general, have omni-directionally equal sensitivity to receive information, i.e. insensitive to a certain direction. However, since the phased sensor array operates as a spatial filter, the array signal processing method can enhance signals a specific direction while eliminating signals from other directions. Signal processing diagram of the phased sensor array is shown in Figure 3.1.

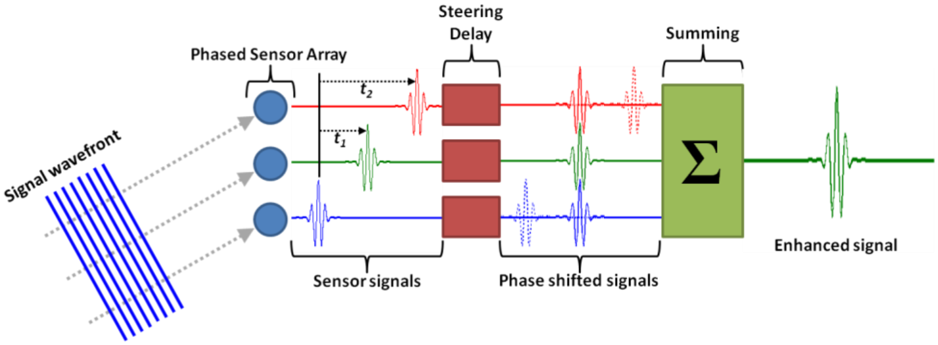

Figure 3.1: Schematic of phased sensor array signal processing

The wavefront of incoming wave arrives at a phased sensor array, and the sensor signals present the time differences of the arrival signals because of the propagation direction of the incoming signal. By using a phased array algorithm, the sensor signals can be phased or delayed for virtually steering a specific direction, i.e. the wave propagation direction, and all of the steered sensor signals are summed to amplify the incoming wave signal at its propagation direction and minimize noise and interference from other directions. The summation amplitude of the raw sensor signals is compared to the phase shifted sensor signals, shown in Figure 3.2. For this case, the ‘Sensor2’ is assumed as the center of the phased sensor array.

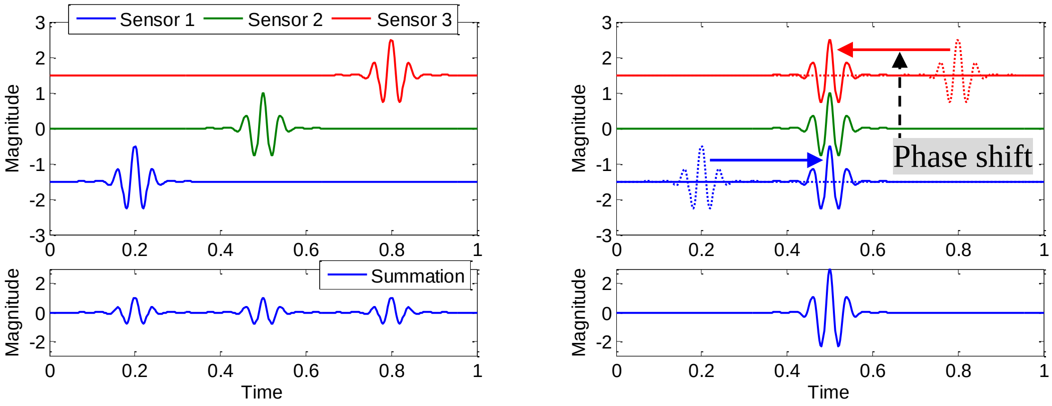

(a) Raw signals and the summation

(b) Phase shifted signals and the summation

Figure 3.2: Fundamental concepts of the phased array signal processing

The virtual array steering may be achieved by the time delay and the phase shift. In this study, the phase shift method with a directional wavenumber filtering algorithm would be used for experimental investigations. Spatial weighting functions would be used for the wavenumber filtering method. Among the four methods based on the beamforming, the beam steering would be applied for damage detection of aluminum plates and composite laminates. The beam steering technique allows the phased sensor array to scan the whole structure under inspection. In this chapter, the fundamentals of the phased sensor array signal processing are to be discussed.

### 3.1 *Fundamentals of Phased Sensor Array Analysis*

Wavenumber filtering based on phased array signal processing is a robust method of post processing for a group of sensor signals. The wavenumber filtering is similar to time-shift method in which individual sensor signals are gathered and directional filtering is performed in a post-processing step based on estimates of travel time from one sensor to the next. The wavenumber filtering method is based on knowledge of the wavenumber-frequency relationship and may be performed in real-time by the use of selective gains applied to each sensor signal that can remove unwanted information while enhancing the desired signal component. The signal processing algorithm of the wavenumber filtering technique discussed in this text is based on the previous research conducted by Purekar [3]. In this study, the algorithm for a linear array configuration is extended for 2-D phased sensor array configuration.

Array response may be evaluated by combining signals captured from an array consisted of multiple sensors at different locations, defined by

$$\psi(t) = \iint v(x, y, t)dxdy \tag{3.1}$$

where $\psi(t)$ is the array response and $v(x, y, t)$ is the sensor signal at $(x, y)$ location.

Adding spatial weights (i.e. the set of gains) to the array sensors, the array response may be characterized depending on the weights, given by

$$\psi(t) = \iint \phi(x, y)v(x, y, t)dxdy \tag{3.2}$$

where $\phi(x, y)$ is the spatial weights at $(x, y)$ location. The content of the array response is dependent upon the spatial weights applied to the array sensors. In general, the weight function is complex in nature and complex signal analysis routines implemented to realize the spatial filtering.

Wavenumber response of the array can be determined by a Fourier identity as shown below,

$$\iint \phi(x,y)v(x,y,t)\,dxdy = \iint \Phi(k_x,k_y)V\big(k_x,k_y,t\big)\,dk_xdk_y \tag{3.3}$$

where

$$\begin{aligned}\Phi\big(k_x,k_y\big) &= \iint \phi(x,y)e^{-i\left(k_xx+k_yy\right)}\,dxdy\\ V\big(k_x,k_y,t\big) &= \iint v(x,y,t)e^{-i(k_xx+k_yy)}\,dxdy\end{aligned} \tag{3.4}$$

where $\Phi\big(k_x,k_y\big)$ and $V\big(k_x,k_y\big)$ are Fourier transformed functions for the spatial weights, $\phi(x,y)$, and the sensor signals, $v(x,y)$, respectively; $k_x$ is the wavenumber along the $x$-axis and $k_y$ is along $y$-axis; *i* is the imaginary unit.

For an ideal filtering for a desired wavenumber, Dirac delta function for the $\Phi\big(k_x,k_y\big)$ may be used as

$$\Phi\big(k_x,k_y\big) = \delta\big(k_x-\bar{k}_x,k_y-\bar{k}_y\big) \tag{3.5}$$

where $\bar{k}_x$ and $\bar{k}_y$ are desired $x$-axis and $y$-axis wavenumber components for the wavenumber filtering. The spatial weights can be determined by the inverse Fourier transform of the given Dirac delta function, $\Phi\big(k_x,k_y\big)$, written by

$$\phi(x,y) = \frac{1}{2\pi}\iint \Phi\big(k_x,k_y\big)e^{i\left(k_xx+k_yy\right)}\,dk_xdk_y \tag{3.6}$$

As a result of the inverse Fourier transform, the spatial weight function can be given by

$$\phi(x,y) = \frac{1}{2\pi} e^{i(\bar{k}_x x + \bar{k}_y y)} \tag{3.7}$$

The spatial weight function may be defined in a more general form, written by

$$\phi(x,y) = e^{i(\bar{k}_x x + \bar{k}_y y)} = \cos(\bar{k}_x x + \bar{k}_y y) + i \sin(\bar{k}_x x + \bar{k}_y y) \tag{3.8}$$

The spatial weight function includes real and imaginary parts that are even and odd functions, respectively.

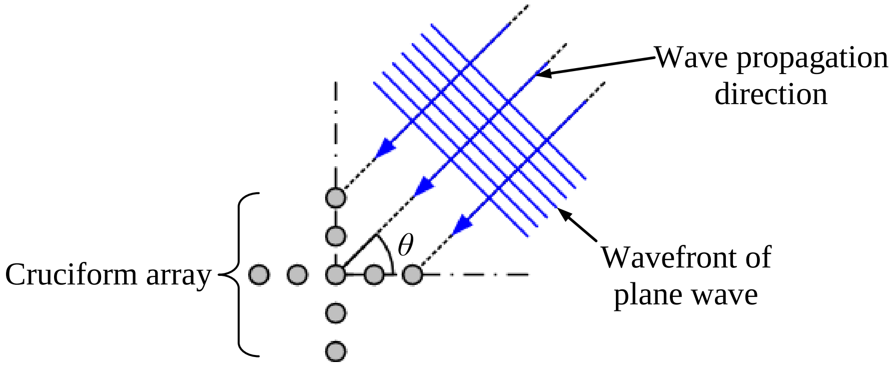

Figure 3.3: Plane wave approaching to an array with cruciform layout

The array response filtered by a desired wavenumber is defined by

$$\psi(t) = \iint e^{i(\bar{k}_x x + \bar{k}_y y)} v(x,y,t)\,dx\,dy \tag{3.9}$$

For the case of a plane wave approaching to a phased sensor array (see Figure 3.3), the wavenumber of the plane wave is written by

$$\boldsymbol{k} = k_x \hat{\imath} + k_y \hat{\jmath} \tag{3.10}$$

$$\begin{aligned} k_x &= |\boldsymbol{k}| \cos\theta \\ k_y &= |\boldsymbol{k}| \sin\theta \end{aligned} \tag{3.11}$$

where $\hat{\imath}$ and $\hat{\jmath}$ are unit vectors.

Hence, the Equation (3.9) can be rewritten by

$$\psi(\theta,t) = \iint e^{i[(\bar{k}\cos\theta)x+(\bar{k}\sin\theta)y]} v(x,y,t)dxdy \tag{3.12}$$

where $\bar{k}$ is a desired wavenumber for filtering and $\theta$ is wave propagation direction, i.e. an array steering angle. By the Euler's identity, the array response directionally filtered by the desired wavenumber is defined by

$$\psi(\theta,t) = \begin{bmatrix} \iint \phi_R(x,y,\theta)v(x,y,t)dxdy \\ +i\iint \phi_I(x,y,\theta)v(x,y,t)dxdy \end{bmatrix} \tag{3.13}$$

where

$$\begin{aligned} \phi_R(x,y,\theta) &= \cos\left[\left(\bar{k}\cos\theta\right)x + \left(\bar{k}\sin\theta\right)y\right] \\ \phi_I(x,y,\theta) &= \sin\left[\left(\bar{k}\cos\theta\right)x + \left(\bar{k}\sin\theta\right)y\right] \end{aligned} \tag{3.14}$$

where $\phi_R$ and $\phi_I$ are the real part and the imaginary part of the spatial weight function, respectively, at the $(x,y)$ location.

Due to the wavenumber-frequency relationship, $k = \omega/C_p$, the directional spatial weight function, $\phi(x,y,\theta)$, for the wavenumber filtering performs the phased shifts (i.e. time delays) for the sensor signals. By using the governing Equation (3.13) for the directional wavenumber filtering algorithm, a desired mode of the GLWs approaching to the sensor array can be scanned over the azimuthal directions, $(0 \le \theta < 360°)$.

In general, the weight function is complex in nature and complex signal analysis routines implemented to realize the spatial filtering. The imaginary part of the array response can be achieved by using a $\pi/2$ phase shift of the sensor signal. In general, integration and differentiation can be applied for the phase shift. Integration is numerically more stable than differentiation, but requires more time to compute. In order to use integration and differentiation for producing the $\pi/2$ phase shift effectively, the candidate signal should be band limited. Another method to produce the $\pi/2$ phase shift is based on the Hilbert transform and can be used instead of the above methods. The Hilbert transform can be used to produce the requisite phase shift regardless of the frequency content of the signal. The different methods to produce the $\pi/2$ phase shift are illustrated in Figure 3.4 from a sample signal

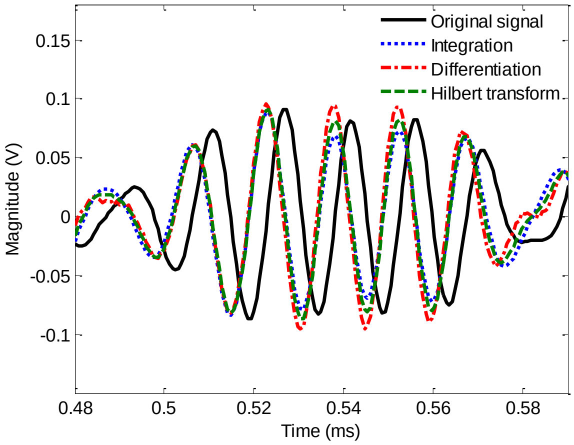

Figure 3.4: Comparison of $\pi/2$ phase shift method

In the research performed, the Hilbert transform was used for the $\pi/2$ phase shift. The corresponding array response from Equation (3.13) can be rewritten as shown below.

$$\psi(\theta,t)=\left\{\begin{array}{c}\iint \phi_R(x,y,\theta)v(x,y,t)dxdy\\ +\iint \phi_I(x,y,\theta)\mathrm{HT}[v(x,y,t)]dxdy\end{array}\right\} \tag{3.15}$$

where $\mathrm{HT}[v(x,y,t)]$ denotes the Hilbert transform of the sensor signal, $v(x,y,t)$. This formulation eliminates the imaginary term shown in Equation (3.13).

For 2-D discrete sensor array with a finite number of sensor elements, Equation (3.15) can be rewritten as shown below.

$$\psi(t,\theta) = \left\{ \begin{array}{c} \dfrac{1}{N}\displaystyle\sum_{n=1}^{N} \phi_R(x_n, y_n, \theta) v(x_n, y_n, t) \\ + \dfrac{1}{N}\displaystyle\sum_{n=1}^{N} \phi_I(x_n, y_n, \theta) \mathrm{HT}[v(x_n, y_n, t)] \end{array} \right\} \tag{3.16}$$

$$\begin{aligned} \phi_R(x_n, y_n, \theta) &= \cos\left(x_n \bar{k} \cos\theta + y_n \bar{k} \sin\theta\right) \\ \phi_I(x_n, y_n, \theta) &= \sin\left(x_n \bar{k} \cos\theta + y_n \bar{k} \sin\theta\right) \end{aligned} \tag{3.17}$$

A diagram for constructing a phased array response using sensor signals obtained from a 2-D sensor array is shown in Figure 3.5.

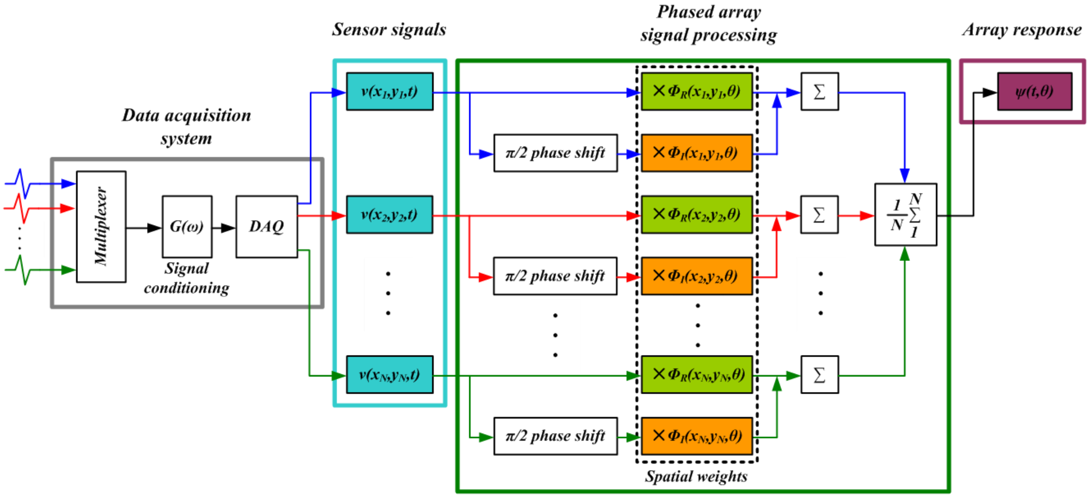

Figure 3.5: Flow diagram of phased array signal processing

## 3.2 *Beam Pattern of Phased Array*

The performance of a phased array is characterized by examining a directivity function (i.e. beam/array pattern) in the wavenumber domain. The directivity function is dependent on the total number of sensors and the corresponding sensor locations used to construct a phased array. The directivity function can be used to quantify sensitivity of the array to waves of different wavelength and travelling direction, and the directivity function is evaluated by using the 2-D Fourier transform (in space) of the array distribution.

The directivity function for a two-dimensional (2-D) array is defined by

$$D(k_x, k_y) = \iint e^{i(k_x x + k_y y)} dx dy \tag{3.18}$$

where $i$ is imaginary unit and $k_x = k \cos\theta$, $k_y = k \sin\theta$, and $k$ is a range of interested wavenumber.

For a 2-D phased array with discrete sensor elements, an equivalent form of the Equation (3.18) is defined by

$$D(k_x, k_y) = \frac{1}{N} \sum_{n=1}^{N} \delta(x - x_n, y - y_n) e^{i(k_x x + k_y y)} = \frac{1}{N} \sum_{n=1}^{N} e^{i(k_x x_n + k_y y_n)} \tag{3.19}$$

In the above expression, $n$ is sensor index so that $(x_n, y_n)$ is the $x$ and $y$ position of the $n$-th sensor element; $N$ is the total number of sensor elements in the array; $\delta$ corresponds to the spatial distribution of points relative to the array.

The directivity function is consisted of three lobes such as main lobe, side lobes, and grating lobes. The main lobe is the lobe containing the maximum beam magnitude. The side lobes are the lobes that are not the main lobe. For the phased arrays, some side lobes become substantially larger in magnitude, and approaching the level of the main lobe, and these are called by the grating lobes.

Virtual steering of the array is accomplished by using selective gains and signal processing technique to artificially modify the directivity function as desired.

### *3.3 Wavenumber Selectivity for Phased Array Steering*

The main advantage of the phased array analysis is the ability to (virtually) steer the array such that the array response contains signals of a desired wavenumber region. The directivity function in the Equation (3.19) is the unsteered condition of the array. By using a spatial weight function, $\Phi(k_x, k_y)$, the directivity function can be virtually steered with respect to a desired wavenumber.

For an ideal filtering for a wavenumber, Dirac delta function is used as the spatial weight function, and the steered directivity function can be determined by

$$\begin{aligned} D(k_x, k_y) * \Phi(k_x, k_y) &= D(k_x, k_y) * \delta(k_x - \bar{k}_x, k_y - \bar{k}_y) \\ &= D(k_x - \bar{k}_x, k_y - \bar{k}_y) \end{aligned} \tag{3.20}$$

where $*$ denotes convolution; $k_x = k\cos\theta$ and $k_y = k\sin\theta$ where $k$ is a range of interested wavenumber and $\theta$ is angular direction of the array steering; $\bar{k}_x = \bar{k}\cos\theta$ and $\bar{k}_y = \bar{k}\sin\theta$ where $\bar{k}$ is a desired wavenumber for filtering.

For a 2-D phased array with discrete sensor elements, an equivalent form of the steered directivity function is expressed by

$$D(k_x - \bar{k}_x, k_y - \bar{k}_y) = \frac{1}{N}\sum_{n=1}^{N} e^{i\left((k_x - \bar{k}_x)x_n + (k_y - \bar{k}_y)y_n\right)} \tag{3.21}$$

where $n$ is sensor index so that $(x_n, y_n)$ is the $x$ and $y$ position of the $n$-th sensor element; $N$ is the total number of sensor elements in the array.

## 3.4 *Overview of 1-D Phased Sensor Array and Phased Array Analysis*

For an one-dimensional (1-D) phased array analysis, the directivity function is a function of wavenumber in *x*-axis only. The directivity function for a 1-D linear array with discrete sensor elements is defined by

$$D(k_x) = \frac{1}{N}\sum_{n=1}^{N} e^{i(k_x x_n)} \tag{3.22}$$

where $x_n = n\Delta x$ and $\Delta x$ is the element spacing along the $x$-axis, and $N$ is total number of sensor elements. The directivity function for the discrete array is re-expressed in a simple closed-form, written by

$$D(k_x) = \frac{\sin\,(k_x N\Delta x/2)}{\sin\,(k_x\Delta x/2)} \tag{3.23}$$

The beam pattern (i.e. directivity function results) of a sample linear array (Figure 3.6(a)) is shown in Figure 3.6(b). The array is consisted of 13 sensor elements that have equal spacing ($\Delta x$=3/16 in.). The main lobe is located at $k_x = 0$ and additional lobes are present as the wavenumber moves outward from the origin. Additional peaks of the same magnitude of the main lobe are shown in the figure and these repeat as the wavenumber range of interest increases. Since the directivity function indicates the sensitivity of an array as a function of wavenumber, it is generally undesirable to have additional lobes of the same magnitude of the main lobe in the wavenumber range of interest. The wavenumber range of interest is generally restricted to $|k_x\Delta x| < 1$. This situation is analogous to sampling in the time domain where a Nyquist frequency exists which is related to the sampling frequency of the system.

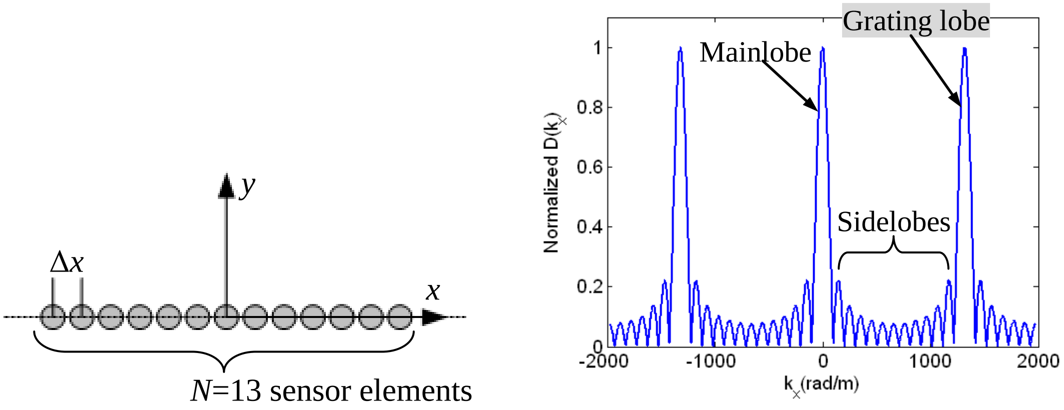

(a) 1-D linear array diagram

(b) Directivity function of the left array

Figure 3.6: Directivity function for an 1-D linear array

Additional parameters of concern are the beamwidth of the main lobe and the height of the sidelobes (Figure 3.7). The beamwidth of the main lobe indicates wavenumber bandwidth of the system. This is shown graphically in the figure and corresponds to the wavenumber range highlighted in the figure and is found by identifying the wavenumber region in which the normalized directivity function is greater than 0.707. The sidelobes as identified in the figure indicates the leakage of information into the array response from undesired wavenumber regions. High sidelobe levels indicate increasing leakage. An ideal directivity function would have a very narrow beamwidth with non-existant sidelobe levels. Techniques exist which aim to narrow the mainlobe beamwidth with the expense of high sidelobe levels. Similarly, techniques which aim to reduce sidelobe levels cause an increase in the beamwidth of the mainlobe.

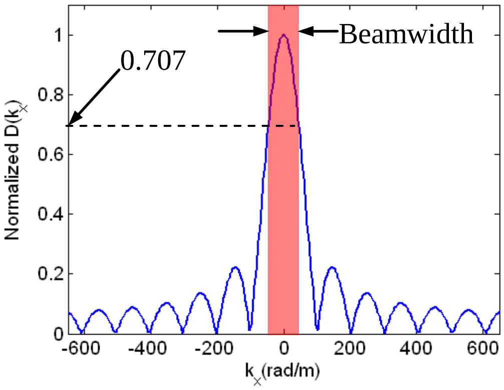

Figure 3.7: Beamwidth for the 1-D linear array with 13 sensor elements

The steered directivity function for the linear array can be determined by from the Equation (3.20),

$$D(k_x) * \Phi(k_x) = D(k_x) * \delta(k_x - \bar{k}_x) = D(k_x - \bar{k}_x) \tag{3.24}$$

For the linear discrete array, an equivalent form of the steered directivity function is given by

$$D(k_x - \bar{k}_x) = \frac{\sin\left((k_x - \bar{k}_x)N\Delta x/2\right)}{\sin\left((k_x - \bar{k}_x)\Delta x/2\right)} \tag{3.25}$$

The beam patterns of the linear array under the steered conditions are evaluated as functions of steering angle and wavenumber, shown in Figure 3.8. The difference of the two figures is due to the nonlinear relations between the steering angle and the desired wavenumber, $\bar{k}_x = \bar{k}\cos\theta$. The beamwidth of the mainlobe increases as the main lobe is steered off of $\theta = 90°$. The ability of the linear array to distinguish between waves coming from different angles depends on the array steering direction, i.e. the beamwidth of the main lobe. The curve in blue is the unsteered directivity function of the linear array. Steering of the array is done using signal manipulation in order to shift the mainlobe to a desired (wavenumber) position, as indicated by the curves in green and red.

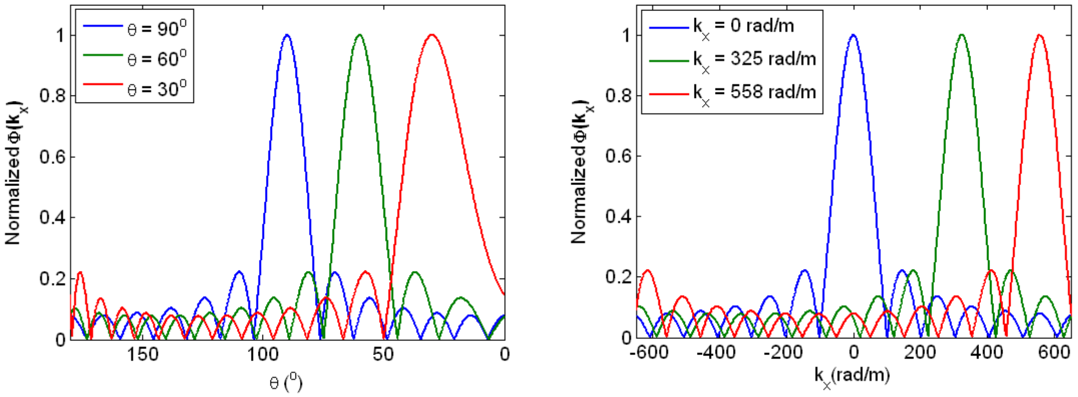

(a) as function of steering angle

(b) as function of wavenumber

Figure 3.8: Steering of 1-D linear array with 13 sensor elements

Array steering is accomplished by modifying the array response by using a spatial weight function, $\phi(x)$, which is determined based on a desired position of the mainlobe in the directivity plots as shown in Figure 3.8. The array response with a given spatial weight function of the linear array is defined by from the Equation (3.13),

$$\psi(\theta,t) = \int \phi(x,\theta)v(x,t)dx \tag{3.26}$$

For the discrete linear array, the array response is rewritten by

$$\psi(\theta,t) = \frac{1}{N}\sum_{n=1}^{N} \phi(x_n,\theta)v(x_n,t) \tag{3.27}$$

$$\phi(x_n,\theta) = e^{ix_n\bar{k}\cos\theta} = \cos\left(\bar{k}\cos\theta\, x_n\right) + i\sin\left(\bar{k}\cos\theta\, x_n\right) \tag{3.28}$$

where $n$ is sensor index so that $(x_n, y_n)$ is the $x$ and $y$ position of the $n$-th sensor element; $N$ is the total number of sensor elements in the array; $\bar{k}$ is a desired wavenumber for filtering.

In the previous phased array researches conducted by Purekar [114, 115], the ability to detect the directionality of approaching wavefronts and capability for damage detection applications have been demonstrated, using the 1-D phased sensor array and the associated signal processing method. However, the phased array technique based on the 1-D linear array has a critical limitation of the inability to distinguish approaching waves coming from the two broadside directions.

## *3.5 2-D Phased Sensor Array*

The primary concepts of the 2-D phased sensor array analysis are analogous to the 1-D counterpart. For the 2-D array analysis, the directivity function is a function of wavenumber in the *x*- and *y*-axis directions which correspond to orthogonal axes as described in Equation (3.19).

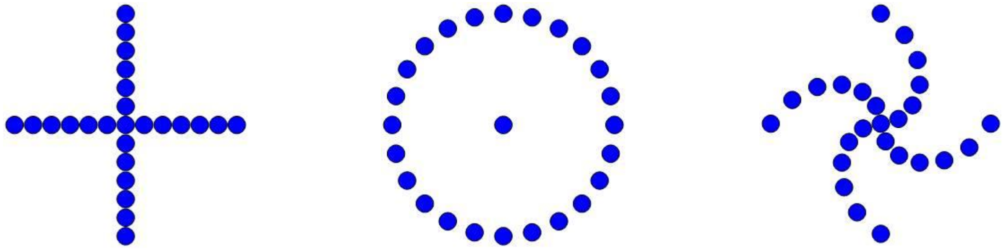

(a) Cruciform (b) Circular (c) Spiral

Figure 3.9: Candidate configurations for the 2-D phased sensor array

A wide variety of sensor array configurations are possible in a 2-D space ranging from a uniform grid like spacing to a random distribution of points. For this study, the three candidate configurations corresponding to cruciform, circular, and spiral shapes are examined for the 2-D array analysis application, shown in Figure 3.9. In order to ensure that the dimension of 2-D phased sensor array was small and the array properties could be compared on a consistent basis, the area covered by the candidate arrays was intentionally limited to fit inside a circular pattern (Figure 3.9(b)) while the total number of elements of each 2-D array was set to 25. The sensor element spacing for the cruciform array (Figure 3.9(a)) was set to 3/16 in., and the circular and spiral arrays have angular spacing of 15 deg. Each of the arrays is able to fit in a circle with a radius of 2.5 in. The maximum wavenumber range of interest was set to $1.8(\pi/\Delta x)$ based on the cruciform array layout in order to be larger than the Nyquist wavenumber, $\pi/\Delta x$, that forms one limit of an 1-D array application where $\Delta x$ indicates the sensor element spacing.

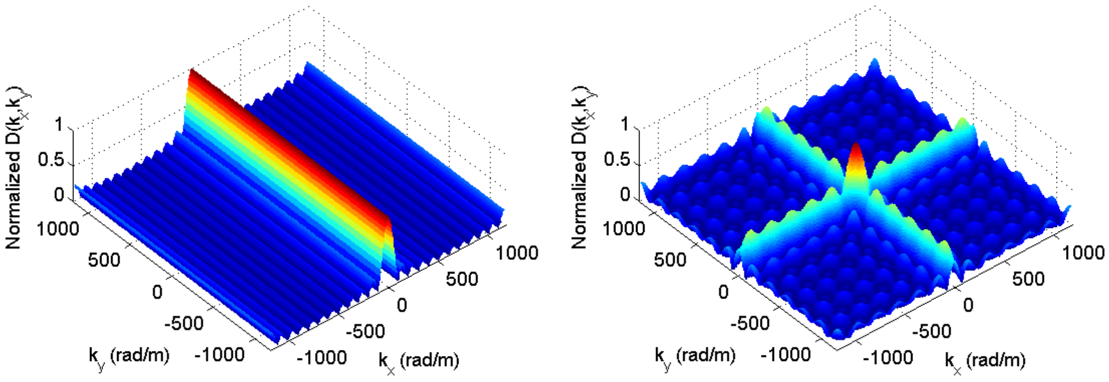

(a) 1-D linear array

(b) 2-D cruciform array

Figure 3.10: Beam pattern comparison of 1-D linear array and 2-D cruciform array

The beam patterns for a 1-D linear array and a 2-D cruciform array are evaluated using the directivity function equation, shown in Figure 3.10, to show the main difference between them. The 2-D cruciform array consists of two linear arrays which intersect at the middle element of each of the linear arrays. For the evaluation of the beam pattern, the arrays were constructed with 13 and 25 sensor elements for the 1-D linear and 2-D cruciform arrays. The sensor element spacing for both of the arrays was set to 3/16 inch. As described before, the beam pattern results demonstrate that the 1-D array has difficulty to extract the directional wave information coming along the $y$-axis direction (Figure 3.10(a)). In contrast, there is no such issue with the 2-D cruciform array (Figure 3.10(b)).

### 3.5.1 Cruciform Array

The cruciform array configuration is shown in Figure 3.11(a) and the corresponding directivity function is determined by the Equation (3.19), shown in Figure 3.11(b). As mentioned before, the cruciform array was designed by using two linear arrays.

The main lobe is at the origin and additional side lobes are present throughout the wavenumber ranges of interest. If the wavenumber range extends far beyond the Nyquist wavenumber ($\pi/\Delta x$), the grating lobes, i.e. side lobes which have the same magnitude as the main lobe, are present in the directivity function result. The main lobe at the origin corresponds to the wavenumber region of interest for phased array analysis. The steering direction is relative to the $k_x$ axis where the direction is indicated by the expression in Equation (3.29). The directivity function along $\theta = 0$

and 45 deg. are shown in Figure 3.11(c) where the wavenumber in a given direction is defined by the expression in Equation (3.30).

$$\theta = \tan^{-1}(k_x/k_y) \tag{3.29}$$

$$k = \sqrt{k_x^2 + k_y^2} \tag{3.30}$$

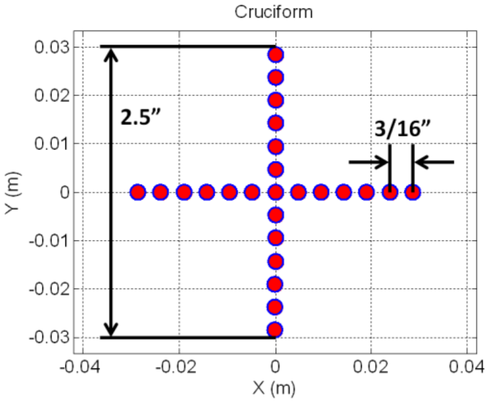

(a) Array configuration

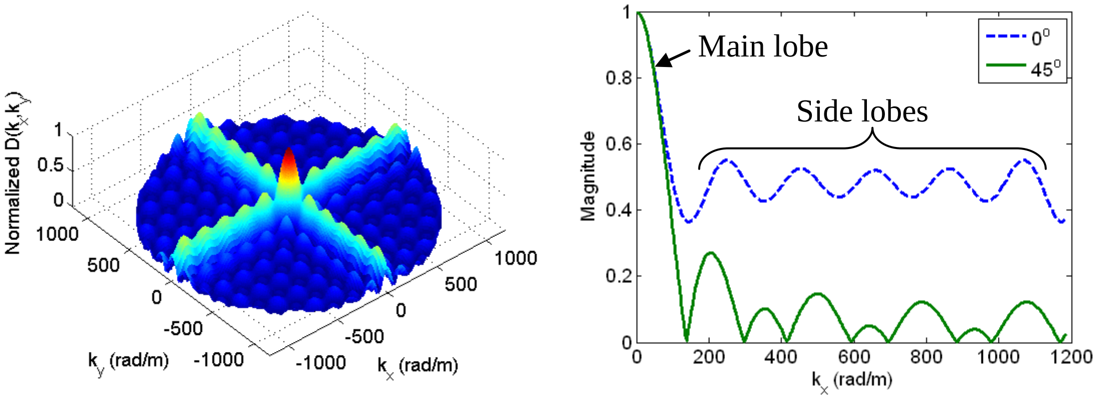

(b) Directivity function

(c) Slices of directivity function on left

Figure 3.11: Cruciform array

### 3.5.2 Circular Array

The circular array configuration is shown in Figure 3.12(a) and the corresponding directivity function is determined by the Equation (3.19), shown in Figure 3.12(b). The circular array consists of a central element with a ring of elements at a defined radius. The number of elements in the circle was set to a multiple of 4 so that the same number of elements would be present in each quadrant.

The main lobe is at the origin and side lobes and distributed over the wavenumber region. The wavenumber range was taken to be the same as the cruciform case shown above. There are no side lobes with the same height as the main lobe in the wavenumber range of interest. The wavenumber range for the circular array can be extended beyond that of the cruciform array. The directivity function along $\theta = 0$ and 45 deg. are shown in Figure 3.12(c). As opposed to the cruciform case, the directivity functions are the same. This is due to the axisymmetric layout of the circular array and indicates one of the benefits of such an arrangement of sensors.

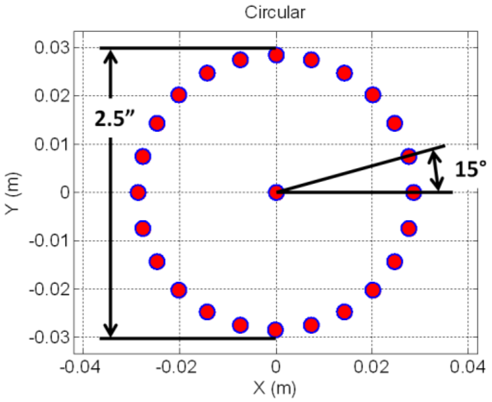

(a) Array configuration

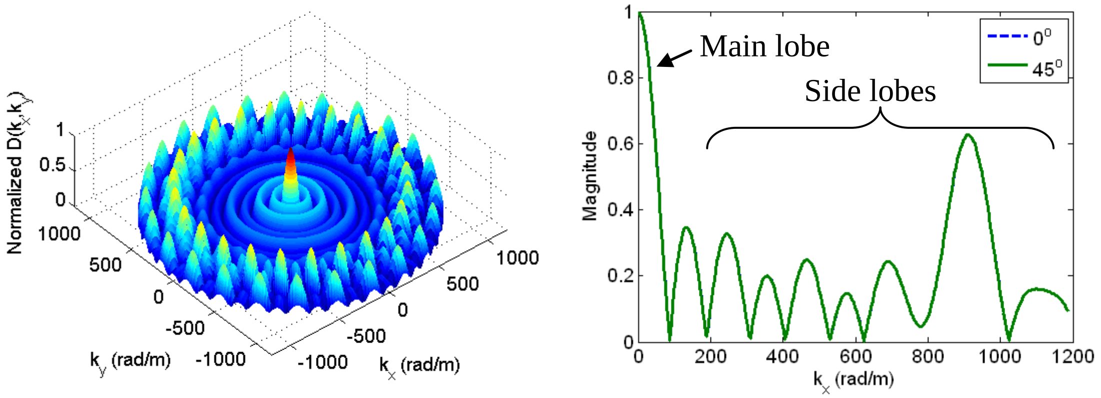

(b) Directivity function

(c) Slices of directivity function on left

Figure 3.12: Circular array

### 3.5.3 Spiral Array

The spiral array configuration is shown in Figure 3.13(a) and the corresponding directivity function is determined by the Equation (3.19), shown in Figure 3.13(b). The spiral array consists of a central element with arms radiating out from the center. Each arm curves so as to form a spiraling feature. For the spiral array case, it was assumed that four arms were used to construct the array and each arm contained the same number of elements.

The main lobe is at the origin and side lobes and distributed over the wavenumber region in a much more dispersed manner than the cruciform or circular array cases. The wavenumber range was taken to be the same as the previous cases. As with the circular distribution, there are no side lobes with the same height as the main lobe in the wavenumber range of interest which indicates that an extended wavenumber range can be used than available for the cruciform case with the same number of elements and same overall dimension of the array. The directivity function along $\theta$ =

0 and 45 deg. are shown in Figure 3.13(c). In this case, the side lobe levels are much more dependent on the steering angle.

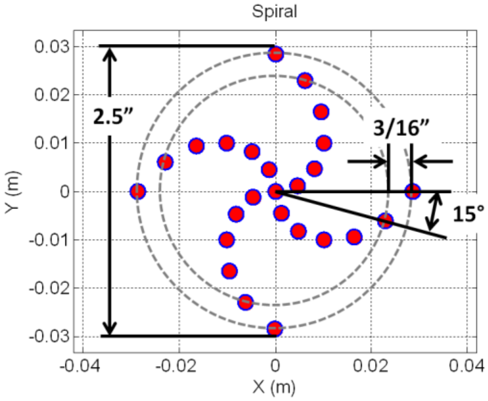

(a) Array configuration

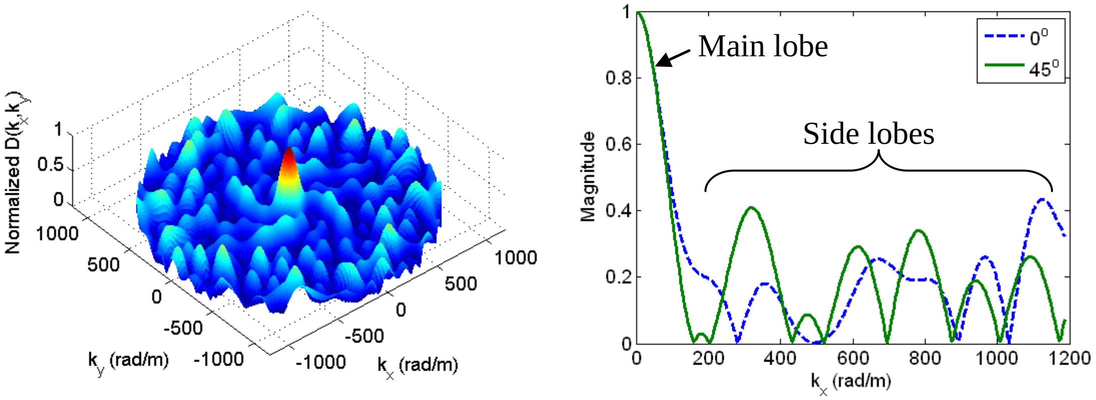

(b) Directivity function (c) Slices of directivity function on left

Figure 3.13: Spiral array

## *3.6 Evaluation of 2-D Phased Sensor Arrays and Phased Array Analysis*

### 3.6.1 Analytical Evaluation of 2-D Phased Sensor Arrays

In order to determine an appropriate 2-D sensor array configuration for evaluation, a method of quantifying the array properties was determined based on the directivity function of the arrays, which have a main lobe and numerous side lobes.

The main lobe, which is the highest peak of the directivity function, indicates the wavenumber region where the array has the highest sensitivity. The width of the main lobe, identified as the approximately 0.707 of the main lobe height (-3 dB level) is used to find the beamwidth. Typically, one would like to minimize the beamwidth of the main lobe as this would produce a directivity function with highly selective filtering capabilities. The diameter of the main lobe was determined as function of steering direction for the candidate 2-D phased sensor arrays and is shown in Figure 3.14, and the result shows the directional dependence on the array sensitivity

As indicated in the figures, the cruciform and spiral arrays have varying main lobe beamwidth as a function of steering angle and this is due to the non-axisymmetric nature of the element layout. The main lobe beamwidth of the circular array is uniform due to the axisymmetric transducer layout. Additionally, the beamwidth of the circular array is lower than that of the equivalent cruciform and spiral arrays.

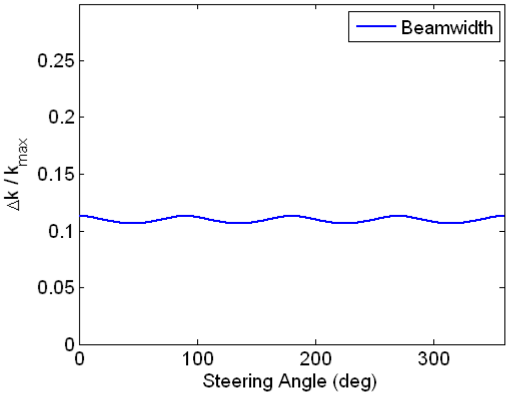

(a) Cruciform

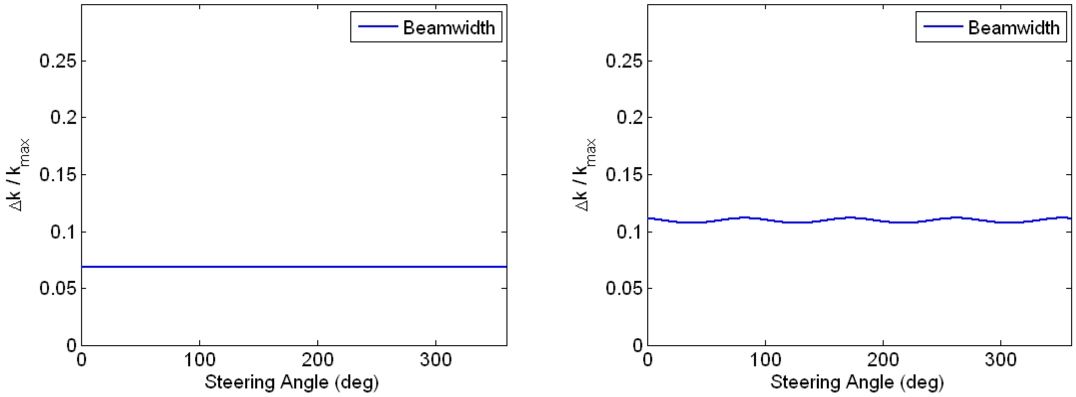

(b) Circular

(c) Spiral

Figure 3.14: Beamwidth of candidate 2-D arrays

The directivity functions of the candidate 2-D sensor arrays show the presence of side lobes which are generally undesirable. The side lobes indicate the leakage of unwanted information to be passed into array response. The peak and average side lobe height are plotted as a function of steering angle for the candidate 2-D arrays with directivity functions in the previous sections (Figure 3.15). The height of the mainlobe is not included in the data used to create these plots. All of the plots are periodic with respect to the steering direction.

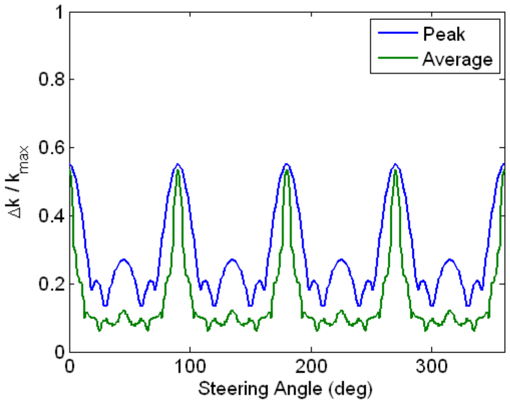

(a) Cruciform

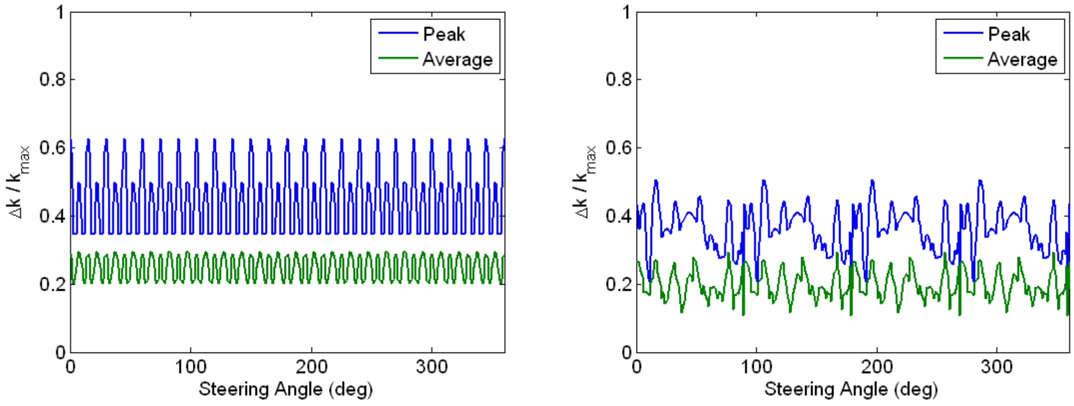

(b) Circular (c) Spiral

Figure 3.15: Peak and average side lobe heights of candidate 2-D arrays

For the cruciform array, the peak and average side lobe height are large, due to presence of the peak side lobes, at the 0, 90, 180, and 270 deg. (see directivity function in Figure 3.11). The results of the peak side lobe height show that the circular array has the largest magnitudes for the wavenumber range of interest among the three candidate arrays. The circular and spiral arrays show a consistent average side lobe height as a function of steering angle.

The beamwidth of the main lobe was averaged for all of the steering angles and the standard deviation was determined for each of the 2-D array cases, shown in Figure 3.16. The averaged results are shown as square and the bars represent a standard deviation from the averaged results. The results show that the circular array has lower beamwidth average and standard deviation as compared to the cruciform and spiral array cases. This was expected and does not change regardless of the wavenumber range of interest.

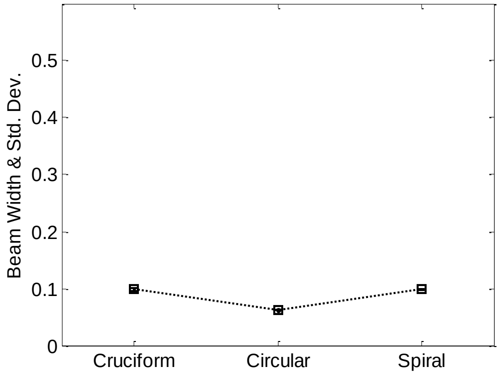

Figure 3.16: Beamwidth averaged across steering angle for candidate 2-D arrays

The peak and average of the side lobe heights were averaged for all of the steering angles and the standard deviation was determined for each of the 2-D array cases, shown in Figure 3.17. The circular array has the largest peak side lobe and average side lobe heights for the given array distribution and wavenumber range of interest. The spiral array has lower standard deviation. The cruciform array performs better on both accounts however the standard deviation is very large compared to the circular and spiral array cases.

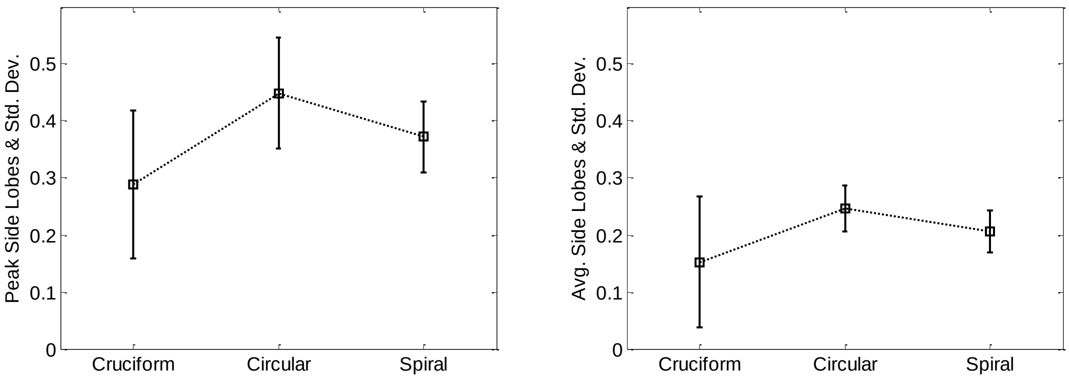

(a) Peak side lobe height (b) average side lobe height

Figure 3.17: Side lobe properties averaged across steering angle for candidate 2-D arrays

While the cruciform and spiral arrays had larger main beamwidth, the properties of the side lobe were of greater importance as this metric corresponds to corruption from unwanted wavenumbers. The cruciform array had lower side lobe heights as compared to the spiral array though the spread, as measure by standard deviation, was much larger. In that respect, the spiral array exhibits better properties. Of the three candidate arrays, the spiral array configuration was chosen for experimental tests.

### 3.6.2 Array Steering of 2-D Phased Sensor Arrays

The directivity function for the 2-D spiral array is shown in Figure 3.18(a) and the directivity function is unsteered. Consider an incoming wave signal with wavenumber 600 rad/m and its direction is 60 deg., which in polar coordinates is $(\bar{k}, \theta) = (600, 60)$. The steered directivity function for the example case is shown in Figure

3.18(b) for the given 2-D spiral array configuration and the wavenumber range of interest.

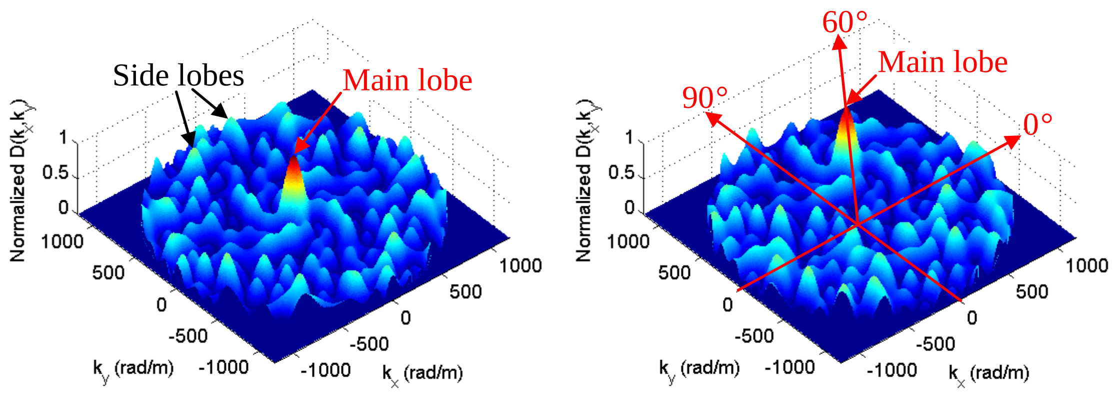

(a) Unsteered directivity function

($\bar{k}$ = 0 rad/m)

(b) Steered directivity function

($\bar{k}$ = 600 rad/m and $\theta$ = 60°)

Figure 3.18: Directional array steering with 2-D spiral array

In order to compare the array steering characteristics, the same example was applied for the candidate 2-D arrays. The unsteered and steered directivity function results for the three array cases are plotted in Figure 3.19. The figures are the top view images of the directivity function results. For the cruciform array, it is readily apparent that the steered directivity function has two large peak side lobes which reach the magnitude of main lobe. These side lobes are undesirable elements for the directional wavenumber filtering method, because they cause the largest corruption due to unwanted waveforms. For the circular array, the beamwidth of the main lobe is the smallest among three candidates, but the steered directivity function result has more noticeable side lobes than the spiral array case.

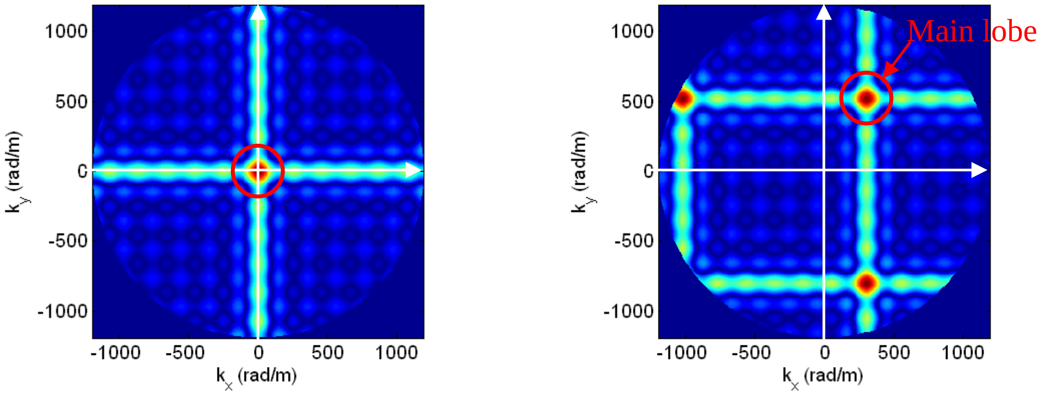

(a) Unsteered cruciform array (b) Steered cruciform array

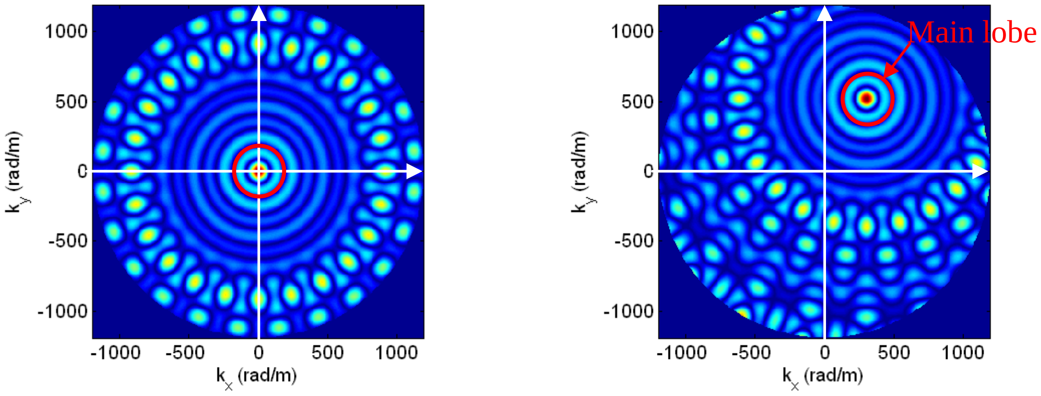

(c) Unsteered circular array (d) Steered circular array

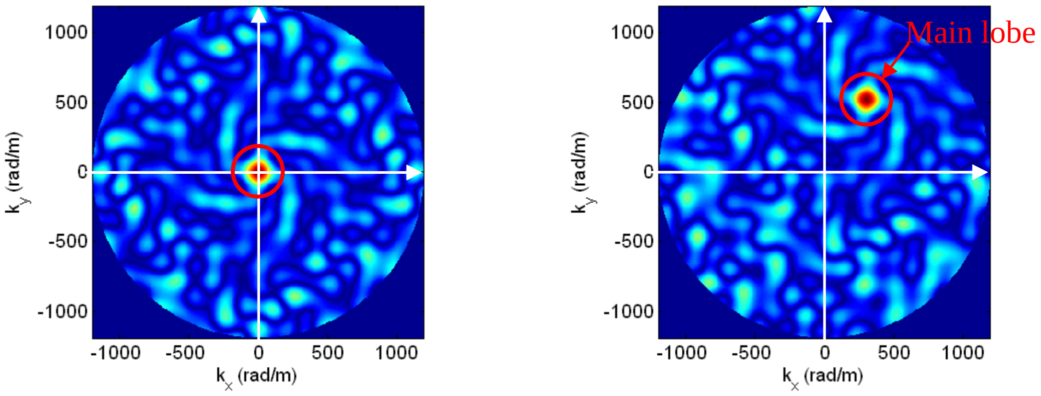

(e) Unsteered spiral array (f) Steered spiral array

Figure 3.19: Comparison of directional array steering with candidate 2-D arrays

If the interested wavenumber range is expanded from the current choice, $1.8(\pi/\Delta x)$ where the $\Delta x$ is the element spacing based on the cruciform array, the steered directivity function will include more side lobes that have large magnitude enough to disturb the directional wavenumber filtering method. The array steering results show that the proposed 2-D spiral phased sensor array is capable of a robust directional wavenumber filtering technique.

### 3.6.3 Evaluation of 2-D Spiral Phased Array

This section discusses the effect of the sensor element increase for the 2-D spiral phased array. The beamwidth of the main lobe, peak and average side lobe heights were averaged for all of the steering angles (from 0 deg. to 360 deg.), and the corresponding standard deviation was determined for 2-D spiral phased arrays with various total number of sensor elements. The results of the spiral array characteristics are shown in Figure 3.20, as a function of the total number of sensor elements. The results note that the beamwidth of the main lobe is consistently decreasing as increasing the sensor elements to form the spiral array. The peak and average side lobes show a trend of decreasing, but it is relatively inconsistent compared to the beamwidth decrease.

To examine the comprehensive effects of the sensor elements increase for the 2-D spiral array, the unsteered directivity function results for the same example (600 rad/m at 60 deg.) in the previous section are inspected for each total sensor number case.

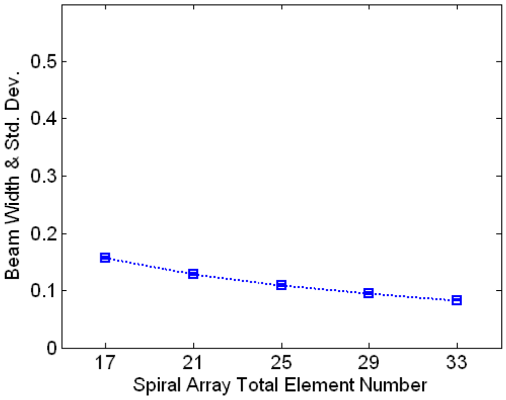

(a) Beamwidth of main lobe

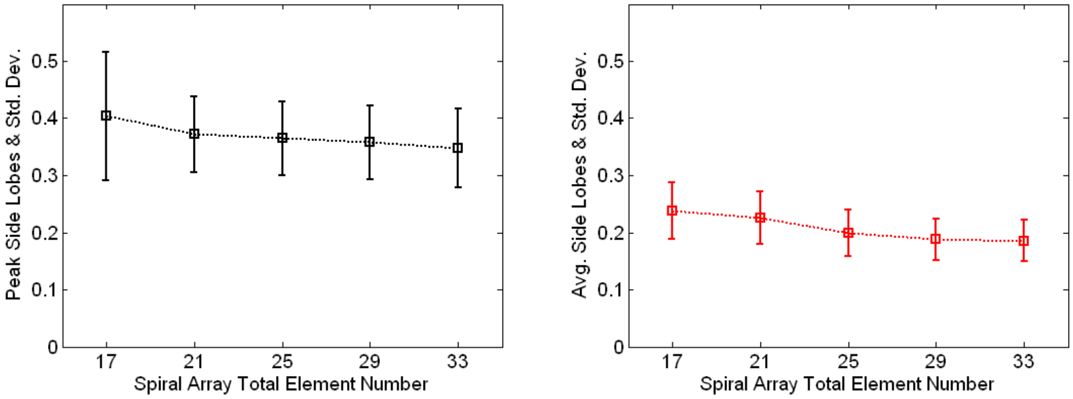

(b) Peak side lobe height

(c) Average side lobe height

Figure 3.20: Spiral array characteristics variation due to the increase of total number of sensor elements

The results in Figure 3.21 show how the directivity function varies with increasing total number of the sensor elements. The figures are the top view of the directivity function results. A threshold setting (e.g. $0.5 * \max\left[D\left(k_x, k_y\right)\right]$) was applied to simplify the steered directivity function images and effectively evaluate the beamwidth of the main lobe and the heights of the side lobes. The Figure 3.21(a) shows the directivity function of the spiral array with 17 sensor elements, and the

Figure 3.21(b) is the corresponding directivity function images filtered with the threshold setting. As the total number of the sensor elements increases, the diameter of the image (with the highest intensity) for the main lobe decreases and the images related to the side lobes are diminished. However, it is observed that a few side lobe images can be found in Figure 3.21(e) while any side lobe image is not visible Figure 3.21(d), and the beamwidth of the main lobe in Figure 3.21(e) is smaller than in Figure 3.21(d).

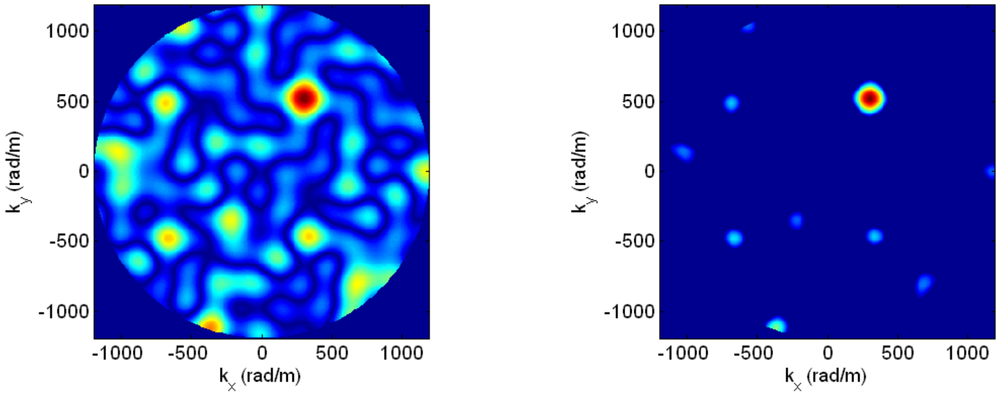

(a) N = 17

(b) N = 17 and 50% Threshold Setting

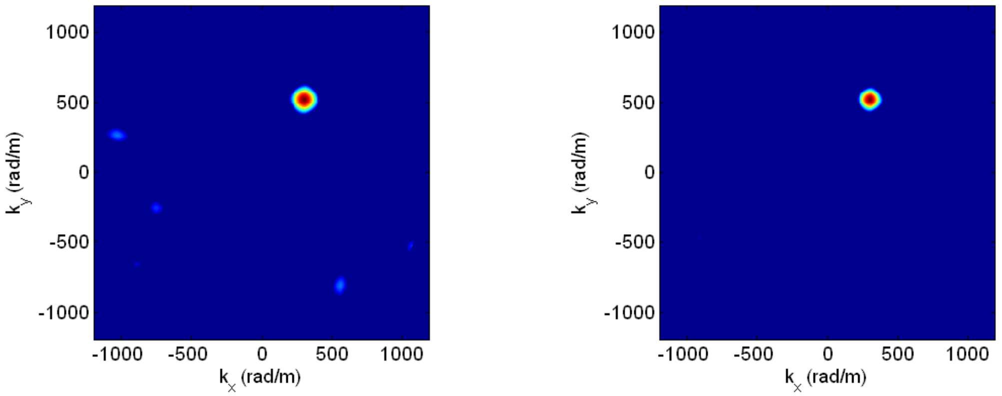

(c) N = 21 and 50% Threshold Setting

(d) N = 25 and 50% Threshold Setting

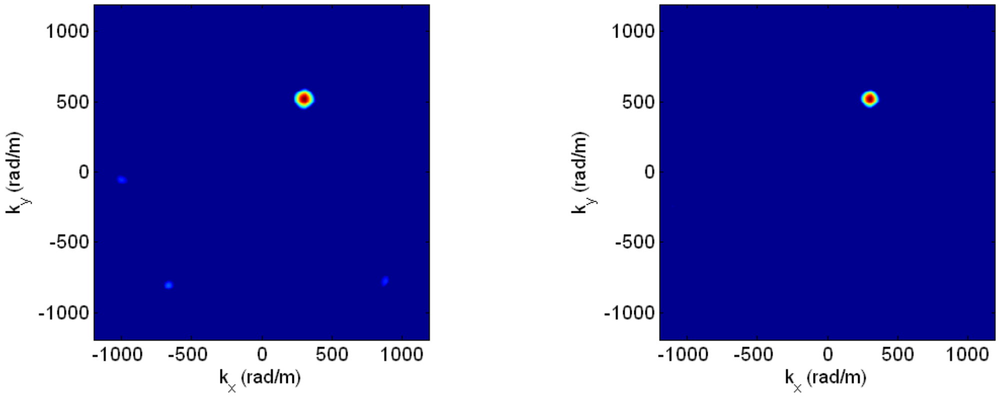

(e) N = 29 and 50% Threshold Setting (f) N = 33 and 50% Threshold Setting

Figure 3.21: Variation of the steered directivity functions of the 2-D spiral phased arrays as increasing the total number of sensor elements

In order to save the signal processing time and provide more robust array technique than the proposed 2-D spiral phased array, further study should be conducted to optimize the configuration of the 2-D phased sensor array, as considering the array size, sensor element spacing, and total number of sensor elements.

### 3.7 *Structural Health Monitoring with Array Response*

By using the array response, $\psi(t,\theta)$, obtained from the Equation (3.16), damage detection tests are conducted for thin aluminum and orthotropic composite panels. A differential array response (i.e. baseline array response – damage array response) is produced to identify damage locations after the phased array signal processing. The baseline array response is evaluated with GLW signal data measured from an undamaged structure, while the damage array response is from the same structure with a defect.

A threshold setting is applied in order to determine more reliable damage location as tracking damage size growth, because the differential array response may include unwanted images due to the side lobes effect of an array layout. The unwanted images are weaker than a damage reflection image in the differential array response. Using the threshold setting, therefore, one can eliminate the unwanted images. Default threshold is given by Equation (3.31),

$$\text{Threshold} = 0.8 * \max\left(|\psi_d(t,\theta)|\right) \tag{3.31}$$

where $\psi_d(t,\theta)$ is differential array response. For this study, the scaling factor is set as 0.8 to enhance the damage reflection image while eliminating the reflections coming boundaries and joint bolt area, and the unwanted images. In order to find damage area level described as Equation (3.32), threshold-filtered differential array response, $\psi_{d1}(t,\theta)$, is defined by Equation (3.33).

$$\text{DamageAreaLevel} = \iint \psi_{d1}(t,\theta)\, dtd\theta \tag{3.32}$$

$$\psi_{d1}(t,\theta) = \begin{cases} 1 \ \text{ if } |\psi_d(t,\theta)| > \text{Threshold} \\ 0 \ \text{ if } |\psi_d(t,\theta)| < \text{Threshold} \end{cases} \tag{3.33}$$

$\psi_{d1}(t,\theta)$ is a two-dimensional array response determined from $\psi_d(t,\theta)$ that has three-dimensional array response information. Another threshold-filtered differential array response, $\psi_{d2}(t,\theta)$, is defined by

$$\psi_{d2}(t,\theta) = \begin{cases} \psi_d(t,\theta) & \text{if } |\psi_d(t,\theta)| > \text{Threshold} \\ 0 & \text{if } |\psi_d(t,\theta)| < \text{Threshold} \end{cases} \tag{3.34}$$

Using the differential array responses filtered with the selective threshold setting, a new damage index (DI) is developed as described in Equation (3.35).

$$\text{DamageIndex} = \iint \psi_{d1}(t,\theta)\, dtd\theta * \max(|\psi_{d2}(t,\theta)|) \tag{3.35}$$

A conceptual step-by-step approach toward damage detection using the 2-D phased sensor array is provided as shown in Figure 3.22. This includes data acquisition, phased array analysis, looking for difference between baseline and damaged case, empirical mode decomposition (EMD) for denoising, locating damage, and quantifying damage.

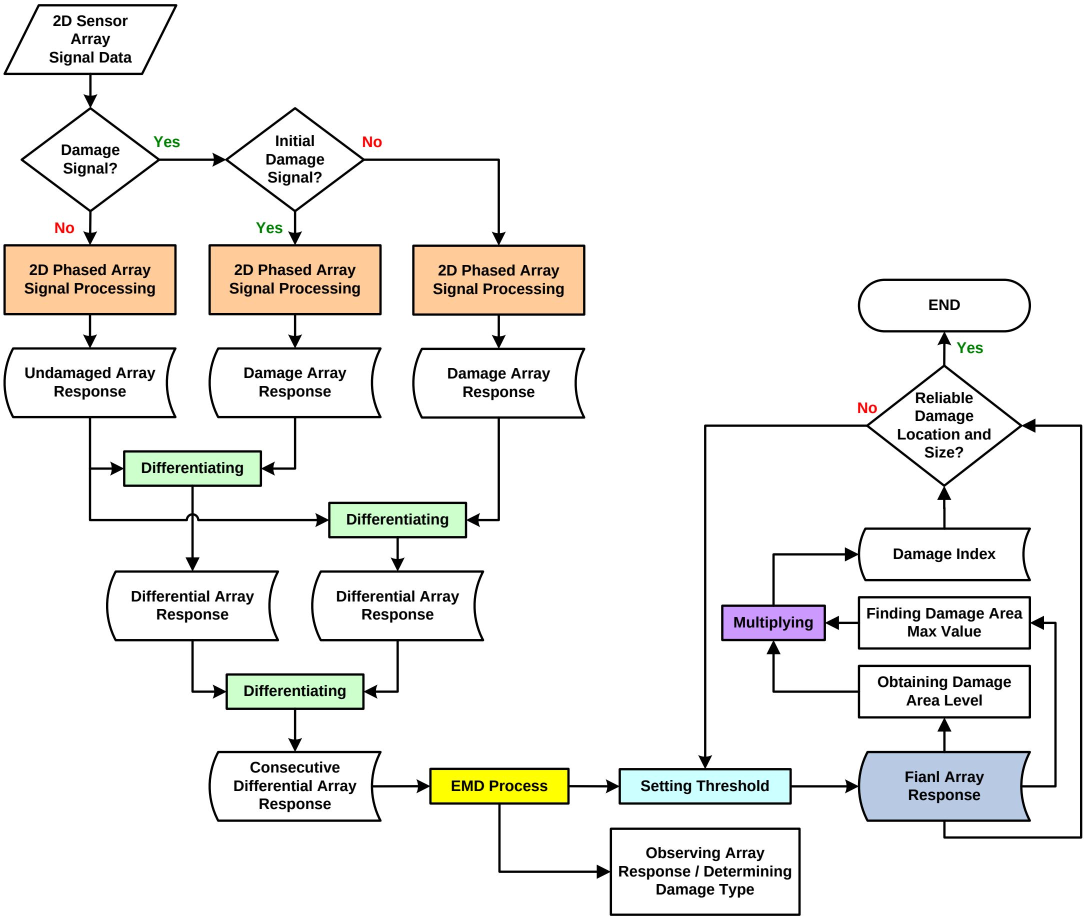

Figure 3.22: Flow chart of proposed damage detection algorithm

### *3.8 MVDR-based Phased Array Technique*

A minimum variance distortionless response (MVDR) method can be used to improve an array response result produced by a phased array signal processing technique with a 2-D spiral phased array. The MVDR method is referred to as minimum variance (MV) method, the Capon's maximum likelihood method (MLM) or simply Capon's method [129]. Originally, the MVDR approach was used for frequency-wavenumber estimation of seismic waves [132]. The MVDR method was modified for the existing 2-D spiral phased array approach. The governing equation of the MVDR-based phased array signal processing method is defined as Equation (3.36), and it can be compared to the original governing equation (Equation (3.37)) for the phased array signal processing.

$$\psi_{MVDR}(t,\theta) = \boldsymbol{w}_{MVDR}^{H}(\theta)\boldsymbol{\psi}(t,\theta) \tag{3.36}$$

$$\psi_{\text{original}}(t,\theta) = \boldsymbol{a}^{H}(\theta)\boldsymbol{\psi}(t,\theta) \tag{3.37}$$

$$\boldsymbol{\psi}(t,\theta) = \frac{1}{N}\boldsymbol{\phi}^{H}(\theta)\boldsymbol{v}(t) \tag{3.38}$$

In above equations, $\boldsymbol{\psi}(t,\theta)$ is an array response vector. The array response vector can be determined by using Equation (3.38). In the equation, the $\boldsymbol{\phi}(\theta)$ is a spatial weighting vector and $\boldsymbol{v}(t)$ is a sensor signal vector received from a sensor array. The spatial weighting vector is based on an ideal wavenumber filter (i.e. Dirac delta function). The $N$ in the Equation (3.38) is the total number of sensor elements to construct the 2-D spiral phased array. The $\boldsymbol{w}_{MVDR}(\theta)$ and $\boldsymbol{a}(\theta)$ are weight vectors for the MVDR-based and the original methods, defined by in Equations (3.39) and (3.40), respectively. The $^{H}$ denotes the conjugate transpose.

$$\boldsymbol{w}_{MVDR}(\theta) = \frac{\widehat{\boldsymbol{R}}^{-1}(\theta)\boldsymbol{a}(\theta)}{\boldsymbol{a}^{H}(\theta)\widehat{\boldsymbol{R}}^{-1}(\theta)\boldsymbol{a}(\theta)} \tag{3.39}$$

$$\boldsymbol{a}(\theta) = \mathbf{1} \tag{3.40}$$

The $\widehat{\boldsymbol{R}}^{-1}(\theta)$ in the MVDR weight vector is second-order statistics of a stationary signal. The second-order statistics are in the form of signal covariance matrix defined by in Equation (3.41). In the equation, the E denotes estimation/expected value and the $\boldsymbol{\psi}(t,\theta)$ is the array response vector. The $N_s$ is the number of samples used for the estimation.

$$\widehat{\boldsymbol{R}}(\theta) = \mathrm{E}[\boldsymbol{\psi}(t,\theta)\boldsymbol{\psi}^{H}(t,\theta)] \approx \frac{1}{N_s}\sum_{t=1}^{N_s} \boldsymbol{\psi}(t,\theta)\,\boldsymbol{\psi}^{H}(t,\theta) \tag{3.41}$$

As an adaptive signal processing tool, the proposed MVDR-based phased array method may be used to analyze experimental data obtained from GLW interrogation tests with various structures.

## 3.9 *Chapter Summary*

This chapter discussed fundamental backgrounds of array signal processing based on 2-D phased sensor arrays. The array signal processing method based on 1-D linear array was reviewed and the limitation of the 1-D array was discussed. Directivity functions were derived for three candidate 2-D phased sensor arrays with cruciform, circular and spiral configurations. The directivity function for each array case was examined based on beamwidth of the main lobe, peak and average side lobe heights. Array steering for the directional wavenumber filtering method was discussed. Among the three candidates of the 2-D arrays, the 2-D spiral phased array was selected for the experimental tests because the spiral array has better properties for the array signal processing. Based on array responses obtained from the phased array signal processing, structural health monitoring (SHM) approach was introduced. In addition, an adaptive array signal processing technique with a minimum variance distortionless response (MVDR) method was introduced as a robust tool for SHM applications.

# 4. Damage Detection in Thin Isotropic Panels

Laboratory evaluations were conducted in order to experimentally validate the data analysis and piezoelectric material based 2-D phased array concept. The 2-D phased arrays were constructed by using piezopaint (piezo-polymer composite) patches and piezoceramic (PZT-5A) elements. Thin 2024-T3 aluminum panels were prepared as test articles. Various damages such as holes, cracks, weights (mass), and rubber patches were simulated as artificial damages at different locations in the aluminum panel. Guided Lamb wave (GLW) method was applied to monitor structural integrity of the testing panels. Two sensor array systems based on the pulse-echo method and the pitch-catch method of the GLW interrogation were introduced and used to detect the simulated damages.

## *4.1 Single-Actuator-based 2-D Phased Sensor Array System*

### 4.1.1 Introduction

Two aluminum panels were prepared for laboratory evaluations. One panel was instrumented with a piezopaint patch consisting of spiral phased array layout, and the other panel included another piezopaint patch with cruciform and circular array layouts. The panels were mounted to an aluminum frame and secured using numerous bolts. A piezoceramic element was bonded on the under-side of the panel to provide an interrogating signal for damage detection. During this portion of the testing, conventional data acquisition hardware was used based on a National Instruments LabView system.

The panel with the piezopaint spiral array was also instrumented with another piezoceramic element located a distance from the center of the array. This piezoceramic element was used as a source in order to validate the phased array signal processing methodology. High frequency tone burst signals were generated in the panel using the off-centered source piezoceramic element. Sensor signal data was acquired from the array and passed through the array processing algorithm which was correctly able to determine the direction of arrival from the off-centered piezoceramic element.

Damage detection cases were run on both the panels where holes were simulated at various locations on the panels. The difference between the baseline and damaged cases was used in order to enhance the reflections from the hole damages. The location and distance of the hole relative to the array was determined based on the phased array signal processing algorithms. A crack damage detection case was evaluated with the panel using the piezopaint spiral array. The Empirical Mode Decomposition proved useful in order to remove spurious noise from the signals. The noise removal process was accomplished using the first two intrinsic mode functions of the sensor signals.

### 4.1.2 Evaluation of Piezopaint Sensor Elements

A piezoelectric composite material called ‘piezopaint’ is composed of fine piezoelectric ceramic powder (filler), resin base (binder) and additives to improve and stabilize paint mixing. The Piezopaint is known as ‘0–3’ piezoelectric composite and the ‘0–3’ means that the piezoelectrically active ceramic particles are randomly dispersed in a three-dimensionally connected polymer matrix. The detailed steps to fabricate the piezopaint will be discussed in the later section.

Before manufacturing 2-D phased sensor arrays based on the piezopaint, piezopaint elements were compared to conventional piezoceramic elements for sensing functionality evaluation. A metallic panel was instrumented with a number of piezopaint and piezocramic elements, and the pitch-catch GLW testing was conducted. It was determined that the piezopaint elements performed suitably as sensor elements and they were applicable to be used as a piezopaint 2-D phased sensor array configuration.

### Piezopaint Sensor Elements

An experimental setup was used to evaluate the sensitivity of the piezopaint elements and compare with piezoceramic elements. A 2024-T3 aluminum panel with a thickness of 0.04 inch was prepared to investigate a sensitivity analysis comparison. Three piezopaint elements with 1/4 inch diameter were manufactured and three piezoceramic elements (one for an actuator and two for sensing receivers) were prepared. The properties of the piezoelectric elements are described in Table 4, and the elements are shown in Figure 4.1.

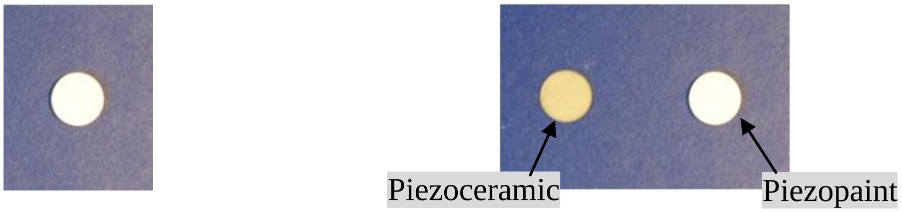

(a) Piezopaint element (b) Comparison with piezoceramic element

Figure 4.1: Piezoelectric elements used for sensitivity evaluations

Table 4: Properties of elements used for evaluations

| **Parameter** | **Material** | **Diameter (inch)** | **Thickness (inch)** | **Capacitance (nF)** |
|---|---|---|---|---|
| Piezopaint | Piezo-polymer composite | 0.25 | 0.0229 | $29.2*10^{-3}$ |
| Piezoceramic | PZT-5A | 0.25 | 0.0075 | 2.7 |

Table 5: Material properties of PZT-5A and Piezopaint

| **Material** | PZT-5A[*] | Piezopaint[**]<br>(40% PZT by volume) |
|---|---|---|
| **$d_{33}$ [pC/N]** | 390 | 6.1 |
| **$-d_{31}$ [pC/N]** | 190 | 2.1 |
| **$k_{33}$** | 0.72 | 0.02 |
| **$k_{31}$** | 0.32 | 0.02 |
| **$-g_{31}$ [$10^{-3}$ Vm/N]** | 11.6 | 18.4 |
| **Curie Temp. [°C]** | 350 | < 200[***] |

[*] Material properties are provided by Piezo Systems Inc., MA.

[**] Material properties are provided by Dr. Yunfeng Zhang, University of Maryland, College Park, MD.

[***] Degradation temperature of resin

A cynoacrylate adhesive (e.g. M-bond), shown in Figure 4.2, was used to bond the piezoceramic and piezopaint elements on the aluminum panel. All piezocramic and piezopaint sensor elements were positioned a distance of 6 inch from the piezoceramic actuator that is positioned in the center of the aluminum plate as shown in Figure 4.3.

Figure 4.2: M-bond 200 adhesive kit

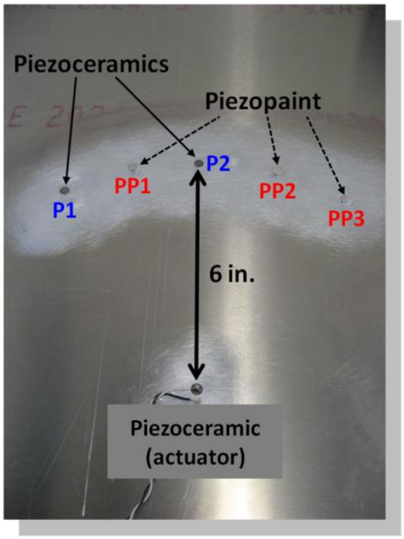

Figure 4.3: Experimental setup for evaluation of piezopaint elements

(a) LabVIEW VI (b) NI USB DAQ systems

Figure 4.4: Data acquisition systems for laboratory evaluations

(a) Linear power amplifier (for actuation)

40 dB signal amplifiers (for sensing)

(b) For piezoceramic (c) For piezopaint

Figure 4.5: Pictures of amplifiers

The data acquisition system was used based on a National Instruments (NI) LabView system (Figure 4.4). For actuation, a linear power amplifier (Figure 4.5(a)) was used to condition the excitation signal provided by the LabVIEW VI. For sensing, 40 dB signal conditioning amplifiers (Figure 4.5(b) and (c)) were designed and used for piezoceramic and piezopaint sensor elements. The excitation signals ranged from ±10 V amplitude. The conventional pitch-catch method was used to acquire the GLW responses in the testing panel. The schematic diagram of the GLW-based experimental set-ups with the projected data acquisition system can be found in Figure 4.6.

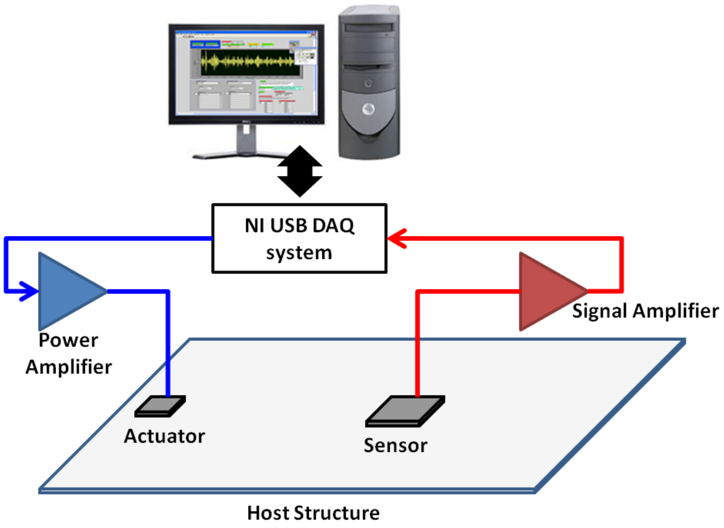

Figure 4.6: Schematic diagram of experimental test set-up

<u>GLW Data Acquisition</u>

The GLW signal data was obtained from two piezoceremic sensors (denoted by P1 and P2) and three piezopaint sensors (PP1, PP2, and PP3). To find the accurate Time-of-Flight (ToF) information from the received GLW signals, the dispersion curves for the panel were examined, and phase and group velocities of the GLW modes can be determined. With the information of the group velocities of S0 and A0 modes, the arrival time of the two fundamental GLW modes can be determined and the A0 mode can be isolated for sensitivity evaluation.

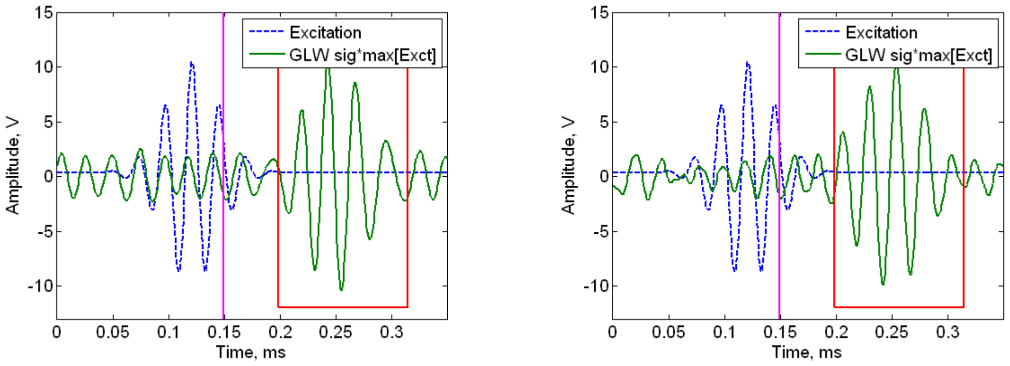

(a) P1 sensor

(b) PP1 sensor

Figure 4.7: GLW signals obtained sensing elements (40 kHz)

The transient GLW signals obtained from P1 and PP1 sensor elements are shown in Figure 4.7, Figure 4.8, and Figure 4.9 for excitation frequencies of 40, 100, and 160 kHz. For the piezoceramic sensor element (P1), the signal conditioner was not used because the amplitude of the received signals was enough to be captured by the data acquisition systems. On the other hand, for the piezopaint sensor element (PP1), the 40 dB amplifier was used for signal conditioning. The red box is a window region for A0 mode isolation and the pink vertical line is the arrival time of the maximum peak of S0 mode estimated from the dispersion curves. As a reference signal, the excitation signal is plotted with blue dotted line in the background and the sensor signals are plotted with a green solid line and are normalized by the maximum value of the excitation signal. This was done because the sensor signals are too small to be compared to the excitation signals.

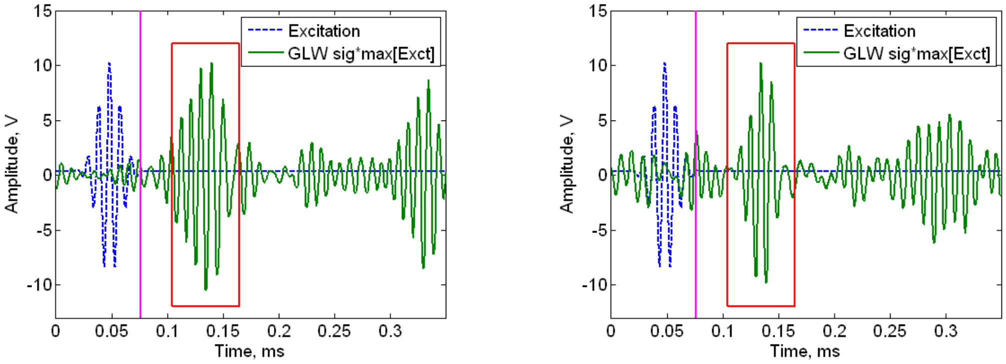

(a) P1 sensor (b) PP1 sensor

Figure 4.8: GLW signals obtained sensing elements (100 kHz)

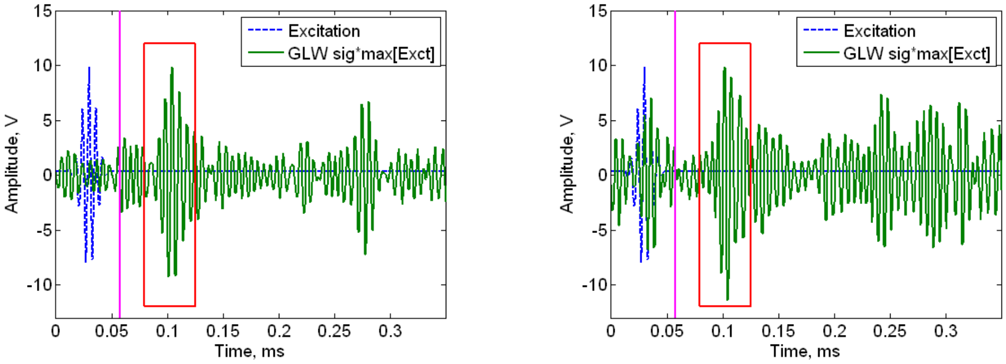

(a) P1 sensor (b) PP1 sensor

Figure 4.9: GLW signals obtained sensing elements (160 kHz)

Although the amplitude of the signals obtained from the piezopaint elements is much smaller than the piezoceramic element case, the GLW responses of the piezoapint sensor element are similar to the piezoceramic sensor element. Vp-p (peak-to-peak voltage) information of the A0 modes of the GLW signals obtained from the piezoceramic element were averaged for the P1 and P2 sensors, and expressed as a function of the excitation frequency. The normalized Vp-p of the A0 modes is shown in Figure 4.10(a) and (b) for piezoceramic element and peizopaint element, respectively. The Vp-p of the A0 mode dramatically decreases when the excitation frequency varies from 40 kHz to 80 kHz and then shows relatively small variations as the excitation frequency increases. In order to evaluate the sensitivity of the sensor elements, the ratio of the average Vp-p of piezopaint sensor element to the average Vp-p of the piezoceramic sensor element is shown in Figure 4.11. The result shows that the sensitivity of the piezopaint element is similar to the sensitivity of the piezoceramic elements in order to capture the GLW behavior in the aluminum panel. Therefore one can use the piezopaint element as a sensor instead of piezoceramic element.

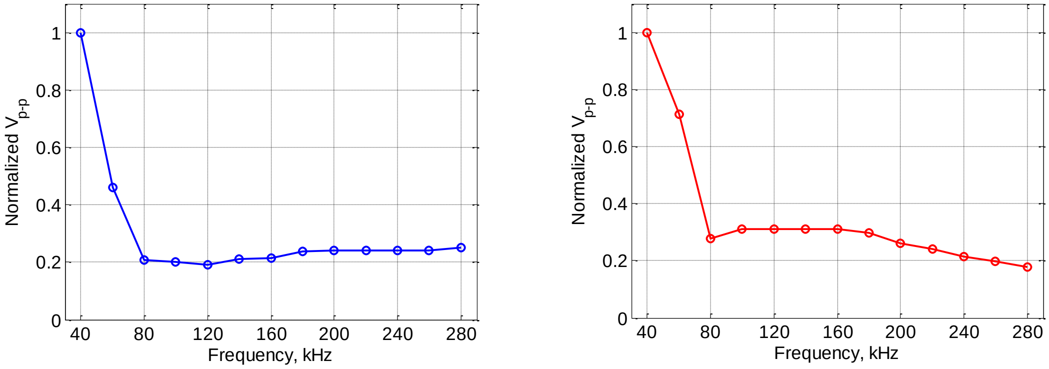

(a) Piezoceramic

(b) Piezopaint

Figure 4.10: Average Vp-p of A0 mode as a function of excitation frequency

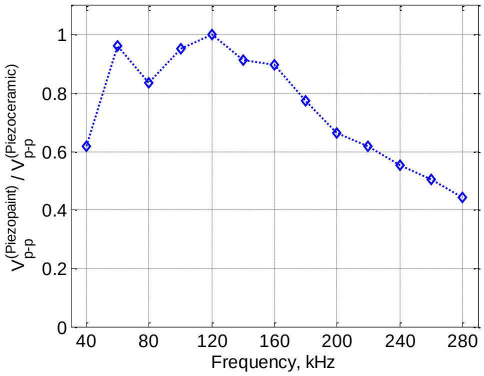

Figure 4.11: Comparison of piezopaint sensor response to piezoceramic

Evaluation of Piezopaint Sensor Elements of Different Size

Another experimental testing was performed on piezopaint elements of 1/8 in. and 3/16 in. diameter. Each of the piezopaint elements was connected to the signal conditioner with 40 dB amplification. The results are shown in Figure 4.12 where the responses of the 3/16 in. and 1/8 in. diameter elements are normalized with the 1/4 in. diameter piezopaint element. The 40 dB amplifier for the piezopaint signal conditioning was a voltage amplifier. The voltage generated on the piezopaint is solely a function of the strain in the material and the piezopaint thickness. Thus the voltage generated between the top and bottom electrodes are independent of the size of the piezopaint element. If an alternate signal conditioning circuit based on charge amplification is used, it is reasonable to expect that the output signals may be a function of the size of the piezopaint element.

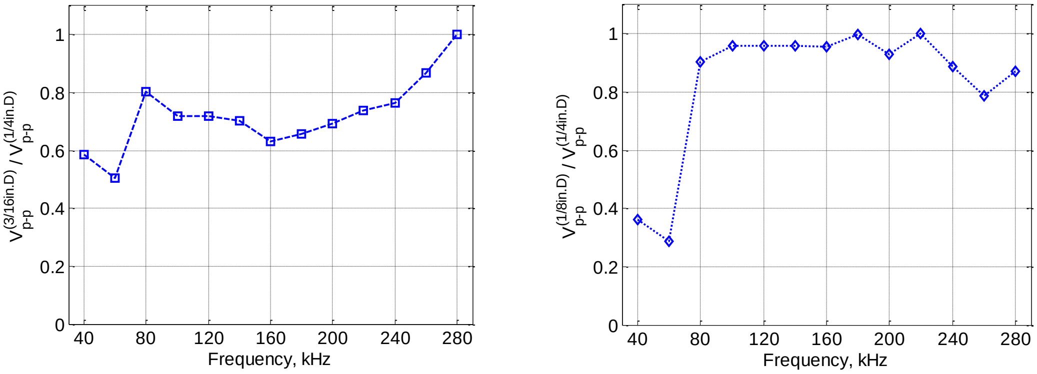

(a) Piezopaint of 3/16 in. diameter

(b) Piezopaint of 1/8 in. diameter

Figure 4.12: Comparison of different size piezopaint elements (normalized to 1/4 in. diameter element)

### 4.1.3 Fabrication of Piezopaint Based 2-D Phased Sensor Arrays

Piezoelectric paint patches were fabricated to construct 2-D phased sensor arrays used for array signal processing evaluation and damage detection applications. Piezoelectric ceramic powder such as lead-zirconate-titanate (PZT-5A) was selected as filler because of its stability with time and temperature, and high sensitivity. For binding polymer, epoxy resin was used because it can be easily mixed with high concentration of PZT powder. It has low viscosity and a simple curing process with time and temperature. Additives were used to ease the mixing and deposition process and to improve paint quality. PZT powder was added into epoxy resin phase (epoxy resin with hardener), and blends were mixed at a controlled speed by a laboratory dissolver. After the mixing process had been completed, a bar film applicator was used to spread the wet piezopaint on a clean surface panel and maintain its thickness corresponding to the gap clearance of the applicator. The wet piezopaint patches may be cured at ambient temperature for 2~3 days or at an elevated temperature in an oven for several hours. The curing process with heat was selected for the piezopaint patch samples before subsequent electroding and poling steps. The cured piezopaint patches were detached from the base panel for next steps of fabrication. The thickness of the patch samples was approximately 0.011 inch. A picture of a couple of the fabricated piezopaint patches is shown in Figure 4.13.

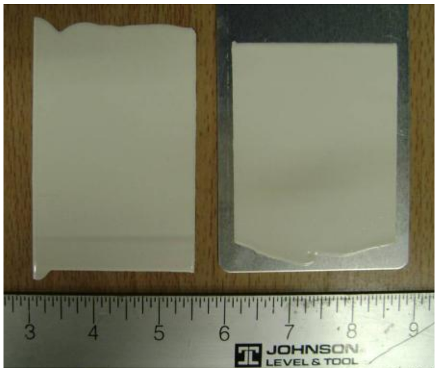

Figure 4.13: Piezopaint patches for 2-D phased sensor array

Conductive silver paint was applied over the piezopaint patches to form electrodes for poling (Figure 4.14). The conductive silver paint on the patches was cured in the laboratory at room temperature. After the curing process for electroding had been completed, poling of the piezopaint patches was performed to activate its piezoelectric effect. The patches were poled by using a conventional electrode poling device (Figure 4.15(a)) at an elevated temperature of 60℃. 2~3 kV using a high voltage amplifier (Figure 4.15(b)) was applied to the piezopaint patch while maintaining that almost no current will flow in order to prevent the patches to be short circuited. After curing and poling of the piezopaint patch, electric charges will be generated in the piezopaint patch in the response to structural vibrations because of its electromechanical coupling property.

(a) Top side (b) Bottom side

Figure 4.14: Electroding of piezopaint patches

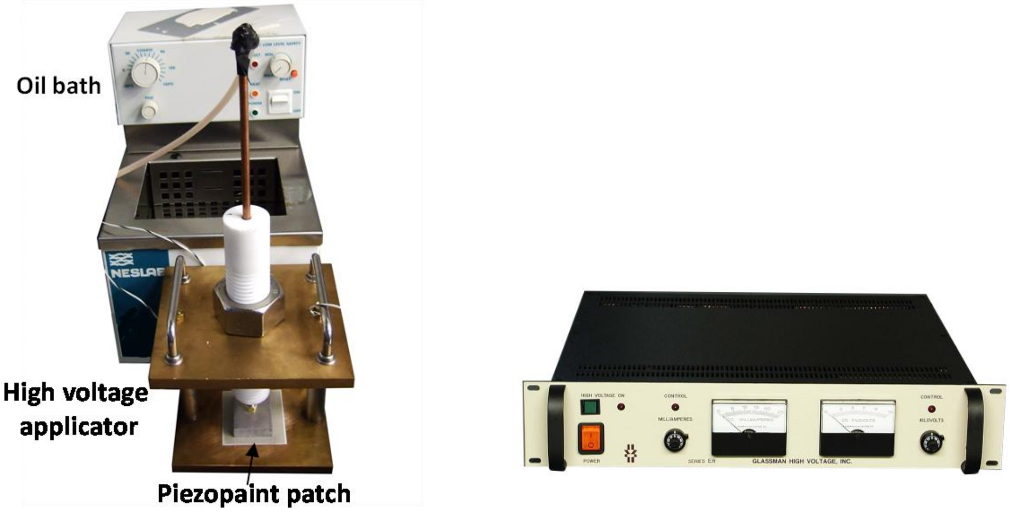

(a) Poling apparatus (b) High voltage amplifier

Figure 4.15: Equipment used to polarize piezopaint material

After the poling process had been completed, the top side electrode was removed with acetone and then conductive silver paint was applied again by using a Frisket stencil including discrete 2-D phased sensor arrays (Figure 4.16).

(a) Removal of electrode after poling (b) Stencil used to create discrete array

Figure 4.16: Construction of discrete 2-D phased sensor array (cruciform array)

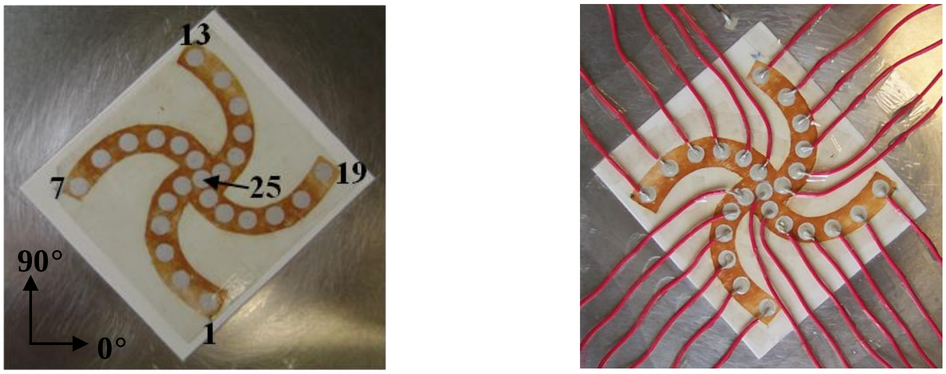

(a) Instrumented on the testing panel (b) Electrical wiring for the spiral array

Figure 4.17: Piezopaint based 2-D spiral sensor array

The complete form of the 2-D phased sensor array sample (with spiral layout) is shown in Figure 4.17(a). Total 25 discrete sensor elements were formed in the piezopaint patch. The size of each element was of 3/17 in. diameter and the element spacing was 3/16 in. based on the cruciform array. Each sensing element of the piezopaint spiral array was connected to the signal conditioning units by using electric wires (Figure 4.17(a)) after mounting onto the testing panel.

Figure 4.18: Silver conductive epoxy

### 4.1.4 Experimental Setup

A 0.04 in. thick 2024-T3 aluminum panel was prepared as a test specimen. The piezopaint 2-D spiral sensor array was mounted at the center of the top surface of the panel by using a silver conductive epoxy (Figure 4.18). In order to ensure thin and uniform epoxy adhesive layer, a vacuum bagging method was applied. After 24 hrs curing process at room temperature had been completed, each of the sensor array elements was instrumented for electrical wiring. After setting up the sensor array, two 1/4 in. diameter piezoceramic actuator elements were bonded to the panel. One piezoceramic actuator was bonded with a cynoacrylate epoxy on the opposite side of the panel positioned at the center of the array. This piezoceramic actuator was used for damage detection tests. An additional piezoceramic actuator was bonded 12 in. distance from the sensor array in the approximate 127 deg. direction. This actuator element was used to validate the directional filtering algorithm. The instrumented panel was mounted on an aluminum frame using bolts which were torqued to nominally 5 N-m, shown in Figure 4.19. The testing system consisted of a data acquisition system with a multiplexer, the linear amplifier (for actuation), and the signal conditioning circuit (for sensing). The 40 dB voltage amplifier was instrumented in order to boost output signals from piezopaint sensor elements of the array. In order to decrease the effect of noise on experimental performance, a running-average method was used when collecting transient responses of the panel. The conventional pitch (piezoceramic) – catch (piezopaint spiral array) method was used to generate the guided Lamb waves (GLW) and acquire the corresponding responses of the panel.

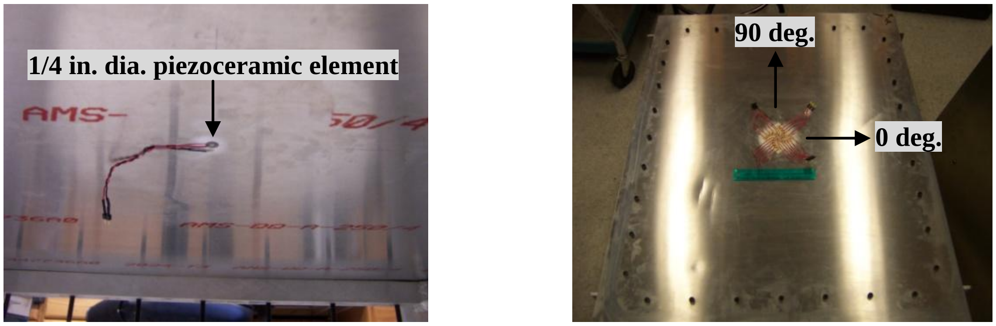

(a) Actuator on under-side of panel (b) Instrumented testing panel

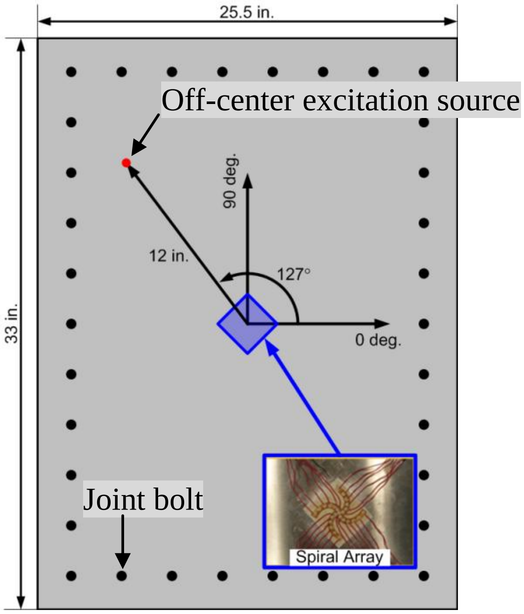

(c) Illustration of evaluation tests for phased array signal processing

Figure 4.19: Instrumented aluminum panel and 2-D spiral sensor array

### 4.1.5 Validation of algorithm of 2-D phased array

The first set of laboratory evaluations were conducted to validate the directional filtering algorithm that are possible with the 2-D phased sensor array. In this testing, the off-center 1/4 in. diameter piezoceramic element was used as excitation source in the test specimen. A close-up picture of the piezopaint spiral array and the piezoceramic excitation source are shown in Figure 4.20 where the excitation source is located approximately 127 deg. relative to the orientation axes of the 2-D spiral array.

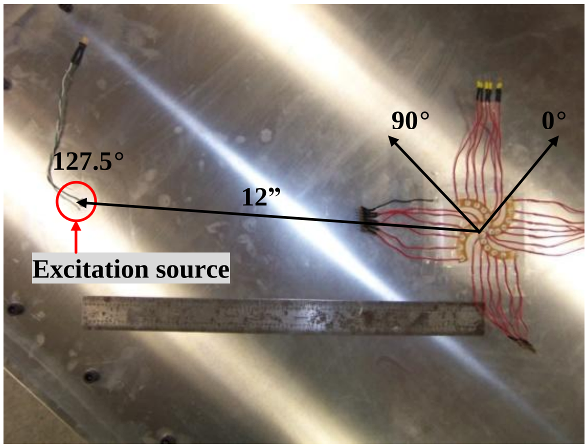

Figure 4.20: Off-centered piezoceramic element used as excitation source

The transient sensor measurements was gathered for cases where the actuator was excited with tone bursts that varied from 40 kHz to 140 kHz in 20 kHz increments and the amplitude of the excitation signal was 80 V. A sample tone burst excitation signal at 60 kHz and the corresponding sensor responses are shown in Figure 4.21(a) and (b), respectively. The initial portion of the sensor signal was due to Electro-Magnetic Interference (EMI) which was discarded for subsequent signal processing routines. The waveform after the EMI is the first anti-symmetric (A0) mode corresponding to the excitation and the A0 mode is highlighted in the Figure 4.21. At the testing frequencies, the dominant mode present was the A0 mode. Phase lag was observed as the A0 mode passed from one end of the piezopaint spiral array to other as indicated in the sensor signals (Figure 4.21(b)).

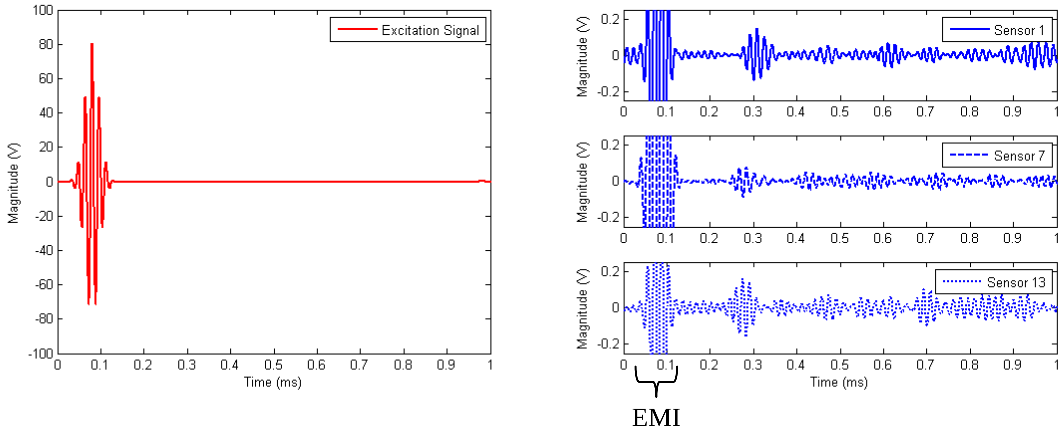

(a) Excitation signal (60 kHz) (b) GLW signals from the array (60 kHz)

Figure 4.21: Excitation signal and sample GLW signals obtained from spiral array

There are two ideas of the process in determining the wavenumber-frequency relationship: (1) reproducing the wavenumber-frequency plot using experimental results, and (2) using this information to do the directional filtering. The way to approach this section is the following:

a) Gather the raw sensor signals.

b) Perform a 2-D Fourier transform in space for a given instant in time corresponding to the arrival of the propagating wave highlighted in Figure 11b in pink.

c) The 2-D Fourier Transform in space should result in a peak at a particular set of $k_x$ and $k_y$.

d) The $(k_x^2 + k_y^2)^{(1/2)}$ should be close the predicted wavenumber of the A0 mode at the given frequency.

e) This repeated over the different frequencies would reproduce the wavenumber-frequency relationship shown in Figure 13.

f) The wavenumber-frequency relationship is used in the wavenumber filtering algorithm to produce the plot in Figure 14 which is based on filtering of a single wavenumber over a range of direction.

With the sensor signals from the piezopaint spiral array, wavenumbers were filtered based on the directional filtering algorithm described in the previous section. The wavenumber filtering result at the off-center excitation source direction is shown in Figure 4.22. The incident waveform for the excitation source includes the components of the main lobe and side lobes. The incident waveforms related to the side lobes are the unwanted information and might be filtered out by increasing the total number of sensor element. The wavenumber corresponding to the maximum value of the filtered wavenumber response was collected for each excitation frequency (40 ~ 140 kHz). The collection of the wavenumbers is an experimental wavenumber-frequency relationship for the aluminum panel and compared with theoretical estimation of wavenumber-frequency relationship as shown in Figure 4.23. The result shows good correlation between them although the experimental results are slightly larger than the theory. For the desired wavenumber of 60 kHz excitation case (from the experimental wavenumber-frequency relationship), the algorithm of the directional filtering with the spiral array was evaluated. The directionally filtered array response for 60 kHz excitation is shown in Figure 4.24. The result shows that the waveforms directly coming from the off-center excitation source can be apparently found and agree with the actual location of the excitation source. The time difference between the excitation source and the center of the array forms the Time of Flight (ToF) information that can be used to determine the actual distance from the center of the panel. The wave reflection (dotted circle) from free boundaries near the excitation source can be found in the same quadrant. In addition, the array response includes the unwanted images. The side lobes effect of the spiral array may influence the unwanted images, and they can be eliminated by using the threshold setting mentioned in a following section.

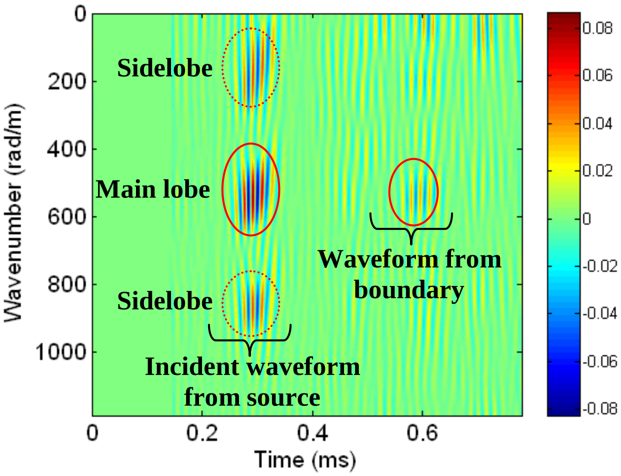

Figure 4.22: Wavenumber filtering array response for the off-centered excitation source case (60 kHz)

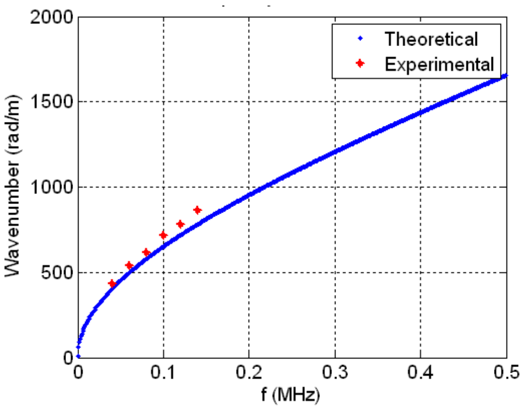

Figure 4.23: Comparison of wavenumber-frequency relationship

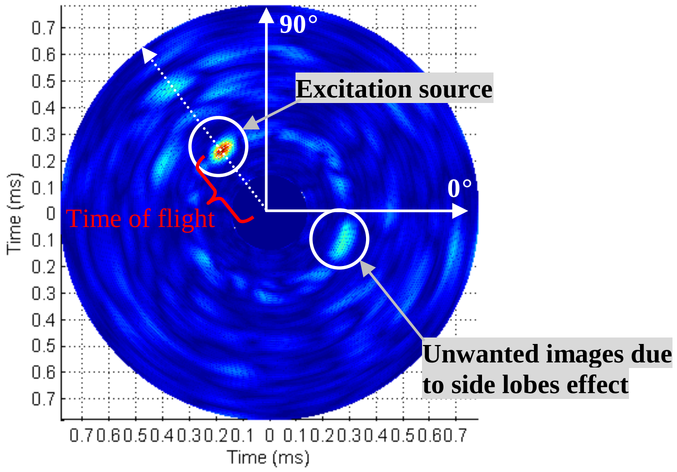

Figure 4.24: Directional filtering array response for the off-centered excitation source case (60 kHz)

### 4.1.6 Experimental Damage Detection Results

Prior to creating actual and permanent damages on the aluminum panel with the spiral sensor array, a mass detection testing was conducted. A mass (5 kg) was mounted at 10 in. distance from the center of the spiral array along with 225 deg. angular direction as shown in Figure 4.25. The piezoceramic element bonded at the center of the under-side of the panel was used as an actuator and excited with tone burst signals at various input frequencies (60, 80, and 100 kHz). The structural response of the panel to the actuation was obtained using the spiral array. The signal data was processed by the phased array signal processing algorithm and array responses were produced to evaluate the difference due to the artificial damage (the 5kg mass in this case) in the panel.

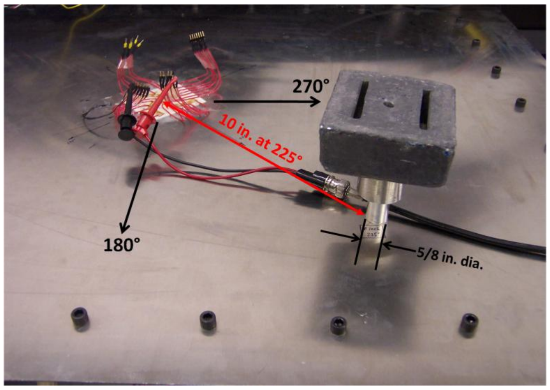

Figure 4.25: Testing set-up for mass mounted on panel

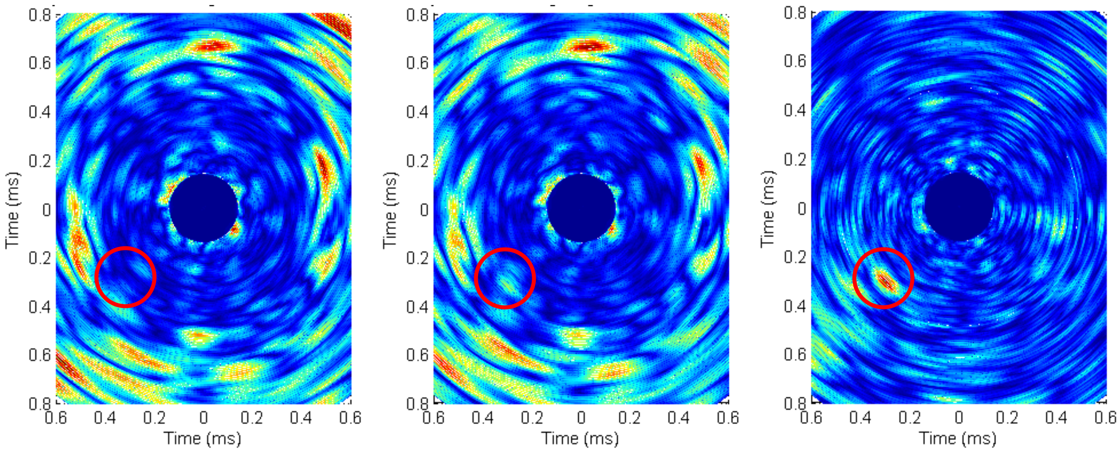

(a) Baseline (Undamaged) (b) Damage (c) Differential

Figure 4.26: Comparison of array responses for mass damage case (60 kHz)

Array responses for undamaged (baseline) and mass damage are illustrated in Figure 4.26(a) and (b), respectively. The estimated damage location was circled in red. In both array responses, there are a lot of reflections from edge boundaries and joint bolts area, so that the differential array response shown in Figure 4.26(c) was produced for obviously detecting mass location. Also, the differential array response includes useless reflections due to signal noise and side lobe effect of the phased array signal processing based on the spiral array configuration.

Three hole damages within the three quadrants of the panel were created for each damage detection testing and a linear crack damage starting at the side of the D3 hole damage location was also created in the same panel, shown Figure 4.27. The crack damage was simulated after the hole damage testing had completed. Various damage locations are detailed in Table 6. Measurement data was acquired after each damage case was applied.

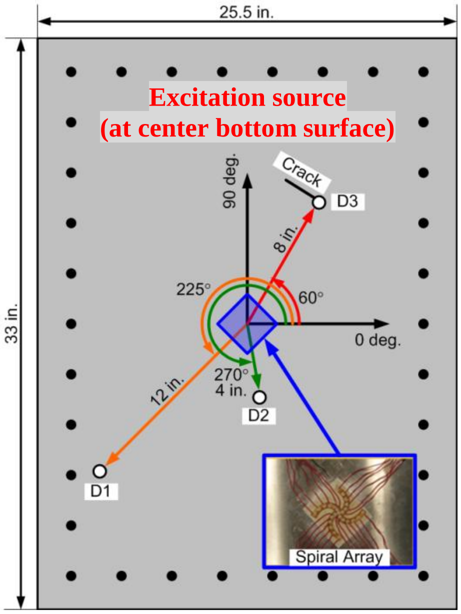

Figure 4.27: Instrumented aluminum panel and 2-D spiral sensor array (for damage detection)

For detecting simulated damages (holes and a linear crack), the 1/4 in. diameter piezoceramic element bonded at the center of the bottom surface of the panel was used as an actuator. The actuator was excited with transient signals at various interrogation frequencies (60, 80 and 100 kHz) and the corresponding response signal from each sensor element of the piezopaint spiral array was gathered and processed to obtain directionally filtered array response, termed just ‘array response’.

Table 6: Damage locations

| **Damage** | **Direction (degree)** | **Distance (inch)** | **Order of Testing** |
|---|---|---|---|
| D1 hole* | 225 | 12 | 1st |
| D2 hole | 280 | 4 | 2nd |
| D3 hole | 60 | 8 | 3rd |
| Crack** | 60 | 8 | 4th |

* The size of the hole is increased from 1/4 in. to 5/8 in. diameter with 1/8 in. diameter increments.

** The length of the crack in increased from 0.5 in. to 2 in. with 0.5 in. increments.

### 4.1.7 Hole Damage

In this subsection, the size of the simulated hole damage was 5/8 in. diameter. The array response results according to the damage sizing variation will be discussed in the later subsection named by ‘Damage Sizing’. The array response (Figure 4.28(a)) for the undamaged panel is compared with the array response (Figure 4.28(b)) for the damaged panel including the D1 hole. The red circles in Figure 4.28 indicate the simulated D1 damage location. The result of D1 damage case shows that the D1 damage location in the array response is not readily observable in the plot because the wave reflection from the damaged region is quite small compared to the wave reflections from free edge boundaries and the joint bolts regions. Hence, the differential array response (i.e. subtraction between the array responses obtained from the undamaged and damaged panel cases) were produced in order to bring out the wave reflection from the damage, while eliminating other reflections. In this same manner, the differential array responses for all hole damages were evaluated. The differential process provided better results for the D2 and D3 damage cases as shown in Figure 4.29. The results in Figure 4.29 noted that the reflection from D1 hole is weak and not readily apparent because the D1 hole damage is located the furthest from the array. A significant delay in data acquisition occurred the undamaged and D1 damage case was suspected as a reason. The reflection from the D2 hole damage is apparent. The reflection from D3 hole damage is weaker than the D2 case because the D3 hole damage is further than the D2 hole damage.

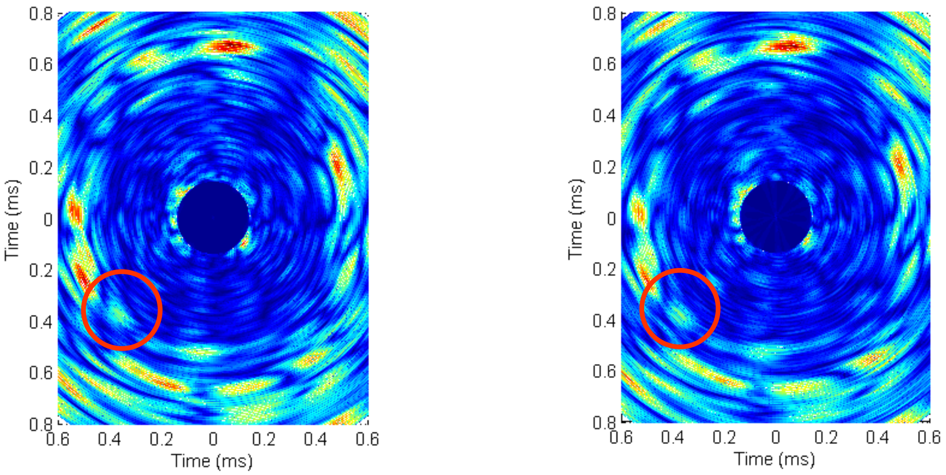

(a) Baseline (Undamaged)

(b) Damage

Figure 4.28: Comparison of array responses for hole damage case (60 kHz)

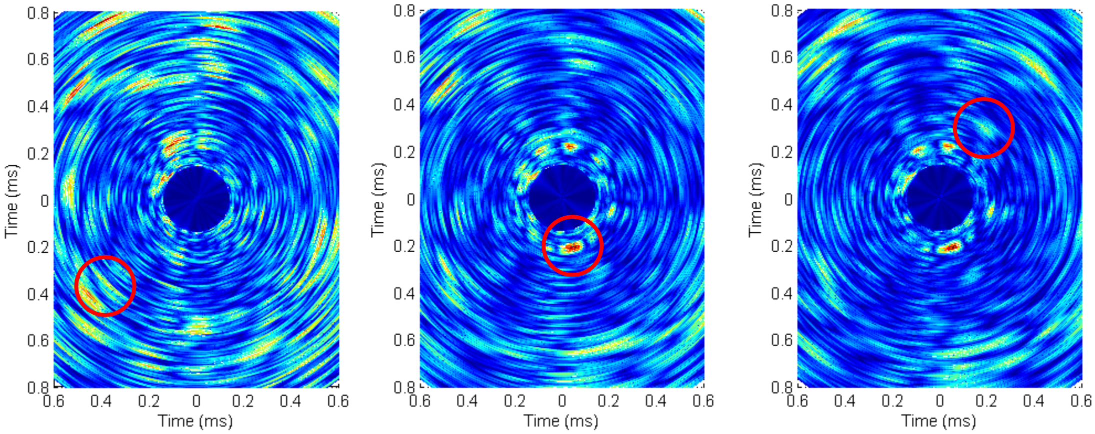

(a) D1 hole (b) D2 hole (c) D3 hole

Figure 4.29: Differential array responses for three hole damage cases (60 kHz)

In order to enhance the damage location in the differential array responses, consecutive differential array response was reproduced by removing differences between consecutive data acquisition events. For example, the consecutive differential array response for the D2 damage was found by subtracting the differential array response for D1 damage case (Figure 4.29(a)) from differential array response for D2 damage case (Figure 4.29(b)). The process results of the consecutive differential array responses are shown in Figure 4.30. While the results for D1 damage shown in Figure 4.30(a) remained the same as the Figure 4.29(a), the consecutive differential array responses for D2 and D3 damages bring out the wave reflections from the hole damage regions in the more significant manner as shown in Figure 4.30(b) and (c). In addition, Empirical Mode Decomposition (EMD) was applied in order to improve the array responses by removing low frequency components in the consecutive differential array responses. The first two intrinsic mode functions (IMFs) were used for the basis of the analysis. The EMD enhanced array responses are shown in Figure 4.31.

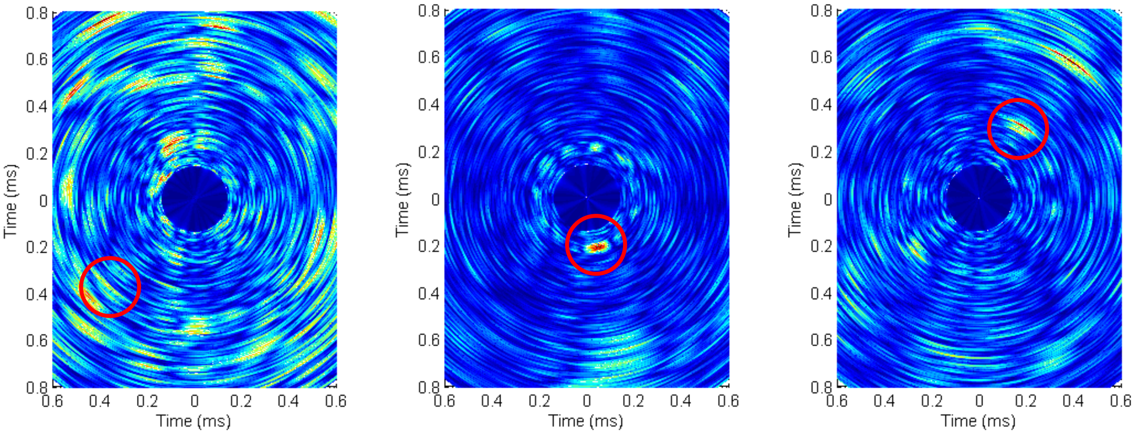

(a) D1 hole (b) D2 hole (c) D3 hole

Figure 4.30: Consecutive differential array responses for three hole damage cases (60 kHz)

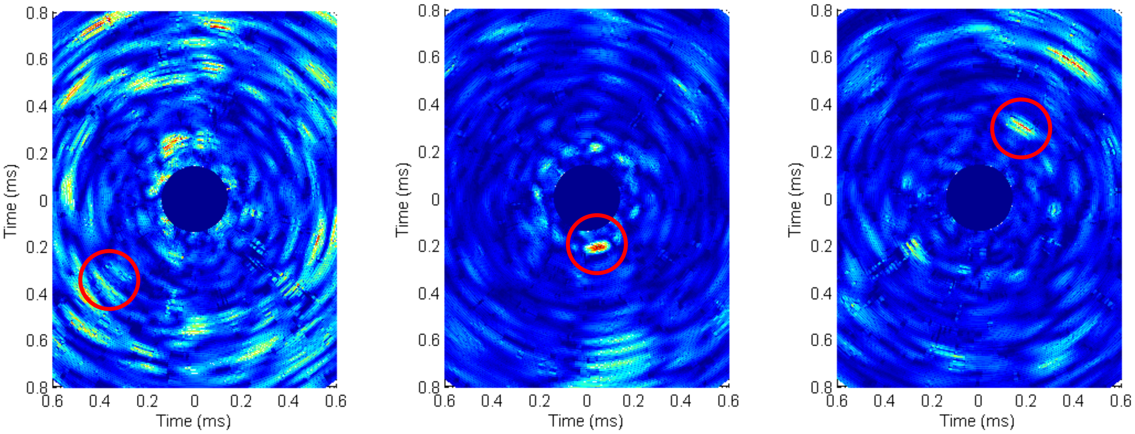

(a) D1 hole (b) D2 hole (c) D3 hole

Figure 4.31: EMD enhanced array responses for three hole damage cases (60 kHz)

### 4.1.8 Damage Detections Using Cruciform and Circular Phased Arrays

In order to evaluate array responses based on different 2-D array layouts and compare the array response results to the spiral array case, a new 2024-T3 aluminum panel (with 0.04 in. thickness) was prepared for additional hole damage detection tests. Two types of 2-D sensor arrays with cruciform and circular configuration were instrumented on the new panel. The two piezopaint sensor arrays and the instrumented panel are shown in Figure 4.32. The experimental set-ups were identical to the previous hole damage detection tests with the spiral array. Three hole damages (denoted by D1, D2, and D3) were simulated on the new panel as shown in Figure 4.32(b). The size of the hole damages were 5/8 in. diameter.

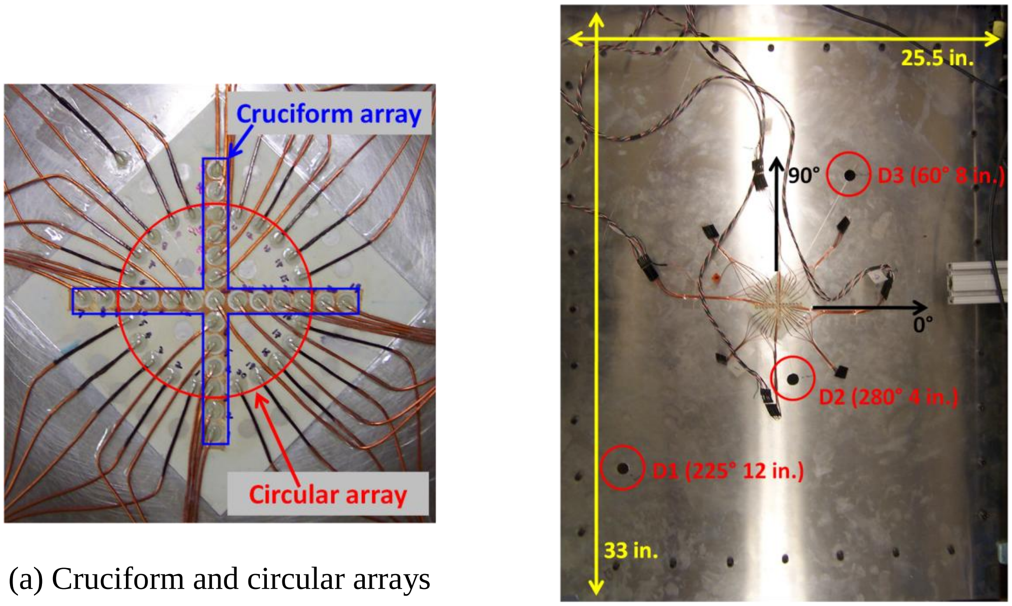

(a) Cruciform and circular arrays

(b) Instrumented aluminum panel

Figure 4.32: Experimental test set-up for hole damage detection tests using cruciform and circular arrays

For each damage case, the GLW signal data was gathered from the cruciform and circular arrays. By using the phased array signal processing method, the array responses for the cruciform and circular arrays were produced in the same manner as for the spiral array case. The consecutive differential signals were used as the EMD was performed to construct a signal based on the first two IMFs generated. The array response results for the damage cases (D1, D2, and D3 hole damage) using the cruciform array are shown in Figure 4.33. The array response results for the hole damage using the circular array are shown in Figure 4.34. The red circles in the Figure 4.33 and the Figure 4.34 are the simulated hole damage locations. The results show that only the D2 hole damage case for the cruciform and circular arrays can be apparently identified in the array responses. The array response in the Figure 4.33(b) includes a significant shadow image whose location is symmetric about the horizontal axis. The shadow image is because of the negative effect of side lobes of the directivity function with the cruciform array configuration. Compared to the array responses using the spiral array, there are lots of unwanted waveform images in the array responses using the cruciform and circular arrays, and the targeting damage images are not obvious in the array response results. These experimental results demonstrate the effectiveness of the proposed 2-D spiral phased array for the directional filtering technique to analyze the GLW signal data.

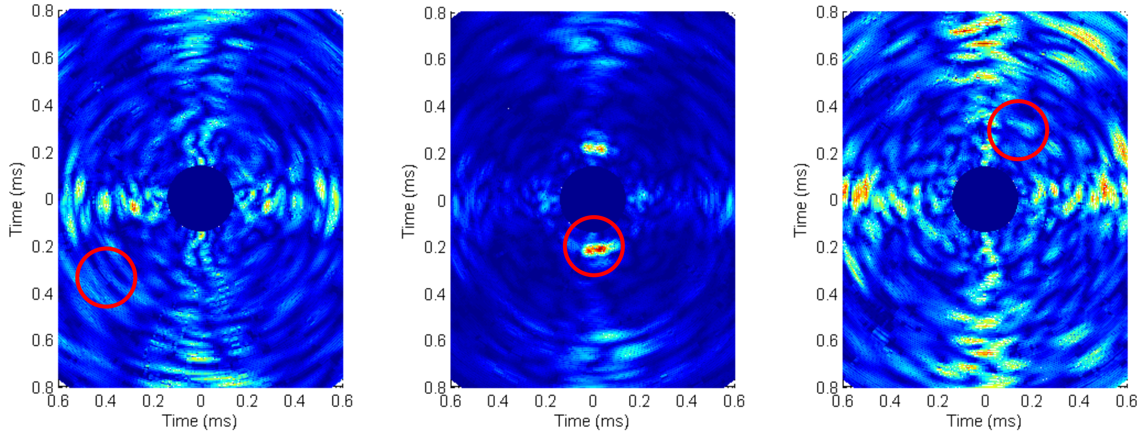

(a) D1 hole (b) D2 hole (c) D3 hole

Figure 4.33: EMD enhanced array responses for three hole damage cases when using cruciform array (60 kHz)

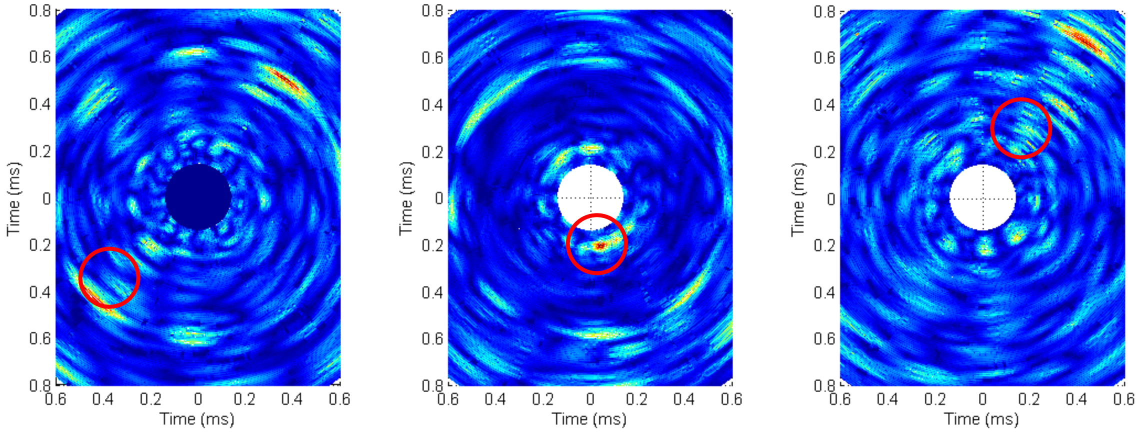

(a) D1 hole damage (b) D2 hole damage (c) D3 hole damage

Figure 4.34: EMD enhanced array responses for three hole damage cases when using circular array (60 kHz)

### 4.1.9 Crack Damage

The panel including the spiral array had three 5/8 in. diameter hole damages due to the former hole damage tests. A linear crack was created from the side of the D3 hole damage location as shown in Figure 4.27. The crack increased from 0.5 in. to 2 in. with 0.5 in. increments. Akin to the former applications, the 1/4 in. diameter piezoceramic bonded on the bottom surface of the panel was used as an actuator. The actuator was excited with a transient signals at various frequencies. The sensor signals from the spiral array were collected and processed to produce array responses.

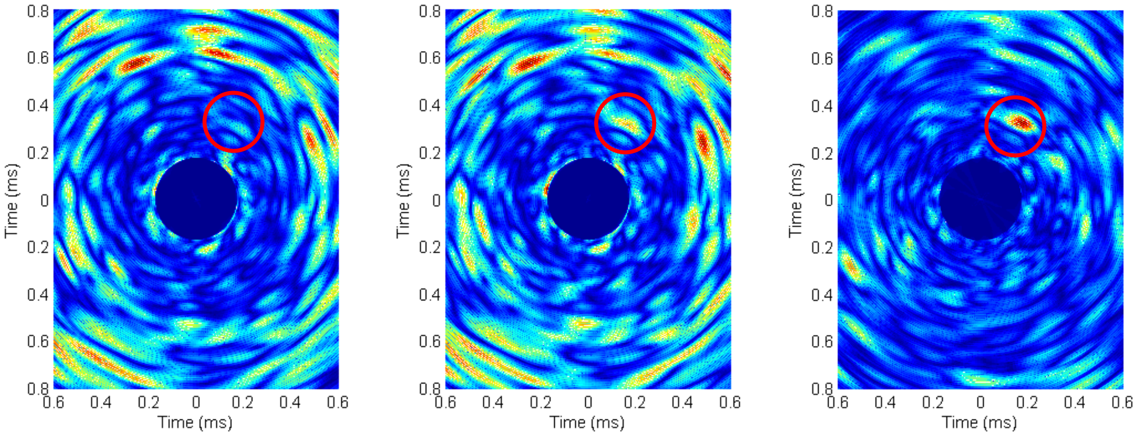

(a) Baseline (b) 0.5 in. crack damage (c) Differential

Figure 4.35: Comparison of array response for simulated crack damage case (60 kHz)

The array responses for baseline (i.e. before crack damage, but still includes three hole damages) and initial crack damage (0.5 in. crack) are shown in Figure 4.35(a) and (b), respectively. The differential array response between them was reproduced as shown in Figure 4.35(c). From the differential array response, the location of the crack damage on the panel can be apparently found because the maximum wave reflections are shown at 60 deg. direction (red circle in Figure 4.35(c)). A damage sizing study including hole and crack damages is shown in the following section.

### 4.1.10 Damage Sizing

The hole size increases from 1/4 in. dia. (R1) to 3/8 in. dia. (R2), 1/2 in. dia. (R3), and 5/8 in. diameter (R4) where (R1 < R2 < R3 < R4). As the wave propagation distance between the excitation source and the hole damage is short, the wave reflection from damage region is stronger in the time domain. D2 hole damage case, therefore, was analyzed in the first assuming the D2 array response result should be the strongest among three hole damage cases. Also, the crack length increases from 0.5 in. (L1) to 1.0 in. (L2), 1.5 in. (L3), and 2 in. (L4) where (L1 < L2 < L3 < L4).

D2 Hole Damage

From the differential array responses, the D2 hole damage region (a maximum of differential array response) can be obviously determined. Although the differential array responses should show the wave reflections from damage region as eliminating other wave reflections from boundaries and joint bolts, all of the differential array responses include unwanted images due to uncertain noise in the experimental signals gathered from the spiral sensor array. The consecutive differential array responses shown in Figure 4.36 were reproduced by subtracting a differential array response from the preceding differential array responses. The threshold setting for the consecutive differential array responses is applied in order to emphasize the damage reflections. The default threshold was set as $Threshold = 0.8 * \max(|\psi_d(t,\theta)|)$.

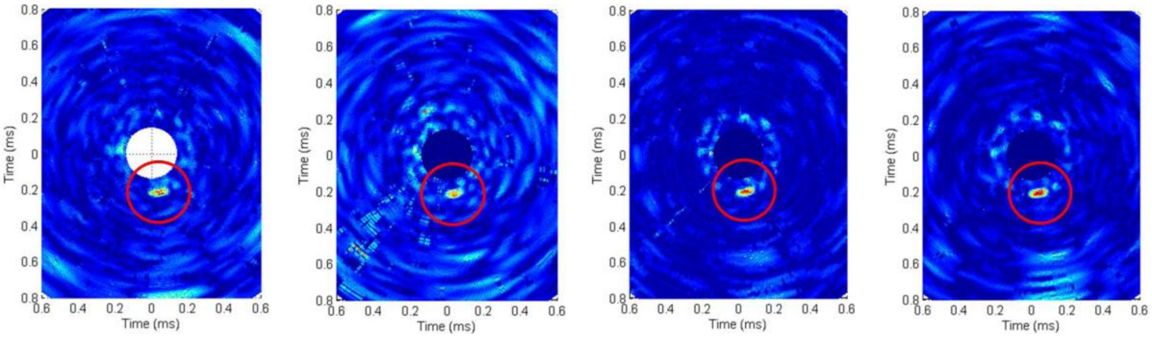

(a) R1 (b) R2 – R1 (c) R3 – R2 (d) R4 – R3

Figure 4.36: Consecutive differential array responses as D2 hole damage increases (60 kHz)

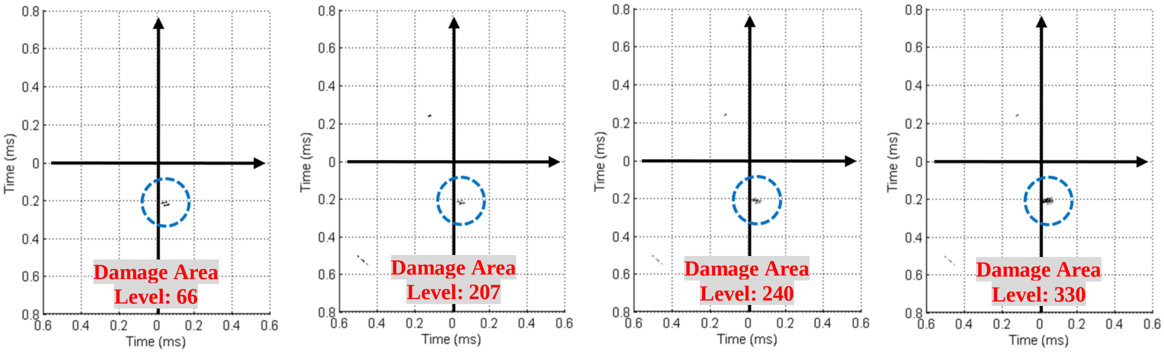

(a) R1 (b) R2 (c) R3 (d) R4

Figure 4.37: Final array responses after setting a threshold for D3 hole damage (60 kHz)

After filtering the consecutive differential array responses based on the threshold, each array response was summed up to reproduce the final array responses as shown in Figure 4.37. The final array response in Figure 4.37(b) was produced by summing up the filtered array responses of the consecutive differential array responses in Figure 4.36(a) and (b). Also, the final array response in Figure 4.37(c) was produced by summing up the filtered array responses of the consecutive differential array responses in Figure 4.36(a), (b) and (c). In the same manner, the final array response in Figure 4.37(d) could be produced.

Damage area level defined as $\iint \psi_{d1}(t,\theta)\,dtd\theta$ was determined for individual final array response. The normalized damage area level was shown in Figure 4.38(a). In addition, the normalized maximum value of the damage area defined as $\max\left(\left|\psi_{d2}(t,\theta)\right|\right)$ was determined as shown in Figure 4.38(b). As the size of the hole grows, the normalized damage area level and the normalized maximum value of the damage area consistently increase.

By multiplying two parameters shown in Figure 4.38, the damage index (DI) result can be determined as shown in Figure 4.39. The DI increases as the D2 hole size grows. In addition, the variation of the Hilbert-Huang transform (HHT) amplitudes at the simulated damage direction (280 deg.) as the hole damage size increases is shown in Figure 4.40. The HHT result indicates the approximate D2 hole damage location (~0.2 ms) in time domain. With group speed of A0 mode at the given excitation frequency (60 kHz), the D2 hole damage location can be estimated. Also, the HHT result show that the reflection energy from the D2 hole damage region increase as the hole size grows.

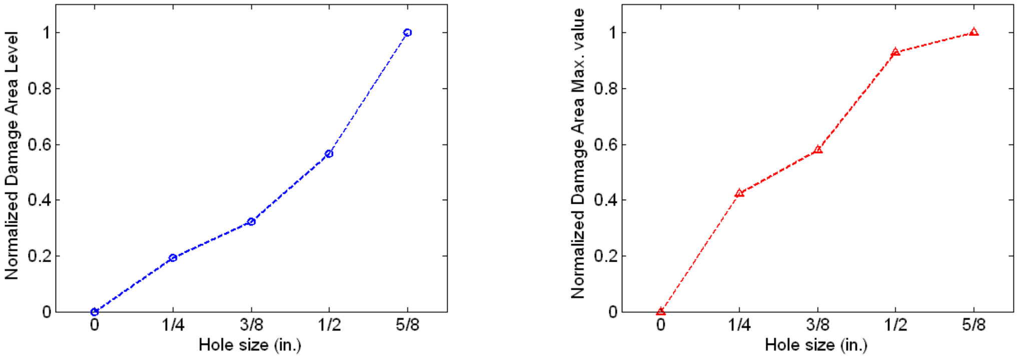

(a) Damage Area level (b) Damage Area maximum value

Figure 4.38: Normalized parameters of Damage Index computation for D2 hole damage case

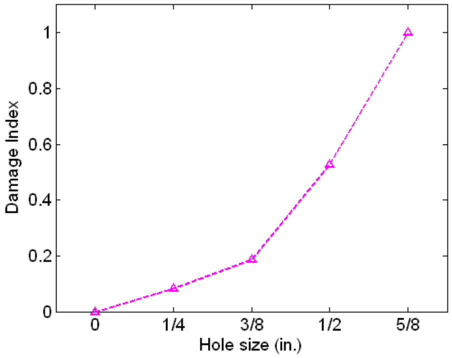

Figure 4.39: Damage Index variation as D2 hole damage increases (60 kHz)

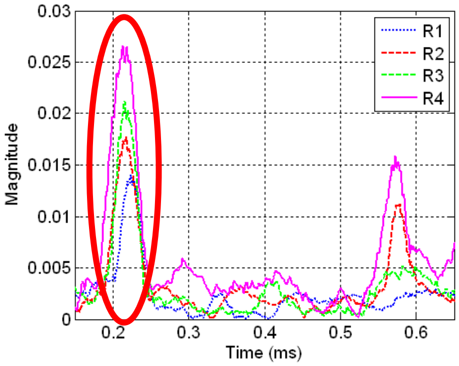

Figure 4.40: HHT amplitude at 280 deg. direction for D2 hole damage case (60 kHz)

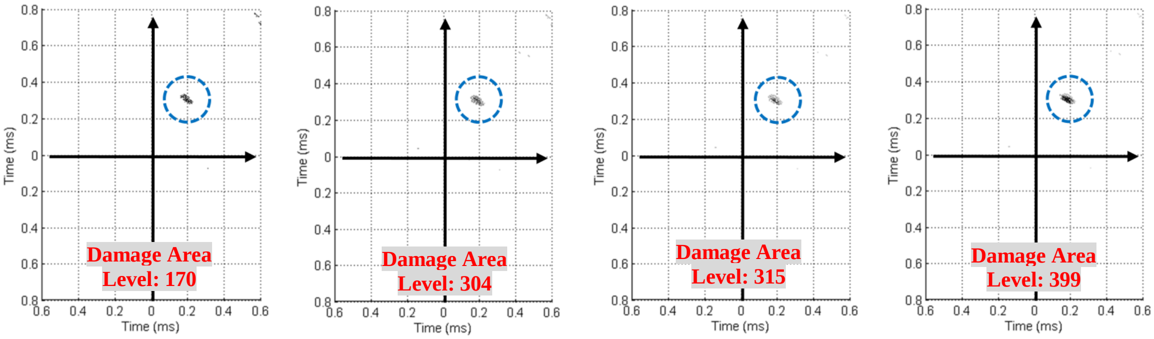

(a) R1 (b) R2 (c) R3 (d) R4

Figure 4.41: Final array responses after a threshold setting for D3 hole damage (60 kHz)

D3 Hole Damage

In the same manner as the D2 hole damage case, the final array responses for the D3 hole damage case were reproduced as shown in Figure 4.41. Using two parameters such as the normalized damage area level and the normalized maximum value of the damage area, the DI for the D3 hole damage was determined as shown in Figure 4.42. The DI increases as the D3 hole size grows. In addition, the variation of the HHT amplitude at the simulated damage direction (60 deg.) as the hole damage size increases is shown in Figure 4.43. The HHT result indicates the approximate D3 hole damage location (~0.35 ms) in time domain. The HHT result show that the reflection energy from the D3 hole damage region increase as the hole size grows.

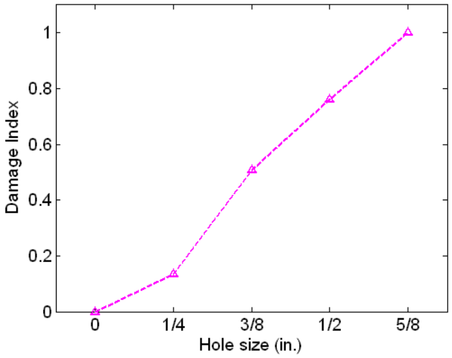

Figure 4.42: Damage Index variation as D3 hole damage increases (60 kHz)

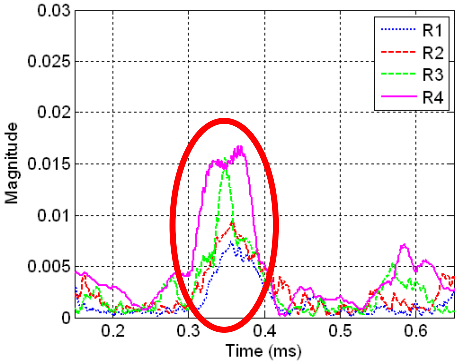

Figure 4.43: HHT amplitude at 60 deg. direction for D3 hole damage case (60 kHz)

D1 Hole Damage

The final array responses for D1 hole damage case were reproduced as shown in Figure 4.44. The final array responses when the threshold factor was set as 0.8 (default) are unable to noticeably estimate the D1 hole damage location, so that the threshold factor was changed from 0.8 to 0.6 and the final array responses were reproduced as shown in Figure 4.45. Using the final array responses based on the two threshold factors, the DIs were evaluated. Although both DI results in Figure 4.46 show that the DIs increase as the hole damage size grows, one can find these DI results are false by examining the final array responses shown in Figure 4.44 and Figure 4.45. The damage area level increases not due to the D1 hole damage, but due to the unwanted images. From the consecutive differential array responses shown in Figure 4.47, it can be found that the maximum array response are not apparent at the approximate D1 hole damage direction (225 deg.). Only the array response in Figure 4.47(c) shows the acceptable wave reflection image from the D1 hole damage location. In addition, the variation of the HHT amplitudes (Figure 4.48) at the simulated damage direction (225 deg.) are insignificantly related to the hole damage size increases. Also, the D1 hole damage location in the time domain is not clearly seen as compared with D2 and D3 hole damage cases. Signal attenuation related to wave propagation distance can be one reason for the inaccurate results of the D1 hole damage case. Ambient noise variation in the laboratory environment could be another influence to weaken the array response results.

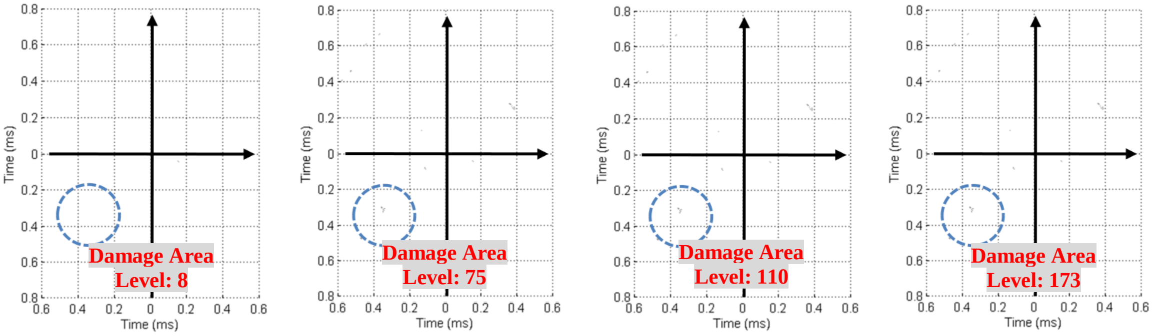

(a) R1 (b) R2 (c) R3 (d) R4

Figure 4.44: Final array responses after a threshold setting, 0.8*max(|$\psi_d(t,\theta)$|), for D1 hole damage (60 kHz)

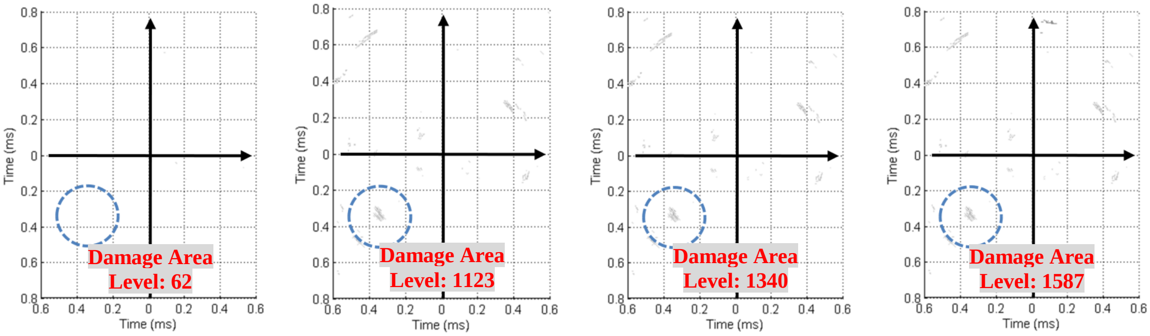

(a) R1 (b) R2 (c) R3 (d) R4

Figure 4.45: Final array responses after a threshold setting, 0.6*max(|$\psi_d(t,\theta)$|), for D1 hole damage (60 kHz)

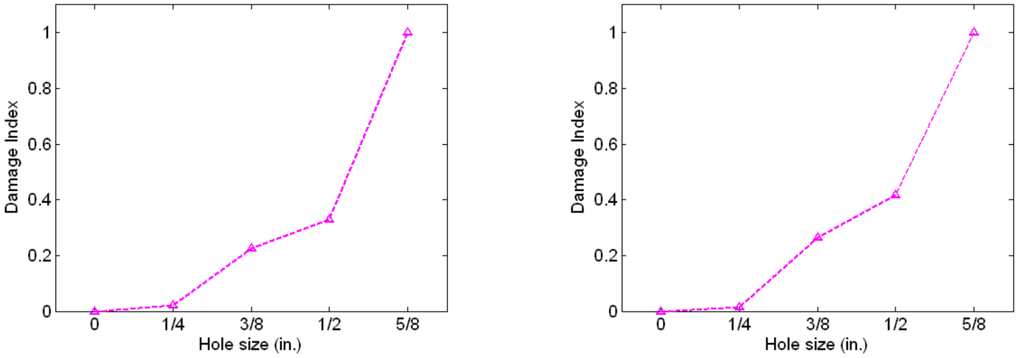

(a) *threshold* = 0.8* max(|$\psi_d(t,\theta)$|) (b) *threshold* = 0.6* max(|$\psi_d(t,\theta)$|)

Figure 4.46: Damage Index variation as simulated D1 hole damage increases (60 kHz)

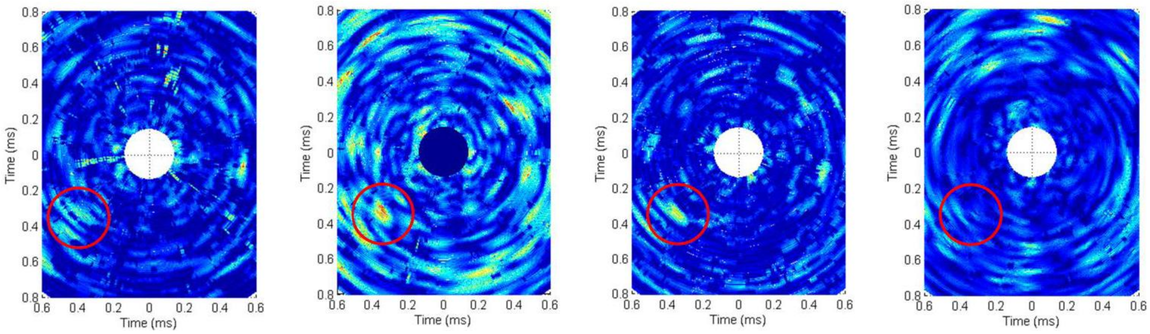

(a) R1 (b) R2 – R1 (c) R3 – R2 (d) R4 – R3

Figure 4.47: Consecutive differential array responses as D1 hole damage increases (60 kHz)

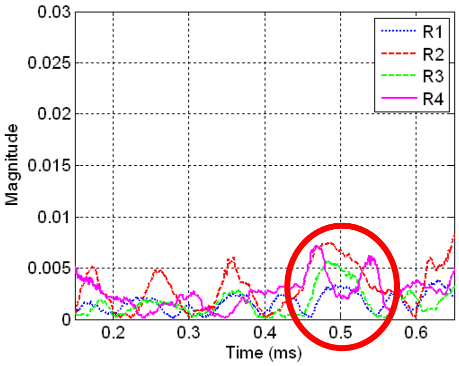

Figure 4.48: HHT amplitude of 225 deg. direction for D1 hole damage (60 kHz)

Crack Damage

The crack starting at the location of the side of the D3 hole damage on the panel with the spiral array was linearly increased toward 90 deg. direction from 0.5 in. up to 2 in. with 0.5 in. increments. The distance between the crack damage location and the center of the spiral array is around 8 in. as shown in Figure 4.27. In the same manner as the previous hole damage detection tests, the final array responses for the crack damage application were produced as shown in Figure 4.49, and the corresponding DI was evaluated as shown in Figure 4.50. The results show the final array response can clearly identify the crack damage location and its severity, and the DI increases as the crack size grows. In addition, the variation of the HHT amplitudes at the simulated damage direction (60 deg.) as the crack size increases is shown in Figure 4.51. The HHT result indicates the crack damage location (~0.35 ms) in time domain. The result, however, shows that the wave reflection energy at 60 deg. direction is inconsistent with the increase of crack length, as compared with the D2 and D3 hole damage cases. It is because the center of the crack damage was moving from 60 deg. direction toward 90 deg. direction while the center of the hole damage was almost fixed at the hole damage direction.

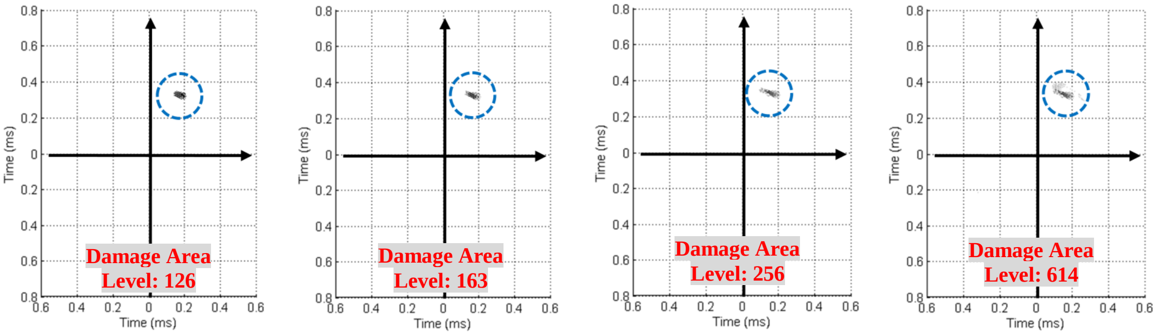

(a) L1 (b) L2 (c) L3 (d) L4

Figure 4.49: Final array responses after a threshold setting for crack damage (60 kHz)

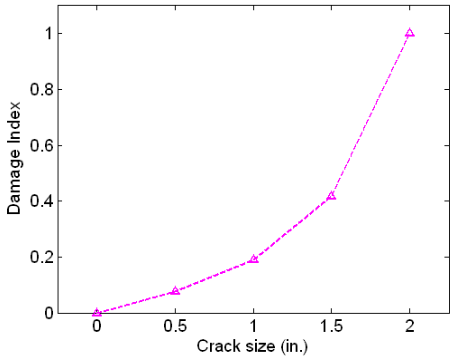

Figure 4.50: Damage Index variation as crack damage increases (60 kHz)

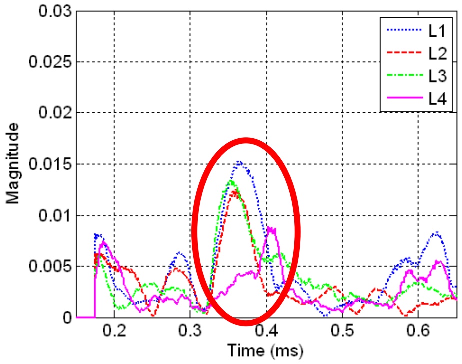

Figure 4.51: HHT amplitude at 60 deg. direction (60 kHz)

### 4.1.11 Compensation Techniques for Piezopaint Spiral Array

Two types of signal compensation factors, based on the capacitance of the piezopaint sensor elements and the peak-to-peak voltage (Vp-p) of A0 mode captured from the piezopaint sensor elements, were examined to improve the array response by refining the proposed phased array technique. The capacitance of the sensor elements of the spiral array was measured using a capacitance meter as shown Table 7. With the measured capacitances of all of the sensor elements, the capacitance compensation map shown in Figure 4.52(a) was constructed. To assess the Vp-p of A0 mode, the experimental signals of the spiral array using the off-center piezoceramic actuator were recalled. The Vp-p of incident A0 mode from the off-centered excitation source was measured as shown in Table 8. With the measured Vp-p of the incident A0 modes of all of the sensor elements, the Vp-p compensation map shown in Figure 4.52(b) was constructed like the capacitance compensation map. The white small circles in the figures indicate the sensor element positions of the spiral array. The results of two compensation factors note that the capacitance is not directly related to output signal strength of the piezopaint sensor elements.

Table 7: Capacitance measurement examples for the spiral array

| **Sensor 1** | **Sensor 6** | **Sensor 7** | **Sensor 12** | **Sensor 25** |
|---|---|---|---|---|
| 57.2 | 54.6 | 62.4 | 82.6 | 59.3 |
| **Sensor 13** | **Sensor 18** | **Sensor 19** | **Sensor 24** | Unit: (pF) |
| 62.8 | 50.1 | 66.9 | 55.5 | |

Table 8: Vp-p measurement examples of incident A0 modes for the spiral array

| **Sensor 1** | **Sensor 6** | **Sensor 7** | **Sensor 12** | **Sensor 25** |
|---|---|---|---|---|
| 0.2181 | 0.3125 | 0.3953 | 0.1860 | 0.1061 |
| **Sensor 13** | **Sensor 18** | **Sensor 19** | **Sensor 24** | Unit: (V) |
| 0.2945 | 0.3450 | 0.3720 | 0.0983 | |

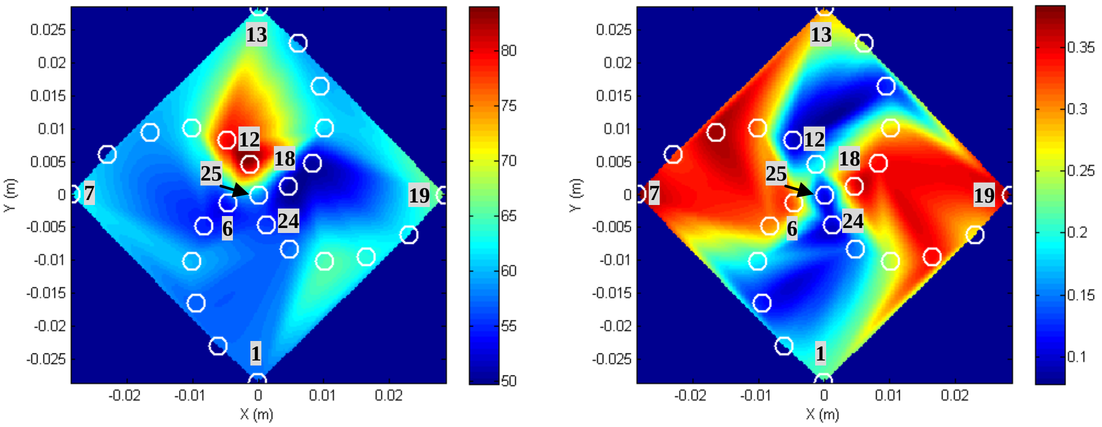

(a) Capacitance compensation factor map (b) Vp-p compensation factor map

Figure 4.52: Compensation factor maps

Applying the compensation factors to the GLW signal data obtained from the spiral array, the differential array responses were reproduced as shown in Figure 4.53. The results demonstrate that the proposed compensation factors are unable to significantly improve the differential array responses.

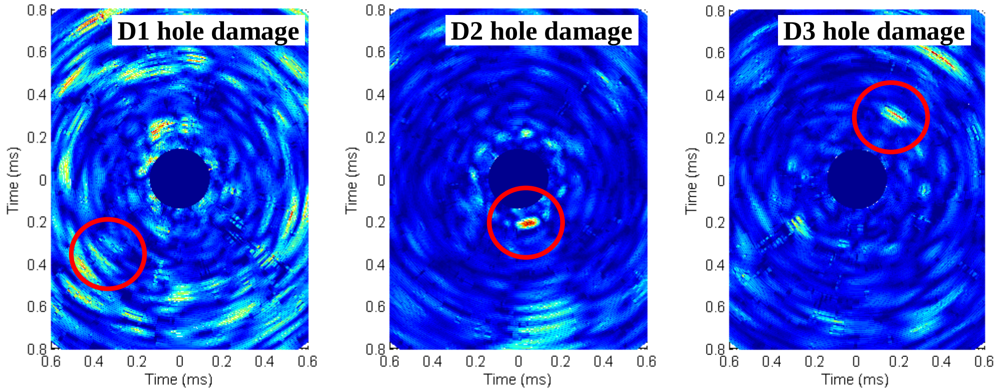

(a) Without applying compensation factors

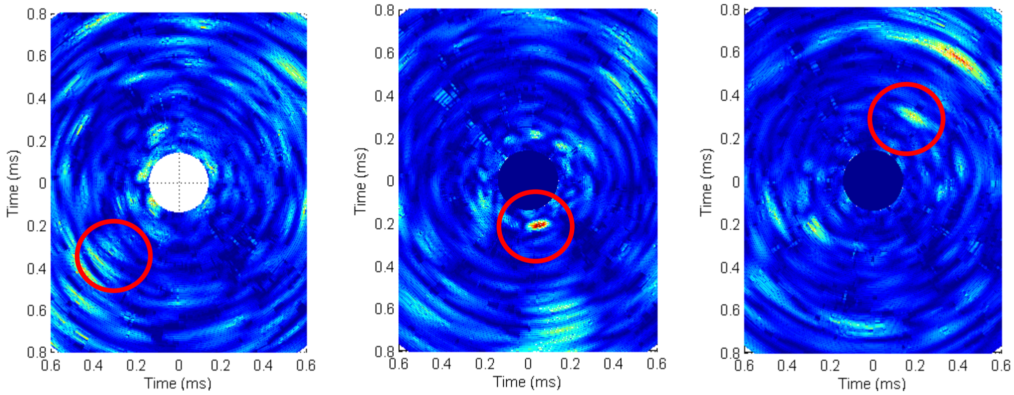

(b) With applying capacitance compensation factor

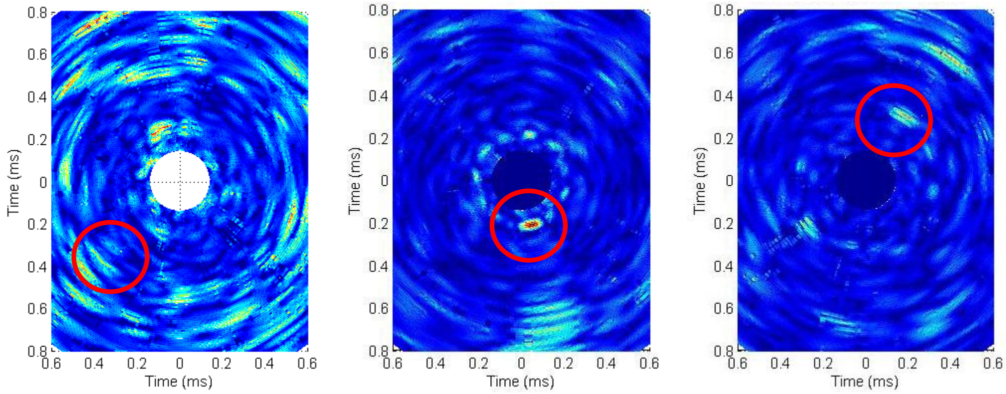

(c) With applying Vp-p compensation factor

Figure 4.53: Comparison of differential array responses with compensation factors

## 4.2 *Multi-Location-Actuator-based 2-D Phased Sensor Array System*

### 4.2.1 Introduction

From previous experimental tests, it was observed that the properties of GLW reflections from boundaries/damages are closely related to the type of damage and the locations of actuators and sensors. For circular damage such as holes, there are apparent omni-directional wave reflections from the damage regardless of the origin of the incident GLW which propagates in a thin panel. The propagating GLW is scattered due to the boundary geometry of the circular damage and the reflecting GLW can be detected at the sensor located any place in the panel as shown in Figure 4.54(a), except for the shadow area created by the circular damage shape. The level of the GLW energy detected at a sensor is dependent on wave attenuation factors such as propagation distance and material properties of the panel. However, if the panel has a linear crack created along a straight line between the positions of the actuator and the sensor, the wavefront of the propagating GLW is perpendicular to the crack orientation as shown in Figure 4.54(b). In this condition, there are weak wave reflections from the crack damage as most of the GLW energy is transmitted through the crack damage area.

For the crack damage described above, the general 2-D phased array technique using a single actuator, located near the center of the array, is unable to detect the crack damage even though it is considerably severe. Therefore most researchers [104, 133, 134], who studied the SHM based on the 2-D phased array approach simulated linear crack damages almost parallel to the wavefront of the propagating GLW in order to obtain the maximum wave reflections from the crack damages. In this paper, a new and robust 2-D phased array technique with multiple distributed actuators is presented, which builds on the previous 2-D phased array research conducted by the authors, in order to overcome the limitation of the general 2-D phased array technique using a single actuator. Array responses are produced by using the associated 2-D phased array signal processing algorithm [134]. An additional GLW propagation and reflection analysis technique is implemented to detect the damage location and its growth because multiple actuators are used for interrogation. Gangadharan et al. [135] showed one can find acoustic emission (AE) source location by virtually tracking GLW in reverse along the wave propagation paths within structures. In this study, a new backward GLW propagation approach using fundamental physics-based wave reflection theory is applied to find the actual damage location by virtually tracking the GLW reflections in the resultant final array responses corresponding to the actuator positions.

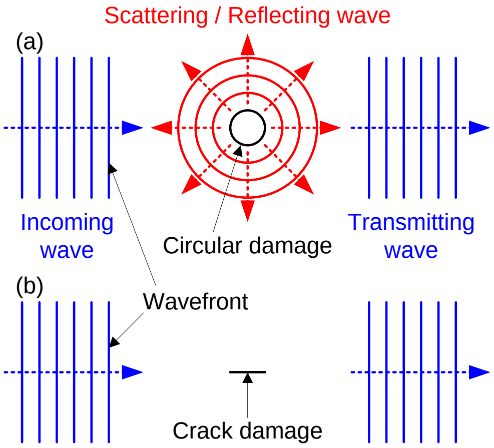

Figure 4.54: Diagram of wave reflection and transmission with respect to type of damage; (a) for circular damage and (b) linear crack damage

### 4.2.2 Estimation of Baseline Response Using Virtual Source Image

Prior to examining GLW reflections from damage, boundary wave reflections and the associated virtual images of excitation sources were studied to estimate baseline array responses. A theoretical model was developed by using fundamental law of reflection in order to evaluate the baseline array responses depending on excitation source locations and geometrical boundaries of panels. The governing equation for the model is described in Equation (4.1) and the associated diagram is illustrated in Figure 4.55. As the governing equation was applied for the top edge boundary and an excitation source ($\boldsymbol{p}_{exct}$) is located at the middle of the right edge boundary, a virtual image of the excitation source can be determined as shown in Figure 4.55. For evaluating additional virtual images for the same excitation source ($\boldsymbol{p}_{exct}$), the other three edge boundaries should be applied to the governing equation.

$$\boldsymbol{V}_{image} = 2 * \{\boldsymbol{V}_{in} - (\boldsymbol{V}_{in} \bullet \boldsymbol{W}_{bound}) * \boldsymbol{W}_{bound}\} \tag{4.1}$$

$$\boldsymbol{W}_{bound} = \boldsymbol{p}_{i+1} - \boldsymbol{p}_i \text{ for } i = 1,2,3,\text{and } 4 \tag{4.2}$$

$$\boldsymbol{V}_{in} = (\boldsymbol{p}_{i+1} + \boldsymbol{p}_i)/2 - \boldsymbol{p}_{exct} \tag{4.3}$$

where $\boldsymbol{p}_i$ for $i = 1,2,3,4$ are (x,y) locations of four corners of the given rectangular panel and $\boldsymbol{p}_{exct}$ is the (x,y) location of an excitation source. A boundary vector ($\boldsymbol{W}_{bound}$) and an input vector ($\boldsymbol{V}_{in}$) are described by Equations (4.2) and (4.3). The input vector can be determined by connecting from the $\boldsymbol{p}_{exct}$ to the middle point of the boundary vector.

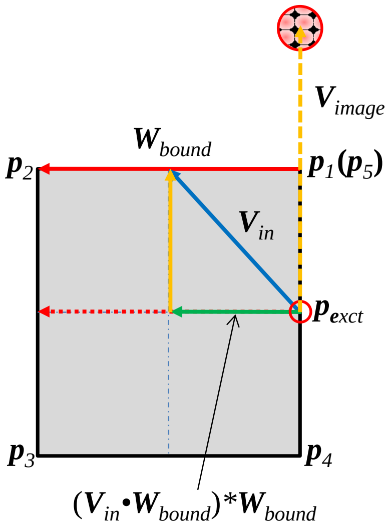

Figure 4.55: Diagram of modeling for virtual source image evaluation

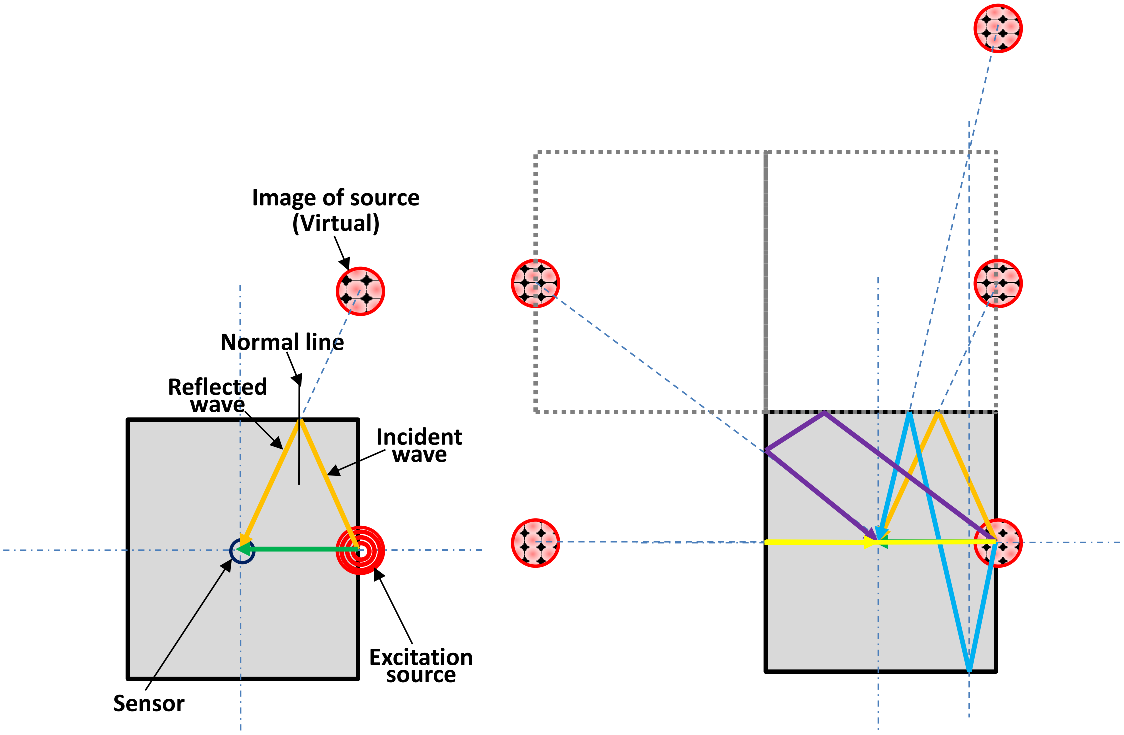

(a) Description (b) Determined virtual source images

Figure 4.56: Virtual source images for an excitation source and the associated wave paths

Using the estimated locations of the virtual source images, wave propagation paths in the panel can be estimated. Figure 4.56(a) shows how the excitation wave reflects from the top edge boundary and arrives at the center of the panel (i.e. sensor position). Other virtual images of the excitation source and the associated wave propagation paths are shown in Figure 4.56(b). There are additional virtual source images and the corresponding wave propagation paths can be found in the same manners, by using the proposed governing equation. An extension of this technique could be made to curved boundaries by modifying Equations (4.1) through (4.3).

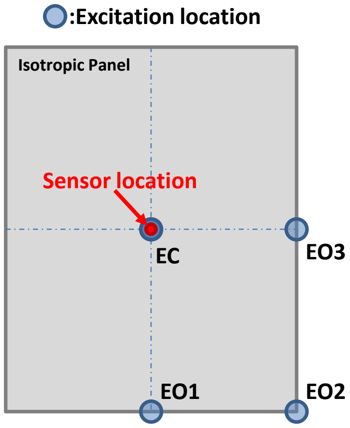

Figure 4.57: Configuration for virtual image source modeling with a rectangular panel with multi-location actuators and a sensor at the center of a panel

A diagram of virtual source image modeling for actual experimental tests is shown in Figure 4.57. Virtual source images (related to baseline array responses) for various excitation sources (EO1, EO2, EO3, and EC) were evaluated by using the algorithm based on the governing equation (Equation (4.1)) and the resultant virtual source images are shown in Figure 4.58.

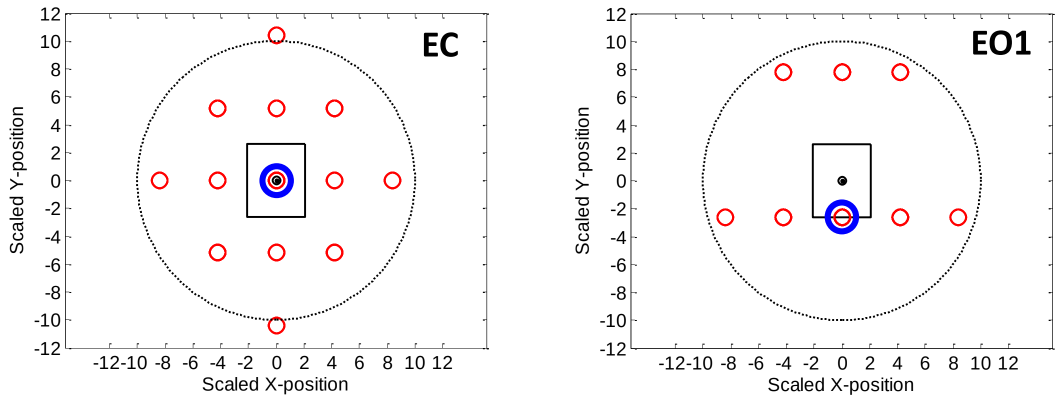

(a) EC

(b) EO1

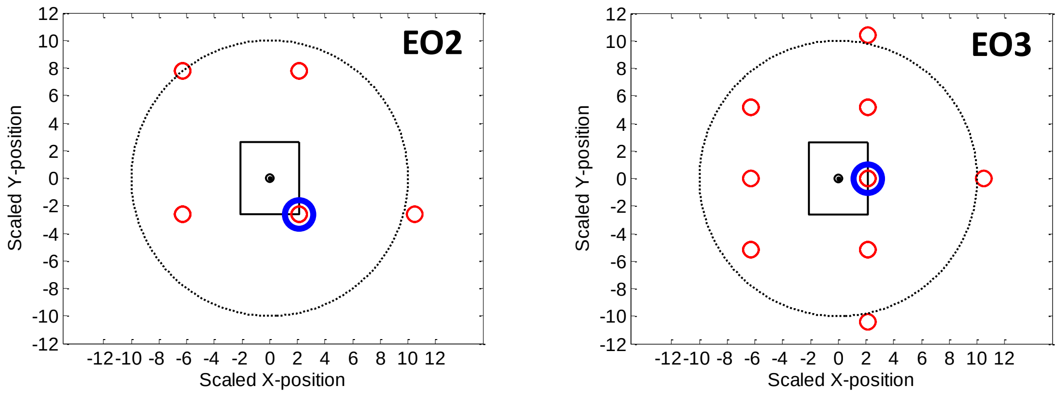

(c) EO2

(d) EO3

Figure 4.58: Virtual source image evaluation according to four excitation sources (Circles in blue)

The rectangle at the center of the figures indicates the actual geometry of the panel. The large black dotted circle represents a scaled version of the baseline response of the 2-D phased array where the size of the circle depends on the excitation frequency and the length of the time domain signal. The area circled in blue indicates the incident wave traveling directly from the actuator to the sensor location. The modeling results will be compared with baseline array response results (based on experiments) obtained from the 2-D phased array signal processing. X and Y axes are the scaled positions dependent on the group velocity.

### 4.2.3 Experimental Setup

A piezoceramic (PZT-5A) based 2-D phased array was instrumented for laboratory evaluation for various damage detection tests, because the sensitivity of the piezoceramic is much greater than other piezoelectric-based alternatives. Based on the previous research about the characteristic evaluation of the 2-D phased arrays [134], the spiral configuration was selected to form the piezoceramic based 2-D phased array. The element spacing was 3/16 in. and 25 discrete sensor elements (1/8 in. x 1/8 in.) were used as shown in Figure 4.59. The 2-D spiral array was instrumented on the center of the panel and four 1/4 in. diameter piezoceramic actuators (identified as EC, EO1, EO2, and EO3) were mounted at different locations onto the panel as shown in Figure 4.60 and the testing panel was under free-free boundary conditions. Structural vibration responses of the panel at various excitation frequencies (60, 80, and 100 kHz) were gathered from the sensor array, and they were processed using the 2-D phased array algorithm to yield the array responses. A tone burst excitation signal at 60 kHz and the associated sample signals obtained from three sensor elements of the spiral array are shown in Figure 4.61, as the EO1 actuator was used as the excitation source. Figure 4.61(b) shows that the A0 mode (the largest waveform in the signals) exhibits a phase lag between the sensor signals due to differing propagation distance from the actuator to the different sensors. Also the S0 mode and numerous boundary reflections of the GLW modes are shown in the figure of the sample signals. Three excitation frequencies (60, 80, and 100 kHz) are low frequency cases in the dispersion curves of the GLW for the testing panel. This denotes that A0 modes are dominant in the signal, and the group velocity of the A0 mode is much slower than S0 mode's velocity. In this paper, the phased array algorithm was based on the directional wavenumber filtering method, which means that the A0 mode was intentionally filtered in the array signals because the A0 modes have most of the GLW energy. Ideally, this method should remove other GLW modes except for the A0 modes in the signals. Hence, this paper was focused on tracking the A0 mode and its scattering/reflection.

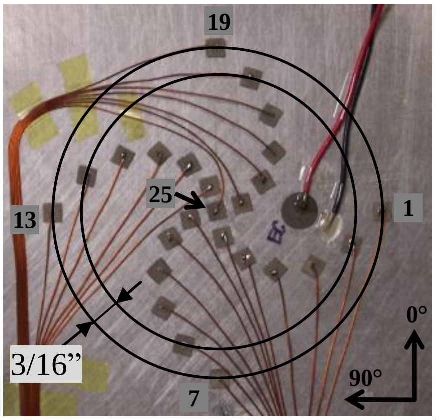

Figure 4.59: Picture of piezoceramic based 2-D spiral phased array

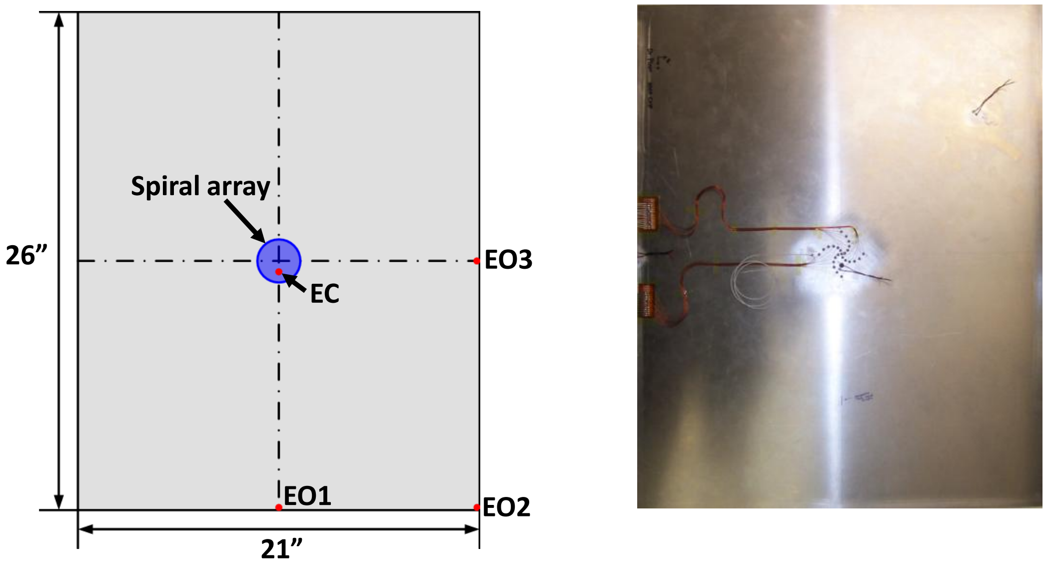

(a) Schematic diagram of testing panel

(b) Picture of testing panel

Figure 4.60: Testing panel with multi-location actuators and 2-D spiral array

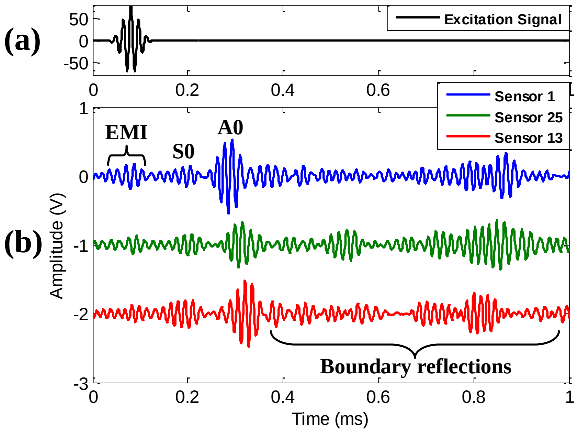

Figure 4.61: Sample sensor signals when exciting EO1 actuator at 60 kHz; (a) excitation signal and (b) three sensor signals obtained from the spiral array

The wavenumber of the A0 mode in the sensor signals may be determined using the 2-D spatial Fourier transform and the results are shown in Table 9 according to each excitation frequency case. This information is used as selective wavenumbers for the directional filtering in the 2-D phased array signal processing algorithm described in the previous section. For the panel under no damage condition, the array response results for the various excitation sources were produced as shown in Figure 4.62. They are saved as baseline array response results that should be used to determine differential array responses (i.e. Baseline – Damage array response). In order to focus on the GLW reflections from boundaries and damage, the strong incident wave signals coming from the EC actuator positioned inside the spiral array region were intentionally removed. Hence, the waveform image for the EC excitation source is invisible in Figure 4.62(a). The off-centered excitation sources (EO1, EO2, and EO3) can be clearly located in the baseline array response results, which validate the 2-D phased array signal processing methodology as the incident signal is positioned correctly in the array response in terms of incident direction and time of flight (i.e. traveling distance). It is readily apparent that wave reflections from the boundary conditions are considerably weaker than the incident GLW. The array responses can be compared with the virtual source image estimation results (shown in Figure 4.58) to evaluate which waveforms represent boundary reflections in the array response results. Other artifacts are present in the array response results which are due to the wavenumber filtering characteristics of the 2-D spiral phased array. They are dependent on factors such as the sensor array layout configuration and total number of sensor elements used in the array. The undesirable artifacts in the array responses can be effectively removed by evaluating the final differential array responses that are produced by subtracting the baseline array responses from damage array responses, and by averaging with the differential array responses for the three excitation frequency cases (60, 80, and 100 kHz).

Table 9: Experimentally determined wavenumber

| **Frequency (kHz)** | 60 | 80 | 100 |
|---|---|---|---|
| **Wavenumber (rad/m)** | 505.7 | 579.8 | 671.1 |

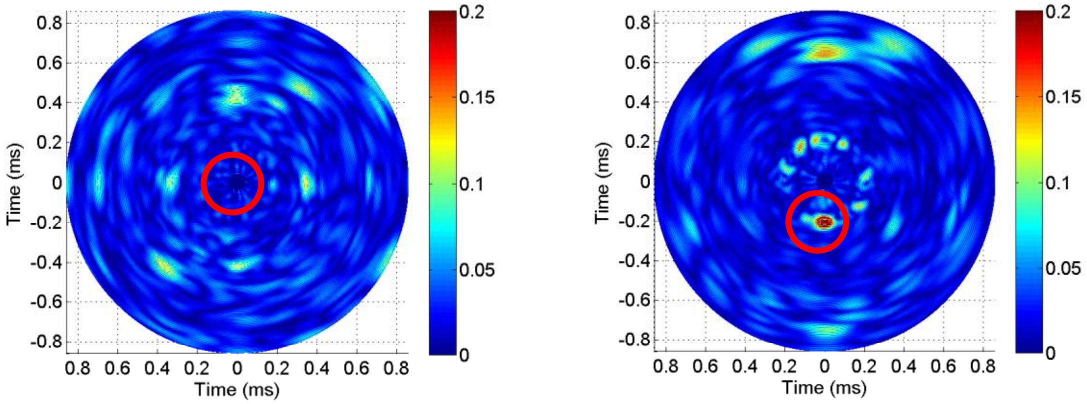

(a) EC actuator (red circle)

(b) EO1 actuator

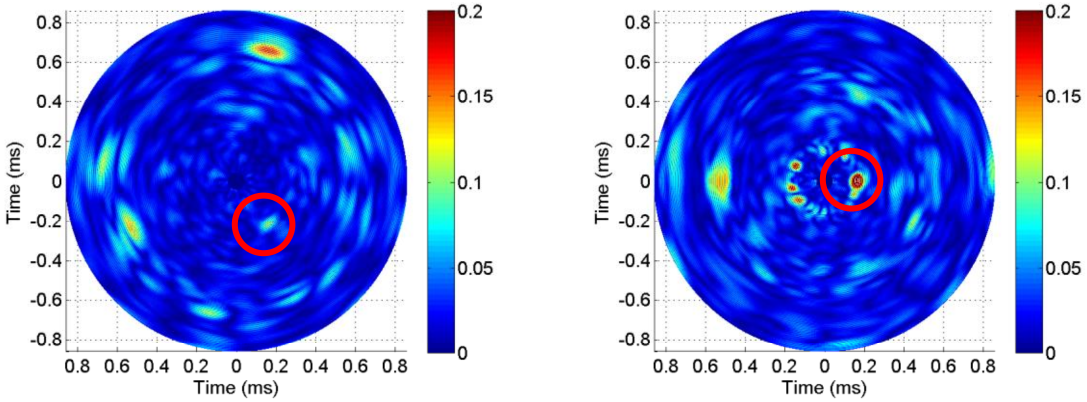

(c) EO2 actuator

(d) EO3 actuator

Figure 4.62: Baseline array responses for four actuator cases (60 kHz)

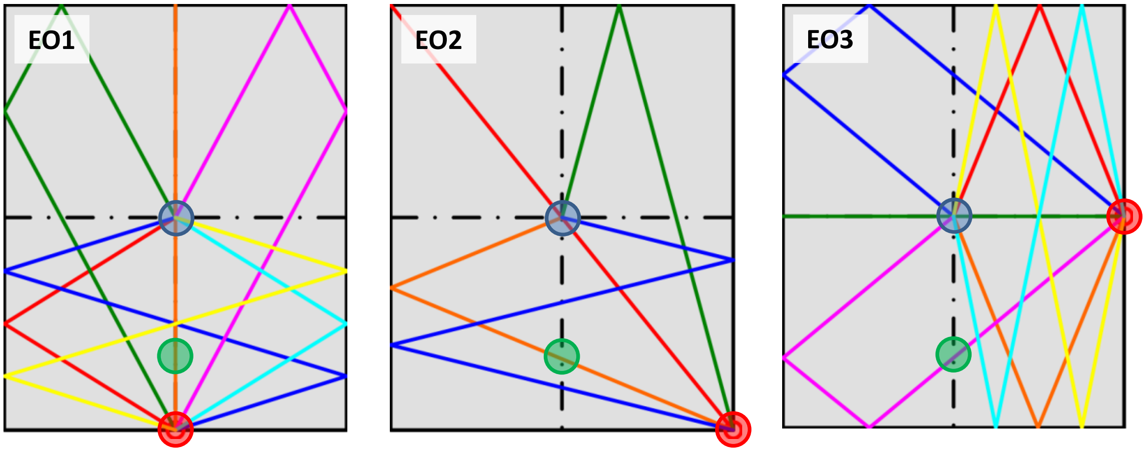

(a) EO1 actuator (b) EO2 actuator (c) EO3 actuator

Figure 4.63: Wave propagation path based on actuator (red circles) and sensor (blue circles) locations

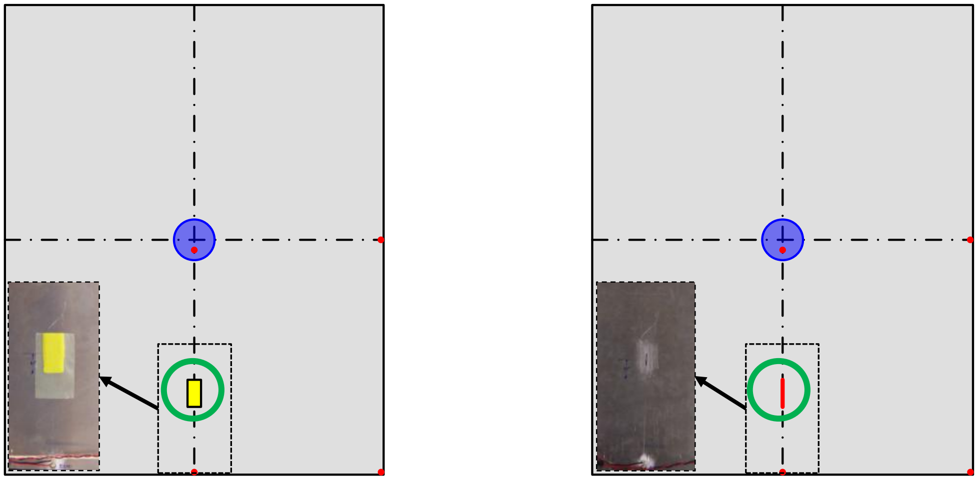

(a) For rubber patch (b) For linear crack

Figure 4.64: Two different damages (green circles) in the testing panel

### 4.2.4 Damage Detection with Differential Array Response

Various wave propagation paths in the panel were examined to find the best location for damage simulation and to create actual damages at the location (Figure 4.63). The evaluation results are to be used to detect the simulated damage location after producing the final differential array responses. Only two boundary reflections were set as a maximum reflection because the waveforms reflected from more than two boundaries were weak in the experimental sensor signals. The wave propagation paths corresponding to the positions of an excitation source (red circle) and sensor (blue circle) were determined by using the fundamental law of reflection described in the previous section. From the results, the area circled in green was determined as the prospective damage location, because the incident GLW propagating from the EC and EO1 actuator locations will less interfere with simulated damage than the GLW from the EO2 and EO3 actuator locations. It is assumed that the differential array response results using the EO2 and EO3 actuator cases will be more apparent due to the damage than those of EC and EO1 actuator cases. Two types of damages were simulated in the panel as shown in Figure 4.64. Before creating an actual linear crack in the panel, a rubber patch (0.75 in. width and 1.5 in. length) was bonded at the proposed damage location for preliminary evaluations. For the real damage case, a 0.5 in. linear crack was initially created along a straight line between the positions of the EO1 actuator and the center of the spiral array. The linear crack was created by using a metal saw blade and the crack gradually increased from 0.5 in. (L1) to 1.0 in. (L2), 1.5 in. (L3), and 2 in. (L4) where L1 < L2 < L3 < L4. The crack was centered at 4.5 in. distant from bottom edge boundary of the panel. The rubber patch disturbs

GLW propagation in several paths so that excitation GLW energy dissipates while the excitation GLW energy reflects/scatters for the crack damage case.

Differential array responses were determined in time domain after the 2-D phased array signal processing. Because the actuators' locations are known in the panel, group velocity of the A0 mode at a given frequency can be determined from the baseline array response results. Figure 4.65 shows the differential array response results of the EO1 actuator case when the panel has the rubber patch. By using the group velocity, the differential array responses could be converted from the time domain into the space domain as shown in Figure 4.65(a–c) for the rubber patch case. A frequency averaged differential array response (Figure 4.65(d)) was produced by averaging with the differential array responses for the three excitation frequency cases. In the same manner, the frequency averaged differential array responses with respect to the different actuators were produced for the rubber patch case, as shown in Figure 4.66. The red boxes in the Figure 4.66 indicate the actual geometry of the testing panel. All of the differential array responses show the effect of the artificial damage (rubber patch) on the panel. The array response results show that the GLWs traveling from the excitation sources do not reflect from the rubber patch, but dissipate due to the damage area. In Figure 4.66(b), one can find how the side lobe may influence the array response in negative way. There are the noticeable waveform images around the red rectangle (i.e. geometrical boundary of the panel) except for the waveform images at the EO1 actuator location. The waveform images are the side lobe effects according to the waveform images (the red circle in Figure 4.66(b)) with the highest intensity. Especially the waveform images for the side lobe effects are apparent due to the relatively low color scale in the figure. The intensity of the images can be lowered by changing the color scale based on the maximum value of the highest intensity waveform image (shown in the red circle in Figure 4.66(b)). A method to estimate the location of the rubber patch will be discussed in the next section.

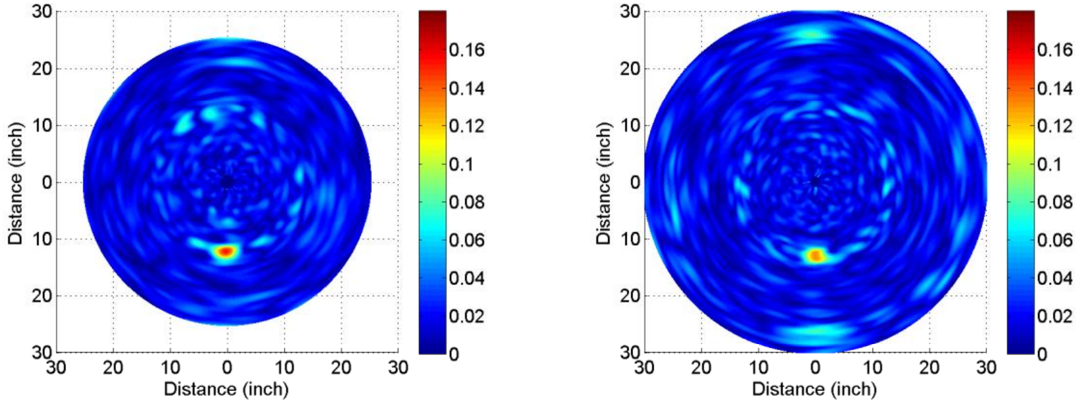

(a) EC actuator (60 kHz)

(b) EC actuator (80 kHz)

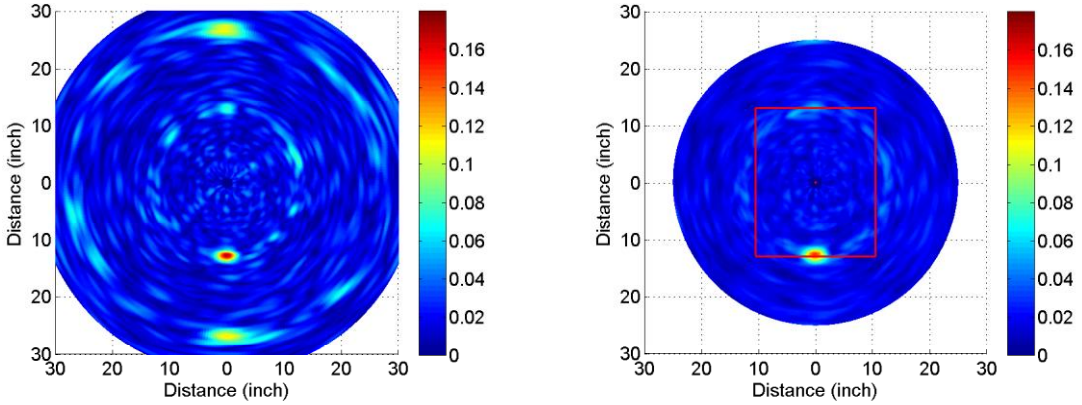

(c) EC actuator (100 kHz)

(d) EC actuator (Frequency Average)

Figure 4.65: Differential array responses for rubber patch case with EO1 actuator case at various excitation frequencies

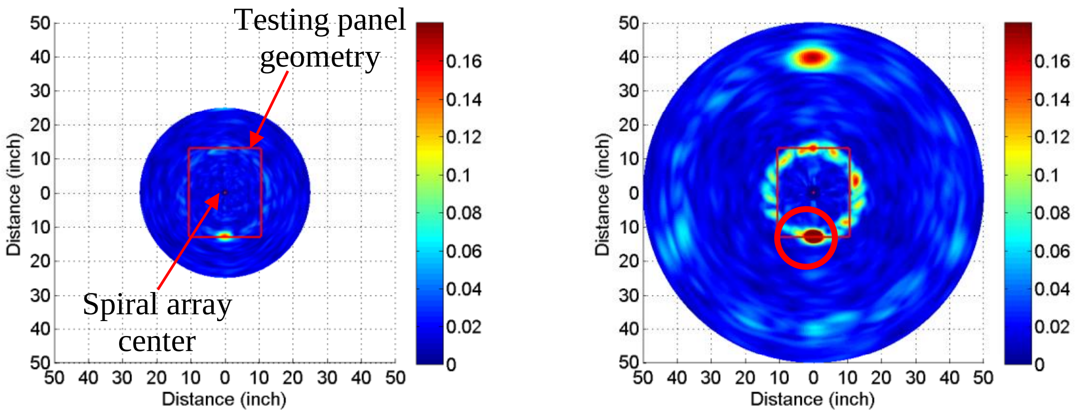

(a) EC actuator

(b) EO1 actuator

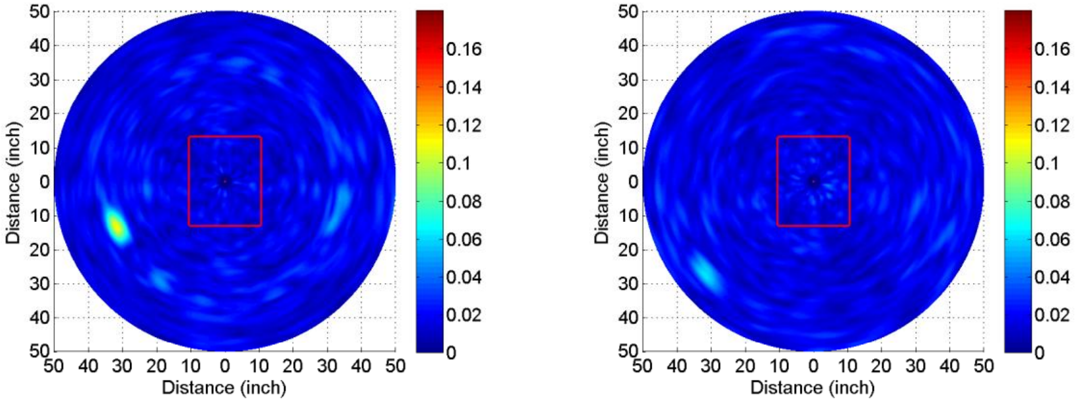

(c) EO2 actuator

(d) EO3 actuator

Figure 4.66: Frequency averaged differential array responses of four different actuator cases (for rubber patch case)

Frequency averaged differential array responses for multiple actuators were produced for the 2 in. linear crack damage (L4) case and they are shown in Figure 4.67. Even though the crack damage is severe, there are no noticeable waveform images due to the crack in the differential array response when using the EC actuator located near the center of the panel, as shown in Figure 4.67(a).

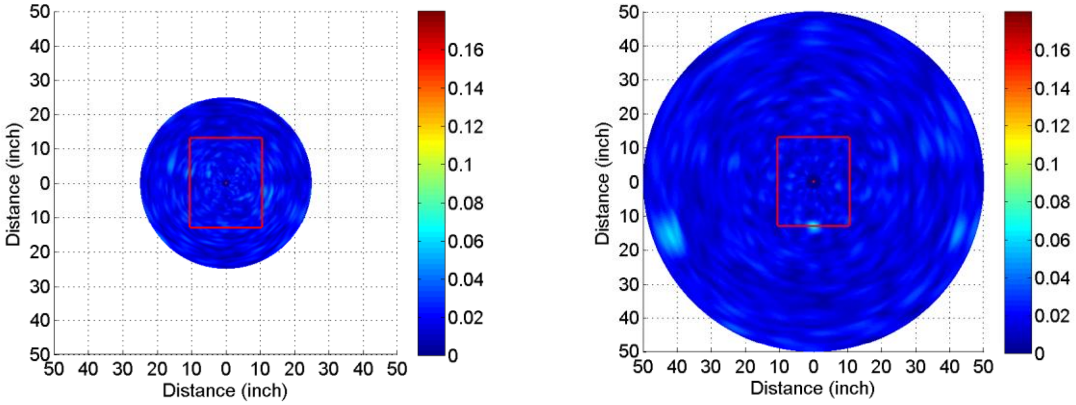

(a) EC actuator (L4)

(b) EO1 actuator (L4)

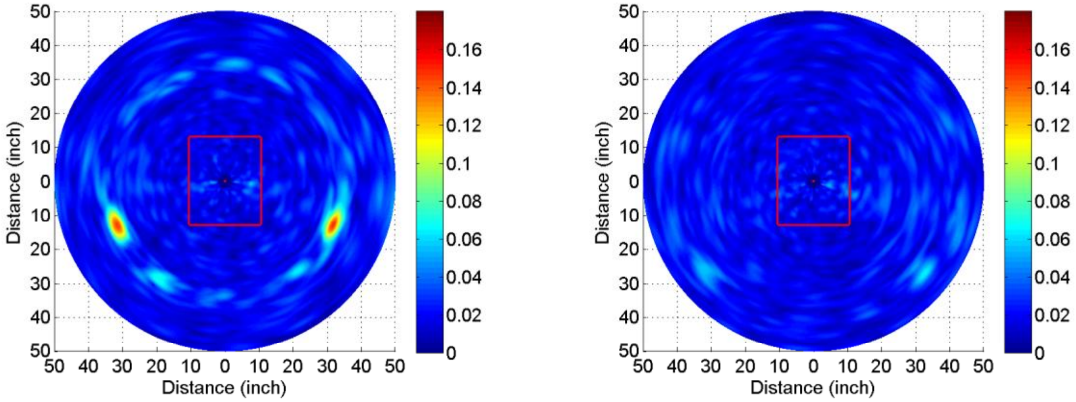

(c) EO2 actuator (L4)

(d) EO3 actuator (L4)

Figure 4.67: Frequency averaged differential array responses of different actuator cases (for linear crack case)

It is because most of the GLW energy from EC excitation source is passing through the crack due to its orientation. However, it is feasible to indentify the crack damage in the differential array response when using the off-centered actuators, shown in Figure 4.67(b–d). Especially for the EO2 actuator case, the waveform images due to the crack damage are readily noticeable in the differential array response as shown in Figure 4.67(c). In Figure 4.68, frequency averaged differential array responses of the

EO2 actuator case were produced to monitor the increase of the crack length. The results show the maximum value of the differential array response consistently increases as the crack grows in the panel.

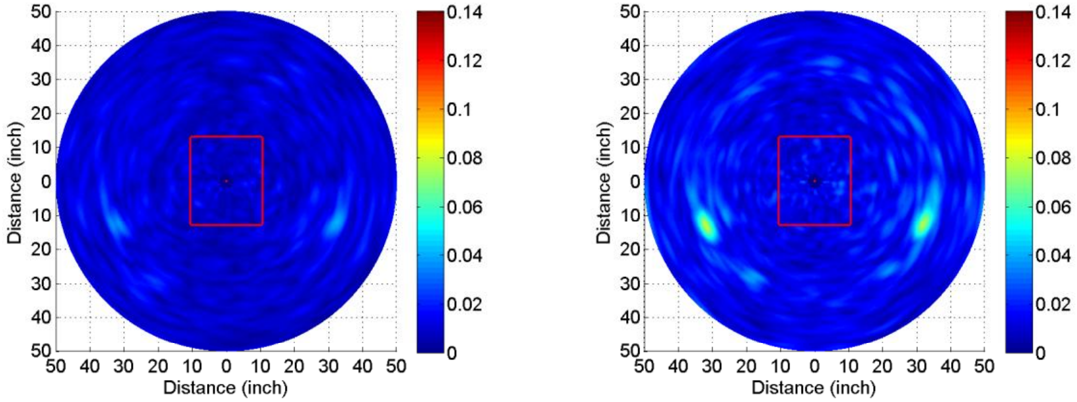

(a) EO2 actuator (L1 (0.5 in.))

(b) EO2 actuator (L2 (1 in.))

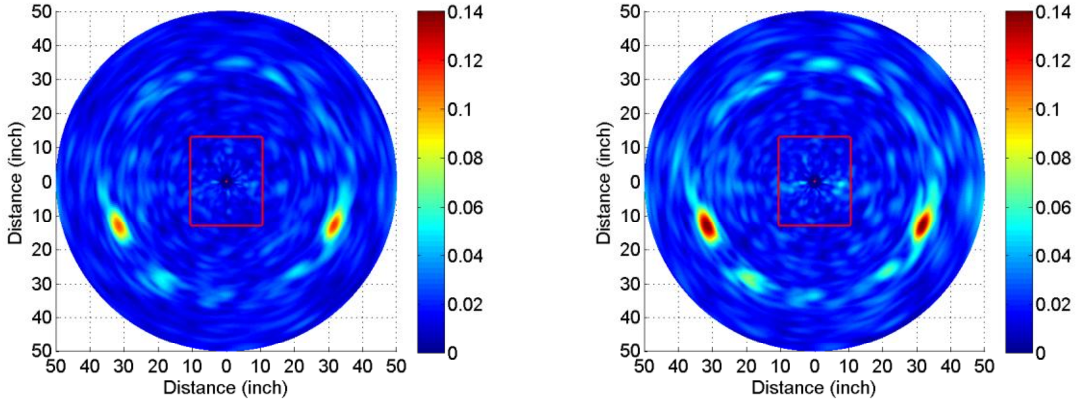

(c) EO2 actuator (L3 (1.5 in.))

(d) EO2 actuator (L4 (2 in.))

Figure 4.68: Frequency averaged differential array responses of EO2 actuator case for various crack length

### 4.2.5 Damage Location Evaluation

An additional analysis technique was used to determine the damage location because the multiple distributed actuators were used for SHM application in conjunction with the GLW interrogation. A backward wave propagation technique using a fundamental physics-based boundary reflection approach is applied to detect the actual damage location in the panel. The damage location can be estimated by virtually tracking the waveforms due to the damages in the frequency averaged differential array responses corresponding to the actuator locations. The steps of damage location evaluation process are described as the following:

1) Look at the final differential array responses and determine which waveform images have high intensity in the responses.
2) Consider the waveform images as damage images.
3) In the array response results, construct a straight line between the position of damage waveform image(s) and the center of the 2-D phased array (i.e. sensor location).
4) As considering wave reflections within the geometrical boundaries (red rectangles), determine the paths by virtually backward tracking the propagating GLW from the actuators to the center of the sensor array.
5) Analytically estimate damage location(s) based on the wave propagation.

For the rubber patch case, the wave propagation paths (a, b, c, and d) were determined as shown in Figure 4.69(a-d) as following the above evaluation steps. The waveform images in red circles were considered as GLW interference due to the artificial damage (rubber patch). By plotting all of the wave propagation paths in the same panel geometry, the intersection can be found as shown in Figure 4.69(e) and considered as an approximate damage location. The estimated damage location agreed with the actual location of the rubber patch in the testing panel.

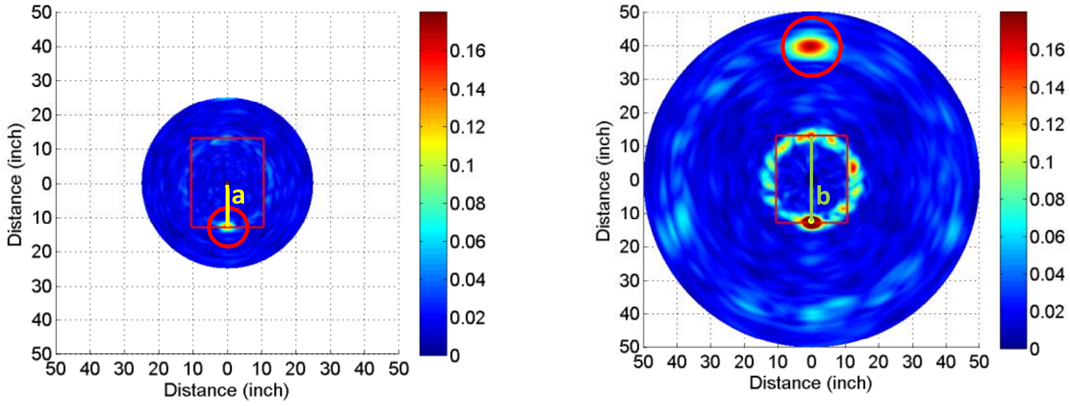

(a) EC actuator

(b) EO1 actuator

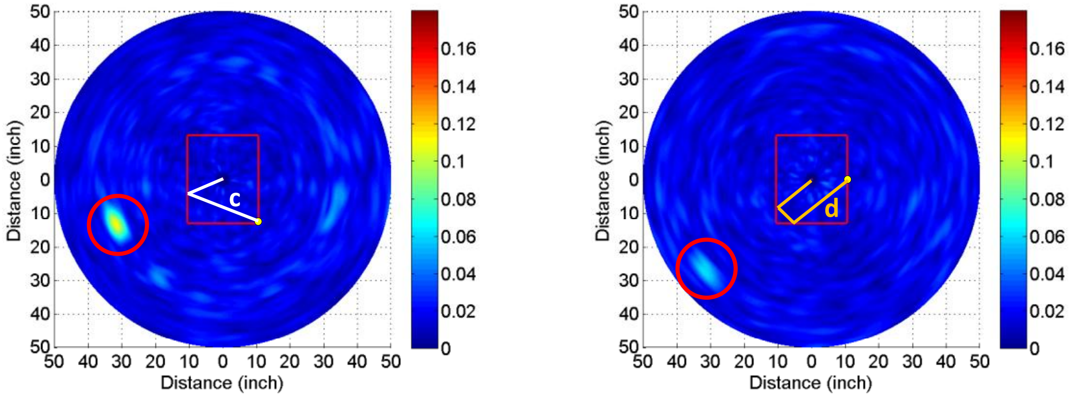

(c) EO2 actuator

(d) EO3 actuator

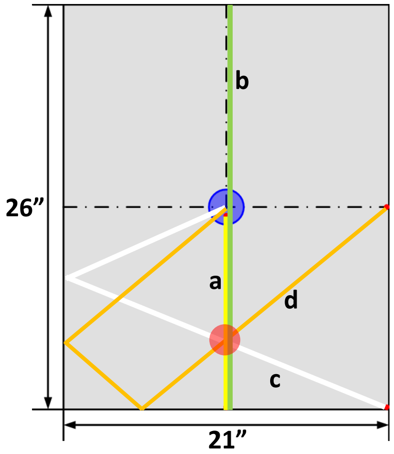

(e) Damage location estimation

Figure 4.69: Frequency averaged differential array responses of different actuator cases and damage location estimation for rubber patch case

The linear crack damage location can be estimated in the similar manner as the rubber patch case. Using the array responses in Figure 4.67(b–d) and following the damage location evaluation steps, wave propagation paths for three off-centered actuator cases may be determined for the linear crack. An intersection related to the crack damage can be determined as shown in Figure 4.70. However, in this case, some of noticeable waveform images related to the crack damage may be discarded during the process. Therefore, an additional analytical approach (i.e. ellipse construction) may be applied for the damage location evaluation. The wave propagation path corresponding to the second damage waveform image, shown in the right side of the Figure 4.71, is unable to be determined because the propagating GLW reflects not only from a geometrical boundary but also the simulated crack damage. An ellipse can be constructed as shown in Figure 4.72. The ellipse is created by using a general equation of ellipse based on ***ellipse*** = ***f***(P1,P2,L), where P1 is the EO2 actuator position, P2 is the boundary reflection position, and L is the length between the P2 and the second damage waveform image in the differential array response. By plotting the wave propagation path and the constructed ellipse in the same panel geometry, the intersection was found as shown in Figure 4.72 and it is considered as an approximate damage location. The estimated damage location agreed with the actual linear crack location. The ellipse construction approach can be also applied for the EO3 actuator case.

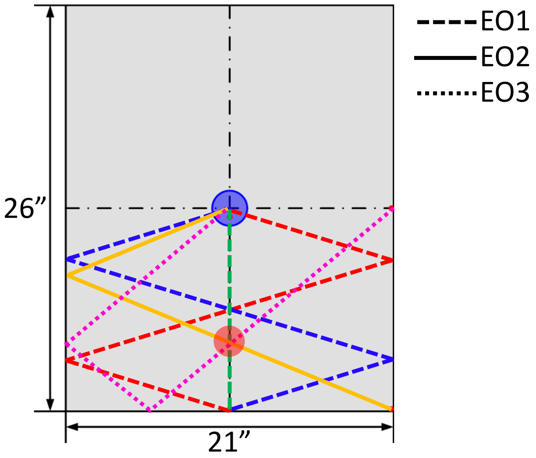

Figure 4.70: Damage location estimation for linear crack case using frequency averaged differential array responses for EO1, EO2, and EO3 actuators

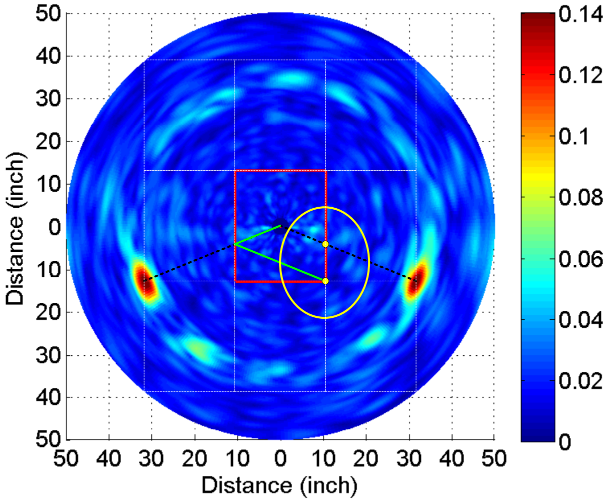

Figure 4.71: Damage location estimation based on frequency averaged differential array response of EO2 actuator case for 2 in. linear crack case

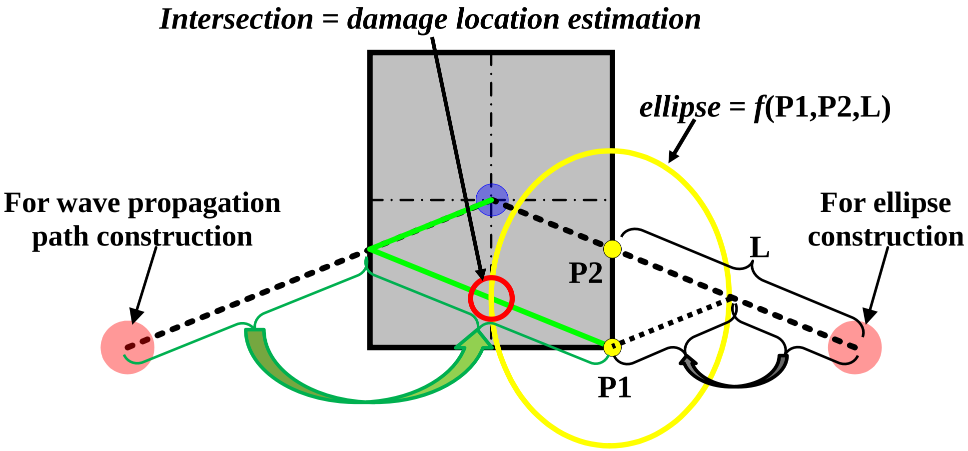

Figure 4.72: Detailed diagram of damage location estimation for 2 in. linear crack case

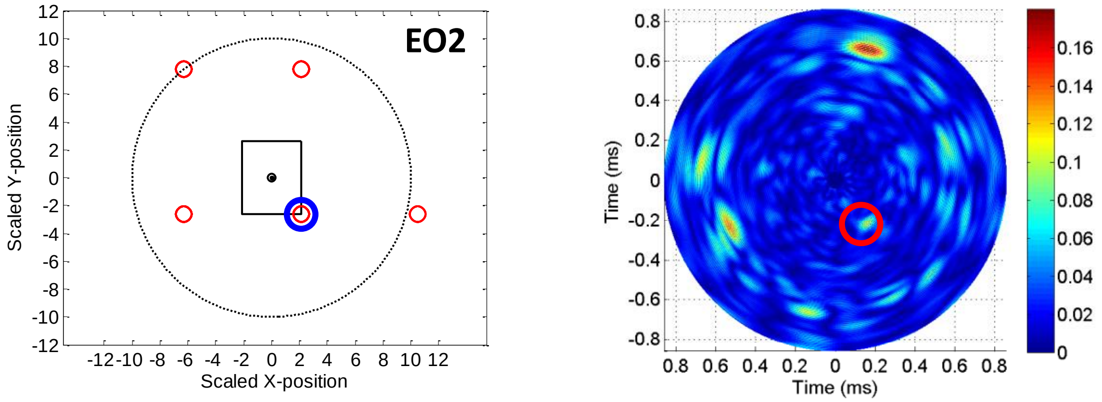

(a) Virtual source image estimation (b) Baseline

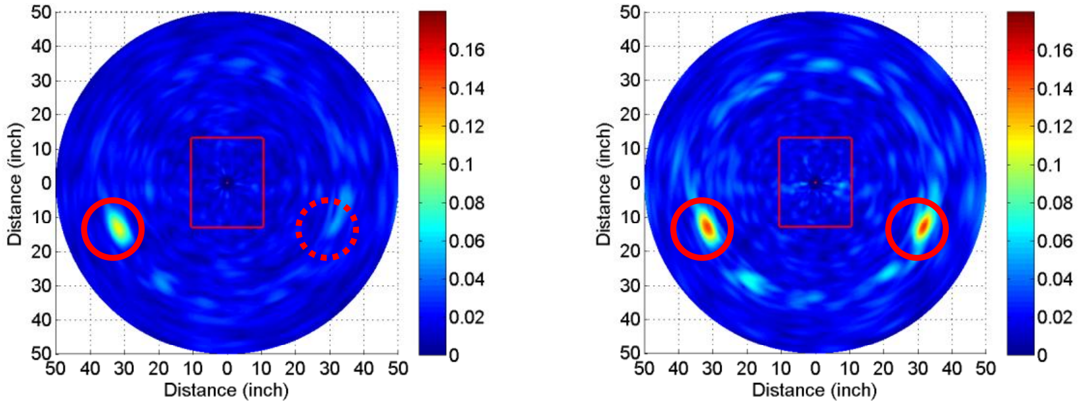

(c) Differential (for rubber patch) (d) Differential (for linear crack)

Figure 4.73: Comparison of frequency averaged array responses when using EO2 actuator

In addition, the type of damage (rubber patch or linear crack) can be distinguished by examining the differential array responses for the EO2 actuator case. Virtual source images and the frequency averaged baseline array response are shown in Figure 4.73(a) and (b), respectively. The frequency averaged differential array responses for two different damage cases are shown in Figure 4.73(c) and (d). For the rubber patch case, there was one significant waveform image in the differential array response because the propagating GLW was not strongly reflected but dissipated due to the damping properties of the rubber patch. On the other hand, there were two significant waveform images in the differential array response for the linear crack case (Figure 4.73(d)) because the propagating GLW was reflected from the crack damage and also degraded due to the damaged area in the panel. In the differential array response shown in the Figure 4.73(d), the left area circled in red was due to the wave scattering/dissipation and the other area circled in red was due to the wave reflection.

### 4.2.6 Summary and Discussions

In this section, a multi-location-actuator-based 2-D phased sensor array system was discussed to improve the damage detection capability using the 2-D phased array as a sensor system. A 2-D phased array technique using a single actuator located near the center of the array is unable to detect a linear crack, if the orientation of the crack is normal to the wavefront of the GLW excited from an actuator. In this condition, there are very weak GLW reflections from the crack damage area because most of the GLW energy is transmitting through the crack. To overcome the limitation, multiple actuators were used in this study. They are mounted at four different locations on a test panel while the 2-D phased array was instrumented at the center of the panel. A piezoceramic based 2-D phased array with a spiral configuration was used as a sensor array. The associated array signal processing was used to produce array responses and to detect two types of damages (rubber patch and crack) in the panel. An additional GLW propagation/reflection analysis technique named by ‘backward wave propagation approach’ was implemented to evaluate the damage locations within the panel geometry. From the experimental results, the estimated damage locations were in good agreement with the actual damage locations of the rubber patch and the crack. In addition, the type of damage can be distinguished by examining the final differential array responses.

## *4.3 Chapter Summary*

This chapter discussed experimental evaluations to validate the 2-D phased sensor array concept described in the previous chapter and to detect various damages in thin isotropic panels by using the array systems. The sensor array systems used the Guided Lamb wave (GLW) interrogation method to monitor structural integrity of the panels. Two types of the sensor array systems such as single-actuator-based and multi-location-actuator-based 2-D phased sensor array systems were introduced and used for damage detection tests. The main difference between the two array systems was the total number of actuators and their locations with respect to the sensor array location in the panel. In the experiments, the 2-D phased sensor arrays were made of piezoelectric paint (i.e. piezopaint) composites and piezoceramic elements. Thin 2024-T3 aluminum panels were used as testing articles and host structures mounting the 2-D phased arrays and actuators. Various damages were simulated at distributed locations of the testing panels.

First, the single-actuator-based 2-D phased sensor array system was examined to detect artificial damages (holes and a crack) simulated in aluminum panels. The sensor array system for the damage detection was consisted of 2-D phased sensor array and one actuator. The sensor array and the actuator were mounted onto the top-side and under-side of the testing panel, respectively, but they were collocated at the center of the panel. Piezopaint based 2-D phased sensor arrays were used as sensor arrays and piezoceramic elements were used as actuators. The GLW method was used to generate elastic waves in the panel structures and capture the associated wave propagation features such as reflections and transmissions. The phased array signal processing methodology (i.e. directional wavenumber filtering) described in the previous section was used to analyze the GLW signal data gathered from the arrays. The proposed signal processing technique was validated by an experimental test using an off-centered piezoceramic element and a piezopaint 2-D spiral phased array. The off-centered piezoceramic element was used as an excitation source that was obviously identified in array response result determined by the phased array signal processing method. Three piezopaint arrays with spiral, cruciform and circular configurations were used to evaluate hole damage detection tests. Among three arrays, array responses with the spiral configuration showed the hole damage locations the more effective than cruciform and circular arrays. For a crack damage test, therefore, the 2-D spiral phased array was used to detect the presence and the extent of the simulate crack damage. The array responses for the damage cases based on the spiral phased array could apparently detect the damage locations. In addition, compensation factors were studied to improve the array response results. By following innovative damage detection steps using a threshold setting and damage index (DI) calculation, the damage location and its extent could be evaluated more precisely. The DIs consistently increased as the damage (both hole and crack) grows in the panel.

Hilbert-Huang transform (HHT) amplitudes corresponding to the damage locations were explored as an additional damage detection tool.

Secondly, a multi-location-actuator-based 2-D phased sensor array system was discussed to improve the damage detection capability using the 2-D phased array as a sensor system. A 2-D phased array technique using a single actuator located near the center of the array is unable to detect a linear crack, if the orientation of the crack is normal to the wavefront of the GLW excited from the actuator. In this condition, there are very weak GLW reflections from the crack damage area because most of the GLW energy is transmitting through the crack. To overcome the limitation, multiple actuators were used in the experimental study. They are mounted at four different locations on a thin aluminum panel while the 2-D phased array was instrumented at the center of the top-side of the panel. A piezoceramic based 2-D phased array with a spiral configuration was used as a sensor array. The associated array signal processing was used to produce array responses and to detect two types of damages (rubber patch and crack) in the panel. An additional GLW propagation/reflection analysis technique named by ‘backward wave propagation approach’ was implemented to evaluate the damage locations within the panel geometry. From the experimental results, the estimated damage locations were in good agreement with the actual damage locations of the rubber patch and the crack. In addition, the type of damage can be distinguished by examining the final differential array responses.

Experimental results shown in this chapter demonstrate that the damage detection technique using the 2-D phased sensor array systems is capable of evaluating structural integrity of thin isotropic panels. Especially the 2-D spiral phased array showed the best damage detection capability among three candidate arrays including cruciform and circular arrays.

# 5. Damage Detection in Composite Panels

Laboratory evaluations were conducted in order to experimentally validate the data analysis and piezoelectric material based 2-D phased array concept. The 2-D phased arrays were constructed by using piezopaint (piezo-polymer composite) patches and piezoceramic (PZT-5A) elements. Thin 2024-T3 aluminum panels were prepared as test articles. Various damages such as holes, cracks, weights (mass), and rubber patches were simulated as artificial damages at different locations in the aluminum panel. Guided Lamb wave (GLW) method was applied to monitor structural integrity of the testing panels. Two sensor array systems based on the pulse-echo method and the pitch-catch method of the GLW interrogation were introduced and used to detect the simulated damages.

## 5.1 *Motivation and Introduction*

However, the original algorithm of the 2-D phased array signal processing is limited to apply for anisotropic panels (e.g. composite panels) because the GLW propagation speed is dependent on the material properties of the panel structures, which are closely related to the wave propagation direction in the composite panels. The original algorithm assumes that the GLW propagates omni-directionally at the same speed and the phase velocity direction is identical to the group velocity direction (i.e. wavefront curves are perfect circular shapes). On the other hand, wavefront curves in the composite panels are non-perfect circular shapes (e.g. ellipse) due to material anisotropy [24, 59, 136-138]. The GLW skew effect should be taken into account in the modification aspect of the directional wavenumber filtering algorithm. The new 2-

D phased array algorithm (for the directional wavenumber filtering) is developed by applying experimental wavenumber curves and wavefront curves into the same algorithm structure of the original 2-D phased array signal processing used for damage detection in the aluminum panels.

## *5.2 2-D Phased Sensor Array System for Orthotropic Composite Panels*

### 5.2.1 Introduction

The Figure 5.1(a) shows the fundamental assumptions of the original phased array signal processing method. In order to apply the phased array technique for composite laminates, the original signal processing method should be modified based on the configuration shown in Figure 5.1(b). The group velocity direction ($\theta - \alpha$) is not identical to the phase velocity direction ($\theta$) but the group velocity direction is normal to the wavefront in the composite laminates. In the figures, the $k$ is the wavenumber of a GLW mode coming from an excitation source.

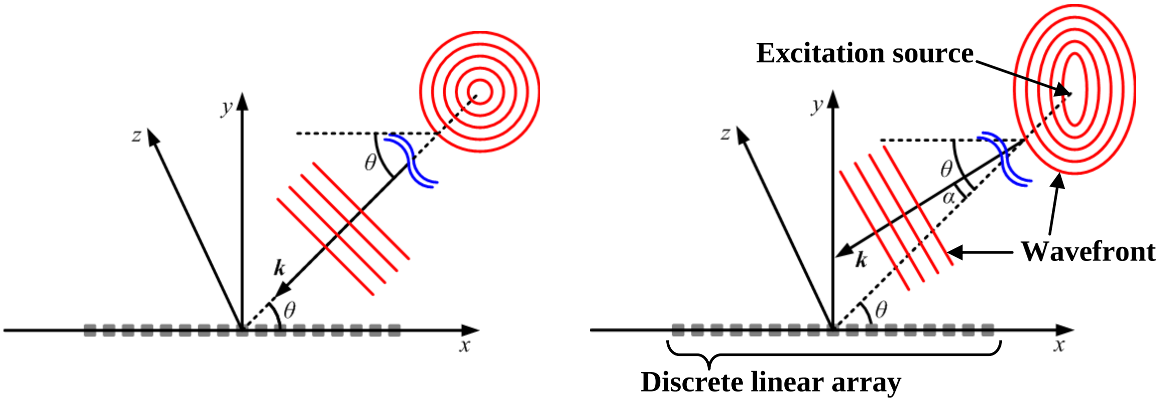

(a) Isotropic panel (b) Anisotropic panel

Figure 5.1: Plane GLW propagation in two different types of panels

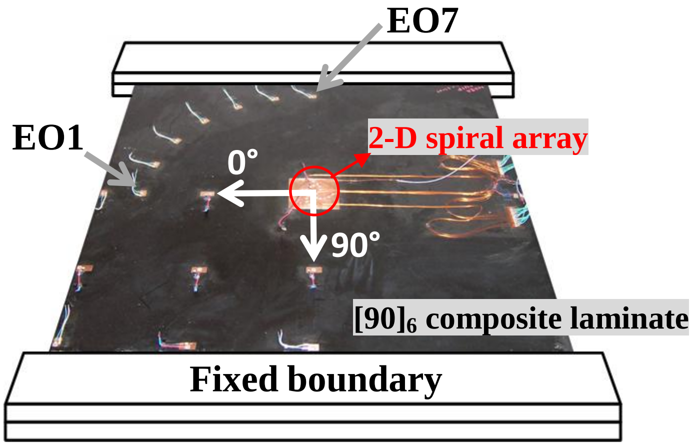

Figure 5.2: Picture of unidirectional composite panel

Table 10: Material properties of IM7/8552 composite

| $E_1$ (GPa) | $E_2$ (GPa) | $v_{12}$ | $G_{12}$ (GPa) | $\rho$ (kg/m3) |
|---|---|---|---|---|
| 170 | 11 | 0.31 | 5.0 | 1430 |

### 5.2.2 Experimental Setup with Unidirectional Composite Panel

A unidirectional composite panel was made of a carbon fiber prepreg made by Hexcel Composites. The IM7/8552 material consists of unidirectional carbon fibers (IM7) impregnated in an epoxy resin (8552) with a nominal fiber volume fraction of 57%. The properties of the material are presented in Table 10. The $E_1$ (longitudinal modulus) indicates the modulus along the fiber direction, and it is much stiffer than the $E_2$ (transverse modulus). The construction of a laminate is described by the stacking sequence of the plies where the rotation of each ply relative to the laminate axes is listed. The unidirectional composite panel was constructed by using $[90]_6$ lay-up sequences with six of the IM7/8552 plies. The two side edges of the composite panel have free boundary conditions while the top and bottom edges are fixed (Figure 5.2). In order to construct ground electrodes, thin copper sheets were bonded onto the composite panel before mounting the 2-D phased sensor array and multiple actuators.

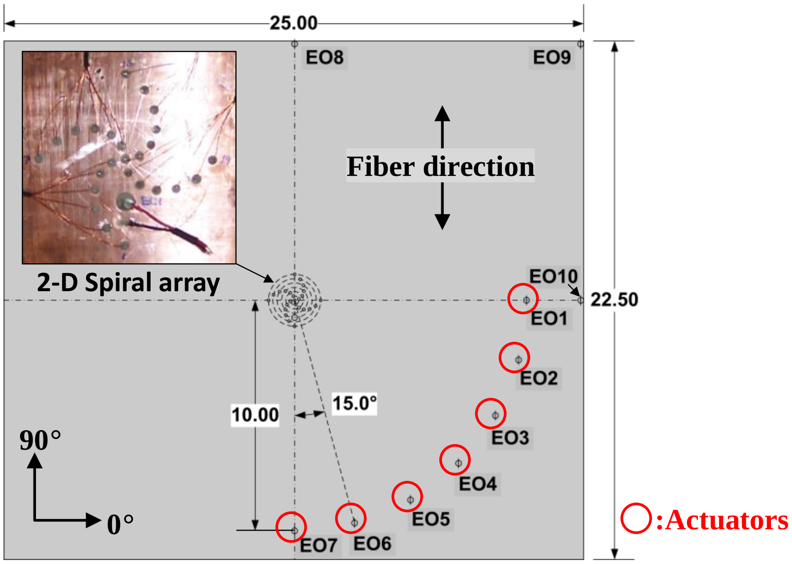

Figure 5.3: Schematic diagram of the unidirectional composite panel for the experimental testing to evaluate wave propagation characteristics

As shown in Figure 5.3, a piezoceramic based 2-D spiral phased array was instrumented at the center of the unidirectional composite panel. The spiral array was made of 25 discrete piezoceramic elements with 1/8 in. diameter. The sensor element spacing was 3/16 in. and the angular spacing was 15 deg. as shown in Figure 5.4. A quadrant of the composite panel (bottom right area) was experimentally examined with the 2-D phased array techniques in conjunction with the GLW interrogation. Seven of 1/4 in. diameter piezoceramic elements were used as off-centered excitation sources (EO1 ~ EO7), from 0 deg. to –90 deg. directions with –15 deg. increments. They were bonded 10 in. distance from the center of the spiral array.

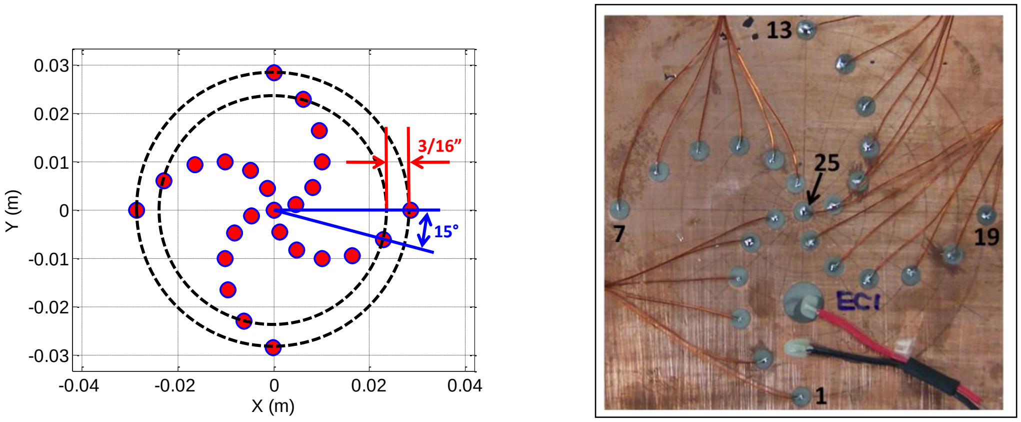

(a) Schematic diagram

(b) Picture of spiral array

Figure 5.4: Piezoceramic based 2-D spiral phased array for unidirectional laminate

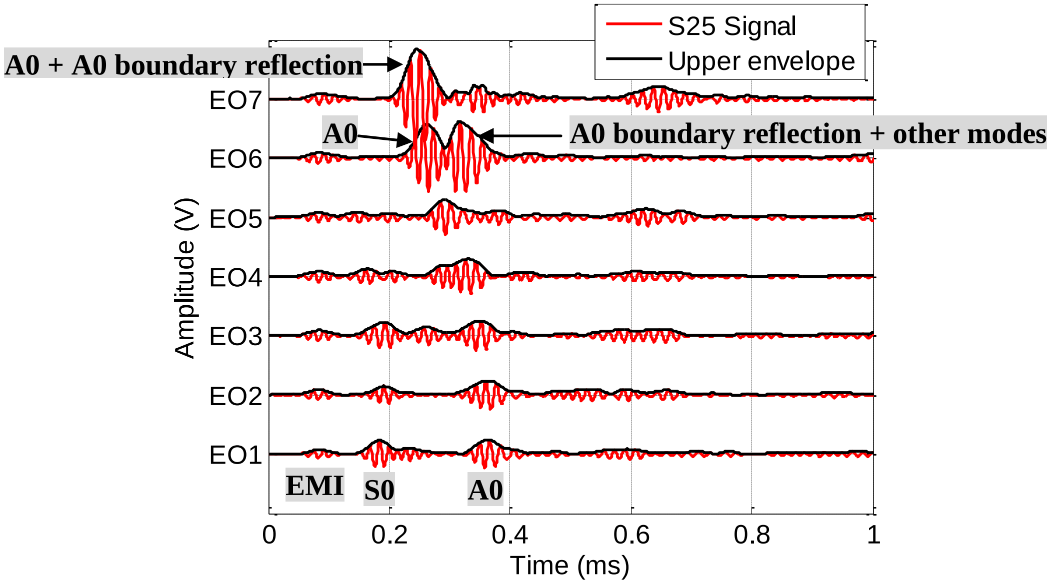

Figure 5.5: Sample sensor signals obtained from ‘S25’ sensor element as exciting EO1 ~ EO7 actuators in the unidirectional laminate (60 kHz)

Gaussian windowed tone burst signals at 60 and 80 kHz were excited from the EO1 through EO7 actuators, and the associated structural response signals were gathered from the spiral array. The groups of the array signals were processed using the original 2-D phased array signal processing algorithm to yield the array responses. As a tone burst signal at 60 kHz was excited from the EO1 through EO7 actuators, the associated sample signals obtained from the center sensor element, denoted as “S25”, of the spiral array are shown in Figure 5.5. It is found that the incident A0 mode (flexural mode) exhibits a phase lag between the S25 sensor signals due to the propagation directions of the GLW generated from the different off-centered actuators. The result is obvious because the wave propagation speed is depending on the fiber orientation (90 deg. in this study). Therefore, one can observe that the propagation speed of the A0 mode excited from the EO7 actuator was the fastest among the seven off-centered actuator cases (EO1 ~ EO7). In addition, electro-magnetic interference (EMI) noise, the S0 mode (extensional mode), and numerous boundary reflections of the GLW modes are shown in the figure of the sample signals.

### 5.2.3 Wave Propagation Characteristics in Unidirectional Composite Panel

The wavenumber of the A0 mode in the experimental sensor signals according to an excitation source may be determined by using the spatial Fourier transform with the 2-D phased spiral array. This process was repeated over the different excitation sources to evaluate directional wavenumber information (i.e. experimental wavenumber curves), which is shown in Figure 5.6(a). Solid circles in red and blue are the experimentally determined wavenumbers relative to the off-centered actuators excited at 60 kHz and 80 kHz, respectively. Due to the symmetrical quadrant properties of the unidirectional composite panel, wavenumber information for the other three quadrants is assumed to be the same as the experimentally evaluated quadrant (bottom right area). Simple cubic spline curve fitting was used to estimate the wavenumber curves (Figure 5.6(b)). In the figure, circles in red and blue are the experimental wavenumbers and the solid line in red and the dotted line in blue are the curve fitting results. This wavenumber curves will play as one of the important parameters to modify the original 2-D phased array signal processing.

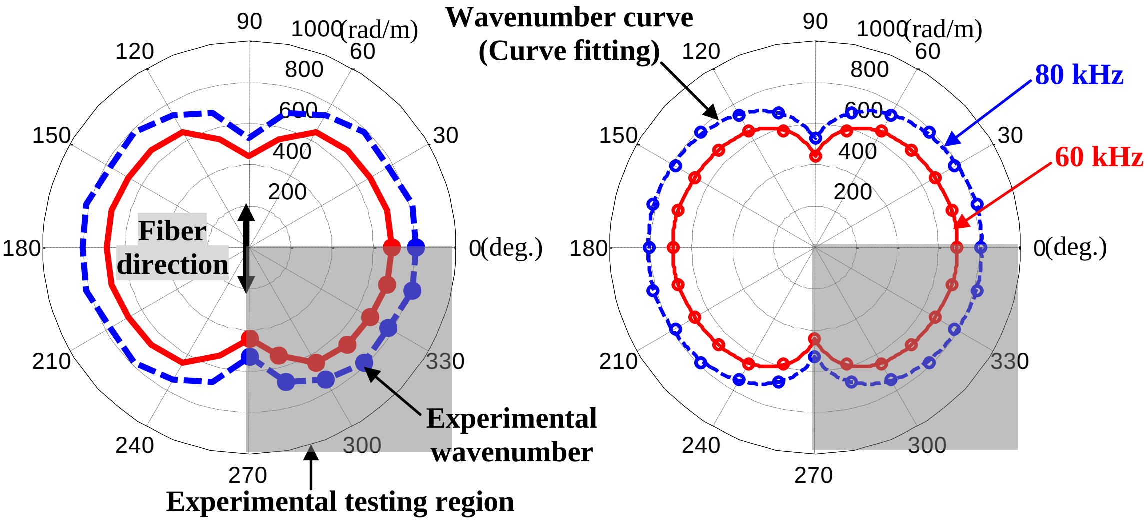

(a) Experiments

(b) Curve Fitting

Figure 5.6: Directional wavenumber curve for A0 mode of guided Lamb wave for unidirectional composite laminate

The array response results according to the various excitation sources (EO1~EO7) were produced by using the original 2-D phased array signal processing that assumes the wavefront curve is a perfect circular shape, and by using the directional wavenumber information shown in Figure 5.6(b). The maximum array response locations (circles in red) shown in Figure 5.7 are much different from the actual excitation source locations (arrows in red) because the wavefront curve in the unidirectional composite panel is not perfect circular shape.

As shown in Figure 5.8(a), the maximum array response locations were evaluated from the array responses (Figure 5.7) determined in the time domain. Due to the symmetrical quadrant properties of the unidirectional composite panel, the maximum array response locations for the other three quadrants of the testing panel are assumed to be the same as the experimentally evaluated quadrant (the highlighted area). The maximum array response locations were compensated by the actual actuators locations while maintaining the time-of-flight (TOF) information, shown in Figure 5.8(b). Because the distance between each actuator and the center of the spiral array was given as 10 in., the directional group velocity information can be determined as shown in Figure 5.8(c).

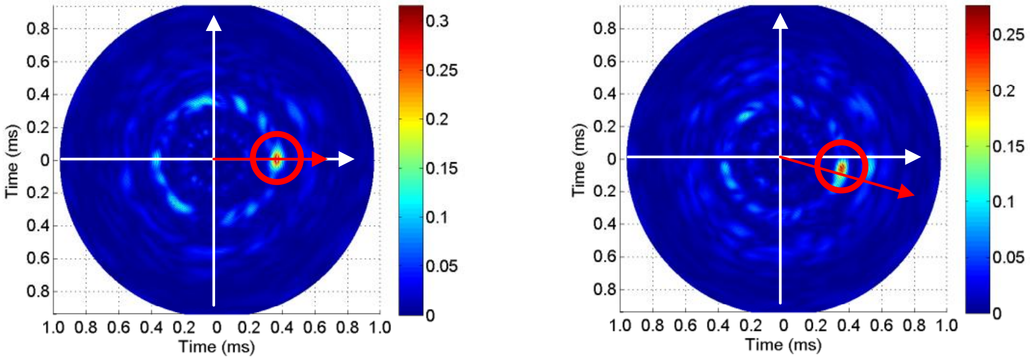

(a) EO1 actuator (0 deg.)

(b) EO2 actuator (-15 deg.)

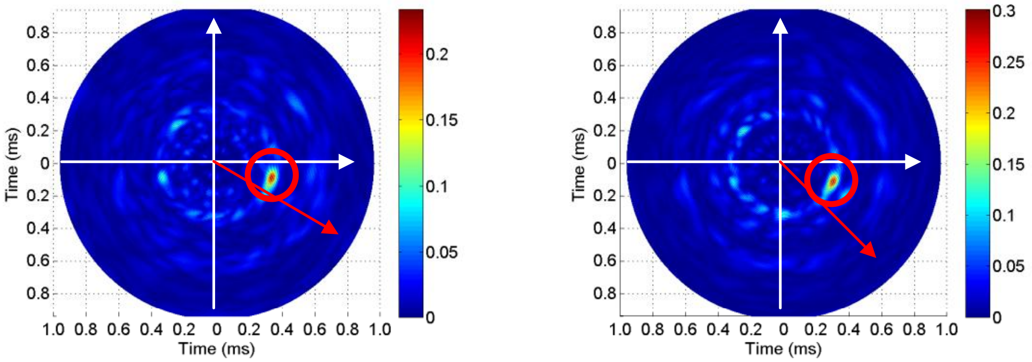

(c) EO3 actuator (-30 deg.) (d) EO4 actuator (-45 deg.)

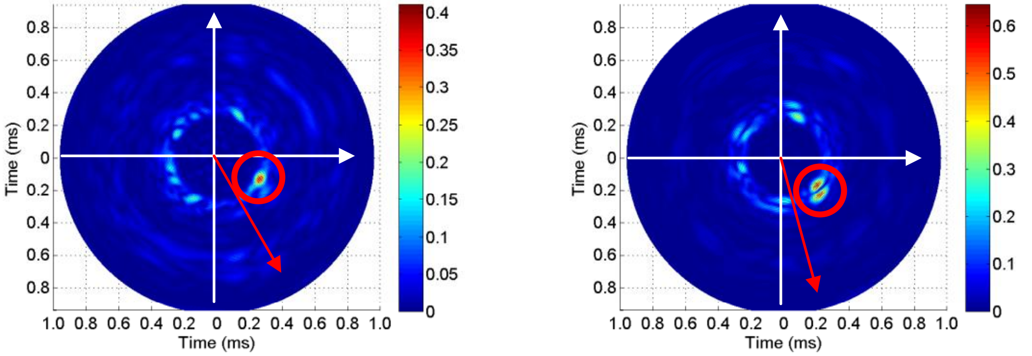

(e) EO5 actuator (-60 deg.) (f) EO6 actuator (-75 deg.)

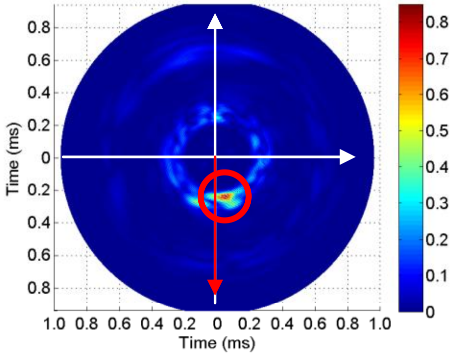

(g) EO7 actuator (-90 deg.)

Figure 5.7: Array responses using conventional wavenumber filtering approach for various off-centered excitation sources located at different directions

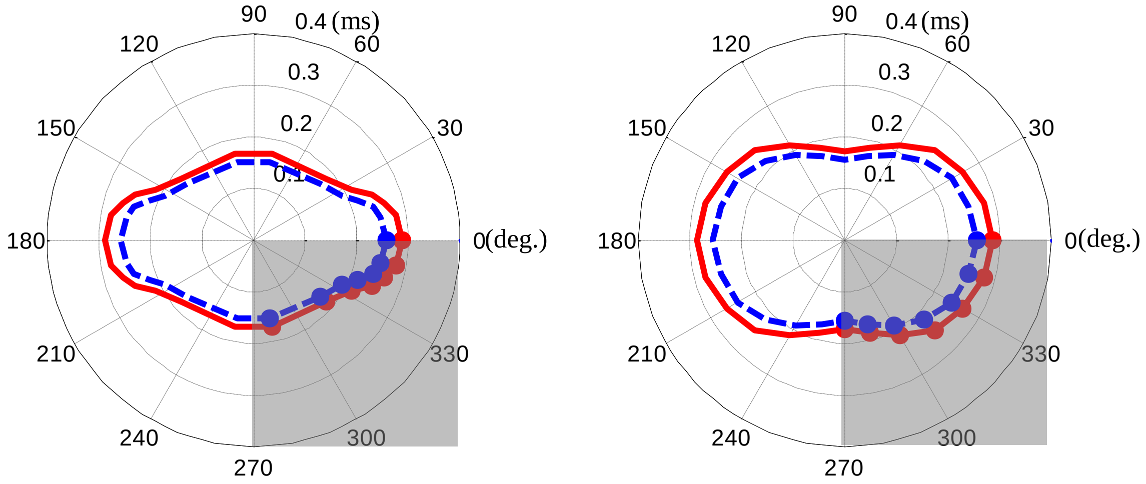

(a) Maximum array response locations (b) Compensation with actuator locations

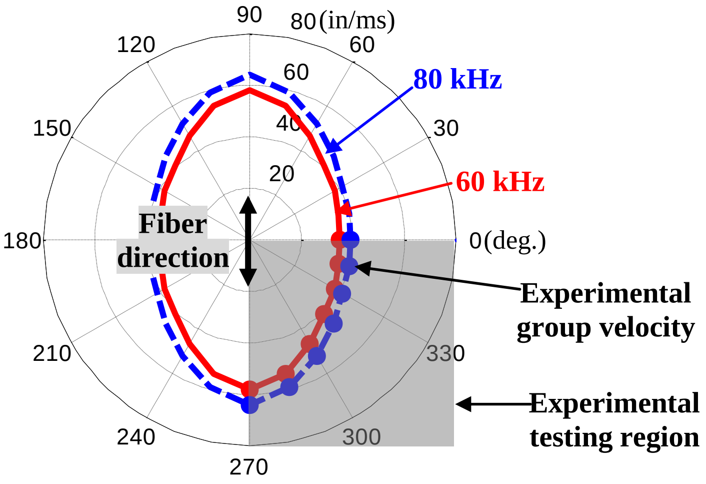

(c) Determined group velocity information

Figure 5.8: Array response results and the associated information

The wave propagation speed is depending on the directional material properties (especially stiffness) of composite panels. Therefore, one can observe that the propagation speed of the A0 mode along the fiber direction (90 deg. in this study) is much faster than normal to the fiber direction.

In order to determine simple curve fitting for the experimental group velocity results shown in Figure 5.8(c), parametric ellipses were constructed by the maximum and the minimum group velocity information, using the associated governing equation is given by

$$r(\theta) = \frac{r_1 \cdot r_2}{\sqrt{(r_2 \sin\theta)^2 + (r_1 \cos\theta)^2}} \tag{5.1}$$

where $\theta$ varies from 0 to 360 deg. In the above expression, the two main parameters ($r_1$ and $r_2$) can be defined by $r_1 = \max\left[C_g(\theta_0)\right]$ and $r_2 = \min\left[C_g(\theta_0)\right]$ where $\theta_0$ varies from 0 to 360 deg. with 15 deg. increments (i.e. the actuator spacing). An example of the ellipse construction is illustrated in Figure 5.10 and it is for the 60 kHz actuation case. The determined wavefront curves based on the parametric ellipse construction are shown in Figure 5.10. In the figure, circles in red and blue are the experimental group velocity information. The solid line in red and the dashed line in blue are the wavefront curves from the ellipse construction.

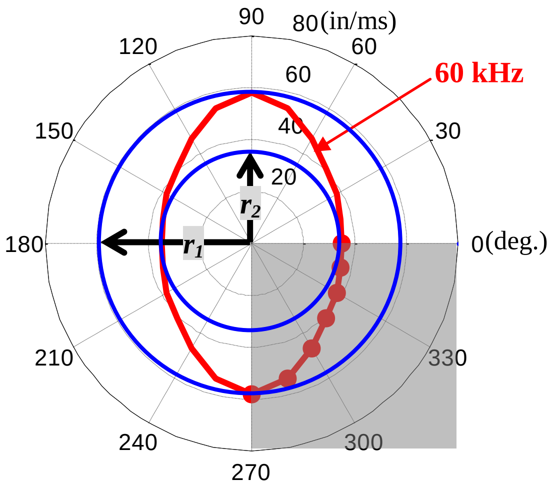

Figure 5.9: Parametric ellipse construction with group velocity information (60 kHz)

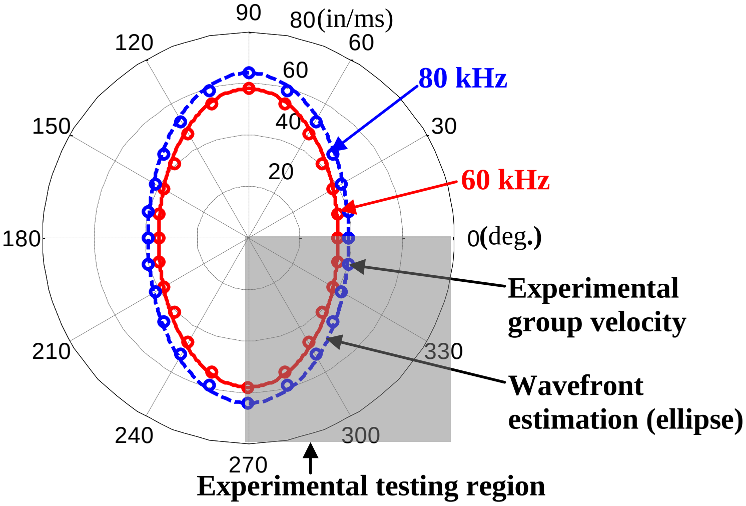

Figure 5.10: Wavefront curves with ellipse construction determined by experimental group velocity information

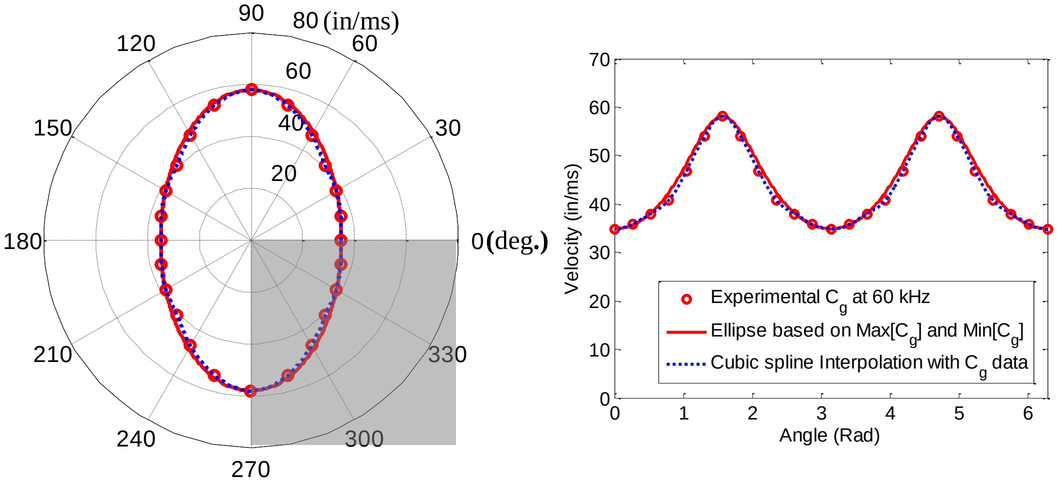

(a) Polar plot (b) Cartesian plot

Figure 5.11: Comparisons of wavefront curves constructed by parametric ellipse (solid line in red) estimation and cubic spline curve fitting (dashed line in blue) with the group velocity information (60 kHz)

An additional method to determine the wavefront curves with the experimental group velocity information is a cubic spline curve fitting. Difference between the ellipse construction and the cubic spline curve fitting can be found in Figure 5.11. The dashed line in blue is for the cubic spline, and the solid line in red is for the ellipse construction. The differential quantity between the two results can be determined by using Equation (5.2).

$$\text{Difference} = \frac{\int \left| C_g^{spline}(\theta) - C_g^{ellipse}(\theta) \right| d\theta}{\int C_g^{spline}(\theta)\, d\theta} \tag{5.2}$$

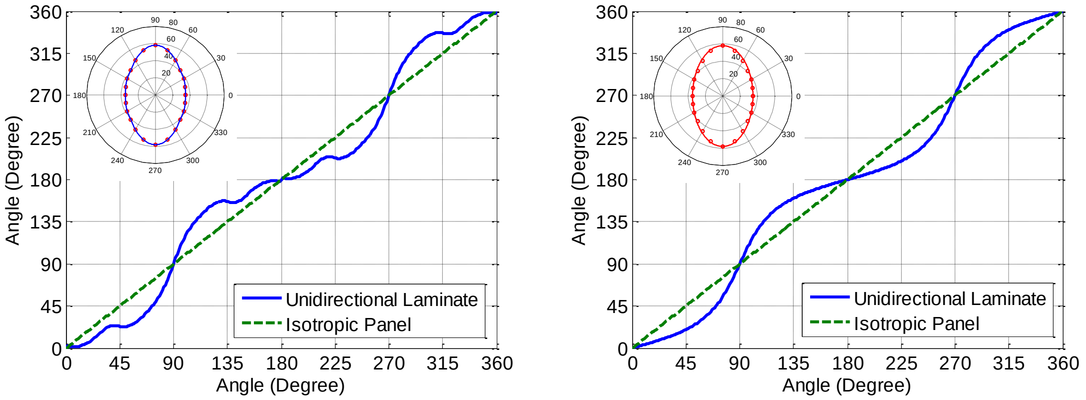

(a) From Cubic spline curve fitting

(b) From Parametric ellipse

Figure 5.12: Group velocity direction estimation with two different wavefront curves (60 kHz)

The differential quantities for 60 kHz and 80 kHz cases were 0.0167 and 0.0188, respectively. Because the differentials between the two methods are so trivial, there is no problem which method is used to determine the wavefront curves. However, when we evaluate group velocity direction that is normal to the wavefront curve, it is a different story. The group velocity directions for 60 kHz actuation case were determined as shown in Figure 5.12. The group velocity direction result determined by the cubic spline curve fitting (Figure 5.12(a)) demonstrates a problem of the determined wavefront curve. The result (blue line in Figure 5.12(a)) shows a flat or negative slope in some angular directions. It must be a problem for the 2-D phased array signal processing as virtually steering the array. On the other hand, the result from the ellipse construction (Figure 5.12(b)) shows no flat or negative slope in all of the angular direction. Therefore, the parametric ellipse construction method was used to determine the wavefront curves with the experimental group velocity information.

Using the experimentally determined wavenumber curves (Figure 5.6(b)) and the wavefront curves (Figure 5.10), the original phased array signal processing method could be modified and the new signal processing method can be developed. As a result, the governing equations of the spatial weighting function (Equation (3.17)) should be modified as below.

$$\begin{aligned}\phi_R(x_n, y_n, \theta) &= \cos\big(x_n\bar{k}(\theta)\cos\big(\theta-\alpha(\theta)\big) + y_n\bar{k}(\theta)\sin\big(\theta-\alpha(\theta)\big)\big)\\ \phi_I(x_n, y_n, \theta) &= \sin\big(x_n\bar{k}(\theta)\cos\big(\theta-\alpha(\theta)\big) + y_n\bar{k}(\theta)\sin\big(\theta-\alpha(\theta)\big)\big)\end{aligned} \tag{5.3}$$

In above expression, $\bar{k}(\theta)$ and $\alpha(\theta)$ may be defined from the experimental wavenumber and wavefront curves, respectively.

Figure 5.13(a) shows the maximum value locations of the array responses for the seven off-centered excitation source cases, by using the original phased array signal processing method. The figure is identical to the Figure 5.8(a). On the other hand, the maximum value locations of the array responses shown in Figure 5.13(b) were determined by using the new method using the information of the wavenumber and wavefront curves. By comparing the Figure 5.13(b) with the Figure 5.13(a), one can notice that the array response results were improved to identify the excitation sources. The Figure 5.13(b) shows the more reliable correlation between the maximum array response locations and the actual excitation source locations, than the maximum array response locations in the Figure 5.13(a). However, there are still directional errors in the array response results with the new algorithm, due to the inaccuracy of the curve fitting method for the wavenumver curves and the negative aspect of the ellipse construction for the wavefront curves.

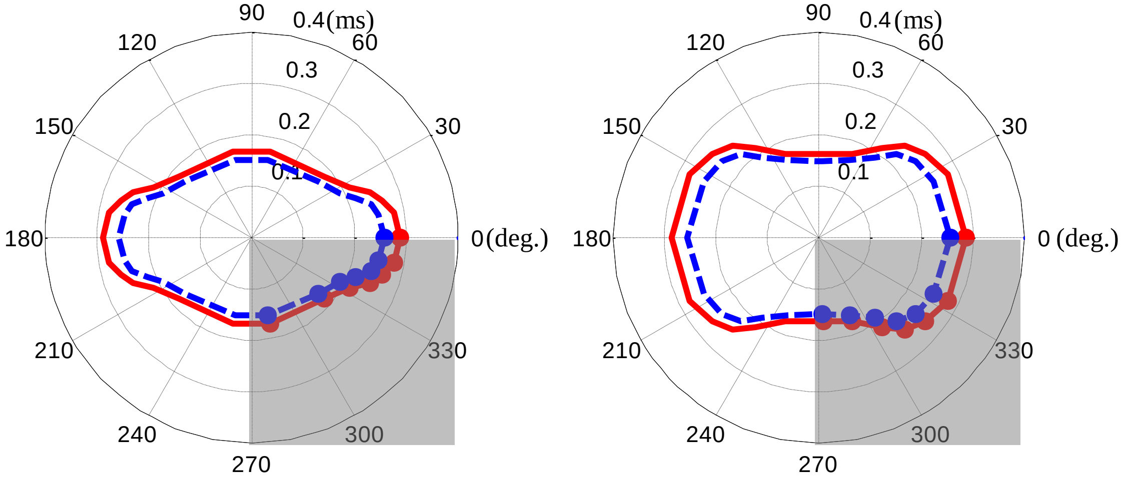

(a) with Original method

(b) with New method

Figure 5.13: Comparison of maximum array response locations using two different methods of 2-D phased array signal processing (for unidirectional composite panel)

### 5.2.4 Damage Detection Test of Unidirectional Composite Panel

It is observed that one single actuator positioned at the center of the testing panel was insufficient to detect simulated damages due to the characteristics of the unidirectional composite panel, like high attenuation factor and significant wave energy variation of the A0 mode according to the propagation directions within the composite panel. Therefore, three 1/4 in. diameter piezoceramic elements were bonded on the same composite panel, and used as off-centered actuators (EO8, EO9, and EO10 shown in Figure 5.14) for damage detection tests. Similar to the previous test (i.e. the experimental test for 2-D phased array algorithm modification), Gaussian windowed tone burst signals at 60 and 80 kHz were excited from the EO8 through EO10 actuators, and the spiral array captured the GLW signals traveling in the composite panel. The structurally responded GLW signals were processed with the new 2-D phased array signal processing algorithm, and produced baseline array responses (for no damage cases) and damage array responses.

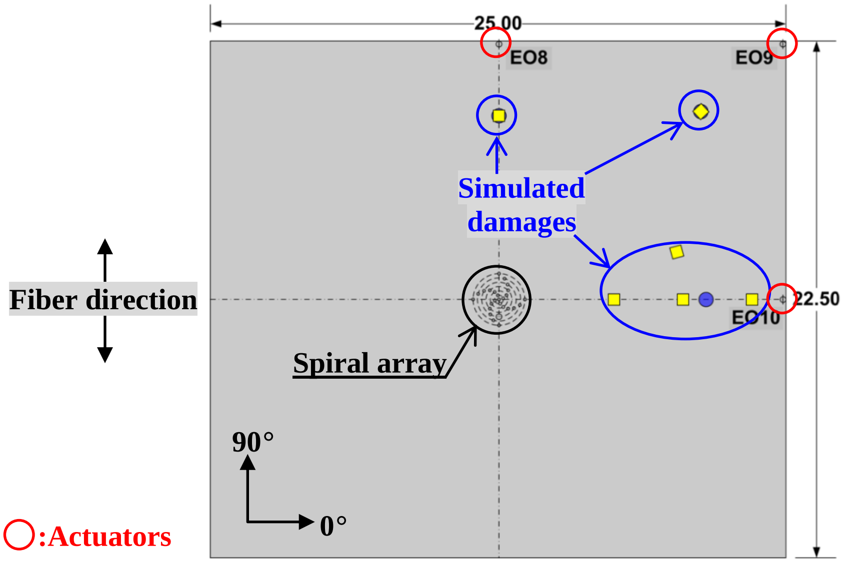

Figure 5.14: Schematic diagram of the unidirectional laminate for the experimental testing of damage detection

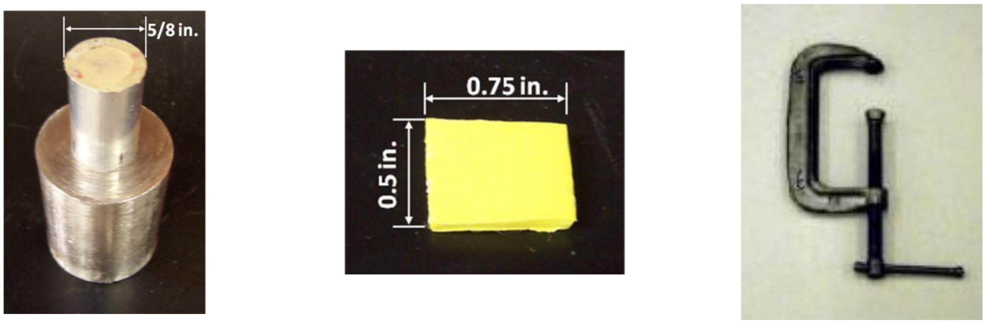

(a) Weight (~300g) (b) Rubber patch (c) C-clamp

Figure 5.15: Pictures of simulated damages

Table 11: Damage type and location according to actuator (for unidirectional laminate)

| Actuator | Damage Type | Damage Location[a] | Index |
|---|---|---|---|
| EO8 | Rubber patch[b] | 8 in. at 90 deg. | UL_EO8_D1 |
| | Weight[c] | 8 in. at 90 deg. | UL_EO8_D2 |
| EO9 | Rubber patch | 12 in. at 43 deg. | UL_EO9_D1 |
| | Clamp[d] | 12 in. at 43 deg. | UL_EO9_D2 |
| EO10 | Rubber patch | 8 in. at 15 deg. | UL_EO10_D1 |
| | Clamp | 9 in. at 0 deg. | UL_EO10_D2 |
| | Rubber patch | 5 in. at 0 deg. | UL_EO10_D3 |
| | Rubber patch | 8 in. at 0 deg. | UL_EO10_D4 |
| | Rubber patch | 11 in. at 0 deg. | UL_EO10_D5 |

[a] from the center of the spiral array to the simulated damage
[b] with 3/4 in. width and 1/2 in. length
[c] with 5/8 in. diameter surface contact area and about 300 g
[d] with a C-shape clamp

Various damages (Figure 5.15) such as rubber patches, clamps, and weights were simulated on the composite panel. The detailed information relative to the damage case is shown in Table 11.

### 5.2.5 Damage Detection Results

Array responses were produced by using the new 2-D phased array signal processing algorithm for the various damages according to the three actuator cases. Differential array responses were reproduced by subtracting the damage array responses from the baseline array responses (no damage cases). The differential array responses are shown in Figure 5.16 (for the EO8 actuator case), in Figure 5.17 (for the EO9 actuator case), and in Figure 5.18 (for the EO10 actuator case).

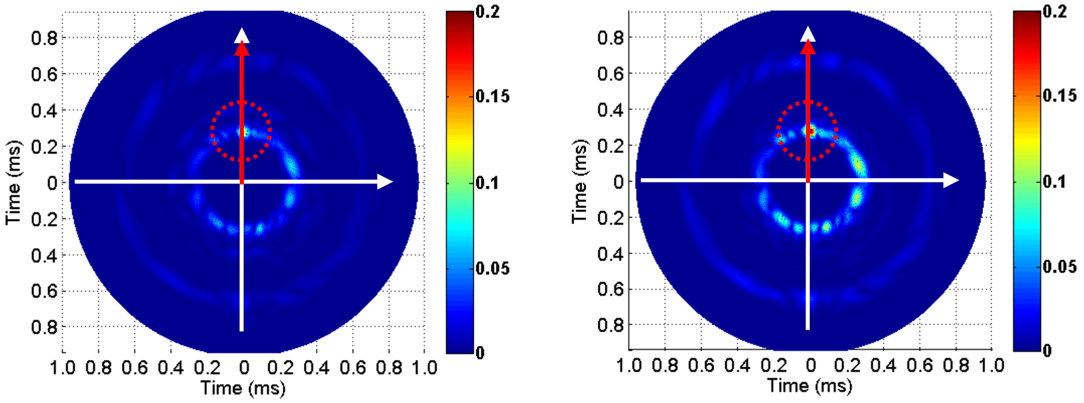

(a) UL_EO8_D1

(b) UL_EO8_D2

Figure 5.16: Differential array response for EO8 actuator case (60 kHz)

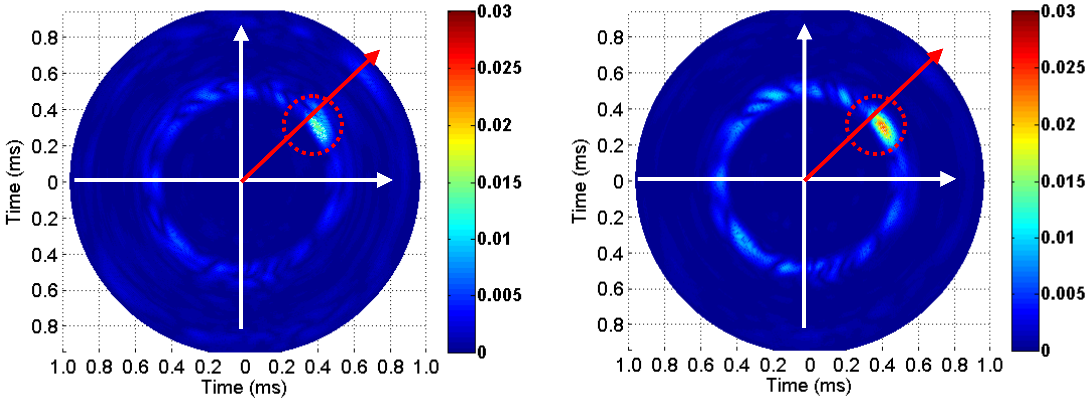

(a) UL_EO9_D1

(b) UL_EO9_D2

Figure 5.17: Differential array response for EO9 actuator case (60 kHz)

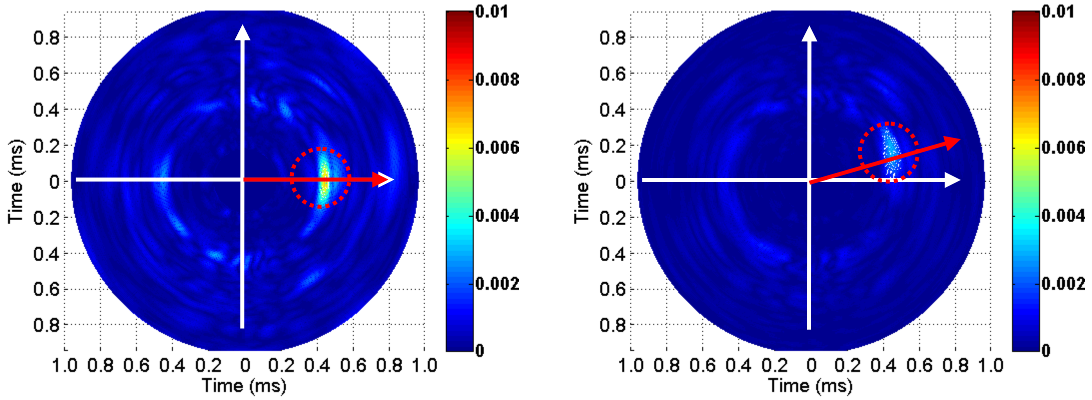

(a) UL_EO10_D1

(b) UL_EO10_D2

Figure 5.18: Differential array response for EO10 actuator case (60 kHz)

In the figures, the red arrows indicate the actual directions of the simulated damages, and the dotted circles in red are the estimated damage locations in the differential array responses (in the time domain). The differential array response results note that there are small directional errors to identify the simulated damages in the results, but the estimated damage locations (waveform images with high intensity) in the array responses are generally in good agreement with the actual damage locations.

In the differential array responses of the Figure 5.16 through Figure 5.18, there are a few considerable waveform images except for the waveform images (within the red rotted circles). The waveform images are the negative filtering effect due to the side lobes of the directivity function for the spiral array, and they are relative to the waveform images with the highest intensity in the array responses. The limitation of the filtering capability with the 2-D spiral phased array can be improved by increasing the total number of the sensor elements or changing the sensor distribution layout.

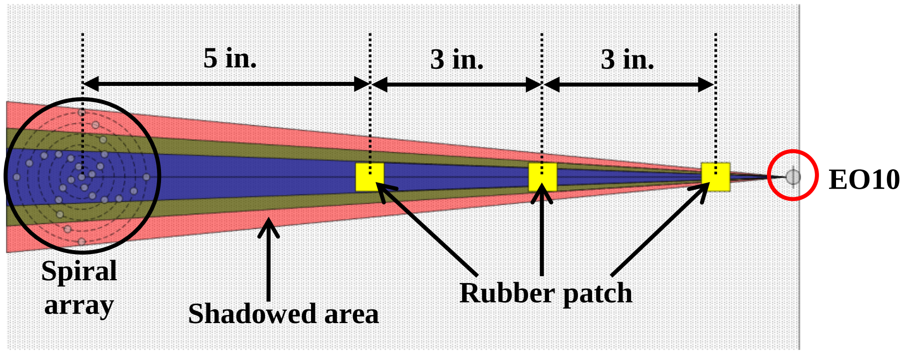

Figure 5.19: Shadowed area due to rubber patch as using EO10 actuator

Figure 5.19 shows a schematic diagram of an additional damage detection test with the current experimental set-up. The EO10 actuator was used to generate the GLWs from the right side edge of the composite panel, and the artificial damage (rubber patch) location was changed. The differential array response results in Figure 5.20 show that the maximum value of the array response increases as the rubber patch comes close to the excitation source (EO10), because the blind area (denoted as "shadowed area") of the phased sensor array increases due to the location variation of the rubber patch as shown in Figure 5.19. The shadowed area colored in red includes the green and blue areas, and the shadowed area in green includes the blue area. The array response results note that the rubber patch disturbed the GLW propagation and the wave energy coming from the excitation source dissipated.

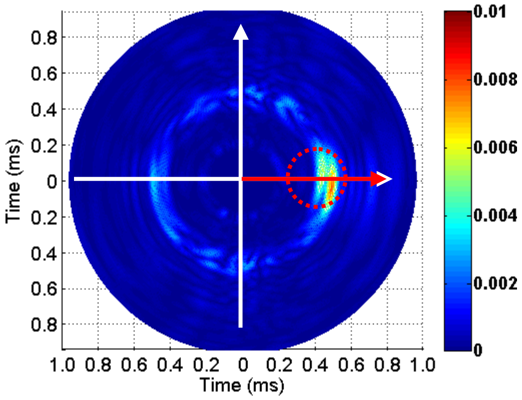

(a) UL_EO10_D3

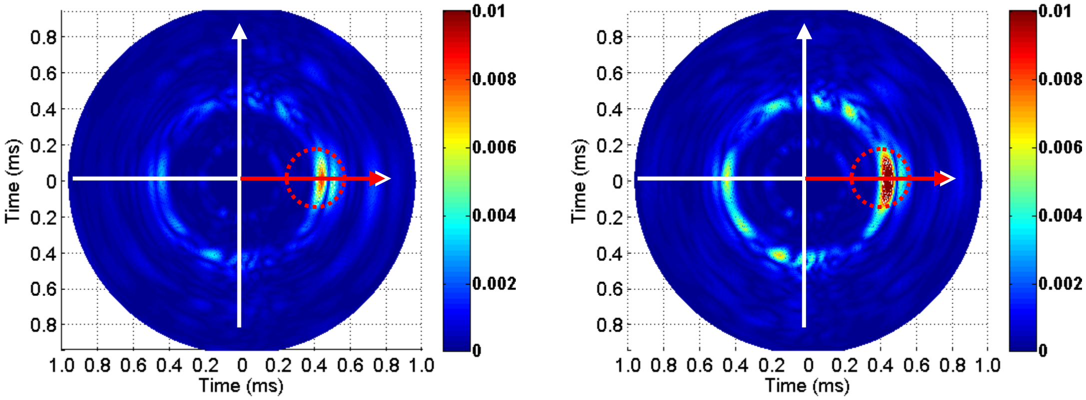

(b) UL_EO10_D4

(c) UL_EO10_D5

Figure 5.20: Differential array response result (with EO10 actuator) for rubber patches on various positions at 0 deg. direction

The relationship between the shadowed areas and the maximum values of the differential array responses was evaluated in Figure 5.21. The result shows that the maximum value of the differential array response consistently increases as the shadowed area expands.

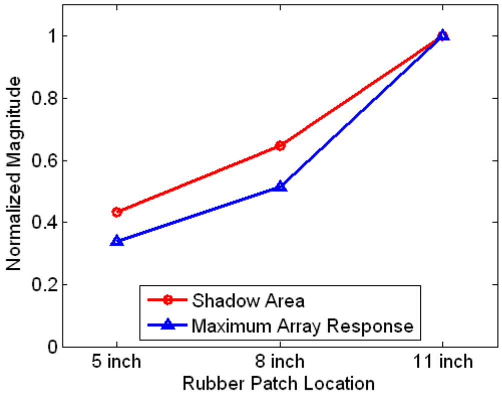

Figure 5.21: Normalized magnitude comparison between shadowed areas and maximum values of array responses for rubber patch cases

### 5.2.6 Experimental Setup with Cross-ply Composite Panel

As the same manner to the previous unidirectional composite pane, a cross-ply composite panel was made of IM7/8552 unidirectional tape with $[90/0/90/90]_{sym}$ lay-up sequences. The composite panel was under fixed-free boundary conditions. Two boundary edges (right and left edges) for the panel were fixed. In order to construct ground electrodes, thin copper sheets were bonded onto the composite laminates before mounting the 2-D sensor array and multiple actuators. As shown in Figure 5.22, piezoceramic-based 2-D spiral phased arrays were instrumented at the center of the composite panel. The spiral array was made of 25 discrete PZT elements with 1/8 in. diameter. The array sensor element spacing was 3/16 in. and the angular spacing was 15 deg. as shown in Figure 5.4(a). A quadrant of the composite laminate was experimentally examined with the 2-D phased array technique in conjunction with the GLW interrogation. Seven PZT elements with 1/4 in. diameter were used as off-centered GLW actuators. They are denoted by EO1 through EO7 in Figure 5.23. They were bonded at 10 in. distance location from the center of the spiral array, and the angular spacing of the actuators was 15 degrees. Gaussian windowed tone burst signals at 60 kHz and 80 kHz were excited from the EO1 through EO7 actuators, and the associated structural response signals were gathered from the spiral array. The groups of the array signals were processed using the original 2-D phased array signal processing method to yield array responses.

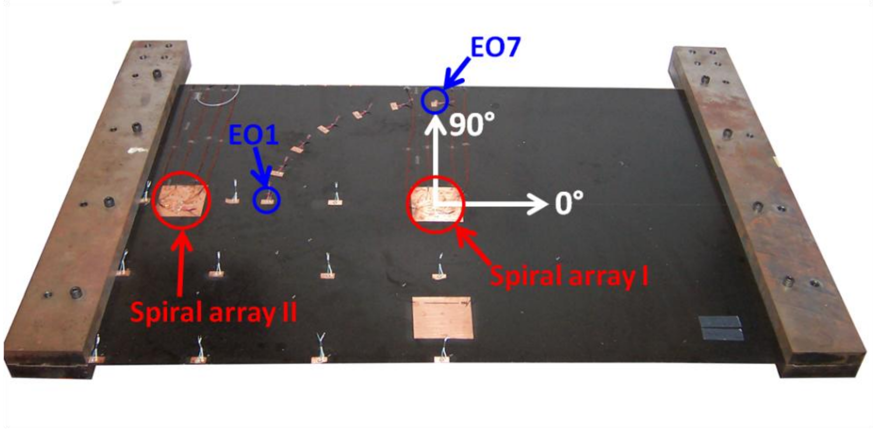

Figure 5.22: Instrumented cross-ply composite panel

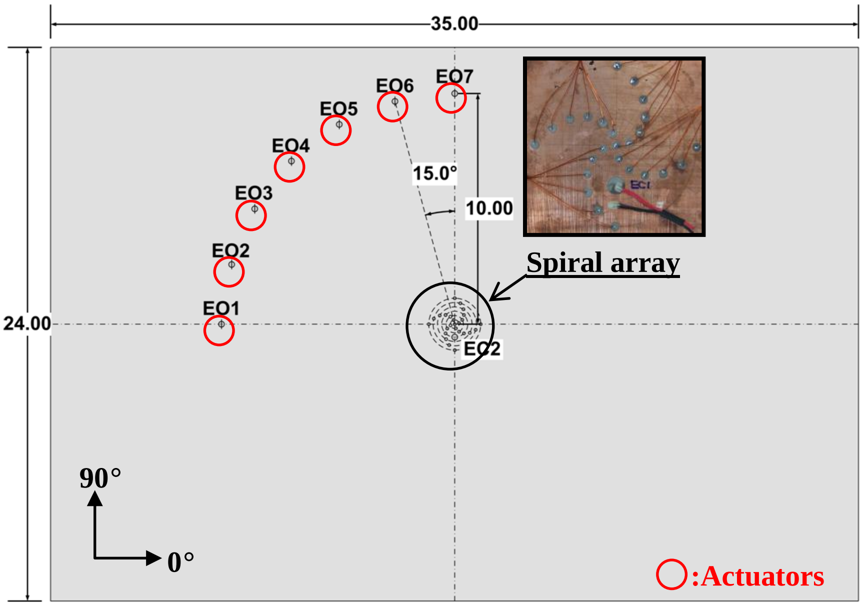

Figure 5.23: Schematic diagram of the cross-ply composite panel for the experimental testing to evaluate wave propagation characteristics

### 5.2.7 Wave Propagation Characteristics in Cross-ply Composite Panel

The wavenumber of the A0 mode in the experimental sensor signals according to an actuator may be determined by using the spatial Fourier transform with the spiral array configuration and the associated sensor signals. This process was repeated over the different actuators (EO1 ~ EO7) to evaluate directional wavenumber information. Due to the symmetrical quadrant properties of the composite laminates, wavenumber information for the other three quadrants is assumed to be the same as the experimentally evaluated quadrant. In the Figure 5.24, small circles in blue and in red are the experimental wavenumbers according to the off-centered actuators excited at 60 kHz and 80 kHz, respectively. And the dotted line in blue and the solid line in red are Cubic Spline curve-fitting results. The curve-fitting results are used as experimental wavenumber curves. In the figures, the highlighted areas are the experimental testing quadrants.

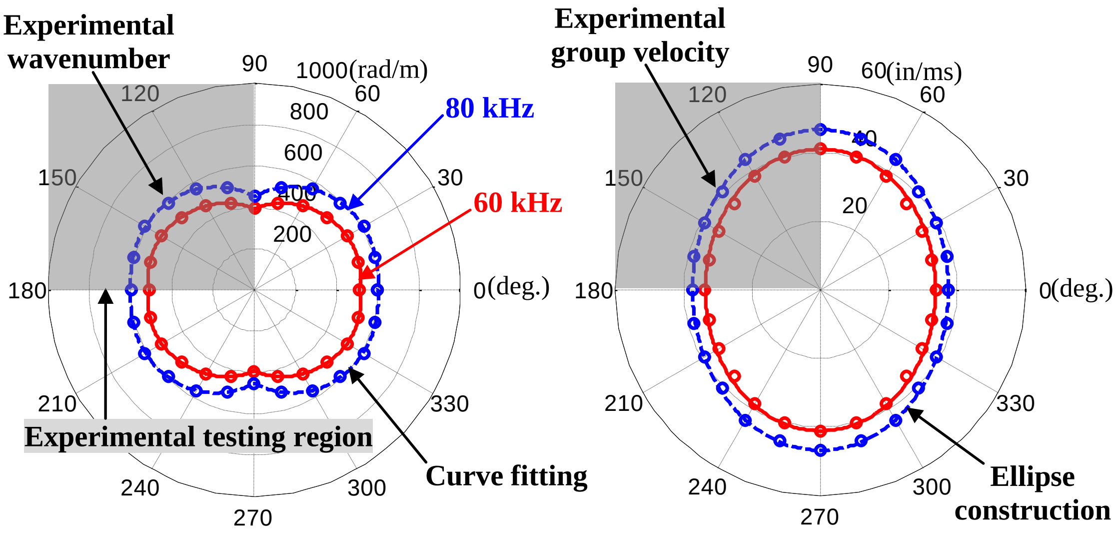

(a) Wavenumber curves (b) Wavefront curves

Figure 5.24: Modification features for new 2-D phased array algorithm for a cross-ply composite panel

Figure 5.25(a) shows the maximum value locations of the array responses for the seven off-centered excitation source cases (EO1 ~ EO7), by using the original phased array signal processing method. On the other hand, the maximum value locations of the array responses shown in Figure 5.25(b) were determined by using the new method using the information of the wavenumber and wavefront curves shown in Figure 5.24. By comparing the Figure 5.25(b) with the Figure 5.25(a), one can notice that the array response results were improved to identify the excitation sources. The Figure 5.25(b) shows the more reliable correlation between the maximum array response locations and the actual excitation source locations, than the maximum array response locations in the Figure 5.25(a). However, there are still directional errors in the array response results with the new algorithm, due to the inaccuracy of the curve fitting method for the wavenumber curves and the negative aspect of the ellipse construction for the wavefront curves.

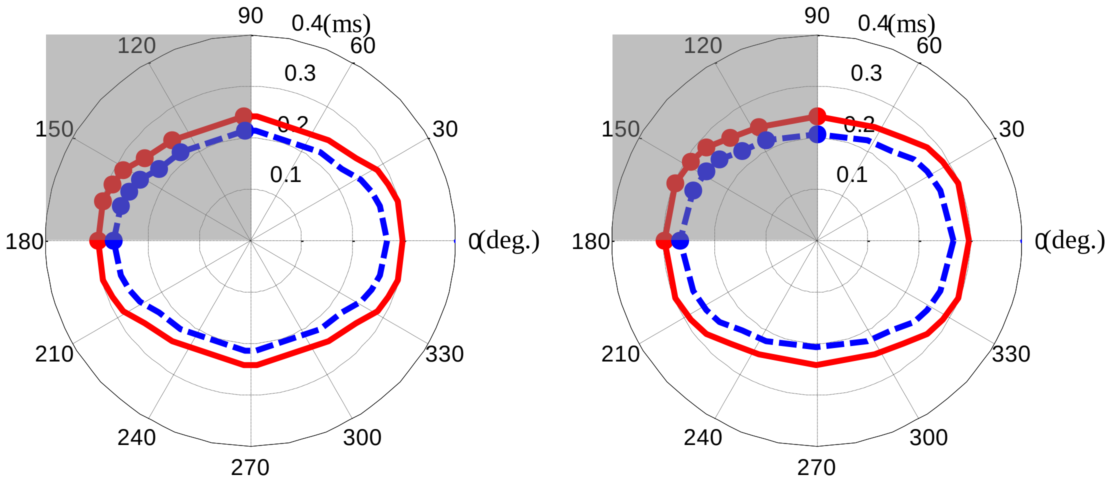

(a) with Original method

(b) with New method

Figure 5.25: Comparison of maximum array response locations using two different methods of 2-D phased array signal processing (for cross-ply composite panel)

### 5.2.8 Damage Detection Test of Cross-ply Composite Panel

The new method of the 2-D phased array signal processing was applied to damage detection of the cross-ply composite panel. An additional spiral array (denoted ‘Spiral array II’) was mounted on the same composite panel as the previous wave propagation characteristics evaluation test. The schematic diagram of the testing panel is shown in Figure 5.26. The distance between two spiral arrays was 15 in. The main reason to use two phased array systems for this study is because one can simply find damage locations based on the array response results determined by the two array systems and the method of vector-based damage localization [139]. The vector-based damage localization will be discussed in the later subsection. Unlike the damage detection tests of the unidirectional composite panel, two 1/4 in. diameter piezoceramic elements were used as actuators denoted by ‘EC1’ and ‘EC2’. It is because there is insignificant wave energy variation of A0 mode according to the propagation directions within the composite panel (Figure 5.27). Each actuator was positioned and bonded within the 2-D spiral phased array to collocate the actuator with the receiver (spiral array), shown in Figure 5.26. Gaussian windowed tone burst signals at 60 and 80 kHz were excited from the EC1 and EC2 actuators, and the spiral arrays captured the GLW signals traveling in the composite panel. The structurally responded GLW signals were processed with the new 2-D phased array signal processing method, and produced baseline array responses (for no damage cases) and damage array responses. Artificial weight damages were simulated at six different locations of the composite panel, shown in Figure 5.26. The detailed information relative to individual damage case is described in Table 12.

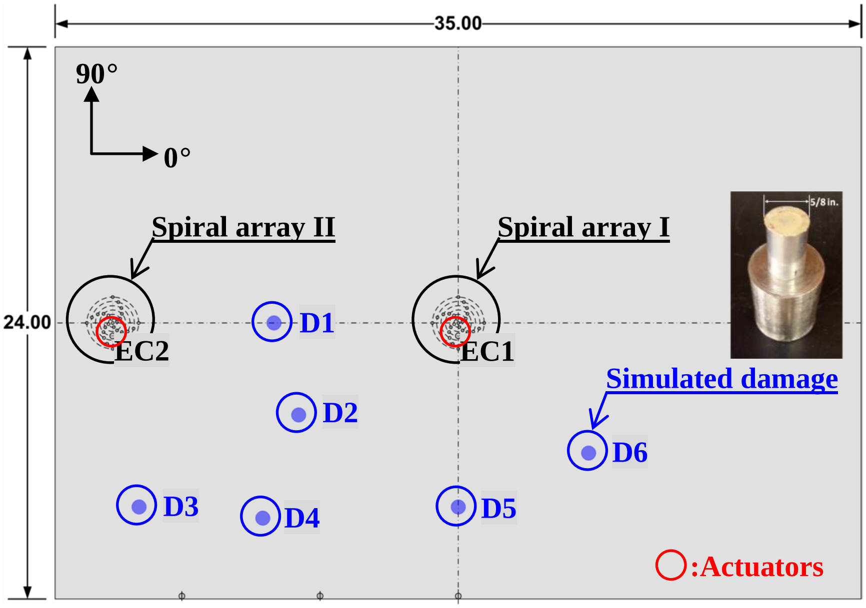

Figure 5.26: Schematic diagram of the cross-ply composite panel for the experimental testing for damage detection

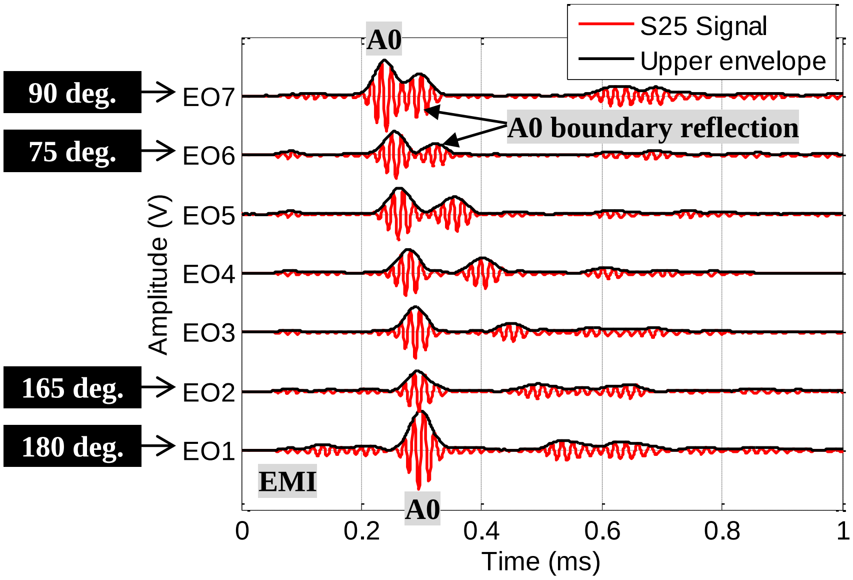

Figure 5.27: Sample sensor signals obtained from ‘S25’ sensor element as exciting EO1 ~ EO7 actuators in the cross-ply laminate (60 kHz)

Table 12: Damage type and location according to actuator (for cross-ply laminate)

| Actuator | Receiver | Damage Type | Damage Location[a] | Index |
|---|---|---|---|---|
| EC1 | Spiral array I[b] | Weight[c] | 8 in. at 180 deg. | CL_EC1_SA1_D1 |
| | | | 8 in. at 210 deg. | CL_ EC1_ SA1_D2 |
| | | | 12 in. at 225 deg. | CL_ EC1_SA1_D4 |
| | | | 8 in. at 270 deg. | CL_ EC1_ SA1_D5 |
| | | | 8 in. at 315 deg. | CL_ EC1_SA1_D6 |
| EC2 | Spiral array II[d] | Weight | 8 in. at 180 deg. | CL_EC2_SA2_D1 |
| | | | 8 in. at 210 deg. | CL_ EC2_ SA2_D2 |
| | | | 16 in. at 210 deg. | CL_ EC2_ SA2_D3 |
| | | | 12 in. at 225 deg. | CL_ EC2_SA2_D4 |

[a] from the center of the cross-ply composite panel to the simulated damage
[b] Spiral array I is located at the center of the cross-ply composite panel
[c] with 5/8 in. diameter surface contact area and about 300 g
[d] Spiral array II is located at 15 in. horizontal distance from Spiral array I

Figure 5.28 shows damage detection coverage areas with two spiral array systems. In the figure, the damage detection coverage areas (dashed-line circle in red and solid-line circle in blue) were determined by the standard equation to construct ellipses (Equations (2.53)). The locations of spiral arrays and actuators were used for the foci of the ellipses, and wave propagation distance was used as an additional parameter for the equation. The damage detection coverage areas seem like circle shapes because the locations of the two foci are almost collocated. In this study, the wave propagation distance was determined by the length of the composite panel. There are strong wave reflections from geometrical edges of a panel structure. Due to the wave reflections, array response produced by phased array signal processing may include unwanted waveform images relative to the wave reflections. The unwanted waveform images are present in the array response results because the directivity function for the 2-D spiral array has negative effect of side lobes. Based on the result shown in Figure 5.28, the damage detection test was divided into three parts: first, damage detection using “Spiral array I” and “EC1” actuator; second, damage detection using “Spiral array II” and “EC2” actuator; third, vector-based damage localization test for the intersection area between the two circles (actually, they are ellipses).

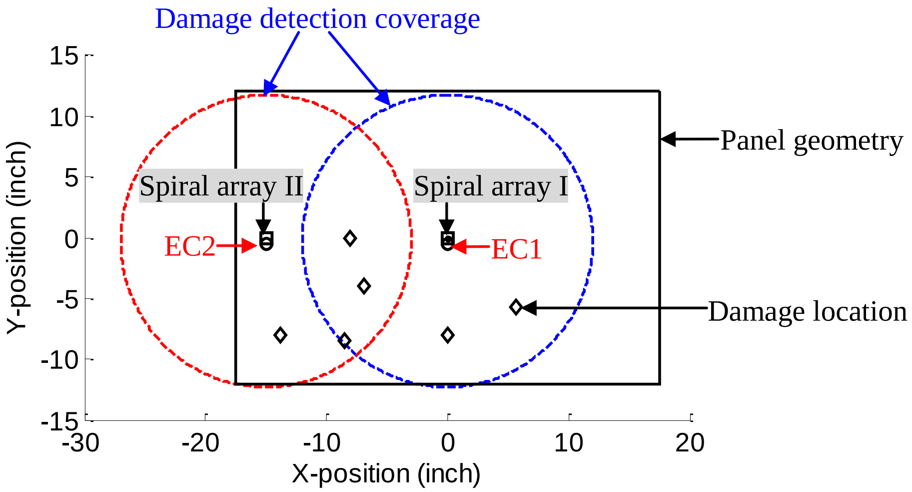

Figure 5.28: Estimation of damage detection coverage for proposed sensor system using ‘Spiral array I’ with EC1 actuator and Spiral array II’ with EC2 actuator

Array responses were produced by using the new 2-D phased array algorithm for the simulated damages according to the actuator cases (Table 12). A threshold setting is applied in order to determine a more reliable damage location, because the differential array response (i.e. baseline array response – damage array response) may include unwanted waveform images due to the side lobes effect of the present spiral array configuration. The threshold-filtered differential array responses, $\psi_{d2}(t,\theta)$ defined in Equation (3.34), shown in Figure 5.29 and Figure 5.30 were reproduced by applying the threshold setting for the differential array responses for each damage case. The threshold-filtered array response results in the Figure 5.29 (for the case of “Spiral Array I” with “EC1” actuator) show that the estimated damage locations (circles in red) are in good agreement with the actual damage directions (arrows in red) on the composite panel. The actual damage location can be determined by using the directional group velocity information of the A0 mode. As one can see in Figure 5.29(c~e), there are another waveform image except for the waveform image due to wave reflection from the simulated damage. They are waveform images related to free edge boundary reflection variation due to the simulated damage on the panel. In Figure 5.29(e), the waveform image due to the damage is unable to be found, but a waveform image related to free edge boundary reflection variation is clearly indicated in the figure. By observing the differential array response shown in Figure 5.29(f), the waveform image due to the damage reflection can be found. In the same manner, the results in the Figure 5.30 (for the case of “Spiral Array II” with “EC2” actuator) show that the estimated damage locations (circles in red) are in good agreement with the actual damage directions (arrows in red) on the panel. In Figure 5.30(d), there are two waveform images in the array response. The first waveform image is due to the direct wave reflection from the simulated “D4” damage and the second waveform image is due to the boundary wave reflection after it bounces from the damage. Figure 5.31 demonstrates how the array response has two waveform images due to the one simulated damage (e.g. CL_EC2_SA2_D4).

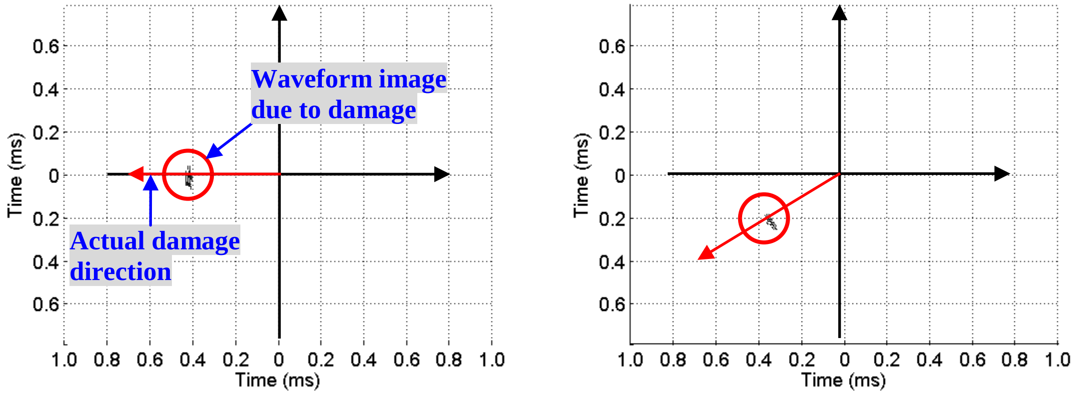

(a) CL_EC1_SA1_D1 (b) CL_EC1_SA1_D2

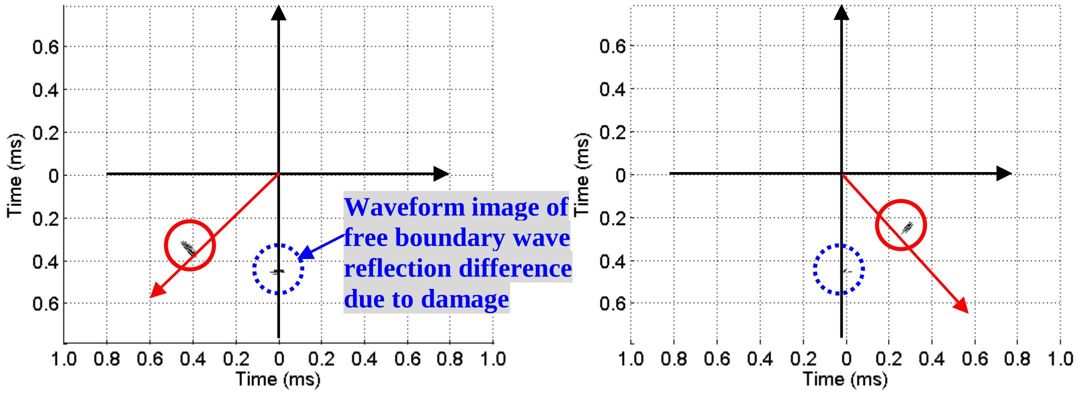

(c) CL_EC1_SA1_D4 (d) CL_EC1_SA1_D6

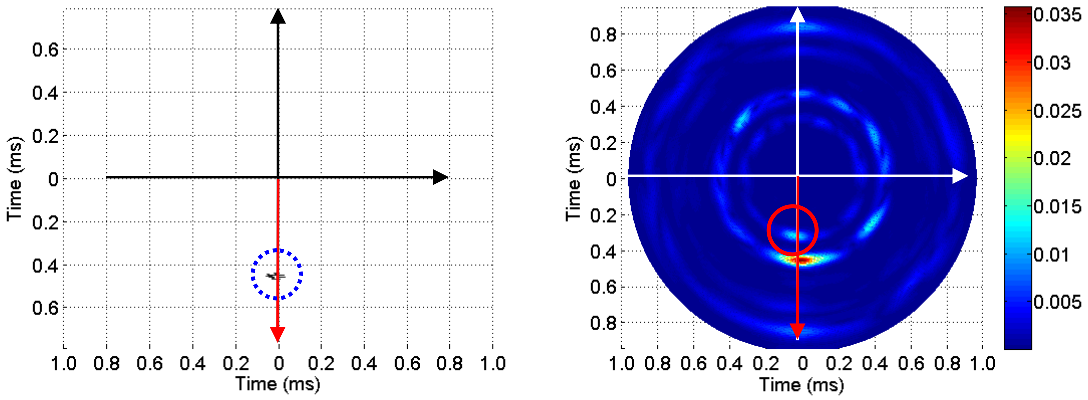

(e) CL_EC1_SA1_D5 (f) CL_EC1_SA1_D5 (Differential)

Figure 5.29: Threshold-filtered differential array response results, using EC1 actuator and Spiral array I

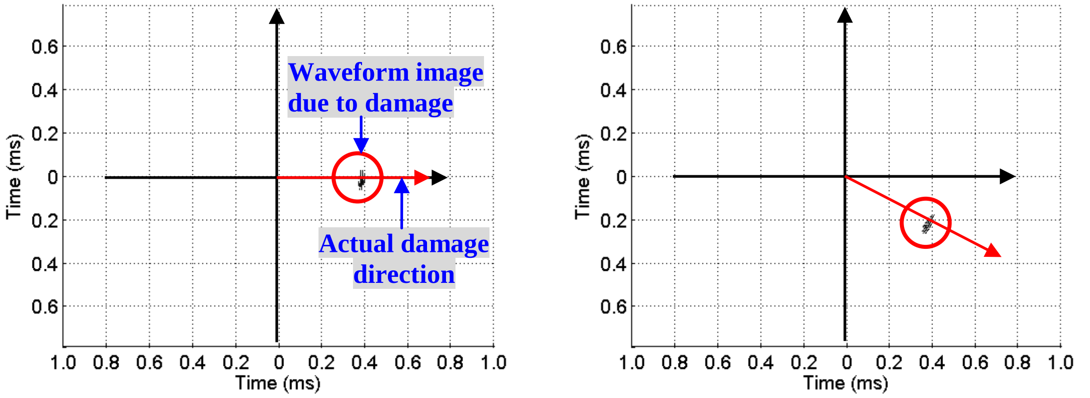

(a) CL_EC2_SA2_D1 (b) CL_EC2_SA2_D2

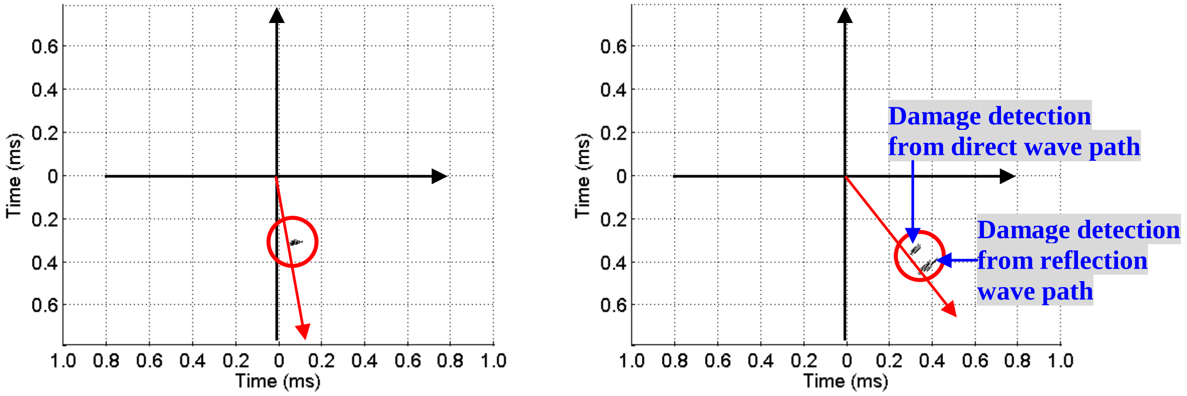

(c) CL_EC2_SA2_D3 (d) CL_EC2_SA2_D4

Figure 5.30: Threshold-filtered differential array response results, using EC2 actuator and Spiral array II

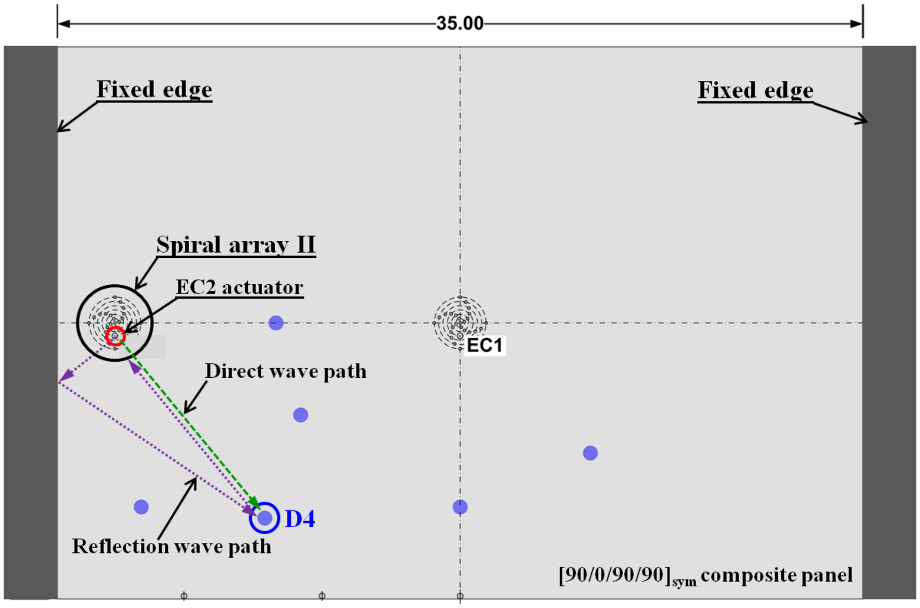

Figure 5.31: Illustration to explain the array response results for CL_EC2_SA2_D4

### 5.2.9 Vector-Based Damage Localization in Cross-ply Composite Panels

The conceptual idea of vector-based damage localization method is illustrated in Figure 5.32. The method is useful for damage detection of anisotropic panels, because we can estimate the damage location based on vectors determined by a given data analysis technique. If only one spiral array system is used to find damage in the composite panel, we need additional information to estimate the actual damage location after producing array responses with the phased array signal processing method. Because the array response was evaluated in time domain, it should be converted into the space domain by applying directional group velocity information. On the other hand, by using multiple spiral array systems, the damage location can be determined without using the directional group velocity information, shown in Figure 5.32. In this study, two spiral arrays bonded on two different locations of the cross-ply composite panel were used and two vectors, $\boldsymbol{V}_{\mathrm{SA1}}$ and $\boldsymbol{V}_{\mathrm{SA2}}$, were determined by the array response results. The intersection of the two vectors is estimated as the damage location.

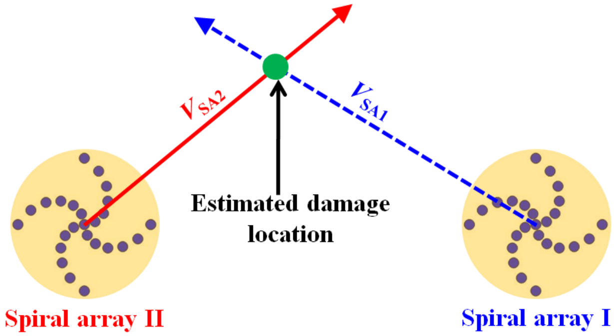

Figure 5.32: Concept of vector-based damage localization method

Damage direction vector can be evaluated by using Equation (5.4), written by

$$\begin{aligned} \psi_d(\theta) &= \sum_t \psi_d(t,\theta) \\ \theta_{\mathrm{damage}} &= \theta_{\max\,[\psi_d(\theta)]} \end{aligned} \tag{5.4}$$

where $\psi_d(t,\theta)$ is the differential array response after the new phased array signal processing.

Figure 5.33 shows the damage direction evaluation results with respect to two array responses obtained from the phased array signal processing for the same damage case (CL_EC2_SA2_D2). For the damage direction estimation with the differential array response result (Figure 5.33(a)), two excitation frequency (60 kHz and 80 kHz) cases were normalized and averaged. On the other hand, two excitation frequency cases were summed for the damage direction estimation with the threshold-filtered differential array response result (Figure 5.33(b)). The maximum value direction (a big arrow in green) is estimated as s damage direction. The result in the Figure 5.33 shows the estimated damage directions based on two array responses are identical. For an easy identification of the simulated damage location, a threshold-filtered differential array response is used to deteremine a damage direction.

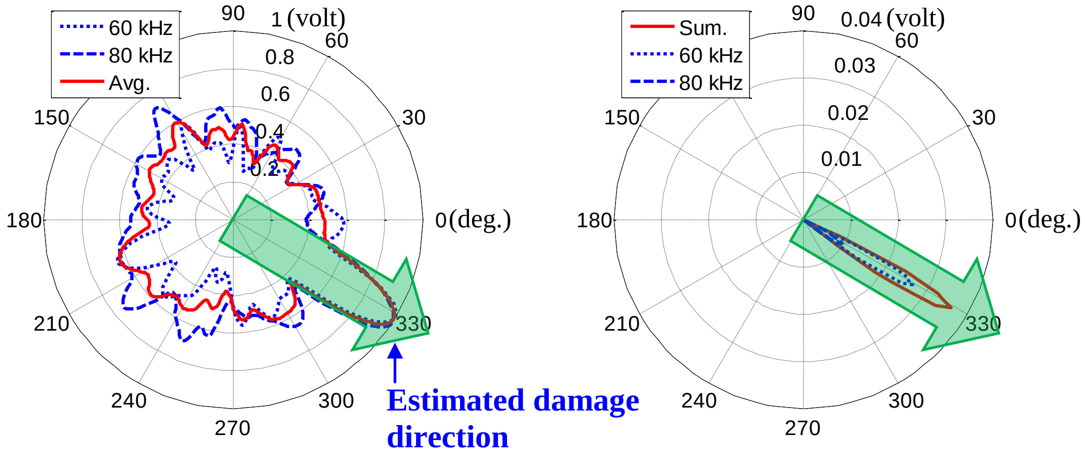

(a) With differential array response

(b) With threshold-filtered differential array response

Figure 5.33: Comparison of damage direction evaluation for CL_EC2_SA2_D2 damage case

In the Figure 5.28, there are three damage cases (D1, D2, and D4) in the intersection area of the two ellipses (i.e. damage detection coverage). For the three damage cases, the threshold-filtered differential array responses were determined for each spiral array and the associated actuator. From the array response results, the damage direction vectors can be determined, shown in Figure 5.34.

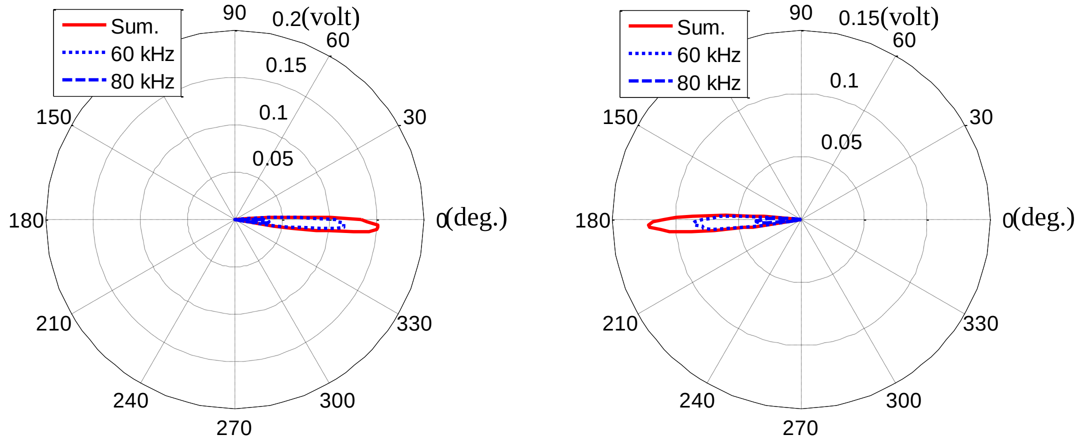

(a) CL_EC2_SA2_D1 (b) CL_EC1_SA1_D1

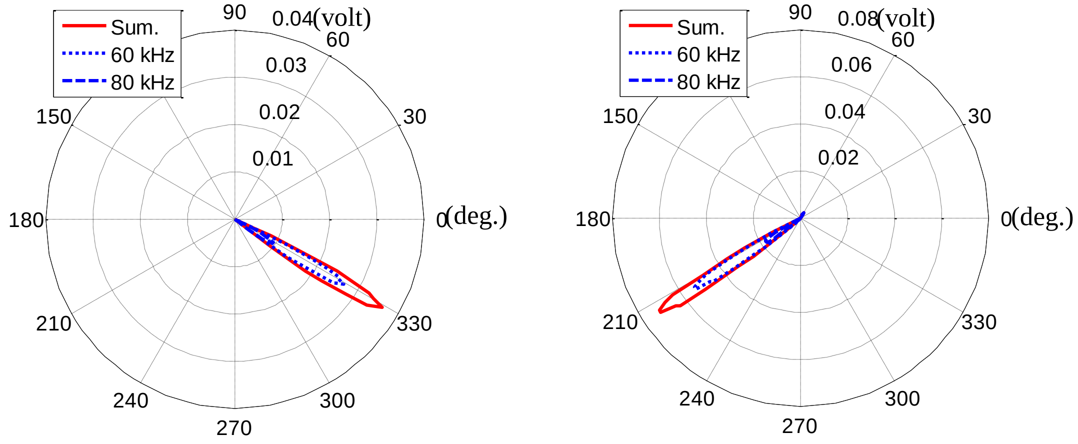

(c) CL_EC2_SA2_D2 (d) CL_EC1_SA1_D2

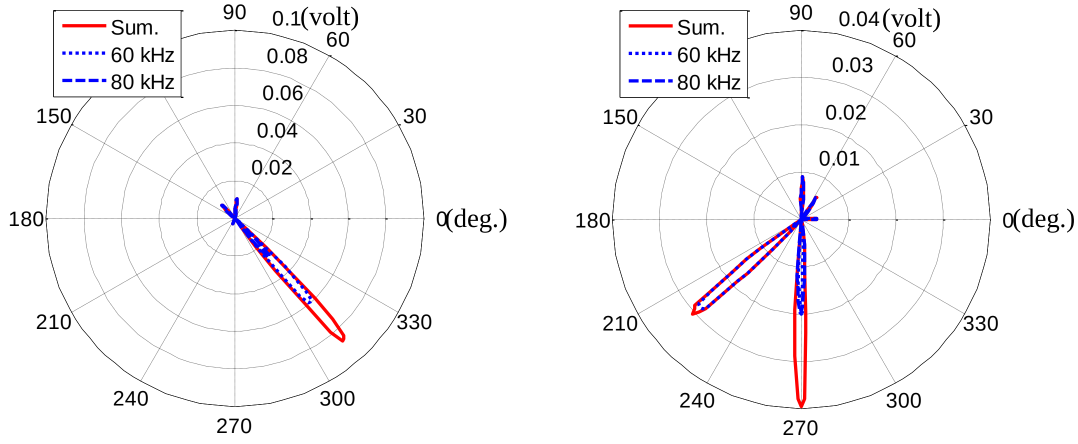

(e) CL_EC2_SA2_D4 (f) CL_EC1_SA1_D4

Figure 5.34: Damage direction evaluation based on the threshold-filtered differential array response results for D1, D2, and D4 damage cases

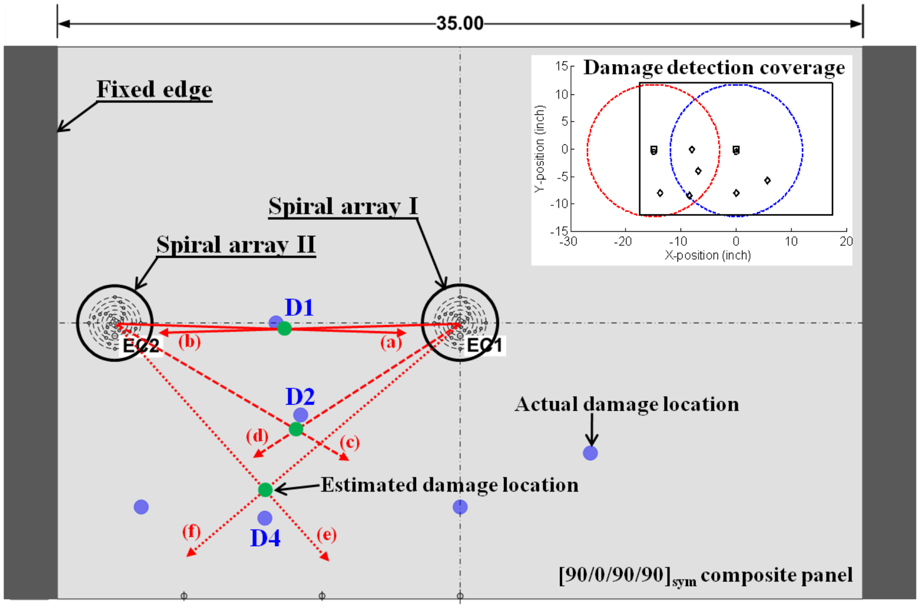

Figure 5.35: Damage location estimation based on intersection of two vectors obtained from threshold filtered differential array response results

Two damage directions can be determined for the case of “CL_EC1_SA1_D4”. Instead, only one intersection within the panel geometry can be found by exploring two results of the Figure 5.34(e) and (f). The intersection of two vectors according to the same damage can be estimated based on the damage direction results from the Figure 5.34. The damage direction vectors for the three damage cases are found in Figure 5.35. The blue filled circles are the simulated damage locations. The intersection locations (filled green circles) are estimated as the damage locations on the panel. From the result, the vector-based method with sensor array systems shows its capability of damage localization.

## 5.3 *Chapter Summary*

In this chapter, a new 2-D phased array signal processing algorithm was developed for structural health monitoring (SHM) application to thin orthotropic composite panels. In previous researches conducted by the authors, a directional wavenumber filtering technique (i.e. one of the phased array signal processing methods) using piezoelectric 2-D spiral phased sensor array combined with guided Lamb wave (GLW) approach has been developed and successfully applied to damage detection/evaluation of thin isotropic panels.

However, the original algorithm of the directional wavenumber filtering technique is limited in its application to anisotropic panels (e.g. composite panels), because the GLW propagation speed is dependent on material properties which are closely related to the wave propagation direction in composite panels. In this study, the new 2-D phased array algorithm was developed by applying experimental wavenumber curves and wavefront curves to the same algorithm structure of the original 2-D phased array signal processing. The wavenumber curves and the wavefront curves were experimentally determined for the unidirectional and cross-ply composite panels.

The new 2-D phased array signal processing algorithm was validated by identifying multiple off-centered excitation sources in the baseline array response results. In addition, the new algorithm was used for damage detection of the thin unidirectional and cross-ply composite panels. The differential array response results demonstrate that the 2-D spiral phased array technique is capable of being used as an effective SHM tool not only for metallic panels, but also orthotropic composite panels.

In addition, a vector-based damage localization method with multiple spiral phased arrays was proposed to identify damage location with limited information obtained from the array response results. The results showed the damage location can be estimated by using damage direction vectors, without using the directional group velocity information.

# 6. Concluding Remarks

## 6.1 *Conclusions and Contributions*

Even though there are many guided Lamb wave (GLW) based structural health monitoring (SHM) systems, a phased array method in conjunction with the GLW approach is capable to provide a damage detection technique of thin plates useful for a variety of aerospace and mechanical structures. Due to the benefit of long distance propagation of the GLW, a wide area can be covered for damage detection application. Since the phased array technique is a robust signal processing methodology to understand the GLW interrogation and the corresponding complexity, two-dimensional (2-D) sensor arrays are applied for monitoring of thin plates. A directional wavenumber filtering method is used for the phased array signal processing algorithm with a given array configuration.

The main purpose of this dissertation is to develop reliable GLW-based 2-D phased array technique and to validate the associated damage detection scheme for thin plate-like structures. The proposed damage detection technique is applied, not only for thin isotropic plates, but also for orthotropic composite laminates. The major conclusions and contributions of this study are summarized and highlighted:

1. 2-D phased arrays are examined in order to overcome limitations of a general 1-D linear phased array. Three candidate 2-D phased arrays with cruciform, circular and spiral configurations are examined in this study. Directivity functions of the three arrays are derived to investigate beam or array patterns relative to phased array signal processing. The resultant directivity functions

are evaluated based on the beamwidth of the main lobe, peak side lobe and average side lobe height. Angular direction selectivity and wavenumber selectivity of the 2-D phased arrays are estimated from the directivity function results. Among three array candidates, the 2-D spiral phased array is selected for experimental tests due to its outstanding directional wavenumber sensitivity.

2. In general, there are four different methods for beamforming techniques; directional transmission, directional reception, target focusing, and beam steering. However, all of the methods converge into one main purpose, target detection. Among the methods, this study is focused on the beam steering with the 2-D spiral phased sensor array. Two array signal processing methods such as delay-and-sum method and phased-and-addition method are commonly used for the beamforming technique. In this study, directional wavenumber filtering method based on the phased-and-addition approach is applied for the GLW inspection and the associated damage detection. The directional wavenumber filtering algorithm is performed for the GLW signal data obtained from the 2-D spiral phased array. Array response corresponding to the spiral array is produced after the directional wavenumber filtering process.
3. Differential array response is reproduced by subtracting baseline array response from damage array response. The baseline array response is determined from an experimental structure with no damage, while the damage array response is from the same structure with defects such as holes and cracks. The differential array response can enhance waveform images

bounced from damage in array response result at the same time as waveform images from boundaries which are negligible for damage detection of testing structures. In addition, damage metrics based on the differential array response are proposed and evaluated to quantify the severity of the damage in the experimental structures. The Hilbert-Huang transform (HHT) method is applied for array response result and provides additional damage identification information.

4. For experimental tests, the 2-D spiral phased sensor array is made of a piezoelectric paint (piezopaint) patch or discrete piezoelectric ceramic (piezoceramic) elements. A piezopaint-based spiral array is fabricated by creating a thin silver conductive layer of discrete electrodes onto a given piezopaint patch. A piezoceramic-based spiral array is constructed by small discrete PZT elements. Both types of the spiral arrays are bonded on one side of a plate surface by conductive epoxy or a cyanoacrylate (M-bond) adhesive.
5. The conceptual ideas of the 2-D spiral phased array and the associated signal processing technique for the directional wavenumber filtering are experimentally validated by identifying a GLW excitation source location in array response. The GLW is excited at a given source location within an aluminum plate, by using a piezoelectric ceramic (e.g. PZT) element permanently bonded onto the plate. A piezopaint-based 2-D spiral phased array is used as a sensor array and bonded to the center of one surface of the plate. The GLW has numerous modes which depend on the excitation frequency and the thickness of the hosting plate, but there are two

fundamental modes (A0 and S0) at relatively low frequency range (40 ~ 120 kHz). Since the A0 mode is dominant at the frequency range, the A0 mode of the GLW coming from the excitation location is filtered by the directional wavenumber filtering technique. The array response result demonstrates that the location of a waveform image (A0 mode) relative to the excitation source correlates to the actual GLW actuation location, so that the phased array signal processing algorithm with the 2-D spiral phase array is apparently validated.

6. For damage detection tests in this study, two types of the sensor array systems: single-actuator-based and multi-location-actuator-based 2-D spiral phased sensor array systems are used for experimental evaluations of thin plate-like structures. The main difference between the two sensor array systems is the total number of actuators and their locations with respect to the sensor array location in a testing plate.

   - For the single-actuator-based sensor array system, a spiral sensor array and one actuator are instrumented on top-side and under-side of a testing structure, respectively. The array and actuator are collocated at around center of the structure. For this case, the pulse-echo method of the non-destructive evaluation (NDE) is useful to analyze the GLW signals obtained from the sensor array. The GLW propagates A target/damage location can be directly identified from the array response after the directional wavenumber filtering process, but the distance between the target and the array center is twice larger than the actual distance because of the double traveling distance of the GLW. The GLW propagates from the actuator and bounces from a target/damage and comes back to the sensor array that is collocated with the actuator.

- For the multi-location-actuator-based sensor array system, a spiral sensor array and multiple actuators are instrumented on one side of a testing structure. The sensor array is mounted at around center of the structure, and the actuators are positioned at various locations within the structure. For this case, both of the pulse-echo and pitch-catch methods of the NDE are used to analyze the GLW signals obtained from the sensor array. In order to detect a target/damage location based on the array response result for each actuator case, an additional GLW propagation/reflection analysis technique should be implemented. For this study, ‘backward wave propagation approach’ is applied to evaluate the target/damage location within the geometry of the structure.

7. For damage detection of a thin aluminum plate, the single-actuator-based 2-D phased sensor array system is used. Piezopaint-based 2-D phased array and one 1/4 in. diameter PZT element are used as the sensor array and actuator. They are collocated at around the center of the aluminum plate. Three holes and a linear crack are simulated as structural damages. Prior to creating actual and permanent damages to the aluminum panel, a mass detection test is conducted as a preliminary investigation. The GLW excited from the PZT actuator due to a tone burst signal at a given high frequency propagates omni-directionally through the plate, and reflects from discontinuities such as edge

boundaries and structural damages. The GLW reflection signals are captured by the sensor array. The GLW signal data is post-processed by the phased array signal processing method (i.e. directional wavenumber filtering technique). To compare the array signal processing potentials of the array configuration cases, three piezopaint arrays with spiral, cruciform and circular layouts are used to evaluate the hole damage detection tests. Among the array response results, the spiral array case shows the hole damage locations more apparently and effectively than the other array configurations. The reason of these results is related to the steered directivity function discussed in the chapter 3.  For the crack damage detection, the 2-D spiral phased array is only used for the experimental evaluations. The resultant array responses show that the 2-D spiral phased array and the associated signal processing technique have high potentials to apparently detect various damages in the aluminum plate.

8. For damage detection of another thin aluminum plate, a multi-location-actuator-based 2-D phased sensor array system is implemented to improve the damage detection capability of the 2-D phased sensor array. A single-actuator-based 2-D phased sensor array system is unable to detect a linear crack, if the crack's orientation is perpendicular to the wavefront of the GLW excited from the actuator. In this condition, there are very weak GLW reflections from the crack because most of the GLW energy is transmitting through the crack damage area. To overcome this limitation of the single-actuator-based sensor array system, the multiple actuators located at various locations are used for

the experimental damage detection tests. A piezoceremic (PZT) based 2-D spiral phased array is mounted at the center of the top-side of the aluminum plate, and four PZT elements with 1/4  in. diameter are bonded at four corner locations of one quadrant section of the plate. Two types of artificial damages such as a rubber patch and linear crack are simulated in the plate. By using the phased array signal processing method with respect to the 2-S spiral array, array response results are produced for each damage case. The array response results are unable to directly indicate the damage locations due to the actuator locations. To analyze the array responses, the additional GLW evaluation method, the backward wave propagation approach, should be applied, so that the damage locations can be identified within the panel geometry. The final results of the array responses and damage location estimation show the damage detection capability of the proposed multi-location-actuator-based 2-D phased sensor array system.

9. For damage detection of thin orthotropic composite laminates, it is necessary to develop a new 2-D phased array signal processing algorithm because of the limitation of the original phased array algorithm, which is used for the SHM application to the thin isotropic plates. The original algorithm assumes that the GLW speed is independent on the propagation direction. However, the GLW speed depends on material properties which are closely related to the wave propagation direction in composite plates. The original algorithm is modified based on the conceptual idea mentioned above, and the new phased array signal processing algorithm is developed for the composite plates.

Experimental wavenumber curves and wavefront curves are used as modification parameters for the new algorithm. For this study, the wavenumber curves and the wavefront curves are experimentally determined for a unidirectional and cross-ply composite laminates. The analysis results show that the array signal processing method with the 2-D spiral phased array has high potentials to identify structural damages not only for isotropic plates, but also anisotropic composite laminates. In addition, a vector-based damage localization method with multiple spiral phased arrays is proposed to identify damage location without using the directional GLW propagation speed information.

## *6.2 Limitation of Current Method*

The array signal processing method based on the 2-D spiral phased array and the GLW inspection approach has many potential benefits, however, there are a few limitations of the current methodology as follows:

1. The directional wavenumber filtering capability is limited by the total number of sensor element in the array and the element spacing. There is a limit of the detectable damage size because of the maximum wavenumber for evalautions. In this study, the maximum wavenumber is set to $1.8(\pi/\Delta x)$ where $\Delta x$ is the sensor element spacing based on the 2-D cruciform array.
2. Differential array response yielded from the directional wavenumber filtering process may include unwanted waveform images relative to a high intensity

damage waveform image. The undesirable waveform images are due to the side lobes effect of the 2-D phased array with a given configuration.

3. The proposed GLW-based phased array technique requires a past baseline data. The differential array response is determined by subtracting the baseline array response from damage array response. If the baseline array response is corrupted by noise or any other reason, the differential array response results will be distorted so that a damage waveform image is unable to be detected apparently.
4. The size of damage waveform image in a resultant array response increases as the distance between the array center position and a damage location grows further apart, even though the actual size of the damage is identical. This is because the proposed phased array method is using the angular direction, $\theta$, for the directional wavenumber filtering algorithm.
5. In this study, experimental tests for the phased array technique are conducted with thin metallic and composite panels. However, there is a limit of the current technique when applying for more realistic structural engineering structures, which are composed of complicated structural components. A webcore sandwich composite panel may be an example of the complicated and realistic structure for various engineering fields. The GLW propagating from an actuator interacts with webcores of the panel and reflects back to a give sensor array. Also, the interacted GLW experience mode conversion and separation. Due to this complicated GLW features in those panels, it is hard to identify the damage location with current approach.

### *6.3 Recommendations of Future Research*

In order to extent the array signal processing method based on the 2-D spiral phased array and the GLW inspection approach, there are several recommended future works to explore. A few are listed as follows:

1. Additional signal processing may be performed with previous experimental test data with the listed ideas below:
    - For the directional wavenumber filtering method, the dispersive A0 mode of the GLW is used because the A0 mode is dominant at the excited frequency region. Dispersion compensation and removal methods described in chapter 2 can be applied for the GLW signals obtained from the sensor array, and array response can be evaluated by the array signal processing technique.
    - Mode conversion and separation feature due to a simulated damage is not considered in the current experimental studies. At the excitation frequency region, there are two fundamental GLW modes (S0 and A0) propagating throughout the hosting plate. The S0 mode may be considered for the damage detection applications instead of the A0 mode. This would provide a more reliable damage detection approach.
    - Adaptive array signal processing technique like the minimum variance distortionless response (MVDR) method can be used to improve the image resolution of the array response. The adaptive array signal processing technique has the ability to adjust its performance to certain directions by

using a special weighting function for the array. The MVDR-based array signal processing method can be found in chapter 3.

2. Further experimental studies can be conducted with various complicated structures by isotropic and anisotropic materials, because the current experimental tests are explored with thin simple plate structures. The GLW propagation characteristics are different for the type of structures. This would make this technique more attractive. Valuable experimental ideas are listed as follows:
    - The GLW-based phased array technique would be applied for simple plate-like structures with various thickness. Both isotropic and anisotropic plates can be tested by the current methodology. Also, the proposed technique may be applied for curved panels or pipes, which are more generally used structures made of plates. The current method can be evaluated with respect to variations in curvature of a structure.
    - For more practical engineering applications, complicated structures such as jointed/bonded structures and composite sandwich panels would be considered as testing articles for the phased array technique and the GLW interrogation.
3. Sensitivity of the current 2-D spiral phased array can be examined to evaluate the coverage range for damage detection application. This study would help to determine optimal positioning of sensor arrays and a number of array nodes. In addition, new2-D phased array architectures can be developed except for the array candidates examined in this study. The new array configuration

should improve the directional wavenumber filtering method, by solving the issue of side lobe effect and maintaining/reducing the main lobe beamwidth.

4. In order to understand the GLW propagation features for various structures, theoretical modeling study should be explored. A number of numerical methods can be used for the modeling to simulate the GLW propagation and its interaction with discontinuities of a structure. The simulation method includes finite difference method (FDM), finite element method (FEM), boundary element method (BEM), finite strip element method (FSEM), mass-spring lattice model (MSLM), spectral element method (SEM), and local interaction simulation approach (LISA). Recently, the LISA-based modeling gains popularity due to high adaptability to model complex geometries and time-efficiency for computation [140-146].

# Appendices

## A. Fundamentals of Hilbert-Huang Transform (HHT)

# A. Fundamentals of Hilbert-Huang Transform (HHT)

## *A.1 Hilbert Transform (HT)*

Hilbert transform is defined by

$$\mathrm{HT}[X(t)] = Y(t) = \lim_{\tau\to\infty}\left[\int_{-\infty}^{0-\tau}\frac{X(\tau)}{\pi(t-\tau)}d\tau + \int_{0-\tau}^{\infty}\frac{X(\tau)}{\pi(t-\tau)}d\tau\right] \tag{A.1}$$

Assuming $\int_{-\infty}^{\infty}[X(t)]^2\,dt < \infty$, Equation (A.1) becomes

$$\mathrm{HT}[X(t)] = Y(t) = \frac{1}{\pi}P\int_{-\infty}^{\infty}X(\tau)\frac{1}{t-\tau}d\tau \tag{A.2}$$

where $P$ denotes the Cauchy principal value.

It defines as the convolution of $X(t)$ with $1/t$, therefore it gives emphasis to the local properties of $X(t)$, even though $X(t)$ is transformed globally. Also it defines as a natural $\pi/2$ phase shifter, which means magnitude is unchanged, but the phase of all frequency components is changed by $\pi/2$, as shown in Figure A.1.

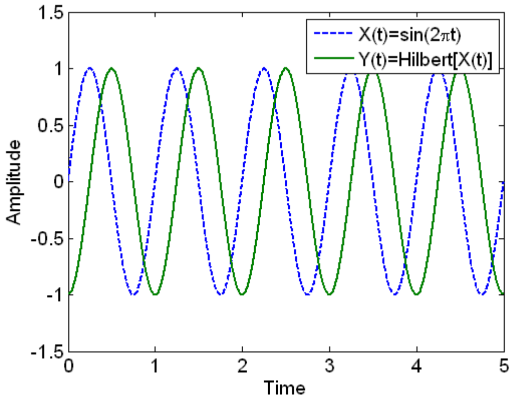

Figure A.1: Hilbert transform of sine wave

From the definition of the Hilbert transform, $Y(t)$ is the complex conjugate of $X(t)$ and the analytical signal, $Z(t)$ is defined by

$$Z(t) = X(t) + iY(t) \tag{A.3}$$

and Equation (A.3) can be rewritten in the polar coordinate system;

$$Z(t) = a(t)e^{i\theta(t)} \tag{A.4}$$

where

$$a(t) = \sqrt{X(t)^2 + Y(t)^2} \tag{A.5}$$

$$\theta(t) = \tan^{-1}\left(\frac{Y(t)}{X(t)}\right) \tag{A.6}$$

where $a(t)$ is the instantaneous amplitude and real positive value; $\theta(t)$ is the instantaneous phase.

The instantaneous frequency is defined as the rate of phase change:

$$\begin{gathered} \omega(t) = \frac{d\theta(t)}{dt} \\ f(t) = \frac{1}{2\pi}\frac{d\theta(t)}{dt} \end{gathered} \tag{A.7}$$

With the definition of instantaneous frequency, Equation (A.4) can be rewritten by

$$Z(t) = a(t)e^{i\int \omega(\tau)d\tau} = a(t)e^{i\int 2\pi f(\tau)d\tau} \tag{A.8}$$

Since the sine wave signal includes a single frequency component, the instantaneous amplitude and the instantaneous frequency are constants and the instantaneous phase angle is a linear function, as shown in Figure A.2.

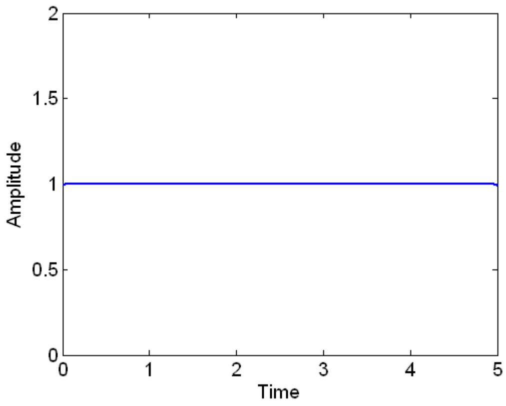

(a) Instantaneous amplitude

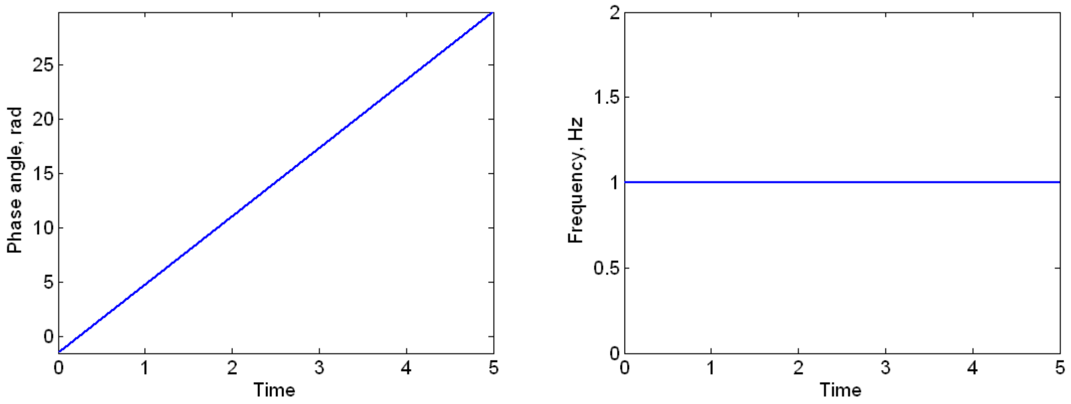

(b) Instantaneous phase

(c) Instantaneous frequency

Figure A.2: Properties of Hilbert transform of the sine wave

The “instantaneous” frequency obtained from the Hilbert transform provides ‘local’ frequency information about the signal at one time, while the frequency obtained from the Fourier transform gives ‘global’ frequency information about the signal at all times, as shown in Figure A.3.

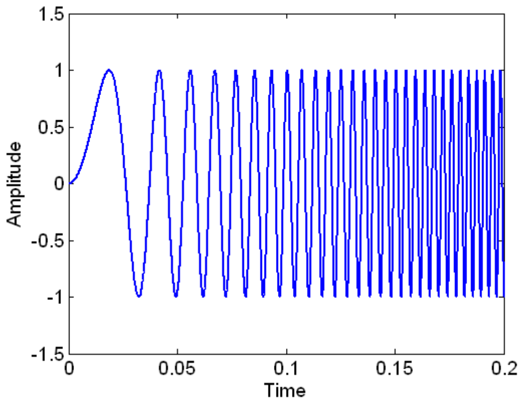

(a) Linear chirp signal

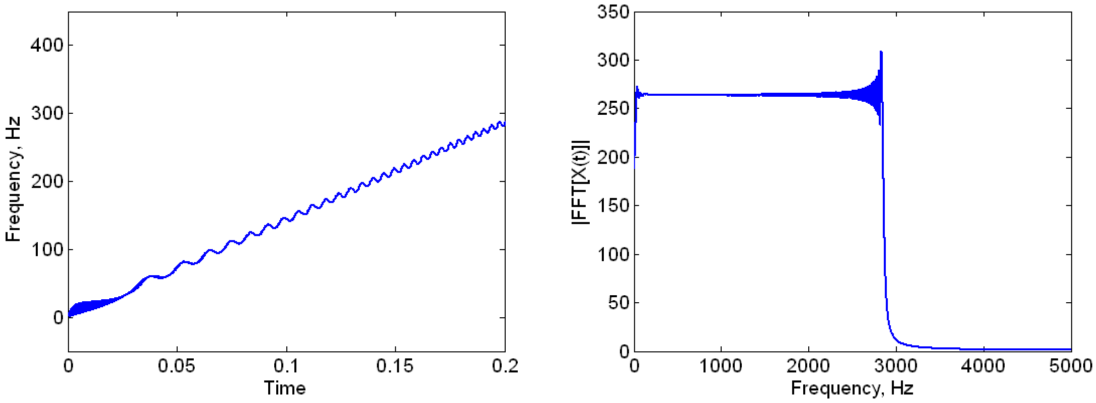

(b) Instantaneous frequency

(c) Fourier transform

Figure A.3: Analysis of linear chirp signal

The Hilbert transform gives the frequency variation in the time domain. However, when the chirp is represented in the Fourier domain the result contains a large number of various frequency components and the simple nature of the signal is lost.

In order to obtain the meaningful information, the instantaneous frequency has necessary limitations on data. The instantaneous frequency can be defined only if we can restrict the signal to be symmetrically with respect to the zero mean level and this restriction is local.

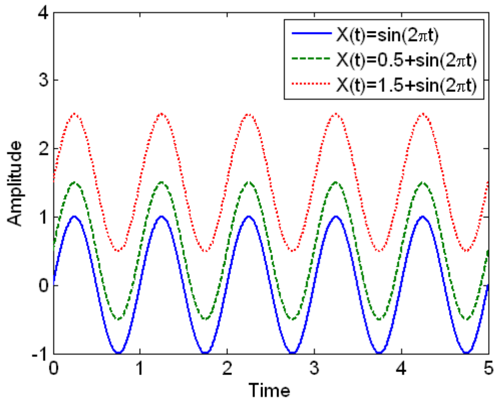

(a) Time domain sine wave signals

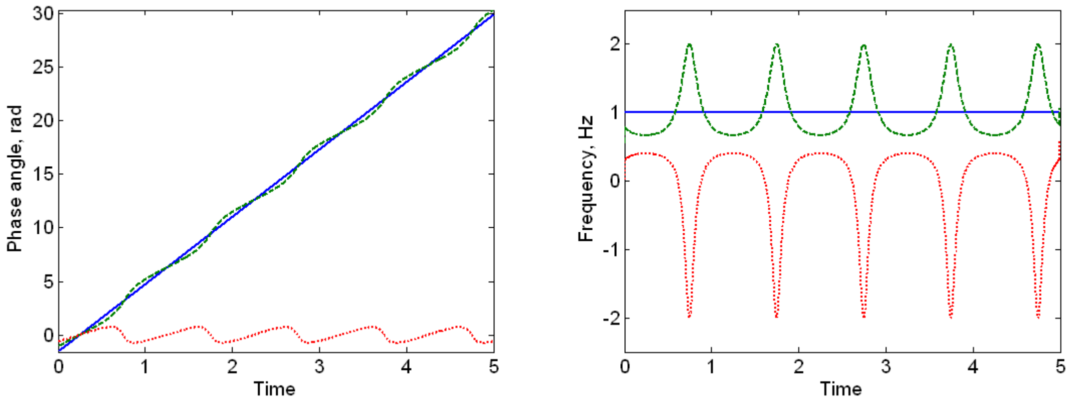

(b) Instantaneous phase

(c) Instantaneous frequency

Figure A.4: Analysis of various sine wave signals

For example, the function $X(t) = \alpha + \sin(2\pi t)$ for $\alpha = 0$, 0.5, and 1.5 can be considered (Figure A.4). By computing the instantaneous phase and the instantaneous frequency for various $\alpha$, the limitation is illustrated clearly. The instantaneous phase of $\sin(2\pi t)$ is a linear function. If we change the signal mean by adding a small amount $\alpha$, the instantaneous phase is not a linear function any more. If $\alpha < 1$, the mean zero-crossing frequency is still the same as the signal frequency. This case corresponds to any asymmetric waveform. However, if $\alpha > 1$, both the instantaneous phase and the instantaneous frequency will be assumed as negative values, which are physically meaningless. This case corresponds to any riding waves.

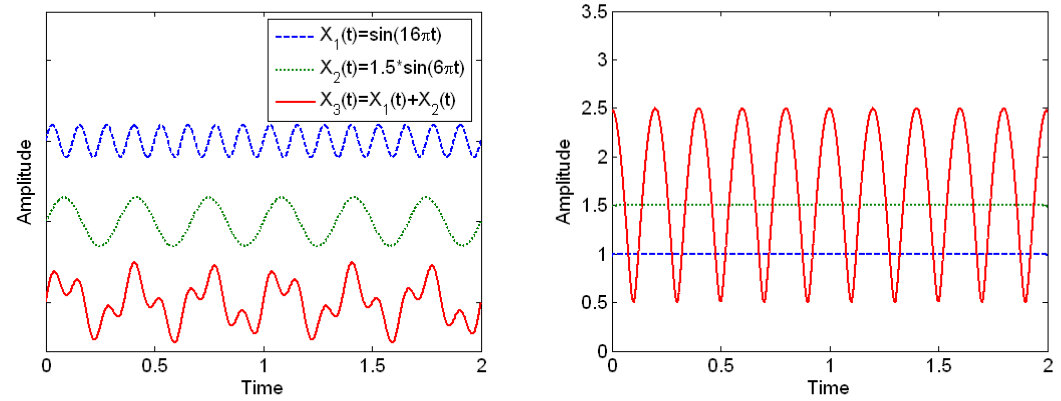

(a) Time domain signals (b) Instantaneous amplitude

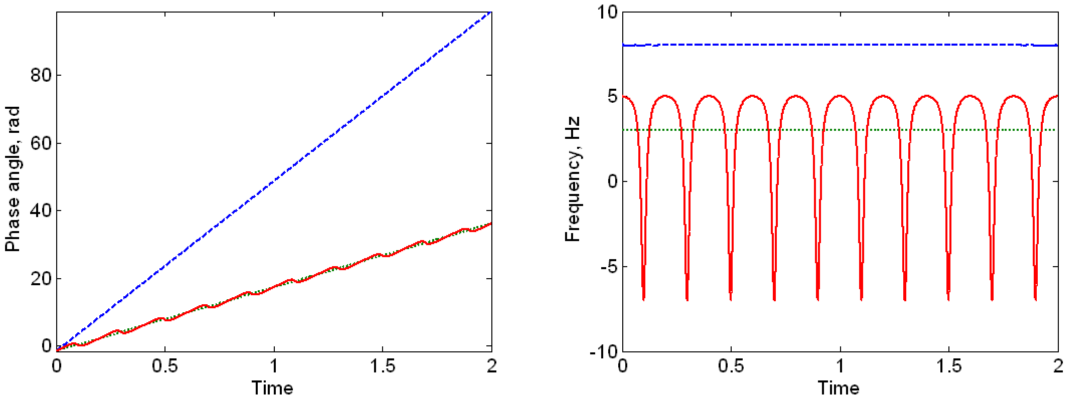

(c) Instantaneous phase (d) Instantaneous frequency

Figure A.5: Analysis of amplitude and frequency modulated signals

There is an additional limitation of the instantaneous frequency based on the Hilbert transform. The notion of instantaneous frequency implicitly assumes that, at each time instant, there exists only a single frequency component. Hence, if the time series data is the multi-component signals, the instantaneous frequency based on the Hilbert transform is meaningless. This is shown in an example in. For example, the superposition of two sine waves with different frequency modulations can be considered. At each time instant, an ideal time-frequency representation should represent two different frequencies. As shown in Figure A.5, however, the result of the instantaneous frequency is completely different.

It is necessary to introduce a new method in order to decompose any signal data into a superposition of multiple signals with well-defined instantaneous frequency. This method will have to locally eliminate riding waves and asymmetries (by using the envelope of extrema) in order to obtain a collection of monocomponent contributions.

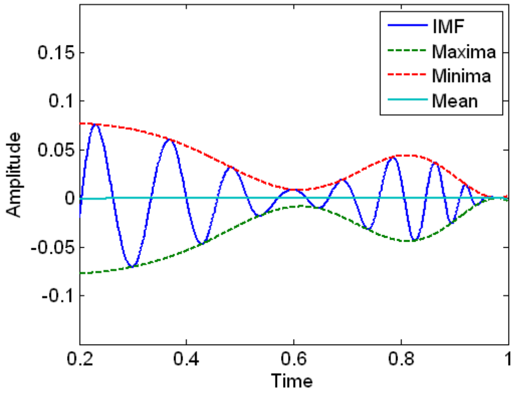

Figure A.6: Example of an Intrinsic Mode Function

### A.2 <u>Instantaneous Mode Function (IMF)</u>

An Intrinsic Mode Function (IMF) is a mono-component function and the IMF must satisfy two conditions according to Huang [83]. (1) Over the entire length of data, the number of extrema and the number of zero crossings must either be equal or differ at most by one; and (2) at any point, the mean value of the envelope defined by the local maxima and the envelope defined by the local minima is zero. An example of an IMF is plotted in Figure A.6.

IMFs represent oscillatory modes embedded within signal data where each IMF involves only one mode of oscillation with no complex riding waves present. Hence, an IMF can be non-stationary and either be amplitude or frequency modulated. Also, the IMFs always have positive frequencies since the oscillations in IMFs are symmetric with respect to the local mean.

### *A.3 Empirical Mode Decomposition (EMD)*

Empirical Mode Decomposition (EMD) method is designated to deal with nonstationary and nonlinear signals. This method is based on the simple assumption that any data consists of different simple intrinsic modes of oscillations. Using sifting process of the EMD method, a complicated experimental signal can be decomposed into a finite set of oscillatory modes, known as the Intrinsic Mode Functions (IMFs). Each IMF has meaningful instantaneous frequencies. The EMD method is based on three important assumptions as listed below:

- The signal has at least two extremas (one maximum and one minimum)
- The characteristic time scale is defined by the time lapse between the extrema
- If the data are totally devoid of extrema but contained only inflection points, then it can be differentiated once or more times to reveal the extrema.

The sifting process of EMD method includes several steps to find the IMFs from a signal, $X(t)$, shown in Figure A.7(a). The process steps are listed as follows:

1. Find all local maxima and minima by locating local peaks in the global signal as shown in Figure A.7(b).
2. Construct the upper and lower envelope by using spline interpolation of the local maxima and the local minima. They are denoted as $e_{\max}(t)$ and $e_{\min}(t)$, respectively, shown in Figure A.7(c).
3. Compute the mean of the upper envelope and the lower envelope for each time instant.

$$m_1(t) = \frac{e_{\max}(t) + e_{\min}(t)}{2} \tag{A.9}$$

   This signal is referred to as the envelop mean, shown in Figure A.7(d).

4. Subtract the envelope mean from the signal, $X(t)$.

$$h_1(t) = X(t) - m_1(t) \tag{A.10}$$

   This is the first iteration of the sifting process of the EMD and the resulting signal, $h_1(t)$ should be verified whether it is an IMF or not. The first iteration signal is shown in Figure A.7(e). The sifting process terminates when the difference between two consecutive siftings is smaller than a selected threshold, $SD$, defined by

$$SD = \sum_{t=0}^{T} \left[ \frac{\left| h_{1(k-1)}(t) - h_{1k}(t) \right|^2}{h_{1(k-1)}^2(t)} \right] \tag{A.11}$$

5. If $h_1(t)$ is not an IMF, iterate by repeating the sifting process from step (1) with the resulting signal, $h_1(t)$. In the second iteration of the sifting process, $h_1(t)$ is therefore treated as the input signal data,

$$h_{11}(t) = h_1(t) - m_{11}(t) \tag{A.12}$$

6. Repeat this sifting procedure $k$ times, until the $h_{1k}(t)$can be considered as an IMF by satisfying the desired stop criterion.

   $$h_{1k}(t) = h_{1(k-1)}(t) - m_{1k}(t) \tag{A.13}$$

   Finally, the first IMF is determined as

   $$C_1(t) = h_{1k}(t) \tag{A.14}$$

   The first IMF of the original signal is shown in Figure A.7(f). After obtaining the first IMF $C_1(t)$, the residue $r_1(t)$ is computed by subtracting the first IMF from the original signal, $X(t)$.

   $$r_1(t) = X(t) - C_1(t) \tag{A.15}$$

   The residue (Figure A.7(g)) will be used as the new input signal instead of $X(t)$.

7. The next IMF is found by starting over from step (1) with the residue.

The sifting process of the EMD is completed when the final residue is either a constant or a monotonic function that does not include any extrema. The original signal can be expressed as the sum of the IMFs and the final residue.

$$X(t) = \sum_{j=1}^{n} C_j(t) + r_N(t) \tag{A.16}$$

where $C_j(t)$ is the *j*-th intrinsic mode function and $r_N(t)$ is the last residue that is a constant or a monotonic function, shown in Figure A.7(h).

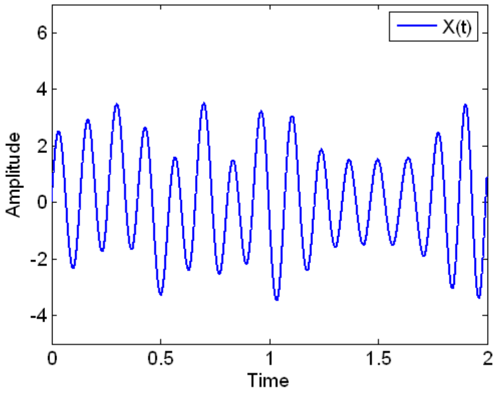

(a) Input signal

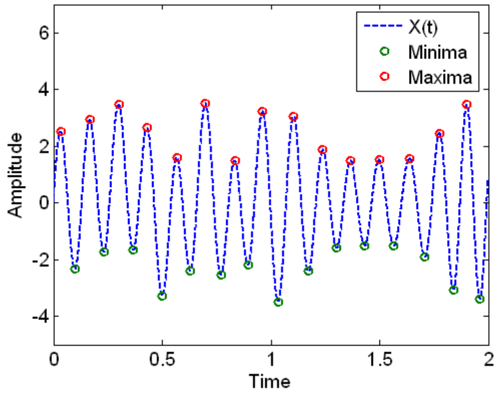

(b) Finding extrema

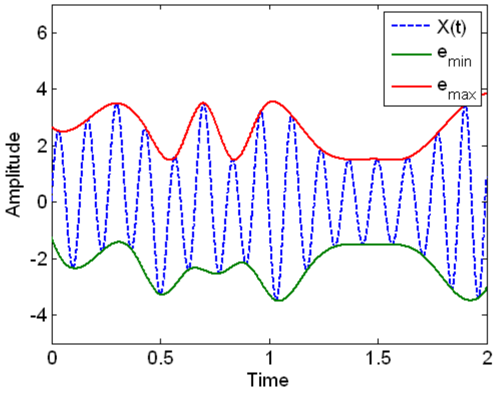

(c) Constructing envelopes

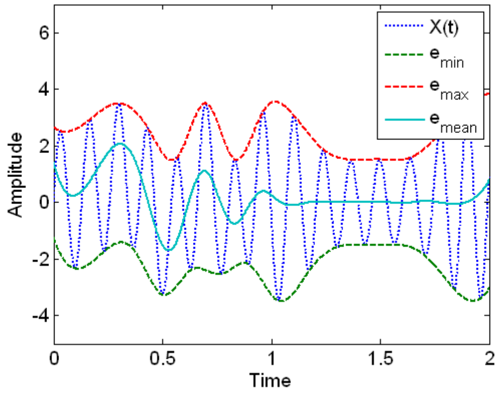

(d) Finding envelope mean

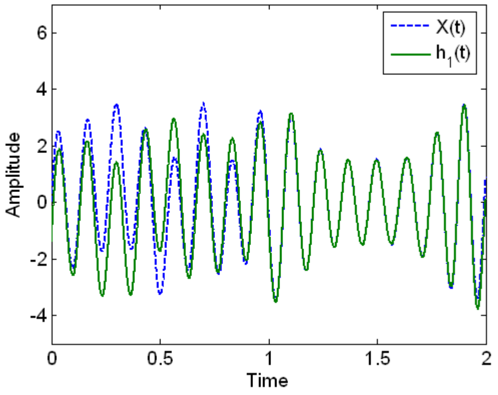

(e) Signal after one iteration

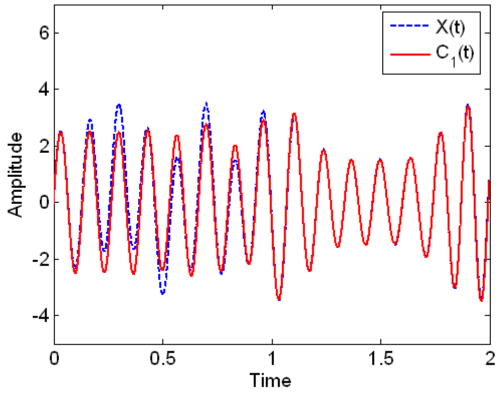

(f) First IMF

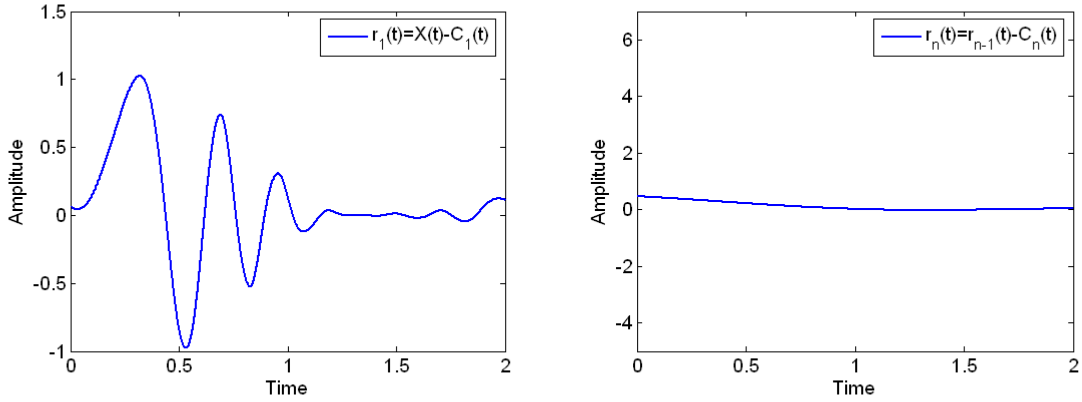

(g) Residue (h) Final residue

Figure A.7: Steps in Empirical Mode Decomposition

As shown in the Figure A.7, the sifting process serves two purposes: to eliminate riding waves in the input signal and to make the wave profiles more symmetric. The first purpose is designed for separating the intrinsic modes with meaningful instantaneous frequencies, and the second purpose is for the case the neighboring wave amplitudes have too large a disparity. The sifting process step should be set to a limit in order to preserve the natural amplitude variations of the oscillatory modes.

Another way of explaining how the EMD works is that it picks out the highest frequency oscillation that remains in the signal. Thus, locally, each IMF contains lower frequency components than the one extracted just before. The set of IMFs obtained is unique and specific for the particular time series since it is based on and derived from the local characteristics of these data. Hence, the sifting process allows one to decompose the data into *n*-empirical modes and a residue. The input signal shown in the Figure A.7(a) is decomposed into a few IMFs and a residue. The Fourier spectra of the extracted IMFs can be found in Figure A.8 and show the frequency characteristics of each mode.

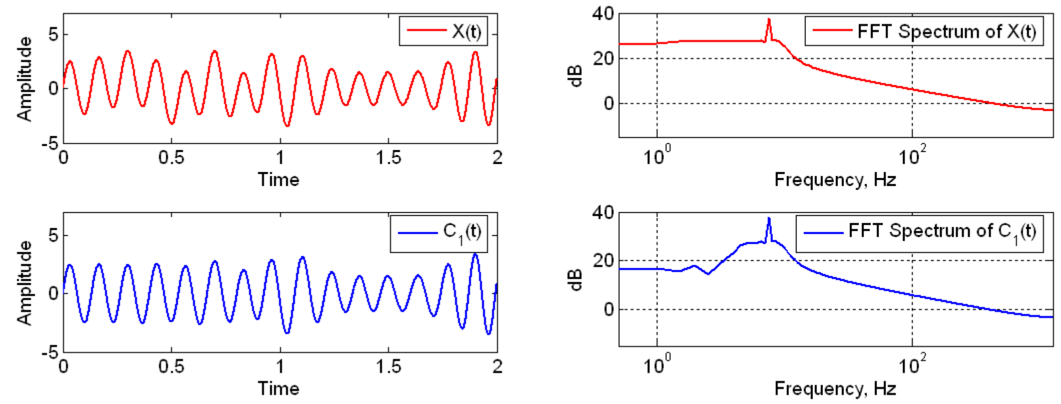

(a) Input signal and first IMF

(b) Fourier spectra of signals on left

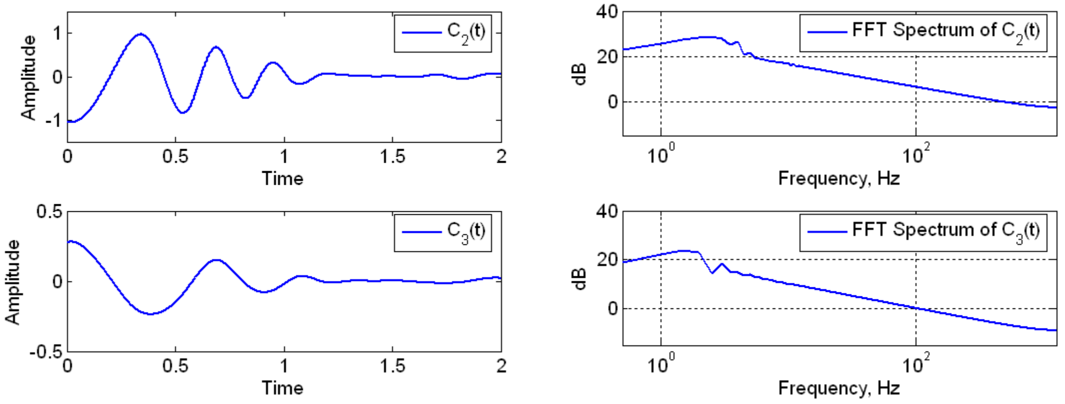

(c) Second and third IMFs

(d) Fourier spectra of signals on left

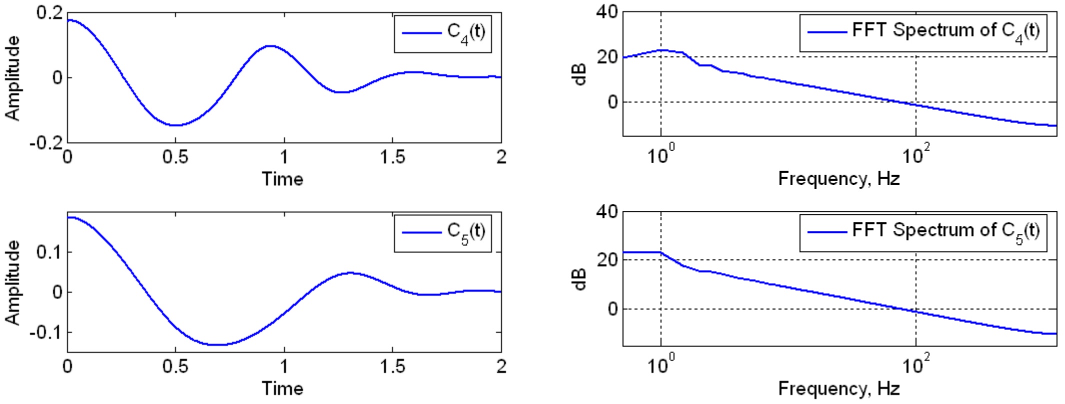

(e) Fourth and fifth IMFs

(f) Fourier spectra of signals on left

Figure A.8: Intrinsic Mode Functions and the corresponding Fourier spectra

EMD process results of an experimental sensor signal are shown in Figure A.9. Only six IMFs and a residue are plotted, and the first subplot is the original sensor signal. The unwanted frequency component negatively influences array response after the phased array signal processing, so that EMD process can be applied to eliminate the frequency component and improve the array response. The EMD denoising approach can be found in Chapter 4.

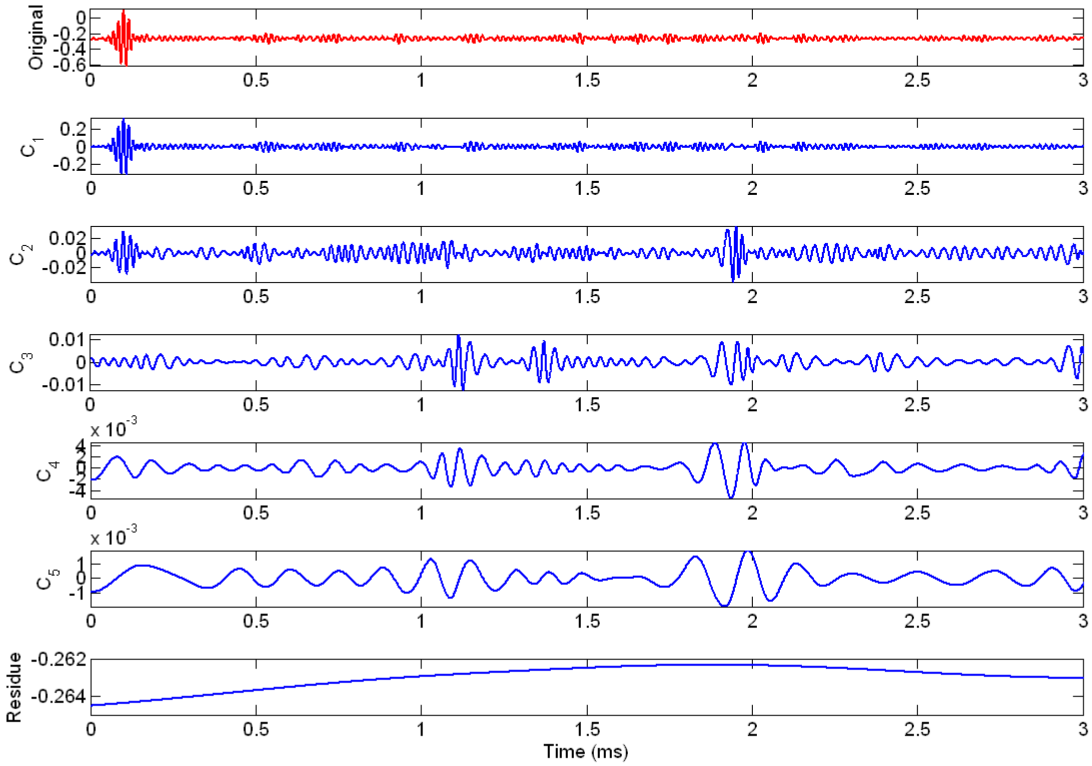

Figure A.9: EMD process results of a sample sensor signal

# Bibliography

[1] C. R. Farrar and K. Worden, "An introduction to structural health monitoring," *Philosophical Transactions of the Royal Society a-Mathematical Physical and Engineering Sciences,* vol. 365, pp. 303-315, Feb 2007.

[2] A. Rytter, "Vibration based inspection of civil engineering structures," Ph.D., Aalborg University, Denmark, 1993.

[3] A. S. Purekar, "Piezoelectric Phased Array Acousto-Ultrasonic Interrogation Of Damage In Thin Plates," Ph.D., Aerospace Engineering, University of Maryland, College Park, MD, 2006.

[4] Z. Su and L. Ye, *Identification of Damage Using Lamb Waves*: Springer, 2009.

[5] J. L. Rose, "Ultrasonic Guided Waves in Structural Health Monitoring," *Key Engineering Materials,* vol. 270 - 273, pp. 14-21, 2004.

[6] L. Rayleigh, "On Waves Propagated along the Plane Surface of an Elastic Solid," *Proceedings of the London Mathematical Society,* vol. s1-17, pp. 4-11, 1885.

[7] H. Lamb, "On Waves in an Elastic Plate," *Proceedings of the Royal Society of London. Series A, Containing Papers of a Mathematical and Physical Character,* vol. 93, pp. 114-128, 1917.

[8] I. Viktorov, *Rayleigh and Lamb Waves: Physical Theory and Applications*: New York: Plenum, 1967.

[9] D. C. Worlton, *Experimental Confirmation of Lamb Waves at Megacycle Frequencies* vol. 32: AIP, 1961.

[10] J. D. Achenbach, *Wave Propagation in Elastic Solids*: North Holland, 1975.

[11] K. F. Graff, *Wave Motion in Elastic Solids*: Dover Publications, 1991.

[12] B. A. Auld, *Acoustic Fields and Waves in Solids* vol. 1 and 2. New York: Wiley, 1990.

[13] P. Fromme, "MONITORING OF PLATE STRUCTURES USING GUIDED ULTRASONIC WAVES," *AIP Conference Proceedings,* vol. 975, pp. 78-85, 2008.

[14] P. Fromme, "Influence of guided ultrasonic wave scattering directionality on the detection sensitivity for SHM of fatigue cracks," 2010.

[15] D. E. Chimenti, "Guided Waves in Plates and Their Use in Materials Characterization," *Applied Mechanics Reviews,* vol. 50, pp. 247-284, 1997.

[16] J. L. Rose, "Guided wave nuances for ultrasonic nondestructive evaluation," *Ultrasonics, Ferroelectrics and Frequency Control, IEEE Transactions on,* vol. 47, pp. 575-583, 2000.

[17] J. D. Achenbach, "Quantitative nondestructive evaluation," *International Journal of Solids and Structures,* vol. 37, pp. 13-27, 2000.

[18] J. L. Rose, "A baseline and vision of ultrasonic guided wave inspection potential," *Journal of Pressure Vessel Technology, Transactions of the ASME,* vol. 124, pp. 273-282, 2002.

[19] C. Boller, "Ways and options for aircraft structural health management," *Smart Materials and Structures,* vol. 10, p. 432, 2001.

[20] A. J. Croxford, P. D. Wilcox, B. W. Drinkwater, and G. Konstantinidis, "Strategies for guided-wave structural health monitoring," *Proceedings of the Royal Society a-Mathematical Physical and Engineering Sciences,* vol. 463, pp. 2961-2981, Sep 2007.

[21] P. D. Wilcox, G. Konstantinidis, A. J. Croxford, and B. W. Drinkwater, "Strategies for Guided Wave Structural Health Monitoring," *AIP Conference Proceedings*, vol. 894, pp. 1469-1476, 2007.

[22] Z. Su, L. Ye, and Y. Lu, "Guided Lamb waves for identification of damage in composite structures: A review," *Journal of Sound and Vibration,* vol. 295, pp. 753-780, 2006.

[23] A. Raghavan and C. E. S. Cesnik, "Review of guided-wave based Structural Health Monitoring," *The Shock and Vibration Digest,* vol. 39, pp. 91-114, 2007.

[24] J. L. Rose, *Ultrasonic Waves in Solid Media*: Cambridge University Press, 1999.

[25] A. H. Nayfeh, *Wave Propagation in Layered Anisotropic Media with Applications to Composites*: Elsevier Science, 1995.

[26] R. M. Jones, *Mechanics of Composite Materials*: CRC Press, 1998.

[27] L. Wang and F. G. Yuan, "Group velocity and characteristic wave curves of Lamb waves in composites: Modeling and experiments," *Composites Science and Technology,* vol. 67, pp. 1370-1384, 2007.

[28] I. L. Paris, R. Krueger, and T. K. O'Brien, *Effect of Assumed Damage and Location on Delamination Onset for Skin-Stiffener Debonding* vol. 49: AHS, 2004.

[29] J. L. Rose, "A Baseline and Vision of Ultrasonic Guided Wave Inspection Potential," *Journal of Pressure Vessel Technology,* vol. 124, pp. 273-282, 2002.

[30] J. L. Rose, S. P. Pelts, and M. J. Quarry, "A comb transducer model for guided wave NDE," *Ultrasonics,* vol. 36, pp. 163-169, Feb 1998.

[31] A. A. Bent and N. W. Hagood, "Piezoelectric Fiber Composites with Interdigitated Electrodes," *Journal of Intelligent Material Systems and Structures,* vol. 8, pp. 903-919, 1997.

[32] W. K. Wilkie and J. W. High, "Method of Fabricating NASA-Standard Macro-Fiber Composite Piezoelectric Actuators," NASA2003.

[33] K. I. Salas, "Directional Transduction for Guided Wave Structural Health Monitoring," Ph.D., Aerospace Engineering, University of Michigan, 2009.

[34] J. M. Hale and J. Tuck, "A novel thick-film strain transducer using piezoelectric paint," *Proceedings of the Institution of Mechanical Engineers, Part C: Journal of Mechanical Engineering Science,* vol. 213, pp. 613-622, 1999.

[35] S. Egusa and N. Iwasawa, "Piezoelectric paints: preparation and application as built-in vibration sensors of structural materials," *Journal of Materials Science,* vol. 28, pp. 1667-1672, 1993.

[36] Y. Zhang, "Piezoelectric Paint Sensor for Nondestructive Structural Condition Monitoring," in *SEM X International Congress & Exposition on Experimental & Applied Mechanics*, Cost Mesa, CA, USA, 2004.

[37] Y. Zhang, "In Situ Fatigue Crack Detection using Piezoelectric Paint Sensor," *Journal of Intelligent Material Systems and Structures,* vol. 17, pp. 843-852, 2006.

[38] R. S. C. Monkhouse, P. D. Wilcox, and P. Cawley, "Flexible interdigital PVDF transducers for the generation of Lamb waves in structures," *Ultrasonics,* vol. 35, pp. 489-498, 1997.

[39] P. D. Wilcox, P. Cawley, and M. J. S. Lowe, "Acoustic fields from PVDF interdigital transducers," *Science, Measurement and Technology, IEE Proceedings* -, vol. 145, pp. 250-259, 1998.

[40] H. Gao, M. J. Guers, and J. L. Rose, "Flexible ultrasonic guided wave sensor development for structural health monitoring," 2006.

[41] V. Giurgiutiu, "Tuned lamb wave excitation and detection with piezoelectric wafer active sensors for structural health monitoring," *Journal of Intelligent Material Systems and Structures,* vol. 16, pp. 291-305, Apr 2005.

[42] G. B. Santoni, L. Yu, B. Xu, and V. Giurgiutiu, "Lamb wave-mode tuning of piezoelectric wafer active sensors for structural health monitoring," *Journal of Vibration and Acoustics, Transactions of the ASME,* vol. 129, pp. 752-762, 2007.

[43] A. Raghavan and C. E. S. Cesnik, "Modeling of piezoelectric-based Lamb-wave generation and sensing for structural health monitoring," in *Smart Structures and Materials 2004: Sensors and Smart Structures Technologies for Civil, Mechanical, and Aerospace Systems,* San Diego, CA, USA, 2004, pp. 419-430.

[44] A. Raghavan and C. E. S. Cesnik, "Piezoelectric-actuator excited-wave field solutions for guided-wave structural health monitoring," in *Smart Structures and Materials 2005: Sensors and Smart Structures Technologies for Civil, Mechanical, and Aerospace Systems,* San Diego, CA, USA, 2005, pp. 313-323.

[45] P. D. Wilcox, "A rapid signal processing technique to remove the effect of dispersion from guided wave signals," *Ultrasonics, Ferroelectrics and Frequency Control, IEEE Transactions on,* vol. 50, pp. 419-427, 2003.

[46] B. Xu, L. Yu, and V. Giurgiutiu, "Lamb wave dispersion compensation in piezoelectric wafer active sensor phased-array applications," 2009.

[47] L. Liu and F. G. Yuan, "A Linear Mapping Technique for Dispersion Removal of Lamb Waves," *Structural Health Monitoring,* vol. 9, pp. 75-86, 2010.

[48] M. Engholm, "Ultrasonic Arrays for Sensing and Beamforming Lamb Waves," PhD, Uppsala University, 2010.

[49] D. N. Alleyne and P. Cawley, "The measurements and prediction of Lamb wave interaction with defects," in *Ultrasonics Symposium, 1991. Proceedings., IEEE 1991,* 1991, pp. 855-857 vol.2.

[50] D. N. Alleyne and P. Cawley, "The interaction of Lamb waves with defects," *Ultrasonics, Ferroelectrics and Frequency Control, IEEE Transactions on,* vol. 39, pp. 381-397, 1992.

[51] V. Giurgiutiu, J. Bao, and W. Zhao, "Piezoelectric wafer active sensor embedded ultrasonics in beams and plates," *Experimental Mechanics,* vol. 43, pp. 428-449-449, 2003.

[52] J. B. Ihn and F. K. Chang, "Detection and monitoring of hidden fatigue crack growth using a built-in piezoelectric sensor/actuator network: I. Diagnostics," *Smart Materials and Structures,* vol. 13, pp. 609-620, 2004.

[53] J.-B. Ihn and F.-K. Chang, "Pitch-catch Active Sensing Methods in Structural Health Monitoring for Aircraft Structures," *Structural Health Monitoring,* vol. 7, pp. 5-19, 2008.

[54] D. E. Chimenti and A. H. Nayfeh, "Leaky Lamb waves in fibrous composite laminates," *Journal of Applied Physics,* vol. 58, pp. 4531-4538, 1985.

[55] D. E. Chimenti and R. W. Martin, "Nondestructive evaluation of composite laminates by leaky Lamb waves," *Ultrasonics,* vol. 29, pp. 13-21, 1991.

[56] N. Guo and P. Cawley, "The interaction of Lamb waves with delaminations in composite laminates," *Journal of the Acoustical Society of America,* vol. 94, pp. 2240-2246, 1993.

[57] C. H. Keilers and F.-K. Chang, "Identifying Delamination in Composite Beams Using Built-In Piezoelectrics: Part I—Experiments and Analysis," *Journal of Intelligent Material Systems and Structures,* vol. 6, pp. 649-663, 1995.

[58] Z. Su, L. Ye, and X. Bu, "A damage identification technique for CF/EP composite laminates using distributed piezoelectric transducers," *Composite Structures,* vol. 57, pp. 465-471, 2002.

[59] C. T. Ng and M. Veidt, "A Lamb-wave-based technique for damage detection in composite laminates," *Smart Materials and Structures,* vol. 18, 2009.

[60] S. K. Seth and et al., "Damage detection in composite materials using Lamb wave methods," *Smart Materials and Structures,* vol. 11, p. 269, 2002.

[61] S. Seung Bum Kim and Hoon, "Instantaneous reference-free crack detection based on polarization characteristics of piezoelectric materials," *Smart Materials and Structures,* vol. 16, p. 2375, 2007.

[62] C. Younho, "Estimation of ultrasonic guided wave mode conversion in a plate with thickness variation," *Ultrasonics, Ferroelectrics and Frequency Control, IEEE Transactions on,* vol. 47, pp. 591-603, 2000.

[63] Y. Cho and J. L. Rose, *A boundary element solution for a mode conversion study on the edge reflection of Lamb waves* vol. 99: ASA, 1996.

[64] I. J. Oppenheim, D. W. Greve, and N. L. Tyson, "Lamb wave behavior in bridge girder geometries," 2006.

[65] D. W. Greve, N. Tyson, and I. J. Oppenheim, "Interaction of defects with lamb waves in complex geometries," in *Ultrasonics Symposium, 2005 IEEE,* 2005, pp. 297-300.

[66] J. Fourier, *Theorie Analytique de la Chaleur,* 1822.

[67] D. N. Alleyne and P. Cawley, "A 2-dimensional Fourier transform method for the quantitative measurement of Lamb modes," in *Ultrasonics Symposium, 1990. Proceedings., IEEE 1990,* 1990, pp. 1143-1146 vol.2.

[68] W. Gao, C. Glorieux, and J. Thoen, "Laser ultrasonic study of Lamb waves: determination of the thickness and velocities of a thin plate," *International Journal of Engineering Science,* vol. 41, pp. 219-228, 2003.

[69] K. e. a. Loewke, "Signal identification in smart composite materials using the two-dimensional fast Fourier transform," *Smart Materials and Structures,* vol. 14, p. 895, 2005.

[70] D.-U. Sung, J.-H. Oh, C.-G. Kim, and C.-S. Hong, "Impact Monitoring of Smart Composite Laminates Using Neural Network and Wavelet Analysis," *Journal of Intelligent Material Systems and Structures,* vol. 11, pp. 180-190, 2000.

[71] M. Niethammer, L. J. Jacobs, J. Qu, and J. Jarzynski, *Time-frequency representation of Lamb waves using the reassigned spectrogram* vol. 107: ASA, 2000.

[72] A. Zemmour, "The Hilbert-Huang Transform for Damage Detection in Plate Structures," M.S., Aerospacing Engineering, University of Maryland, College Park, MD, 2006.

[73] W. H. Prosser, M. D. Seale, and B. T. Smith, *Time-frequency analysis of the dispersion of Lamb modes* vol. 105: ASA, 1999.

[74] S. U. Lee, D. Robb, and C. Besant, "THE DIRECTIONAL CHOI-WILLIAMS DISTRIBUTION FOR THE ANALYSIS OF ROTOR-VIBRATION SIGNALS," *Mechanical Systems and Signal Processing,* vol. 15, pp. 789-811, 2001.

[75] I. Daubechies, "The wavelet transform, time-frequency localization and signal analysis," *Information Theory, IEEE Transactions on,* vol. 36, pp. 961-1005, 1990.

[76] D. E. Newland, "Wavelet Analysis of Vibration: Part 1---Theory," *Journal of Vibration and Acoustics,* vol. 116, pp. 409-416, 1994.

[77] D. E. Newland, "Wavelet Analysis of Vibration: Part 2---Wavelet Maps," *Journal of Vibration and Acoustics,* vol. 116, pp. 417-425, 1994.

[78] K. H. Ip and et al., "Extraction of patch-induced Lamb waves using a wavelet transform," *Smart Materials and Structures,* vol. 13, p. 861, 2004.

[79] L. Fucai, M. Guang, K. Kageyama, S. Zhongqing, and Y. Lin, "Optimal Mother Wavelet Selection for Lamb Wave Analyses," *Journal of Intelligent Material Systems and Structures,* vol. 20, pp. 1147-1161, 2009.

[80] H. Jeong and Y.-S. Jang, "Wavelet analysis of plate wave propagation in composite laminates," *Composite Structures,* vol. 49, pp. 443-450, 2000.

[81] S. Legendre, D. Massicotte, J. Goyette, and T. P. Bose, "Wavelet-transform-based method of analysis for Lamb-wave ultrasonic NDE signals," in *Instrumentation and Measurement Technology Conference, 1999. IMTC/99. Proceedings of the 16th IEEE,* 1999, pp. 860-865 vol.2.

[82] C. A. Paget, S. Grondel, K. Levin, and C. Delebarre, "Damage assessment in composites by Lamb waves and wavelet coefficients," *Smart Materials and Structures,* vol. 12, pp. 393-402, 2003.

[83] N. E. Huang, Z. Shen, S. R. Long, M. C. Wu, H. H. Shih, Q. Zheng, N.-C. Yen, C. C. Tung, and H. H. Liu, "The empirical mode decomposition and the Hilbert spectrum for nonlinear and non-stationary time series analysis,"

*Proceedings of the Royal Society of London. Series A: Mathematical, Physical and Engineering Sciences,* vol. 454, pp. 903-995, 1998.

[84] S. T. Quek and et al., "Detecting anomalies in beams and plate based on the Hilbert–Huang transform of real signals," *Smart Materials and Structures,* vol. 12, p. 447, 2003.

[85] B. Yoo, D. Pines, and A. S. Purekar, "Guided Lamb Wave Interrogation of a Curved Composite Plate [0/90] Using the Hilbert-Huang Transform Approach," *ASME Conference Proceedings,* vol. 2008, pp. 239-246, 2008.

[86] D. Pines and L. Salvino, "Structural health monitoring using empirical mode decomposition and the Hilbert phase," *Journal of Sound and Vibration,* vol. 294, pp. 97-124, 2006.

[87] D. P. Jansen and D. A. Hutchins, "Lamb wave tomography," in *Ultrasonics Symposium, 1990. Proceedings., IEEE 1990,* 1990, pp. 1017-1020 vol.2.

[88] W. Wright, D. Hutchins, D. Jansen, and D. Schindel, "Air-coupled Lamb wave tomography," *Ultrasonics, Ferroelectrics and Frequency Control, IEEE Transactions on,* vol. 44, pp. 53-59, 1997.

[89] K. R. Leonard, E. V. Malyarenko, and M. K. Hinders, "Ultrasonic Lamb wave tomography," *Inverse Problems,* vol. 18, pp. 1795-1808, Dec 2002.

[90] M. Fink, "Time reversal of ultrasonic fields. I. Basic principles," *Ultrasonics, Ferroelectrics and Frequency Control, IEEE Transactions on,* vol. 39, pp. 555-566, 1992.

[91] F. Wu, J. L. Thomas, and M. Fink, "Time reversal of ultrasonic fields. Il. Experimental results," *Ultrasonics, Ferroelectrics and Frequency Control, IEEE Transactions on,* vol. 39, pp. 567-578, 1992.

[92] D. Cassereau and M. Fink, "Time-reversal of ultrasonic fields. III. Theory of the closed time-reversal cavity," *Ultrasonics, Ferroelectrics and Frequency Control, IEEE Transactions on,* vol. 39, pp. 579-592, 1992.

[93] R. K. Ing and M. Fink, "Self-focusing and time recompression of Lamb waves using a time reversal mirror," *Ultrasonics,* vol. 36, pp. 179-186, Feb 1998.

[94] H.-J. Kim, J.-H. Seo, S.-J. Song, J.-H. Kim, and H.-S. Eom, "A Study on the Time Reversal Method for Focusing Ultrasonic Guided Waves Using Array Transducers," *AIP Conference Proceedings,* vol. 894, pp. 775-782, 2007.

[95] H. W. Park, H. Sohn, K. H. Law, and C. R. Farrar, "Time reversal active sensing for health monitoring of a composite plate," *Journal of Sound and Vibration,* vol. 302, pp. 50-66, 2007.

[96] C. H. Wang, J. T. Rose, and F. K. Chang, "A synthetic time-reversal imaging method for structural health monitoring," *Smart Materials & Structures,* vol. 13, pp. 415-423, Apr 2004.

[97] B. Xu and V. Giurgiutiu, "Single Mode Tuning Effects on Lamb Wave Time Reversal with Piezoelectric Wafer Active Sensors for Structural Health Monitoring," *Journal of Nondestructive Evaluation,* vol. 26, pp. 123-134-134, 2007.

[98] J. E. Michaels, J. S. Hall, and T. E. Michaels, "Adaptive imaging of damage from changes in guided wave signals recorded from spatially distributed arrays," San Diego, CA, USA, 2009, pp. 729515-11.

[99] E. M. Jennifer, "Detection, localization and characterization of damage in plates with an in situ array of spatially distributed ultrasonic sensors," *Smart Materials and Structures*, vol. 17, p. 035035, 2008.

[100] J. E. Michaels and T. E. Michaels, "Guided wave signal processing and image fusion for in situ damage localization in plates," *Wave Motion,* vol. 44, pp. 482-492, 2007.

[101] J. E. Michaels and T. E. Michaels, "Enhanced differential methods for guided wave phased array imaging using spatially distributed piezoelectric transducers," 2006, pp. 837-844.

[102] H. e. a. Gao, "Ultrasonic guided wave tomography in structural health monitoring of an aging aircraft wing," in *ASNT Fall Conference,* Columbus, OH, 2005, pp. 412-415.

[103] X. Zhao, H. Gao, G. Zhang, B. Ayhan, F. Yan, C. Kwan, and J. L. Rose, "Active health monitoring of an aircraft wing with embedded piezoelectric sensor/actuator network: I. Defect detection, localization and growth monitoring," *Smart Materials and Structures,* vol. 16, pp. 1208-1217, 2007.

[104] F. Yan, R. L. Royer Jr, and J. L. Rose, "Ultrasonic guided wave imaging techniques in structural health monitoring," *Journal of Intelligent Material Systems and Structures,* vol. 21, pp. 377-384, 2010.

[105] F. Albiruni, J. Lee, Y. Cho, J. H. Lee, and B. Y. Ahn, "Hybrid non-contact guided wave tomography for imaging of defects in plate-like structure using a probabilistic algorithm," 2010, pp. 758-765.

[106] T. R. Hay and et al., "A comparison of embedded sensor Lamb wave ultrasonic tomography approaches for material loss detection," *Smart Materials and Structures,* vol. 15, p. 946, 2006.

[107] J. S. Hall, P. McKeon, L. Satyanarayan, J. E. Michaels, N. F. Declercq, and Y. H. Berthelot, "Minimum variance guided wave imaging in a quasi-isotropic composite plate," *Smart Materials and Structures,* vol. 20, 2011.

[108] J. S. Hall and J. E. Michaels, "Minimum variance ultrasonic imaging applied to an in situ sparse guided wave array," *Ultrasonics, Ferroelectrics and Frequency Control, IEEE Transactions on,* vol. 57, pp. 2311-2323, 2010.

[109] J. E. Michaels, J. S. Hall, G. Hickman, and J. Krolik, "SPARSE ARRAY IMAGING OF CHANGE-DETECTED ULTRASONIC SIGNALS BY MINIMUM VARIANCE PROCESSING," *AIP Conference Proceedings,* vol. 1096, pp. 642-649, 2009.

[110] W. A. K. Deutsch, A. Cheng, and J. D. Achenbach, "Self-Focusing of Rayleigh Waves and Lamb Waves with a Linear Phased Array," *Research in Nondestructive Evaluation,* vol. 9, pp. 81-95-95, 1997.

[111] P. Wilcox, M. Lowe, and P. Cawley, "Lamb and SH wave transducer arrays for the inspection of large areas of thick plates," *AIP Conference Proceedings,* vol. 509, pp. 1049-1056, 2000.

[112] P. D. Wilcox, "Omni-directional guided wave transducer arrays for the rapid inspection of large areas of plate structures," *Ieee Transactions on Ultrasonics Ferroelectrics and Frequency Control,* vol. 50, pp. 699-709, Jun 2003.

[113] P. Fromme, P. D. Wilcox, M. J. S. Lowe, and P. Cawley, "On the development and testing of a guided ultrasonic wave array for structural

integrity monitoring," *Ultrasonics, Ferroelectrics and Frequency Control, IEEE Transactions on,* vol. 53, pp. 777-785, 2006.

[114] A. S. Purekar and et al., "Directional piezoelectric phased array filters for detecting damage in isotropic plates," *Smart Materials and Structures,* vol. 13, p. 838, 2004.

[115] A. S. Purekar and D. J. Pines, "Damage Detection in Thin Composite Laminates Using Piezoelectric Phased Sensor Arrays and Guided Lamb Wave Interrogation," *Journal of Intelligent Material Systems and Structures,* vol. 21, pp. 995-1010, Jul 2010.

[116] J. Rajagopalan, K. Balasubramaniam, and C. V. Krishnamurthy, "A single transmitter multi-receiver (STMR) PZT array for guided ultrasonic wave based structural health monitoring of large isotropic plate structures," *Smart Materials & Structures,* vol. 15, pp. 1190-1196, Oct 2006.

[117] J. Vishnuvardhan, A. Muralidharan, C. V. Krishnamurthy, and K. Balasubramaniam, "SHM of orthotropic plates through an ultrasonic guided wave STMR array patch," 2008, pp. 1445-1452.

[118] J. Vishnuvardhan, A. Muralidharan, C. V. Krishnamurthy, and K. Balasubramaniam, "Structural health monitoring of anisotropic plates using ultrasonic guided wave STMR array patches," *NDT & E International,* vol. 42, pp. 193-198, 2009.

[119] V. Giurgiutiu and J. Bao, "Embedded-ultrasonics structural radar for in situ structural health monitoring of thin-wall structures," *Structural Health Monitoring-an International Journal,* vol. 3, pp. 121-140, Jun 2004.

[120] V. Giurgiutiu, L. Y. Yu, J. R. Kendall, and C. Jenkins, "In situ imaging of crack growth with piezoelectric-wafer active sensors," *Aiaa Journal,* vol. 45, pp. 2758-2769, Nov 2007.

[121] L. Yu and V. Giurgiutiu, "In situ 2-D piezoelectric wafer active sensors arrays for guided wave damage detection," *Ultrasonics,* vol. 48, pp. 117-134, Apr 2008.

[122] L. Yu and V. Giurgiutiu, "In-situ optimized PWAS phased arrays for lamb wave structural health monitoring," *Journal of Mechanics of Materials and Structures,* vol. 2, pp. 459-488, 2007.

[123] D. H. Johnson and D. E. Dudgeon, *Array signal processing: concepts and techniques*. Upper Saddle River, NJ: Prentice-Hall, 1993.

[124] F. Yan and J. L. Rose, "Guided wave phased array beam steering in composite plates," in *Proceedings of SPIE,* 2007.

[125] D. Kim and M. Philen, "Guided Wave Beamsteering using MFC Phased Arrays for Structural Health Monitoring: Analysis and Experiment," *Journal of Intelligent Material Systems and Structures,* vol. 21, pp. 1011-1024, 2010.

[126] S. E. Olson, M. P. DeSimio, and M. P. Derriso, "Beam forming of lamb waves for structural health monitoring," *Journal of Vibration and Acoustics-Transactions of the Asme,* vol. 129, pp. 730-738, Dec 2007.

[127] A. Velichko and P. D. Wilcox, "Post-processing of guided wave array data for high resolution pipe inspection," *The Journal of the Acoustical Society of America,* vol. 126, pp. 2973-2982, 2009.

[128] A. Velichko and P. D. Wilcox, "Guided wave arrays for high resolution inspection," *The Journal of the Acoustical Society of America,* vol. 123, pp. 186-196, 2008.

[129] M. Engholm and T. Stepinski, "Direction of arrival estimation of Lamb waves using circular arrays," *Structural Health Monitoring*, 2010.

[130] M. Engholm and T. Stepinski, "Adaptive beamforming for array imaging of plate structures using lamb waves," *Ultrasonics, Ferroelectrics and Frequency Control, IEEE Transactions on,* vol. 57, pp. 2712-2724, 2010.

[131] E. Marcus and et al., "Imaging and suppression of Lamb modes using adaptive beamforming," *Smart Materials and Structures*, vol. 20, p. 085024, 2011.

[132] J. Capon, "High-resolution frequency-wavenumber spectrum analysis," *Proceedings of the IEEE*, vol. 57, pp. 1408-1418, 1969.

[133] L. Yu, V. Giurgiutiu, and J. R. Kendall, "Omnidirectional guided wave PWAS phased array for thin-wall structure damage detection," in *Sensors and Smart Structures Technologies for Civil, Mechanical, and Aerospace Systems 2007, March 19, 2007 - March 22, 2007,* San Diego, CA, United states, 2007, pp. SPIE; American Society of Mechanical Engineers, ASME, USA.

[134] B. Yoo and et al., "Piezoelectric-paint-based two-dimensional phased sensor arrays for structural health monitoring of thin panels," *Smart Materials and Structures,* vol. 19, p. 075017, 2010.

[135] R. Gangadharan, G. Prasanna, M. R. Bhat, C. R. L. Murthy, and S. Gopalakrishnan, "Acoustic emission source location and damage detection in a metallic structure using a graph-theory-based geodesic approach," *Smart Materials and Structures,* vol. 18, 2009.

[136] S.-H. Rhee, J.-K. Lee, and J.-J. Lee, "The group velocity variation of Lamb wave in fiber reinforced composite plate," *Ultrasonics,* vol. 47, pp. 55-63, 2007.

[137] F. Yan, C. J. Lissenden, and J. L. Rose, "Directivity profiles of ultrasonic guided wave phased arrays for multilayer composite plates," in *Health Monitoring of Structural and Biological Systems 2009, March 9, 2009 - March 12, 2009*, San Diego, CA, United states, 2009.

[138] K. I. Salas, "Directional Transduction for Guided Wave Structural Health Monitoring," PhD dissertation ed. University of Michigan, 2009.

[139] S. S. Kessler and A. Raghavan, "Vector-based Damage Localization for Anisotropic Composite Laminates," in *The 7th International Workshop on Structural Health Monitoring*, Stanford, CA, 2009.

[140] G. Dobie, A. Spencer, K. Burnham, S. G. Pierce, K. Worden, W. Galbraith, and G. Hayward, "Simulation of ultrasonic lamb wave generation, propagation and detection for a reconfigurable air coupled scanner," *Ultrasonics,* vol. 51, pp. 258-269, Apr 2011.

[141] S. Sundararaman and D. E. Adams, "Accuracy and convergence using a local interaction simulation approach in one, two, and three dimensions," *Journal of Applied Mechanics, Transactions ASME,* vol. 76, pp. 1-10, 2009.

[142] S. Sundararaman and D. E. Adams, "Modeling guided waves for damage identification in isotropic and orthotropic plates using a local interaction

simulation approach," *Journal of Vibration and Acoustics, Transactions of the ASME*, vol. 130, 2008.

[143] B. C. Lee and W. J. Staszewski, "Lamb wave propagation modelling for damage detection: I. Two-dimensional analysis," *Smart Materials and Structures*, vol. 16, pp. 249-259, 2007.

[144] B. C. Lee and W. J. Staszewski, "Lamb wave propagation modelling for damage detection: II. Damage monitoring strategy," *Smart Materials and Structures*, vol. 16, pp. 260-274, 2007.

[145] B. C. Lee and W. J. Staszewski, "Modelling of Lamb waves for damage detection in metallic structures: Part I. Wave propagation," *Smart Materials and Structures*, vol. 12, pp. 804-814, 2003.

[146] B. C. Lee and W. J. Staszewski, "Modelling of Lamb waves for damage detection in metallic structures: Part II. Wave interactions with damage," *Smart Materials and Structures*, vol. 12, pp. 815-824, 2003.